Near-Infrared [Fe II] Emission in Starburst Galaxies

by
Kathleen Labrie
B.Sc., Université Laval, 1994

A Thesis Submitted in Partial Fulfillment of the
Requirements for the Degree of

PH.D

in the Department of Physics and Astronomy

We accept this thesis as conforming
to the required standard.

Dr. C. J. Pritchet, Supervisor (Department of Physics & Astronomy)

Dr. F. D. A. Hartwick, Departmental Member (Department of Physics & Astronomy)

Dr. D. A. VandenBerg, Departmental Member (Department of Physics & Astronomy)

Dr. D. A. Harrington , Outside Member (Department of Chemistry)

Dr. J. B. Oke, Outside Member (Herzberg Institute for Astrophysics)

Dr. R. Doyon , External Examiner (Département de physique, Université de Montréal)

Supervisor: Dr. C J. Pritchet

Abstract

We used the near-infrared [Fe II] emission line signature to detect supernova remnants (SNRs) in the nearby starburst galaxies NGC 1569, NGC 3738 and NGC 5253. The near-infrared narrow-band imaging program has led to the detection of 10 SNR candidates in NGC 1569, 7 in NGC 5253, and none in NGC 3738. A spatially extended component to the [Fe II] line emission is observed in NGC 1569 and NGC 5253. This component dominates the integrated [Fe II] luminosity in both galaxies, the compact sources accounting for 14% and 7% of the total [Fe II] luminosity of NGC 1569 and NGC 5253, respectively.

Despite the starburst environment, the [Fe II] luminosity of the individual SNRs is two orders of magnitude lower than the luminosities observed for SNRs in M82. We find that the density and the structure of the interstellar medium is a more important factor than the starburst nature of a galaxy in determining the average [Fe II] luminosity of a SNR. We caution against the blind usage of supernova rate vs [Fe II] luminosity relations, which are most often calibrated with the average luminosity of the remnants in M82.

We suggest that a significant fraction of the ISM in NGC 1569 and NGC 5253 is under the influence of SNRs. This does not appear to be the case in M82, where the impact of the SNRs is limited to high density knots. Also, we find evidence for an [Fe II]-emitting lifetime as long as $10^5\,yrs$, which contrasts with the $10^4\,yrs$ derived from SNRs in M82-like galaxies.

We find that the [Fe II] morphology, and the integrated luminosity observed in our sample galaxies, can be reproduced from a [Fe II]-emitting SNR population, as long as the pre-shock density is kept as low as $1\,cm^{-3}$. Higher pre-shock density models are strongly rejected. We find a supernova rate of $0.006\,\mathrm{SN}/yr$ for NGC 1569 and $0.005\,\mathrm{SN}/yr$ for NGC 5253.

Examiners:

Dr. C. J. Prichet, Supervisor (Department of Physics & Astronomy)

Dr. F. D. A. Hartwick, Departmental Member (Department of Physics & Astronomy)

Dr. D. A. VandenBerg, Departmental Member (Department of Physics & Astronomy)

Dr. D. A. Harrington, Outside Member (Department of Chemistry)

Dr. J. B. Oke, Outside Member (Herzberg Institute for Astrophysics)

Dr. R. Doyon , External Examiner (Département de physique, Université de Montréal)

Table of Contents

List of Tables

List of Figures

Acknowledgements

I remember a *very* cold January night, back home in Abitibi. Crazy Kathleen was outside, half frozen, with her telescope set in the front yard, desperately trying to see something interesting, anything other than yet another star. It had not been a very successful night. At least that was until her younger sister Marie-Claude joined her, maybe out of curiosity, but more likely out of sympathy. "Have you seen anything pretty?", she asked, "What's that bright star?", she added, pointing strait up to this bright shiny white dot. Although not very skilled with the telescope, Crazy Kathleen knew enough to recognize that the bright "star" did not look quite like a star. Not sure what to expect, she aimed the telescope at the mysterious object. When she peeked through the eyepiece, this large disc with faint dark bands showed up, flanked by four little dots lined up with the bands: the planet Jupiter it was.

This first sighting of Jupiter made quite an impression on me. It is on that night that, for the first time, I considered a career in astronomy. I have not steered away from that goal since. Over the years, a number of people have helped me in this endeavour, and I would like to take a moment here to thank them.

Foremost, I would like to thank my supervisor, Chris Pritchet, for his guidance, advice and financial support during my study. The extent of his knowledge, and more importantly his understanding of astronomy never ceases to amaze me. His expertise as an observer has been, without question, an invaluable asset during both the observing runs and the data reduction. Also, I wish to especially thank him for his patience over all these long years. To my committee members, I want to express my appreciation for all the comments and suggestions that were contributed. The final product has undoubtedly been greatly improved thanks to these people.

Over the years, other people have also help me achieve my goal, and I wish to officially thank them here. In particular, when I first came to Victoria, it is Luc

Simard who initiated me to the world of Unix and IRAF. As a fellow Québécois, he also helped me with overcoming the language barrier. I am also grateful to the computer gurus who have crossed my path over the years: Stephenson Yang, Robert Greimel, John Ouellette. Their infinite patience and dedication have been a tremendous help toward the completion of this work. Finally, I wish to thank the secretarial staff, past and present, for all their help whenever I had to venture in the mysterious world of Administration. Particular thanks are expressed to Gerry Blake, who's encouragement in the last few months often made a miserable day more bearable.

This acknowledgement would not be complete if I did not thank my fellow graduate students and friends for the all the good times and the great memories. From the Blue Stragglers (Editions softball, volleyball and soccer), to the always eventful camping trips, without forgetting the oddities (some precious stories are found in this category!...), they have helped make my experience here most enjoyable. I could fill pages with anecdotes and priceless stories, but I do not think I could do them justice; they need a live audience. Of the friends I made here, most are now gone, many I have not seen in years. I wish I will have the opportunity to meet them again, but no matter what happens, I will always cherish those precious moments I spent with them.

I doubt I would be a position to write this acknowledgement if it had not been for the unconditional love and support I received from my family throughout my life. As far back as I can remember, my parent, Lyna and Claude Labrie, have always encouraged me in my numerous, sometimes short-lived, interests. I feel very fortunate to have been brought up in such a loving and stimulating home. During my time here, the highlight of each week has been the weekend cross-continental phone call to home for good doses of common sense from my mother, and off-the-wall humour from my father. And I should not forget my sister Marie-Claude who keeps reminding me that there is life outside work. Her busy (this is probably an understatement) lifestyle never fails to amaze me. I am also grateful to my godmother, Jeannine Perron, for

all the happy moments we have spent together, and for offering me, a long time ago, my very first telescope.

And finally, (this is my reward!) I would like to thank myself for not giving up, and for all the sacrifices I have made to reach my goal.

My study has been in part funded by the *Fonds pour la Formation de Chercheurs et l'Aide à la Recherche* (FCAR) and the *National Science and Engineering Research Council of Canada* (NSERC).

Chapter 1

Introduction

The process of star formation is an obvious fundamental ingredient to galaxy formation and evolution; but the death of stars, as supernovae, also plays a major role that we must study to better understand, for example, how galaxies in the early universe differ from galaxies today.

The energy input to the interstellar medium (ISM) provided by supernova explosions is considerable[1]. This is particularly true during a starburst episode, when the supernova frequency is higher due to the rapid evolution of newly-formed massive stars. The expulsion of a galaxy's gas content, a possible way to explain gas-poor dwarf galaxies, is an extreme example of the impact supernovae can have on the evolution of a galaxy.

Knowing how often these powerful events happen in different types of galaxies over the history of the Universe would provide an important piece of the puzzle that is galaxy evolution.

Supernova rates are generally measured using multi-epoch observations of a large sample of galaxies. This method works well but requires a large amount of telescope time. An alternative and potentially more efficient approach to measure the supernova

[1]The initial kinetic energy of a supernova explosion is $\sim 10^{51}$ ergs. This is about 1% of the total energy of the outburst.

rate is to study supernova remnants (SNRs). A supernova is visible for a fairly limited time interval; on the other hand, a supernova remnant's interaction with the interstellar medium (ISM) will stay detectable for thousands of years.

Supernova remnants are well known as non-thermal radio synchrotron sources. They are also known for their optical emission lines. And, the youngest remnants are known to be X-ray emitters. A less known observational characteristic of supernova remnants is their emission features in the near-infrared domain, from 1 to 2.5 microns. In particular, supernova remnants display strong forbidden Fe+ emission features. The Fe+ upper levels are believed to be populated by collisional excitation of ground level Fe+ ions. This emission is much weaker in photo-ionized gas clouds.

Because the near-infrared forbidden Fe+ line emission is so characteristic of supernova remnants (Section 1.2.3), the long-term hope is to develop a reliable technique for measuring the supernova rate of a galaxy from its total near-infrared [Fe II] line emission. The general idea was first proposed by Greenhouse et al. (1991). The advantage of this technique over a standard supernova search is that the supernova rate for individual galaxies can be directly measured. This can be a great asset in the study of rapidly evolving starburst galaxies.

1.1 Evolution of a Supernova Remnant

Supernova remnant evolution can be divided into four principal stages: an ejecta-dominated phase, an adiabatic (or Sedov-Taylor) phase, then a cooling (radiative) phase, and finally a post-cooling phase in which the remnant returns to a nearly adiabatic behaviour and for which the interior pressure becomes negligible. The problem of modeling the evolution of a supernova remnant is a complex one. With improvements in computing capabilities, it is now possible to study the expansion of a remnant in various environments (e.g. non-uniform densities). The detailed evolution of a supernova remnant, with all its ramifications, is well beyond the scope of this

work, but a general understanding of each phase is essential. A quick overview is presented below.

1.1.1 Ejecta-Dominated Phase

The ejecta-dominated phase is a very early phase for which, as the name suggests, the ejecta mass and energy dominate the swept-up ambient matter. The interior pressure is, at this stage, so high that the ambient pressure is basically negligible. In other words, the supernova ejecta expands into space much like expansion *in vacuo*. The ejecta itself steadily cools down to low temperatures as internal energy is converted to kinetic energy. A young supernova remnant is a particularly strong radio-emitter. The emission mechanism that produces its radio-frequency continuum is well-understood as synchrotron emission, resulting from relativistic electrons spiraling in a magnetic field.

1.1.2 Adiabatic Phase

The transition from the first stage, the free expansion phase, to the second, the Sedov-Taylor expansion phase, is expected to occur when the mass of swept-up ISM is equal to the ejected mass. The transition diameter, D_{ST}, in parsecs, is expressed as (McKee and Truelove, 1995):

$$D_{ST} \approx 4.46 \left(\frac{M_E}{n_0} \right)^{1/3} \tag{1.1}$$

where n_0 is the ambient hydrogen number density in cubic centimeters, and M_E is the ejecta mass in solar units. At this point, the shock velocity is of the order of 10^4 km/s, and until the radiative phase sets in, the dynamics will be governed entirely by the total energy of the remnant and the ambient density.

During the Sedov-Taylor phase of evolution, the cooling is rather inefficient and the remnant is expanding adiabatically. The bulk of the explosion energy is put into

the motion of the matter, rather than into the thermal energy (e.g. Cioffi, McKee and Bertschinger, 1988). Also, at this epoch the distinction between the shell and the bubble is not rigorous, as the thin shell has not yet formed.

The problem of an intense explosion in a gas has been studied quite thoroughly — by Taylor (1950) and a few years later by Sedov (1959) — at a time when the focus of interest was more toward the behaviour of an atomic bomb than of a supernova remnant! Through a dimensional analysis of the problem, Sedov obtained a solution for the time evolution of the shock front radius, R_s, of an adiabatically expanding fireball:

$$R_s = \left(\frac{\xi E}{\rho_0}\right)^{1/5} t^{2/5} \tag{1.2}$$

where E is the initial explosion energy, ρ_0 is the ambient density, t is the time since the explosion, and the numerical constant, ξ, is found to be 2.026 for an adiabatic constant, $\gamma = 5/3$ (Ostriker and McKee, 1988). Converted to more practical units, Equation 1.2 becomes:

$$D_s(t) = 12.5\left(\frac{E_{51}}{n_0}\right)^{1/5} \left(\frac{t}{10^4\,\mathrm{yrs}}\right)^{2/5} \tag{1.3}$$

where D_s is the remnant's diameter in parsecs, E_{51} is the initial explosion energy in units of 10^{51} ergs, n_0 is the ambient number density in cm^{-3}, and t is the time since the explosion in years.

Finally, during the adiabatic phase, the shocks are defined as strong, that is the Mach number, $\mathcal{M}$, is very large. As $\mathcal{M} \to \infty$, it is found that the compression ratio — the post-shock to pre-shock ratio — approaches $(\gamma+1)/(\gamma-1)$ (e.g. McKee and Hollenbach, 1980). Therefore, for $\gamma = 5/3$, the maximum compression ratio achieved in the shock front of an adiabatic SNR is 4.

1.1.3 Radiative Phase

The next transition occurs when the shock front becomes radiative, that is when the cooling time of the shocked gas is short enough so that energy losses due to

recombination become significant. The shock velocity drops down to $< 200\,\mathrm{km/s}$ and the evolution is now governed by the conservation of momentum. This phase is also referred to as *pressure-driven snowplow* (PDS). A thin shell forms at the shock front and the remnant enters the radiative phase. The thermal energy is rapidly radiated away.

More specifically, the transition occurs near the shell-formation time, t_{sf}. Cioffi et al. (1988) defines the adiabatic to radiative phase transition time, t_{PDS}, as

$$t_{PDS} \equiv \frac{t_{sf}}{e}$$
$$t_{sf} = 3.61 \times 10^4 \frac{E_{51}^{3/14}}{\zeta_m^{5/14} n_0^{4/7}} \text{ yrs} \tag{1.4}$$

where e is the base of the natural logarithm and accounts for the effects of radiative losses on the evolution before t_{sf}, E_{51} is the initial SNR energy in units of 10^{51} ergs, ζ_m is the metallicity parameter, $Z/Z_\odot$. The diameter of the remnant at the time of transition, D_{PDS}, is given by (Cioffi et al., 1988):

$$D_{PDS} = 28.0 \frac{E_{51}^{2/7}}{\zeta_m^{1/7} n_0^{3/7}} \text{ pc} \tag{1.5}$$

After the formation of the thin shell, the remnant no longer expands adiabatically. From hydrodynamical simulations, Cioffi et al. (1988) derived an offset power-law analytic solution for the pressure-driven expansion of a supernova remnant into a homogeneous, uniform medium. The diameter of the shock wave at a time t after the explosion is given by:

$$D_s(t) = D_{PDS}\left[\frac{4}{3}\left(\frac{t}{t_{PDS}}\right) - \frac{1}{3}\right]^{3/10} \tag{1.6}$$

Re-arranging the above relation, the age of a radiative remnant can be roughly estimated from its diameter:

$$t(D) = \frac{3}{4}\left[\left(\frac{D}{D_{PDS}}\right)^{10/3} + \frac{1}{3}\right] t_{PDS} \tag{1.7}$$

The cooling of the gas occurs in the post-shock relaxation layer, behind the shock front, through inelastic collisional processes such as ionization, dissociation, collisional excitation, recombination, and molecule formation. The cooling, and the emission lines associated with it, depend on the density of the post-shock gas, and therefore on the shock compression ratio. A purely radiative shock has an index $\gamma \rightarrow 1$. We have seen above that, for strong shocks, the compression ratio approaches $(\gamma+1)/(\gamma-1)$. In contrast to the adiabatic shock, the compression ratio of a radiative remnant can reach extremely large values. In reality, however, magnetic fields prevent the compression ratio from becoming too large. In the presence of a magnetic field, the *maximum* compression ratio is given by (McKee and Hollenbach, 1980):

$$\frac{n_{max}}{n_0} = 77\left(\frac{v_s}{100\text{km/s}}\right)\left(\frac{1\mu G}{B_{0\perp}}\right) \tag{1.8}$$

where n_{max} is the maximum post-shock density, n_0 is the pre-shock density, v_s is the shock velocity in km/s, and the perpendicular magnetic field strength $B_{0\perp}$, in μG, is assumed to be proportional to ${n_0}^{1/2}$ (Mouschovias, 1976).

The compression ratio depends directly on the velocity of the shock. Cioffi et al. (1988) finds a solution for the time evolution of the shock velocity, v_s, in a radiative remnant ($t_{PDS} \leq t \leq 35\, t_{PDS}$):

$$v_s = v_{PDS}\left[\frac{4}{3}\left(\frac{t}{t_{PDS}}\right) - \frac{1}{3}\right]^{-7/10} \tag{1.9}$$

$$v_{PDS} = 413\, {n_0}^{1/7} \zeta_m^{3/14} E_{51}^{1/14} \text{ km/s} \tag{1.10}$$

where v_{PDS} is the shock velocity at the start of the radiative phase. In Figure 1.1, we illustrate the general time evolution of the shock velocity using canonical values for the ambient density, the metallicity, and the initial explosion energy. Following the onset of the radiative phase, the shock velocity drops rapidly, but soon levels off to velocities below 100 km/s. Therefore, large compression ratios are expect only at early times. Over the $t_{PDS} \leq t \leq 35\, t_{PDS}$ time period, the average *maximum* compression ratio is found to be roughly 50 (for $B_{0\perp} = 1\mu$G).

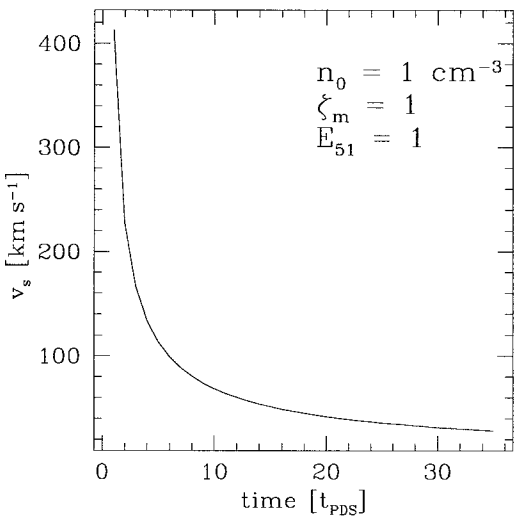

Figure 1.1: Illustrative time evolution of the shock velocity for a radiative supernova remnant using canonical values for the ambient density, the metallicity and the explosion energy. For these canonical values, $t_{PDS} \sim 1.3 \times 10^4$ yrs. The shock velocity model is from Cioffi et al. (1988).

1.1.4 Post-Cooling Phase

Because of the shell's expansion, the density eventually becomes too low for the cooling to be efficient. At some point, the rate of accumulation of thermal energy from the ambient matter due to the expansion of the shell overtakes the remnant's cooling rate. A remnant in the post-cooling phase of its evolution is characterized by a thick shell and a complex velocity profile due to wave interactions between forward and reverse waves initiated during the earlier phases.

As the bubble expands, the interior density decreases and so does the pressure. When the interior pressure is no longer larger than the unshocked ambient pressure, the momentum-conserving snowplow phase starts with $D \propto t^{1/4}$ (e.g. Cioffi et al., 1988). The remnant's evolution is now driven mainly by the acquired momentum. During this phase, the remnant is actually increasing its total and thermal energies through the accumulation of matter from its surrounding as it expands. The moment

at which this phase starts obviously depends on the temperature and density of the ambient medium. In fact, in a low density environment, the supernova remnant is actually more likely to merge with the ISM before the momentum-conserving snowplow stage can be reached.

1.2 The Origin of Near-Infrared [Fe II] Emission

1.2.1 Basic Atomic Information

There are two major infrared forbidden iron emission lines: [Fe II] λ1.257-μm ($a^6D_{9/2} - a^4D_{7/2}$) and [Fe II] λ1.644-μm ($a^4F_{9/2} - a^4D_{7/2}$). They both originate from a level at $\simeq 10^4$ K above the ground level[2]. The transitions are illustrated in a partial Grotrian diagram on Figure 1.2. The emissivity per ion for a transition ($i \rightarrow j$) is given by

$$\varepsilon(\lambda_{ij}) = \frac{N(L,S,J_i)}{N(Fe+)} A_{ij}\, h\nu_{ij} \tag{1.11}$$

where N is the number density per unit volume, A_{ij} and ν_{ij} are the probability and the frequency of the transition. Since the [Fe II] λ1.257-μm and [Fe II] λ1.644-μm lines have the same upper level (same $L\,S\,J$), their emissivity ratio is independent of electron density:

$$\frac{\varepsilon\left(\lambda_{(a^6D_{9/2}-a^4D_{7/2})}\right)}{\varepsilon\left(\lambda_{(a^4F_{9/2}-a^4D_{7/2})}\right)} = \left(\frac{A_{(a^6D_{9/2}-a^4D_{7/2})}}{A_{(a^4F_{9/2}-a^4D_{7/2})}}\right)\left(\frac{\lambda_{(a^4F_{9/2}-a^4D_{7/2})}}{\lambda_{(a^6D_{9/2}-a^4D_{7/2})}}\right) \tag{1.12}$$

Using the transition probabilities from Nussbaumer and Storey (1988), we find that $\varepsilon\,(\lambda 1.257\text{-}\mu\text{m}\,)/\varepsilon\,(\lambda 1.644\text{-}\mu\text{m}\,) = 1.36$.

For the $a^4D_{7/2}$ level, Mouri et al. (2000) have calculated the critical density for collisional de-excitation as a function of the electron temperature T_e (6000 K $\leq T_e \leq$

[2]The ground level of Fe+ is $1s^2\,2s^2\,2p^6\,3s^2\,3p^6\,3d^6\,4s$, (a^6D). Accounting for fine structure splitting, the configuration of the ground level is $a^6D_{9/2}$. The upper level of the [Fe II] λ1.257-μm and [Fe II] λ1.644-μm transitions is $a^4D_{7/2}$. The energy needed to excite the atom to $a^6D_{7/2}$ is $E = hc/\lambda(a^6D_{9/2} \rightarrow a^4D_{7/2}) = hc/1.257\mu\text{m} = 0.986\,\text{eV}$. Since the preferred excitation mechanism is collisional (see Section 1.2.3), it is appropriate to express the energy of a level as a temperature ($E = kT$, where k is the Boltzmann constant). For $a^4D_{7/2}$, $T \simeq 11\,450$ K.

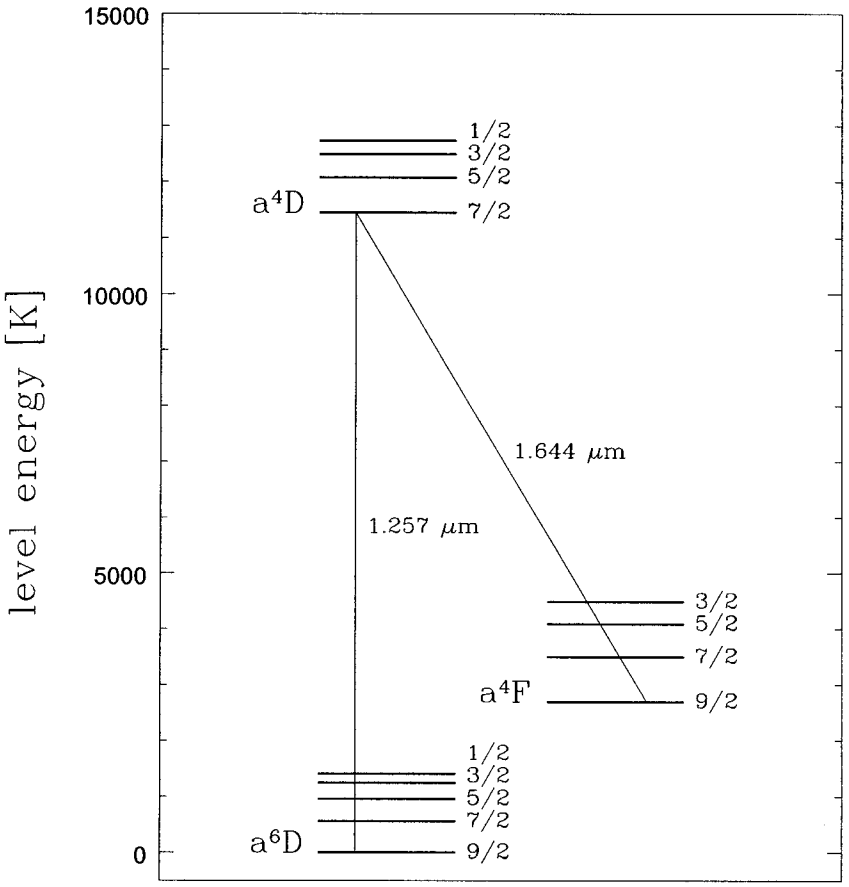

Figure 1.2: Partial Grotrian diagram for [Fe II]. The two strongest near-IR transitions are indicated. Energy levels are from Corliss & Sugar (1982).

10 000 K):

$$n_c = 5.6 \times 10^4 \left(\frac{T_e}{10\ 000\,\mathrm{K}}\right)^{0.66} \mathrm{cm}^{-3} \tag{1.13}$$

The radiative transition probabilities from Nussbaumer and Storey (1988), and the collision strengths from Pradhan and Zhang (1993) were used. As long as the electron density remains less than the critical density, the collisional de-excitation of the level is negligible.

1.2.2 Observations of Near-Infrared [Fe II] in SNRs

Seward et al. (1983) were the first to observe the [Fe II] λ1.644 μm emission line in a supernova remnant. Their low resolution spectrum of a bright knot in MSH 15-52 showed the [Fe II] line as a pronounced emission feature. A few years later, from a low resolution spectra, Graham et al. (1987) not only detected [Fe II] λ1.644 μm line emission from the remnant IC 443 but also found that the [Fe II] λ1.644 μm /Brγ line ratio was about 500 times larger than the value observed in the Orion nebula, an H II region. Subsequent near-IR spectroscopy of other SNRs in the Galaxy and in the Large Magellanic Cloud (hereafter LMC) demonstrated that strong [Fe II] λ1.644 μm emission and large [Fe II] λ1.644 μm /Brγ line ratios were common features in supernova remnants (e.g. Oliva, Moorwood and Danziger, 1989). These observations were reinforced by the detection of enhanced [Fe II] line emission spatially coincident with some non-thermal compact radio sources, believed to be supernova remnants, in M82 and NGC 253 (Greenhouse et al., 1991; Greenhouse et al., 1997; Alonso-Herrero et al., 2001; Forbes et al., 1991), and [Fe II] line emission emanating from confirmed SNRs in M33 (Lumsden and Puxley, 1995; Morel et al., 2002).

1.2.3 Excitation Mechanism in SNRs

While the association between the [Fe II] line emission and the supernova remnants is now clear, the origin of the [Fe II] emission enhancement has been, and is

still to a certain degree, debated. The problem revolves mostly around the possibility of grain destruction by the SNR shock wave.

Grain Destruction

The destruction of dust grains via sputtering has been suggested as an explanation for the enhanced [Fe II] emission (e.g. Greenhouse et al., 1997). Iron is one of the most depleted elements in the interstellar medium, and hence most interstellar iron is believed to be locked up in dust grains. A SNR shock wave can lead to grain destruction, resulting in the return of the depleted iron to the gas phase. A significant increase in the gas-phase iron abundance behind the shock would then explain the observed increase in the forbidden Fe+ line emission.

However, once a popular theory, grain sputtering is no longer believed to be the dominant process explaining the [Fe II] line emission in SNRs. The first indications arguing against the grain destruction hypothesis came from the emitting gas in Galactic and LMC supernova remnants, which was observed to be still highly depleted of iron (Oliva et al., 1989). More evidence comes from the [O I] line at $0.6300\,\mu$m which is excited by electron collision in partially ionized zones. The [Fe II] line is observed to correlate with this [O I] line (Mouri et al., 2000). The presence of a correlation suggests a similar excitation mechanism. Also, since the oxygen is largely undepleted, unlike iron, if the sputtering of iron-bearing dust grain was important, we would not expect the strength of the [Fe II] line to correlate with the [O I] line. Finally, theoretical models have shown that most silicate grains survive shocks similar to the ones observed in supernova remnants, and their survival is even more likely when the dust is made out of grains of different types and sizes as they become more difficult to accelerate (Jones et al., 1996; Jones et al., 1994).

Shock-Heating

In a recent paper by Mouri et al. (2000), the strength of the [Fe II] line emission was found to depend primarily on the ionization structure of the gas rather than on some gas-phase abundance enhancement. The ionization potential for Fe+ in only 16.2 eV. This is too low for most of the Fe+ ions to survive in a fully ionized hydrogen gas[3]. Therefore, [Fe II] line emission is not expected to be strong in such environments, for example H II regions. Rather, the [Fe II] line emission will be favoured in zones of partially ionized hydrogen in which the Fe+ ions are excited by electron collisions; the more extensive the zone is, the stronger the [Fe II] line emission is expected to be. Partially ionized zones are large when the gas is heated by X-rays (power-law photoionization) and by shocks. The first mechanism is characteristic of active galactic nuclei, like Seyfert galaxies. The second mechanism, shock heating, is dominant in supernova remnants and starburst galaxies.

In the shock-heating scenario, the partially ionized zone is heated by photons created near the shock front. The basic parameters for shock-heating calculations are the shock velocity, the pre-shock density, the pre-shock magnetic field and the metal abundance. Using values typical of shocks in radiative supernova remnant, Mouri et al. (2000) calculated the expected ionization structure, and the strength of the [Fe II] and Paβ emission lines. For the sub-solar metallicity models, they obtained good agreement with the observational data. They were able to show that over a large range in hydrogen column density, the temperature is nearly constant at 6000 K, and that in this range the gas is partially ionized. They were able to reproduce the range in the [Fe II]/Paβ ratio observed in supernova remnants. The ratio is found to be independent of the pre-shock density, and it is more or less constant for shock velocities greater than 75 km/s. This should not be interpreted as the [Fe II] line flux being also independent of these parameters. Indeed, from six SNRs in M33, Lumsden

[3]The ionization potential of neutral hydrogen is 13.6 eV.

and Puxley (1995) found that the strength of the [Fe II] line emission correlated best with the shock velocity. Since, as we have discussed above, the compression ratio in a radiative shock front is proportional to the shock velocity, it should not be a surprise that Morel et al. (2002) found a relation between the post-shock electron densities in radiative M33 supernova remnants and their [Fe II] luminosities.

Energetics of the [Fe II] Line Emission

The ratio of the [Fe II] flux to the kinetic energy of a radiative supernova remnant is found to be nearly independent of the shock velocity. The value calculated by Mouri et al. (2000), and supported by observational data, is 2×10^{-3} for the [Fe II] λ1.257-μm emission line. In other words, 0.2% of the initial kinetic energy of the explosion is radiated away as [Fe II] λ1.257-μm line flux. This estimate is valid for any radiative shocks with parameters similar to the ones observed in SNRs. Therefore, it is also applicable to wind-driven shocks, like the ones generated by the collective effect of supernova explosions in starburst galaxies.

1.2.4 [Fe II] Line Emission from Sources other than SNRs

The increased star formation rate observed in starburst galaxies implies a large number of supernova explosions. The source of the strong [Fe II] line emission observed in starburst galaxies is a combination of individual SNRs and the collective effect of the explosions as the SNRs expand further into the ISM. Starburst galaxies are also characterized by a large number of H II regions. Therefore, it is expected that the global [Fe II]/Paβ line ratio of starburst galaxies should be found somewhere between the typical values observed in SNRs and H II regions. This is indeed confirmed by the observational data (see Mouri et al., 2000 for a recent survey of the literature).

We mentioned above that Seyfert galaxies can be a source of [Fe II] line emission. In these objects, the excitation mechanism is believed to be mostly power-law pho-

toionization by X-rays from the nucleus. Some shock excitation due to the nuclear outflow could also contribute, but this process is not dominant. The [Fe II] emission is observed to be coincident with the optical narrow-line regions (Knop et al., 1996). The [Fe II]/Paβ line ratio of Seyfert galaxies is similar to the ratio observed in SNRs. However, the electron temperature in the case of power-law photoionization is predicted to be significantly higher than for shock heating (Mouri et al., 2000).

Blackbody photoionization is the dominant excitation mechanism in H II regions. Although some Fe+ ions can survive in fully ionized zones — the ionization potential of Fe+ is slightly higher than that of hydrogen by 2.6 eV — the [Fe II] flux is not expected, and not observed, to be very strong in such an environment. Also, in a H II region, the boundary between fully ionized and fully neutral hydrogen is quite thin (e.g. Osterbrock, 1989), leaving little room for a partially ionized zone. This can explain the low [Fe II]/Paβ line ratio observed, for example, in the Orion nebula (Lowe et al., 1979).

Bright [Fe II] line emission has recently been detected in the nebula around several luminous blue variables (Smith, 2002a; Smith, 2002b). A luminous blue variable (hereafter LBV) is massive star that has recently evolved off the main sequence, on its way to becoming a Wolf-Rayet star, and that is exhibiting violent mass eruptions. The typical [Fe II]/Paβ line ratio for these stars is similar to that observed in supernova remnants (Smith, 2002b). However, unlike SNRs, these [Fe II] sources are always associated with a bright star. Therefore, the risk of confusing a LBV with a supernova remnant is minimal. Because the LBV stage of the evolution of a massive star, although spectacular, is quite brief, it is unlikely that the LBV would contribute a significant fraction of the total [Fe II] emission of a starburst galaxy.

The [Fe II]/Paβ line ratio is a good diagnostic tool to distinguish between the various types of [Fe II] sources. As a reference for the upcoming discussion, Table 1.1 summarizes the typical [Fe II] λ1.644 μm /Paβ line ratio observed for each category of objects.

Table 1.1: Typical [Fe II] λ1.644 μm /Paβ line ratio for various type of astronomical objects (Mouri et al., 2000, and references therein).

Type	[Fe II] λ1.644 μm /Paβ
H II Regions (Orion)	0.009
Starburst Galaxies	0.07–0.5
Supernova Remnants	0.7–7
Seyfert Galaxies	0.2–3

1.3 Scope of the Present Study

The use of the near-infrared [Fe II] line emission for the study of supernova remnants and their environment is still relatively recent. We mentioned above that one of the interesting uses of the infrared forbidden Fe+ line emission is the measurement of the supernova rate in moderately distant galaxies. However, before one can apply [Fe II] emission to objects at large distances, a good understanding of the relation between [Fe II] line emission and supernova remnants in various environments must be achieved. This dissertation is one step in that direction.

Near-infrared narrow-band [Fe II] and Paβ images of nearby starburst galaxies were obtained in this work. The observing program is described in Chapter 2. Also in that chapter are presented details regarding the pre-processing and the calibration of the data. One of the primary goals of this project is the study of [Fe II]-emitting supernova remnants. This implies the detection of new supernova remnants in the nearby galaxies in our sample. The detailed examination and flux measurements of

the compact [Fe II] sources detected in our images are found in Chapter 3. Previous observations of the starburst galaxies NGC 253 and M82 have shown that the compact [Fe II] sources account for only a small fraction of the total [Fe II] flux in these galaxies (Forbes et al., 1993; Greenhouse et al., 1997). In this dissertation, particular attention is paid to the study of the extended component of [Fe II] line emission in our observed starburst galaxies. These measurements are also presented in Chapter 3, while the analysis and the discussion are found in Chapter 4. We wish to better understand the nature of the extended component in terms of supernova remnants. In the process, we will explore the impact of supernova remnants on the interstellar environment of star-forming galaxies. A short summary of our results and concluding remarks are presented in Chapter 5.

Chapter 2

Observations and Data Reduction

2.1 Observing Program

Narrow-band imaging of NGC 1569, NGC 3738, and NGC 5253 was undertaken at the Canada-France-Hawaii Telescope (CFHT) in January 1998. The program involved the acquisition of images using two narrow-band filters, [Fe II] $\lambda 1.644$ μm and Paβ $\lambda 1.282$ μm, and the corresponding broad-band filters, H and J. The instrument used was the REDEYE Near-IR Camera in the wide field configuration.

2.1.1 Target Selection

The purpose of the observations was to detect individual supernova remnants in near-IR [Fe II] narrow-band images of nearby star-forming galaxies, in the hope of better understanding the link between the [Fe II] line emission and the SNR population. Starburst galaxies offered us the best opportunity to detect supernova remnants since the higher star formation rate necessarily implied a high supernova rate.

The final selection of the star-forming galaxies was in many aspects steered by technical limitations imposed by the instrument, and the time available to complete the observations.

To achieve our goals, individual SNRs had to be resolved. The minimum resolvable diameter we aimed at was 10 parsecs. This requirement, combined with the coarse plate scale of the instrument, 0.5″/pixel, dictated a maximum distance to the selected galaxies of < 5 Mpc. Also, it was important that the whole galaxy be surveyed to allow us to explore the possible use of the integrated [Fe II] luminosity of a galaxy in the derivation of the current supernova rate within that galaxy. The field of view of the near-IR camera was limited to 2′. This imposed some stringent limits on the maximum angular size of the selected galaxies. Because of time constraints, no more than three fields were allowed to survey each galaxy.

Most star-forming galaxies within 5 Mpc are larger than 6′. This made object selection difficult. In the end, three interesting candidates were found: NGC 1569, NGC 3738, and NGC 5253. NGC 1569 is a post-starburst irregular galaxy, famous for its two prominent super-star clusters (SSCs). Massive star formation is still active today, but at the much slower rate of $0.4\,M_{\odot}\,yr^{-1}$ (Waller, 1991). The spectacular appearance of the galaxy underlines recent dramatic events likely caused by violent star formation episodes. A great amount of information is available for this galaxy, from the X-ray domain to radio wavelengths. Considerably less is known about NGC 3738, a small irregular galaxy hosting a few H II regions in its core where signs of ongoing star formation have been detected (Bremnes et al., 2000). Finally, NGC 5253 is a blue compact dwarf galaxy that hosts an extremely young starburst. This galaxy is particularly interesting to this project because of the apparent disagreement between the radio continuum and the [Fe II] luminosity as it relates to the supernova remnant activity. Indeed, the origin of the radio emission is observed to be mostly thermal, suggesting very few SNRs in the starburst core (Turner et al., 1998). Yet, the [Fe II] luminosity is large (Lumsden et al., 1994), which indicates a significant SNR population if the [Fe II] emission is produced solely in supernova remnants.

Some general properties of the sample galaxies can be found in Table 2.1. A more complete description of each galaxy is offered in Chapter 3.

Table 2.1: General properties of the sample galaxies.

Galaxy	Type	D (Mpc)	v_{helio} (km s^{-1})	RA	Dec	l (°)	b (°)
				(*J2000*)			
(1)	(2)	(3)	(4)	(5)	(6)	(7)	(8)
NGC 1569	IBm	2.5	-104	04:30:49.0	+64:50:53	143.7	11.2
NGC 3738	Irr	3.52	229	11:35:48.8	+54:31:26	144.6	59.3
NGC 5253	Im pec	3.33	404	13:39:55.9	−31:38:24	314.9	30.1

Col. (2).– Galaxy morphological type from RC3 (de Vaucouleurs et al., 1991).

Col. (3).– Adopted distance to the galaxy. NGC 1569: O'Connell et al. (1994); NGC 3738: Georgiev et al. (1997); NGC 5253: Gibson et al. (2000).

Col. (4).– Galaxy heliocentric systemic velocity. NGC 1569: Schneider et al. (1992); NGC 3738 and NGC 5253: RC3 (de Vaucouleurs et al., 1991).

Col. (5)-(6).– Galaxy equatorial coordinates. NGC 1569: Clements (1983); NGC 3738: 2MASS (2000); NGC 5253: Beck et al. (1996).

Col. (7)-(8).– Galaxy galactic coordinates. Same references as for the equatorial coordinates.

2.1.2 Description of the Observations

The near-IR domain of the electromagnetic spectrum (1–2.5 μm) lies sufficiently close to the optical domain to require instruments and observing techniques similar, to some degree, to the ones used for optical observations. However, there are some important differences that need to be addressed. One important factor to keep in mind is the rapid variation in sky brightness caused by OH lines in the atmosphere. There is also the problem of the sensitivity of the camera to its own thermal radiation ($\lambda > 2\mu$m) caused by warm components, both along the optical path and in the electronics[1]. Finally, near-IR cameras are usually plagued by stronger instrumental effects (e.g. dark current, read-out noise, etc.) than CCD cameras. Fortunately, the new generation of near-IR cameras is considerably better than the now-retired Redeye camera used for this research project.

[1]We minimized this problem by choosing to observe the Paβ λ1.282 μm hydrogen recombination line over the Brγ λ2.166 μm line (see *Filter Selection* later in this section).

The REDEYE near-IR camera on CFHT

The camera houses a NICMOS3 Hg:Cd:Te infrared array detector manufactured by Rockwell International Science Center. The array is 256×256 pixels wide, each pixel being 40 μm in size. This yields a detector that is 10.24×10.24 mm across. The charges are switched out into one of 4 amplifiers located at the corners of the array. The array is physically composed of four 128×128-pixel sub-arrays that are electronically isolated from each other. The technical specifications for the Redeye camera in its wide-field configurations are summarized in Table 2.2.

The Redeye detector is read out in a different manner than that used with CCDs. After a reset to clear all charges, the array is read out twice. The second read-out is kept in memory. The shutter then opens to take the exposure. At the end of the exposure the array is read out twice. Again, only the second read-out is kept. The read-out stored at the beginning of the exposure is subtracted from the second exposure read-out. As a result, the image that is actually stored on disk has already been corrected for the DC or bias offset.

An important aspect of the optical design of the camera is that the detector itself is not located at the focal plane of the telescope. Rather, the focal plane is coincident with the front apex of the field lens at the front of the camera enclosure. The next optical elements are the filter and a cold stop that reduces the background. Then, the beam is re-imaged onto the array. This configuration has an impact on the final images taken with different filters: a slight variation in the effective plate scale is observed. This became significant when we aligned the broad-band and narrow-band images, in preparation for the continuum subtraction, as the registration required a magnification term in addition to the translation term.

Table 2.2: REDEYE wide field camera specifications. The values are taken from the *Redeye CFHT Infrared Camera Manual* Version 2.0 (March 1994).

Parameter	Units	Value
array format	pixels	256×256
pixel size	μm	40
plate scale	$''$/pixel	0.5
field of view	$''$	128
full well	ADU	20 000
system gain	e^-/ADU	15
read noise	e^-	50
max signal for linearity		~90% full well
dark current	e^-/sec	1[a]

[a] We found a much different value for the dark current. See Section 2.2.1.

Filter selection

A good diagnostic tool to confirm the nature of an [Fe II] source is the ratio of an [Fe II] emission line to a hydrogen recombination line. As explained in the Introduction (Section 1.2), this ratio is typically at least an order of magnitude larger for supernova remnants than it is for H II regions. There are [Fe II] and hydrogen recombination lines in the optical regime but they are found among a jungle of other lines of similar intensity. On the other hand, in the near-IR, the [Fe II] and hydrogen lines stand out as the dominant emission lines, making narrow-band imaging of these lines much easier. Also, the near-IR radiation has the advantage of being able to probe much deeper into the dusty starburst environments than the optical radiation, since longer wavelengths are less affected by extinction.

The two most prominent [Fe II] emission lines in the near-IR domain are the λ1.257-μm ($a^6D_{9/2} - a^4D_{7/2}$) line in the J-band and the λ1.644-μm ($a^4F_{9/2} - a^4D_{7/2}$) line in the H-band. Ideally, it would be preferable to use the λ1.257-μm line over the λ1.644-μm line since, first, the λ1.257-μm line is stronger by a factor of 1.36

over the $\lambda 1.644$-μm line (Prahdan and Zhang, 1993), and second, the proximity to the Paβ line almost eliminates the need for reddening corrections to the line ratio. Unfortunately, $\lambda 1.257$-μm narrow-band filters are, for some reason, not part of the basic filter set of many observatories, CFHT included. We had to resort to the more commonly available [Fe II] $\lambda 1.644$-μm filter.

The brightest hydrogen recombination lines found in the near-IR window are the Brγ $\lambda 2.166$ μm and Paβ $\lambda 1.282$ μm lines. Because the Brγ line is found in the K window, where the sky background is bright and particularly variable, we chose to use the Paβ line. Also, at a temperature of 10 000 K and an electron density of $10^3\,\mathrm{cm}^{-3}$, the Paβ transition is favoured over the Brγ line by a factor of ~ 5.9 (case B recombination, Osterbrock, 1989).

Instead of using narrow-band filters offset from the emission line to measure the continuum emission, we elected to simply use the broad-band images. Two reasons justify this choice. First, the stellar near-IR continuum is relatively flat and does not vary much from one end of the bandpass to the other. Second, the emission lines we are using are more or less at the centre of their respective broad bandpasses. Therefore, the average continuum flux over the broad-band filter is representative of the continuum flux at the line's position. The use of the broad-band filters has the advantage of considerably reducing the observing time needed to estimate the continuum flux.

Observing strategy

The need to detect as many of the faintest supernova remnants as possible, and with a respectable signal-to-noise ratio, implied not only long exposures, but also that particular care be taken in the calibration observations, such as dark current frames, dome flats, blank sky images, etc.

Two fields were required to cover NGC 1569; one was enough for NGC 3738.

Table 2.3: Description of the filters.

Filter ID	Description	$\lambda_{central}$ (Å)	Width (Å)	T_{peak} (%)	0-mag flux (10^{-11} Wm^{-2})
(1)	(2)	(3)	(4)	(5)	(6)
		Warm at f/8			
cfh5103	J-band	12 400	2900	79	58.43
cfh5105	Paβ	12 820	150	65	3.130
cfh5201	H-band	16 500	2800	78	25.03
cfh5202	[Fe II] λ1.644 μm	16 470	180	77	1.716
		Cold at f/8 (approx. blueward 0.004%/°C)			
cfh5103	J-band, cold	12 290	2875	79	59.65
cfh5105	Paβ, cold	12 700	150	65	3.196
cfh5201	H-band, cold	16 360	2775	78	25.59
cfh5202	[Fe II] λ1.644 μm, cold	16 330	180	77	1.755

Col. (1).– ID number from the CFHT filter set.

Col. (3).– Central wavelength (from CFHT).

Col. (4).– Width of the band pass (from CFHT).

Col. (5).– Peak transmission (from CFHT).

Col. (6).– Represents the flux over the whole bandpass. Calibrated on a blackbody at 11 200 K, normalized to Vega's flux at 5550 Å (Bersanelli et al., 1991; Hayes and Latham, 1975)

Three fields were planned for NGC 5253; only two fields were actually completed. In the end, it did not matter since the [Fe II] line emission was found to be limited to the star forming region at the centre of the galaxy.

The full well of the camera is very low, especially considering that the near-IR sky is very bright. To avoid saturation, the exposure times had to be kept very short. Typically, the J- and H-band exposures were limited to 15–30 seconds each, while the Paβ and [Fe II] narrow-band exposures were limited to 200 seconds. The numerous exposures required to accumulate enough signal to reach the desired signal-to-noise ratio were dithered in 2×2 or 3×3 grids with $5''$ offsets. The summary of the observations is given in Table 2.4.

Because the galaxies filled the entire field of view, the sky background had to be monitored separately. A nearby field, devoid of bright stars, was selected for each galaxy. Because of the rapid variations in sky brightness caused by OH lines, the sky was monitored within ~ 20 minutes of the science exposures for the J-band observations, and within ~ 10 minutes for the H-band observations. For the narrow-band images, the sky was not as closely monitored since the limited bandpass reduced the impact of the variation in the sky background. Here, we would like to warn future near-IR observers about the frequency of the sky monitoring in situations where the object observed fills the field of view. The common wisdom suggesting a 20-minute and a 10-minute intervals in J- and H-band, respectively, should be reviewed. We have indeed observed large variations at a much more rapid rate. Also, the variations were observed to be more rapid and more pronounced at the beginning of the night, during the first ~ 3 hours after sunset.

Almost half the observing time was spent for sky monitoring. For each object, in each bandpass, the time spent for sky monitoring was as long as the longest total exposure time of a science target. This was necessary to ensure that the use of the sky fields would not degrade the signal-to-noise ratio of the science images.

Table 2.4: Summary of the observations: Field, filter, seeing for each night, average airmass, total exposure times.

Field	Filter	Seeing	⟨Airmass⟩	Exposure time (s)			
		(″)		29/01/98	30/01/98	31/01/98	Total
(1)	(2)	(3)	(4)	(5)	(6)	(7)	(8)
NGC 1569 Field 1	J-band	1.2/—/0.7	1.45	210.	—	120.	330.
	H-band	1.1/—/—	1.43	240.	—	—	240.
	Paβ λ1.282 μm	1.4/—/0.7	1.68	2400.	—	1600	4000.
	[Fe II] λ1.644 μm	1.3/—/—	1.65	2400.	—	—	2400.
NGC 1569 Field 2	J-band	—/0.7/0.7	1.42	—	135.	120.	255.
	H-band	—/0.8/—	1.42	—	270.	—	270.
	Paβ λ1.282 μm	—/0.9/0.7	1.47	—	2600.	800.	3400.
	[Fe II] λ1.644 μm	—/0.8/—	1.43	—	2400.	—	2400.
NGC 1569 Deep Central[a]	J-band	1.4	1.44				585.
	H-band	1.2	1.42				510.
	Paβ λ1.282 μm	1.6	1.58				7400.
	[Fe II] λ1.644 μm	1.3	1.54				4800.

Table 2.4: *continued*

Field	Filter	Seeing	⟨Airmass⟩	Exposure time (s)			
		(″)		29/01/98	30/01/98	31/01/98	Total
(1)	(2)	(3)	(4)	(5)	(6)	(7)	(8)
NGC 3738	J-band	—/—/1.0	1.51	—	—	1440.	1440.
	H-band	1.7/0.7/—	1.27	1230.	210.	—	1440.
	Paβ λ1.282 μm	—/—/1.0	1.25	—	—	4600.	4600.
	[Fe II] λ1.644 μm	1.6/0.6/—	1.23	2400.	1600.	—	4000.
NGC 5253 Field 1	J-band	1.7/1.0/—	1.62	75.	45.	—	120.
	H-band	—/1.0/—	1.93	—	90.	—	90.
	Paβ λ1.282 μm	1.4/1.0/—	1.61	1600.	1600.	—	3200.
	[Fe II] λ1.644 μm	—/0.9/—	1.79	—	2200.	—	2200.
NGC 5253 Field 2	J-band	—/—/0.9	1.88	—	—	60.	60.
	H-band	—/—/1.0	1.85	—	—	120.	120.
	Paβ λ1.282 μm	—/—/1.2	1.63	—	—	3200.	3200.
	[Fe II] λ1.644 μm	—/—/1.1	1.68	—	—	2800.	2800.

[a] This field is created from the overlapping area of Fields 1 and 2.

2.2 Data Reduction

The data reduction of near-IR images is similar to the standard technique used for CCD images. However, more effort must be put into dark current, illumination and fringe removal. Narrow-band imaging does not always require the removal of the continuum, but in our observations the flux from the continuum is important relative to the line flux, and continuum removal was necessary.

2.2.1 Preprocessing

Before they can be used, the raw images needed to be preprocessed to remove instrumental effects, and then combined into final high signal-to-noise images. The instrumental effects are quite strong in the near-IR infrared windows, to the point that very little of the targeted source can be seen on the raw images. To help the reader visualize the effect and the importance of the data preprocessing, we offer in Appendix A a selection of science and calibration images.

Dark current

The first correction that needed to be applied was the removal of the dark current. The dark current is usually not linear with time. Therefore, we needed to gather dark exposures for each of the different exposure times used. To avoid increasing the noise in the images, the number of dark frames at a given exposure had to be at least equal to the number of scientific exposures. This meant that literally hundreds of dark frames had to be obtained during the day time.

The dark current was subtracted from the flat field, blank sky, calibration and science images.

We looked into the dark current behaviour with time. We found that the average

dark current tightly follows the relation:

$$\langle D \rangle = 9.4 + 6.2 \log t$$

where $\langle D \rangle$ is the average dark current in ADU, and t is the time in seconds.

Bad pixels

A large number of bad pixels plague the detector. The raw, blank sky images in each band were median combined and then used to create a bad pixel map. Each image was searched for bad pixels. A custom-made bad pixel finding algorithm was designed to help in the search. Any pixel with a value 7σ lower or higher than its neighbours was flagged. A visual inspection of the final bad pixel map completed the search. A representation of the map is shown in Figure A.2.

The bad pixels on the flat field, blank sky, calibration and science images were corrected by spline interpolation from the neighbouring pixels along the X and Y axes. Flagged bad pixels were not used in the interpolation.

Flat fields

To correct for pixel-to-pixel response variations, series of dome flats were obtained. On the third night, the upper right section of the array suffered some response problem: the response all across that sub-array was lower than usual. It appears that only the flat fields taken at the beginning of that night were affected, while the scientific data were fine. The solution chosen to solve this problem was to multiply that section of the detector by the appropriate factor, to correct for the weaker response. This operation was done only on the defective flat fields. Tests were conducted to make sure this correction did not affect photometric measurements. The cause of this problem, and why it fixed itself suddenly, is still a mystery. In any case, our solution worked well and the flat fields were used as usual to correct the blank sky,

the calibration and the science images for pixel-to-pixel variations. An example of a final flat field is shown in Figure A.3.

To ensure the quality of the final images, we estimated the amount of noise introduced by each flat field. For each pixel, we calculated the standard deviation of the distribution of values across the set of individual flat field exposures (for a given filter). We found that each pixel of a final flat field introduces at most 1% uncertainties in the pixel values of individual science exposures, the average being closer to 0.5%. This is much less than the photometric errors, as we will see in Chapter 3. Therefore, we can be confident that the flux seen and measured does not result from inadequate flat fielding.

Illumination and fringing

Optical CCD images are rarely corrected for illumination and fringing as these effects are usually minimal. This is certainly not the case in our images. Both effects are quite strong, in the broad-band images as well as in the narrow-band images.

Although the blank sky images were not used for time-dependent sky background removal[2], they proved to be invaluable to the creation of the illumination and fringe patterns. There were two sets of patterns: one for high airmass images, one for low airmass images. The science images were used, along with the blank sky images. The NGC 1569 and NGC 5253 images were used for the high airmass patterns, and the NGC 3738 images were used for the low airmass patterns.

For each night, and for each filter, the science and blank sky images were median scaled and median combined, rejecting the lowest and the highest pixel values in order to eliminate stars and cosmic rays. Also, any pixel value above a certain threshold was rejected to help eliminate stars.

[2]The [Fe II] and Paβ line emission observed in our galaxies does not cover the entire field of view. Instead it is, in all three galaxies, limited to the central regions. Therefore, only the relative sky background variations between the frames needed to be corrected for before the images were combined.

The large scale illumination patterns were obtained from passing these new sky images through a 33 × 33-pixel median-box filter, with sigma clipping to remove any remaining deviant pixels. The calibration and science images were divided by the normalized illumination images.

The fringe images were obtained from the illumination corrected new sky images. The fringe patterns were scaled to the flux of each image, and then subtracted from the image. Both the calibration and the science images were corrected for fringing.

Examples of blank sky images, and illumination and fringe patterns are shown in Figures A.4 and A.5

Alignment and combining of the images

The calibration and science images were aligned using the IRAF[3] task *imalign*. The coordinates of a large number of point sources were first manually extracted from a reference image and fed to the *imalign* task. The task is designed to find the centroid of the corresponding sources in the other images and to calculate the image registration solution. Each night and each filter were treated separately. The alignment involved, at this point, only X-Y offsets. The offsets were rounded to the nearest integer.

Then, the images on a given night were combined. To ensure that the images were photometrically scaled, the mode of each image was calculated and removed, effectively removing the relative variation in the sky background. Then, the flux from a section of the galaxy was used to scale the images before they were median-combined with sigma clipping rejection of the deviant pixels.

Finally, for each field, the combined images for all three nights were aligned to each other. Because the seeing varied from night to night, up to this point the images from different nights were kept separate.

[3]Image Reduction and Analysis Facility, distributed by the National Optical Astronomy Observatories.

2.2.2 Removal of the Continuum Flux

This critical image processing step proved to be the most difficult of all. To obtain a good subtraction of the continuum flux from a narrow-band image, the point-spread function (hereafter PSF) — the instrumental shape of a point source — of the continuum image had to be made identical to the PSF observed on the narrow-band image. For the nights of the observations, the image quality (represented by the *seeing*) was exceptionally good. While for most observing project this would improve the observations, it was not the case for our program! Because of the coarse plate scale of the REDEYE camera (0.5″/pixel), the good atmospheric conditions led to under-sampled images. The inability to calculate a well-sampled PSF complicated the process of matching the PSF of the continuum to the PSF of the narrow-band images[4]. A discussion of the systematic uncertainties due to possible residual continuum signal is provided in Section 3.1.

NGC 1569

For the J-band and the Paβ images, the observations were obtained over two nights. In the case of Field 1, the second night had a much better seeing than the first one. Therefore the PSF of the second night's image had to be *blurred* to match the first night's. Formal PSF matching was attempted but the PSF sampling on the second night's image was not good enough to calculate an acceptable matching kernel. In the end a simple Gaussian filter on the second image gave better results. In the case of Field 2, the PSFs were quite similar but a slight Gaussian filtering on the second night's images helped a little. These steps were not required for the H-band and [Fe II] images as the observations were obtained on a single night.

The images were combined as before to create the final images, one image for each filter. Additionally, since there was a nice overlap of the two fields that happened

[4]Note that we did not have a large enough number of images for the so-called drizzle technique to lead to a useful PSF

to coincide with the core region, the overlapping sections where combined to create a deep image of the nucleus. Mosaics of the three final fields are shown in Figures 2.1, 2.2, 2.4 and 2.5, for the H-band, the narrow-band [Fe II], the J-band and the narrow-band Paβ filters, respectively.

The final, and the most difficult, step in the preparation of the data was the removal of the continuum flux from the narrow-band images. Because of the re-imaging system used by the REDEYE camera, the plate scale of the broad- and narrow-band images were slightly different, and a careful registration of the broad-band images to the narrow-band images had to be done. Then, the PSF of the broad-band images had to be modified to match the PSF of their respective narrow-band images. And, finally, the linear intensity of the broad/narrow pairs had to be matched. Note that the adjustments were done exclusively on the broad-band images to avoid spoiling the flux calibration in the narrow-band images.

The stars used to calculate the PSF matching kernel were manually selected. Various sets of stars were tried out, as well as various kernel sizes, in order to optimize the continuum subtraction in the starburst region. Average intensity stars around the starburst region, and small kernels, led to the best results. The PSF routine uses least-square to calculate the best value of each kernel element. The routine also adjusts the linear intensity of the broad-band image to the intensity of the narrow-band image.

For Field 1, the removal of the continuum from the [Fe II] image was fairly straitforward as all the observations were obtained on the same night. And, more importantly, they were obtained on the first night when the seeing was large enough to prevent the under-sampling of the images.

For Field 2, however, a good PSF matching of the good seeing images was impossible due to under-sampling. The image quality had to be degraded with a Gaussian filter before a reasonable continuum removal could be achieved. Also, the alignment of the individual exposures (Section 2.2.1) proved to be critical as most stars were

little more than a pixel wide. We found that a single misaligned frame was enough to prevent us from obtaining an acceptable result on the continuum subtraction.

Mosaics of the [Fe II] and Paβ line emission images are shown in Figures 2.3 and 2.6, respectively. More continuum subtraction artifacts are seen in the section of the mosaics corresponding to Field 2. However, the artifacts are mostly associated with the brightest stars, away from the starburst core. A contour plot of the [Fe II] emission in the starburst region is presented in Figure 2.7.

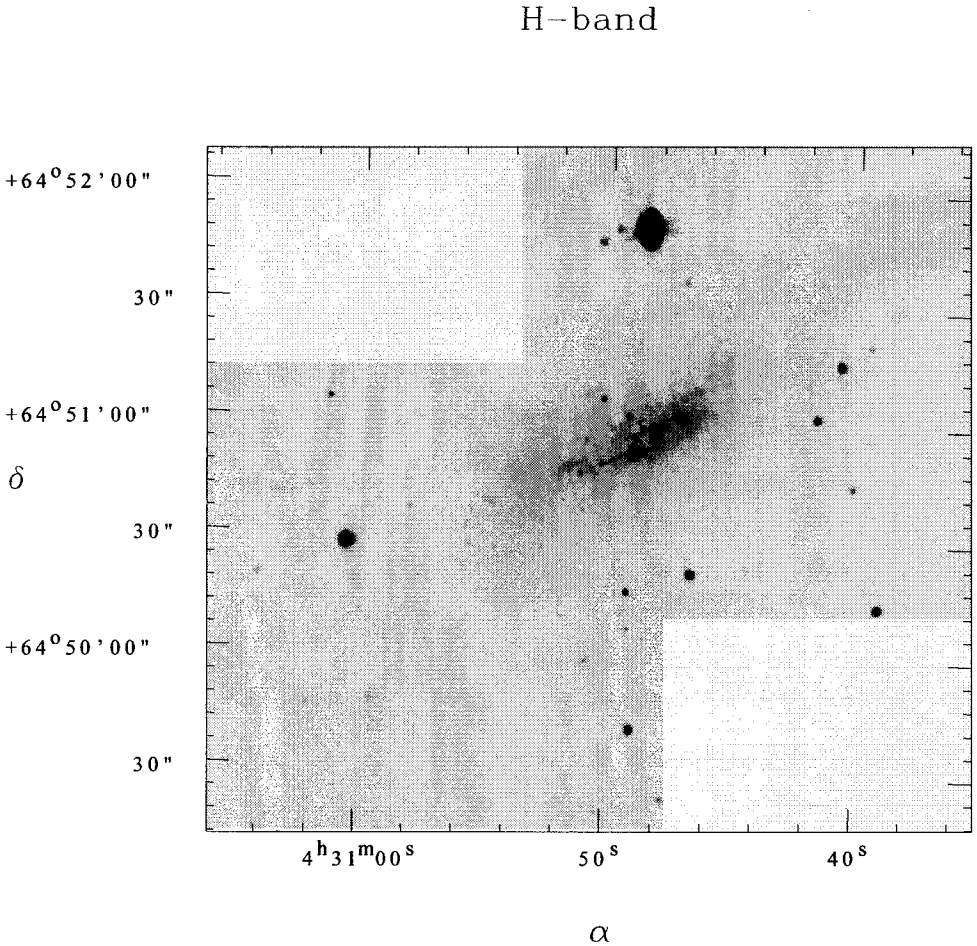

Figure 2.1: Mosaic of the H-band images of NGC 1569.

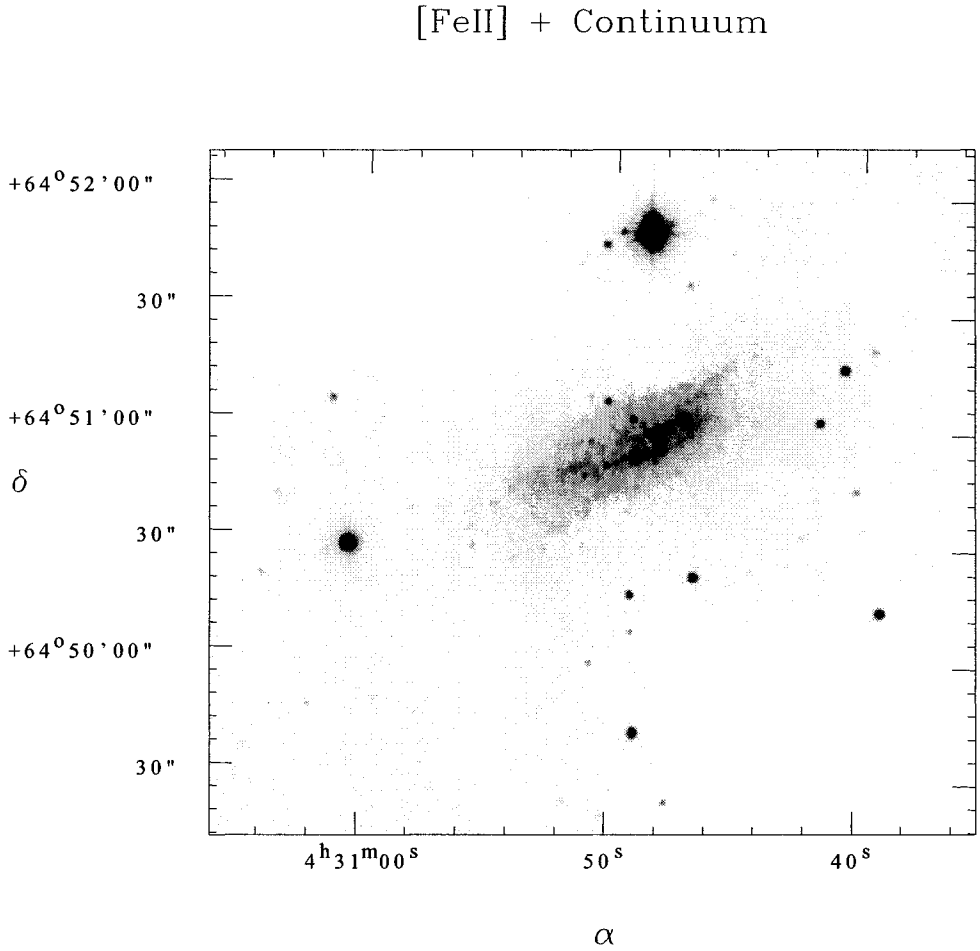

Figure 2.2: Mosaic of the [Fe II] $\lambda 1.644$ μm narrow-band images of NGC 1569.

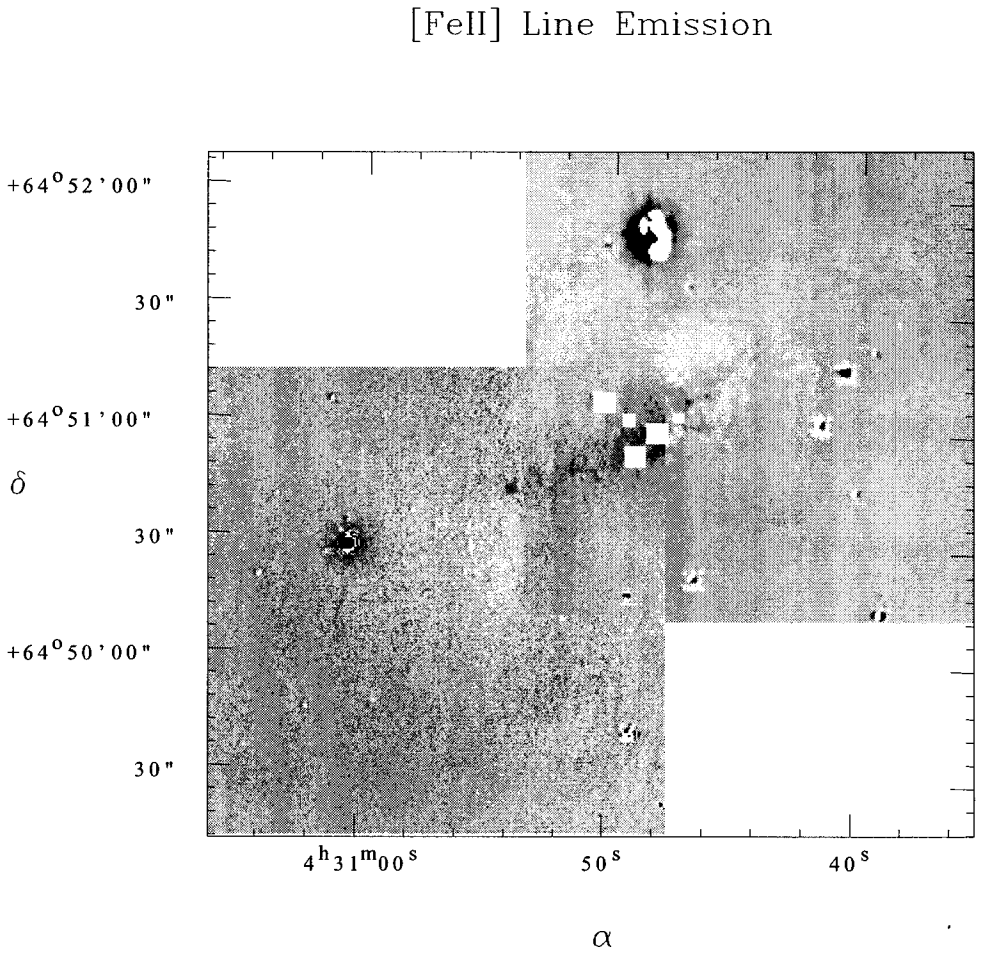

Figure 2.3: Mosaic of the [Fe II] λ1.644 μm emission line images of NGC 1569. The overexposed clusters in the core have been masked out. The continuum subtraction has been optimized to give the best results in the core area. Artifacts from the continuum subtraction were left behind by some stars, especially in Field 2 (to the right).

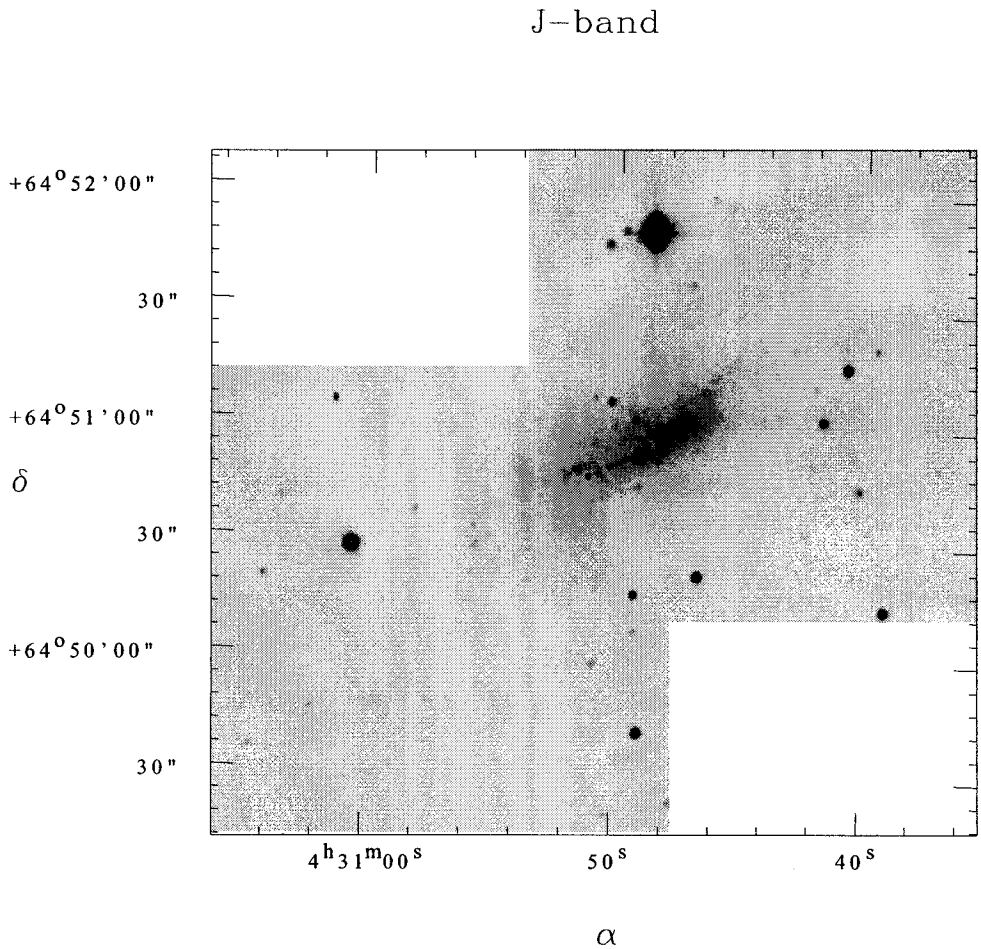

Figure 2.4: Mosaic of the J-band images of NGC 1569.

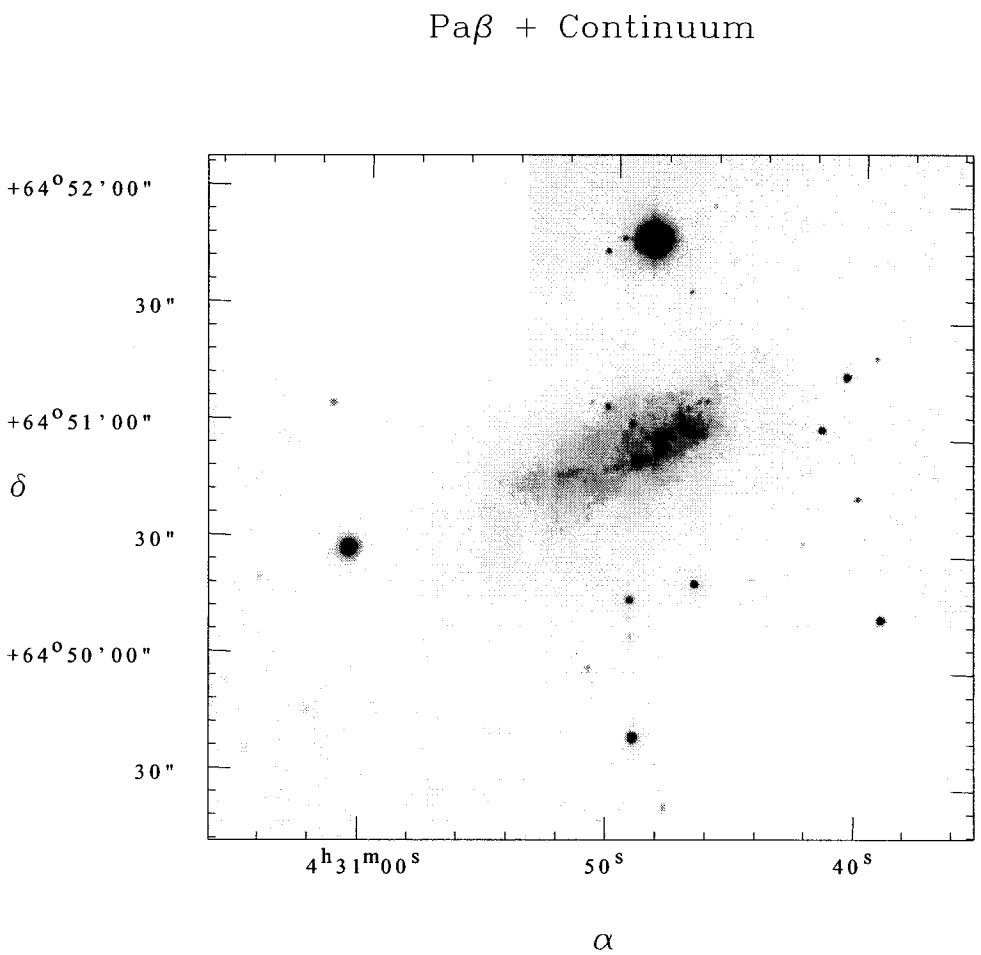

Figure 2.5: Mosaic of the Paβ λ1.282 μm narrow-band images of NGC 1569.

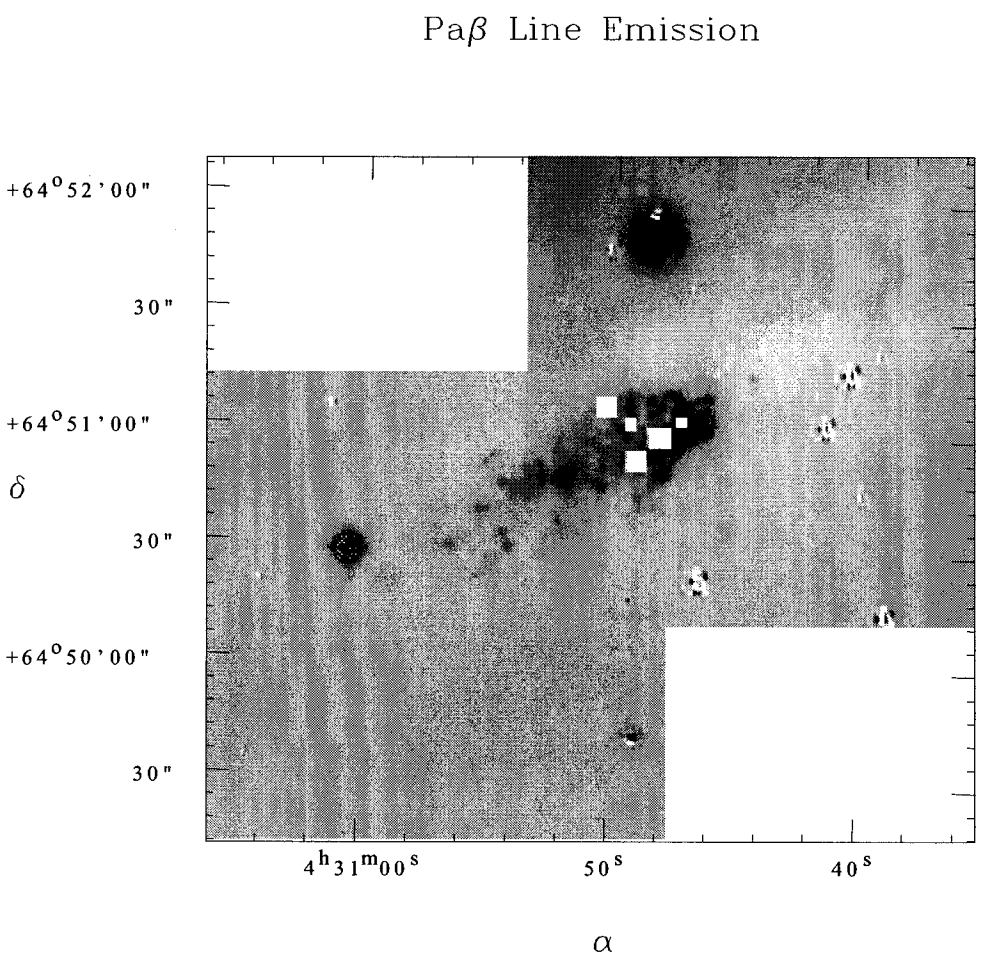

Figure 2.6: Mosaic of the Paβ λ1.282 μm emission line images of NGC 1569. The overexposed clusters in the core have been masked out. The continuum subtraction has been optimized to give the best results in the core area. Artifacts of the continuum subtraction were left behind by some stars, especially in Field 2 (to the right).

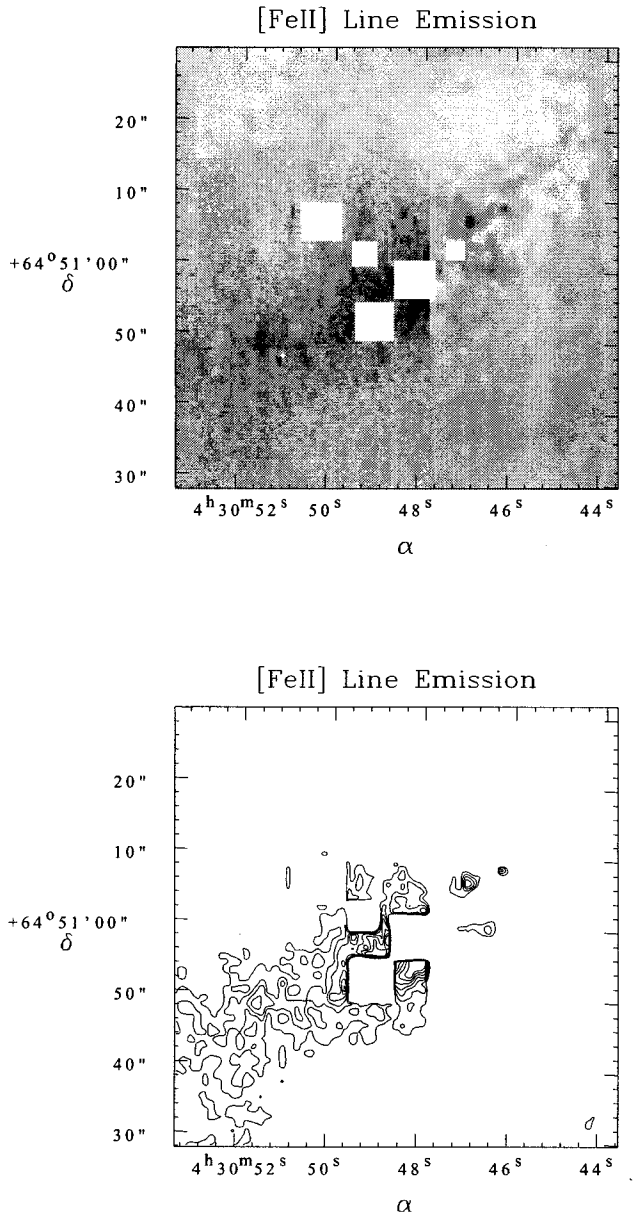

Figure 2.7: Contour plot of the [Fe II] $\lambda 1.644$ μm line emission in the nuclear starburst of NGC 1569. The contours are drawn from the 3σ level to 15σ, by steps of 2σ ($1\sigma = 5$ ADU). The jump in the noise level between the Central Field and Field 2 causes the contours to suddenly stop at the junction.

NGC 3738

The H-band and [Fe II] observations were obtained on different nights, with different seeing. As we did for NGC 1569, Gaussian filtering of the second night's images was done before the images from the different nights were combined. The J-band and Paβ observations were obtained on a single night and did not required further manipulations. The final images are shown in Figures 2.8, 2.9, 2.11 and 2.12 (H-band, narrow-band [Fe II], J-band, narrow-band Paβ, respectively).

No difficulties were encountered during the removal of the continuum flux from the narrow-band images. The broad- and narrow-band images were not as badly under-sampled as the NGC 1569 images. The fact that many more images were obtained for NGC 3738 probably helped defining good PSFs. The same procedure as for NGC 1569 was followed in order to create the emission line images. No image degradation has been required, however. The resulting [Fe II] and Paβ emission line images are shown in Figure 2.10 and 2.13, respectively. A contour plot of the [Fe II] line emission is shown in Figure 2.14; no significant [Fe II] features can be detected. This was somewhat unexpected as the Hα flux observed in NGC 3738 indicates that vigorous star formation is occurring (Hunter, 1984). This will be discussed further in Section 3.3.3.

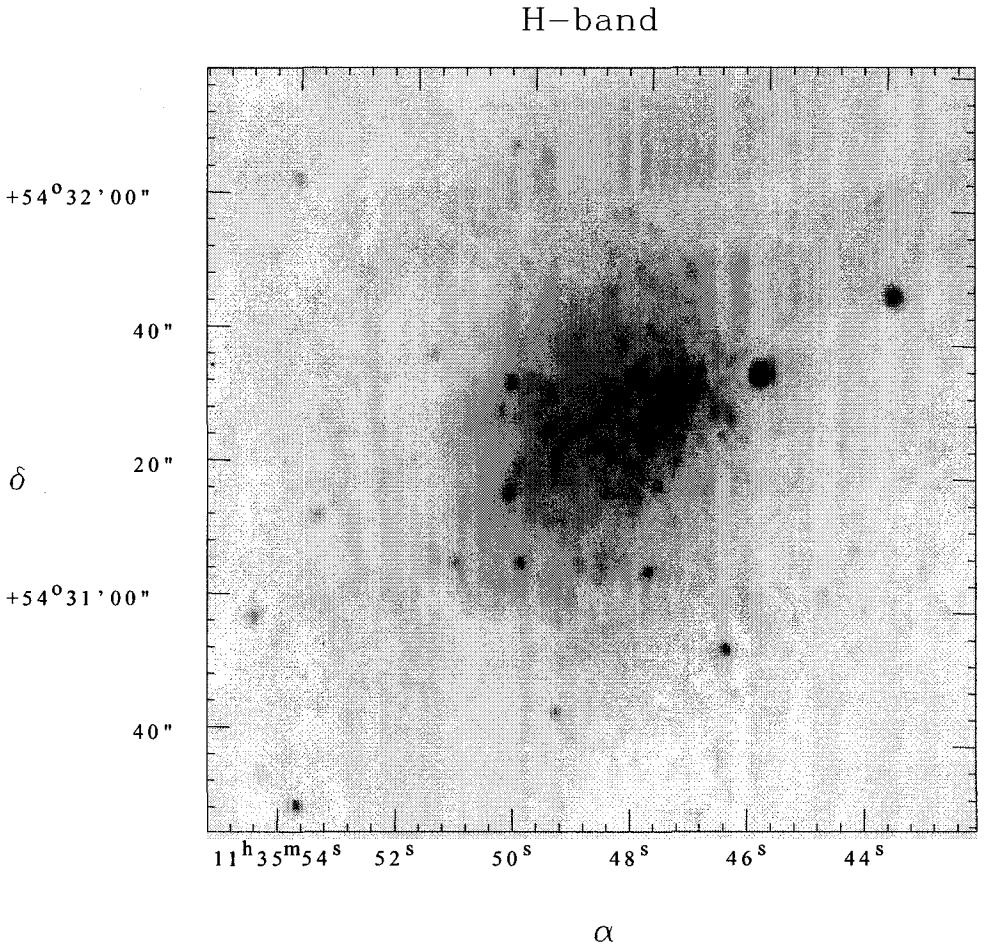

Figure 2.8: H-band image of NGC 3738.

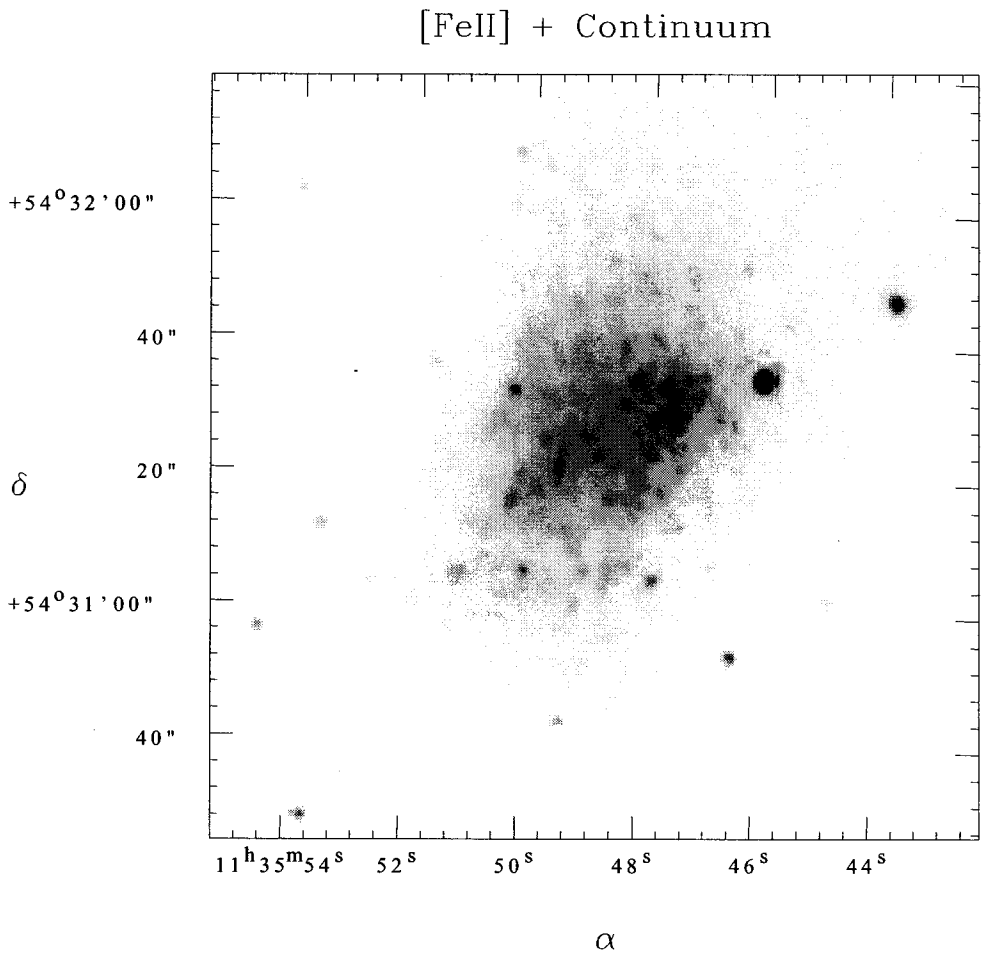

Figure 2.9: [Fe II] $\lambda 1.644$ μm narrow-band image of NGC 3738.

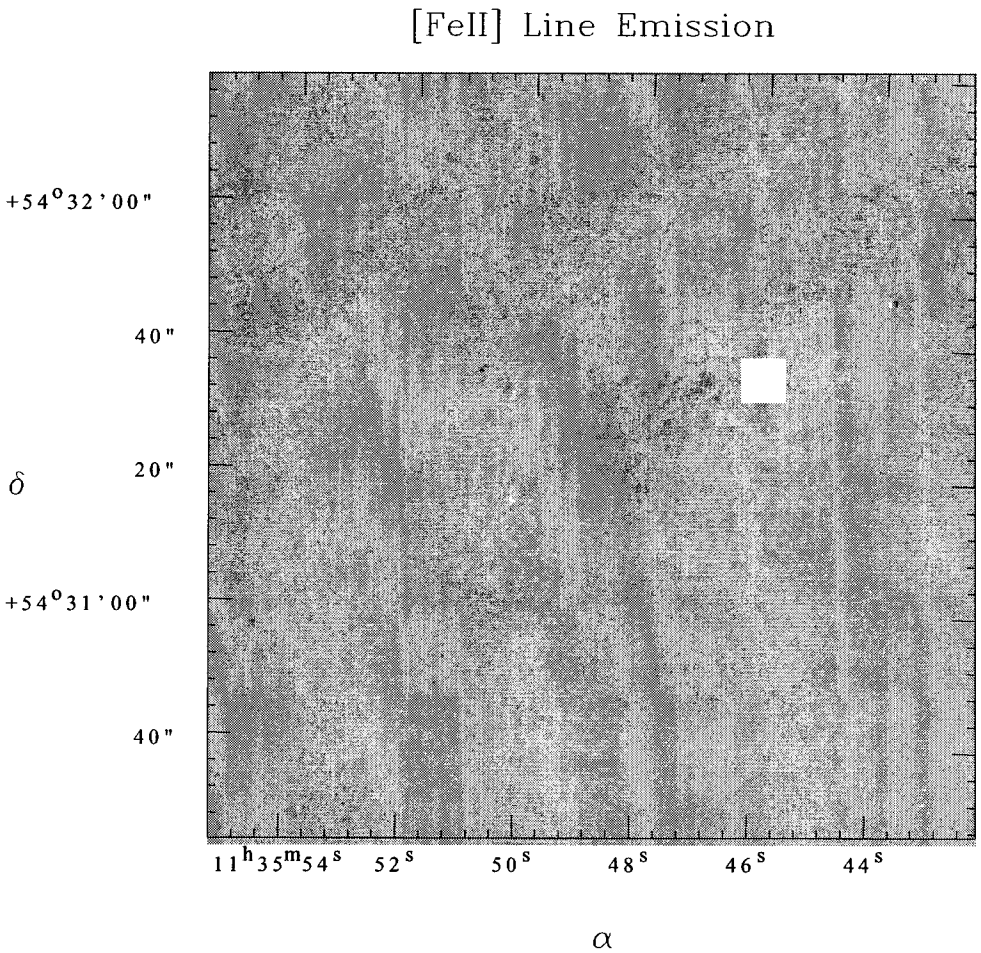

Figure 2.10: [Fe II] $\lambda 1.644$ μm emission line image of NGC 3738.

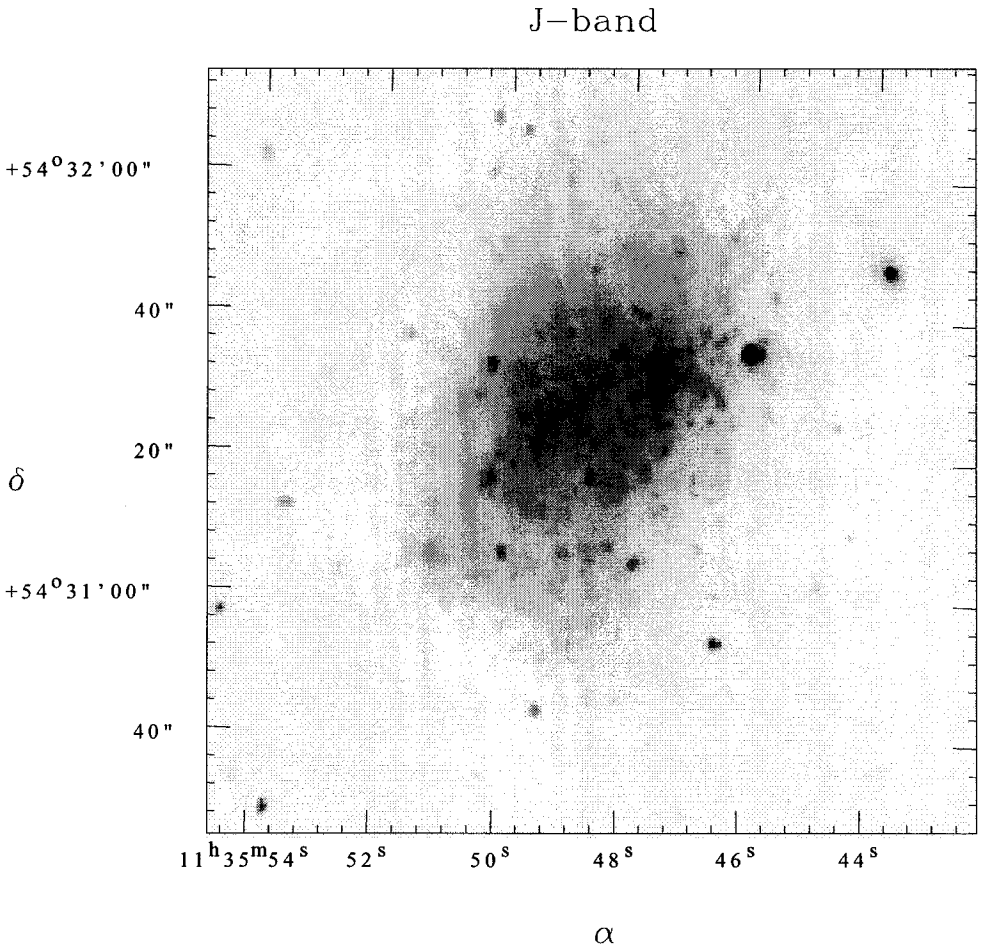

Figure 2.11: J-band image of NGC 3738.

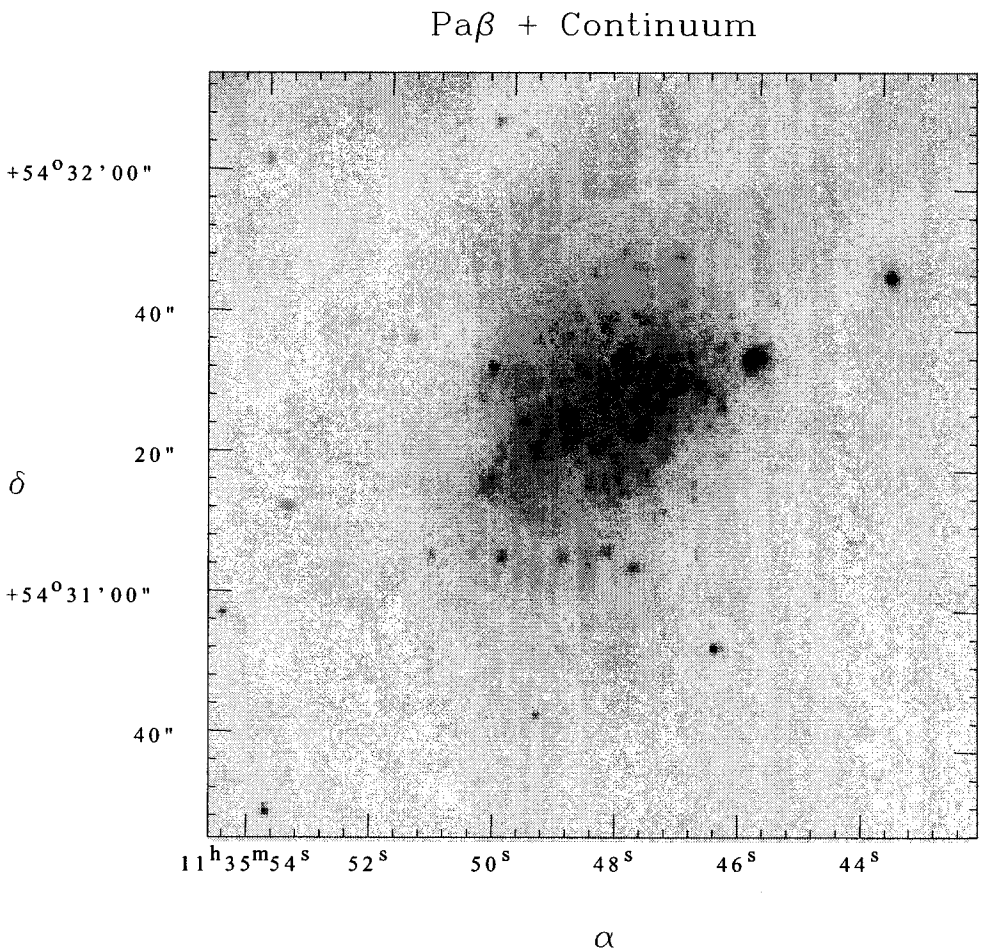

Figure 2.12: Paβ λ1.282 μm narrow-band image of NGC 3738.

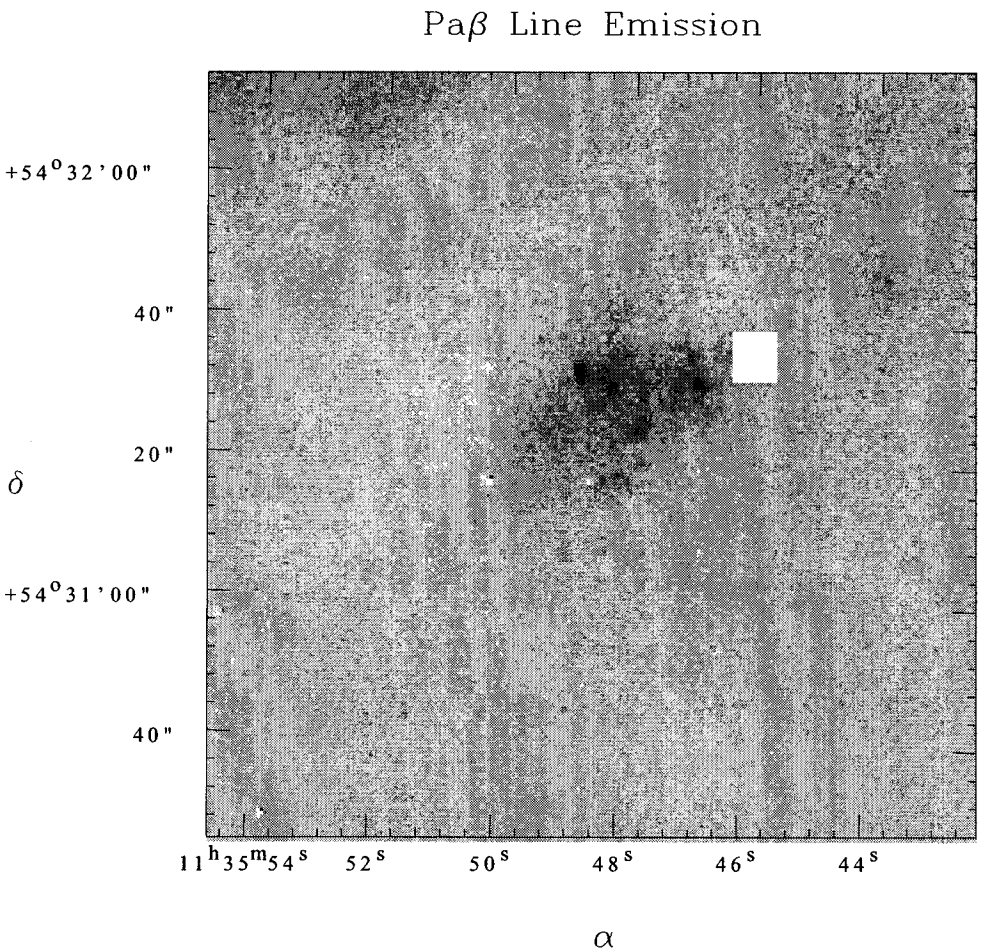

Figure 2.13: Paβ λ1.282 μm emission line image of NGC 3738.

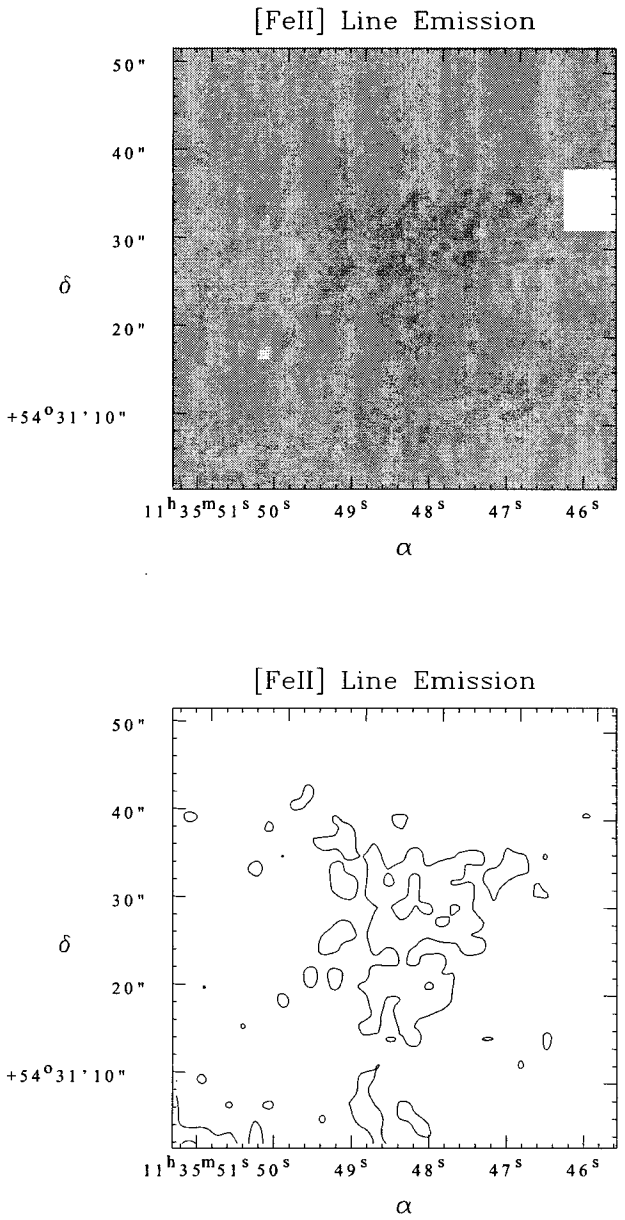

Figure 2.14: Contour plot of the [Fe II] $\lambda 1.644$ μm line emission in the nuclear starburst of NGC 3738. The contour is drawn for the 1σ level ($1\sigma = 3$ ADU).

NGC 5253

Again, the J-band and the Paβ observations were obtained on different nights and the use of a Gaussian filter on the second night's images was required before the images from the two nights were combined together. The H-band and [Fe II] images were obtained on the same night and did not required further manipulations. The final images are shown in Figures 2.15, 2.16, 2.18 and 2.19 (H-band, narrow-band [Fe II], J-band and Paβ, respectively).

To obtain the line emission images, the broad-band images were registered to the narrow-band images. Then, the PSFs of the broad-band images were matched to their respective narrow-band image. The PSF matching routine also matched the linear intensity of the images. As for NGC 1569, the PSF star selection required a few trials. In NGC 5253, many of the bright stars are found in the large, extended continuum flux envelope of the galaxy. Only the broad-band images were modified to fit the characteristics of the narrow-band images in order to protect the photometric calibration. In the end, very good results were achieved; indeed, as seen in Figures 2.17 and 2.20, very few continuum subtraction artifacts were left over. The contour plot of the [Fe II] emission line shows several features (Figure 2.21) that will be discussed in Chapter 3.

Note that no line emission has been detected in Field 2, except in the small section corresponding to the starburst core. Therefore, Field 2 will not be used in the following chapters.

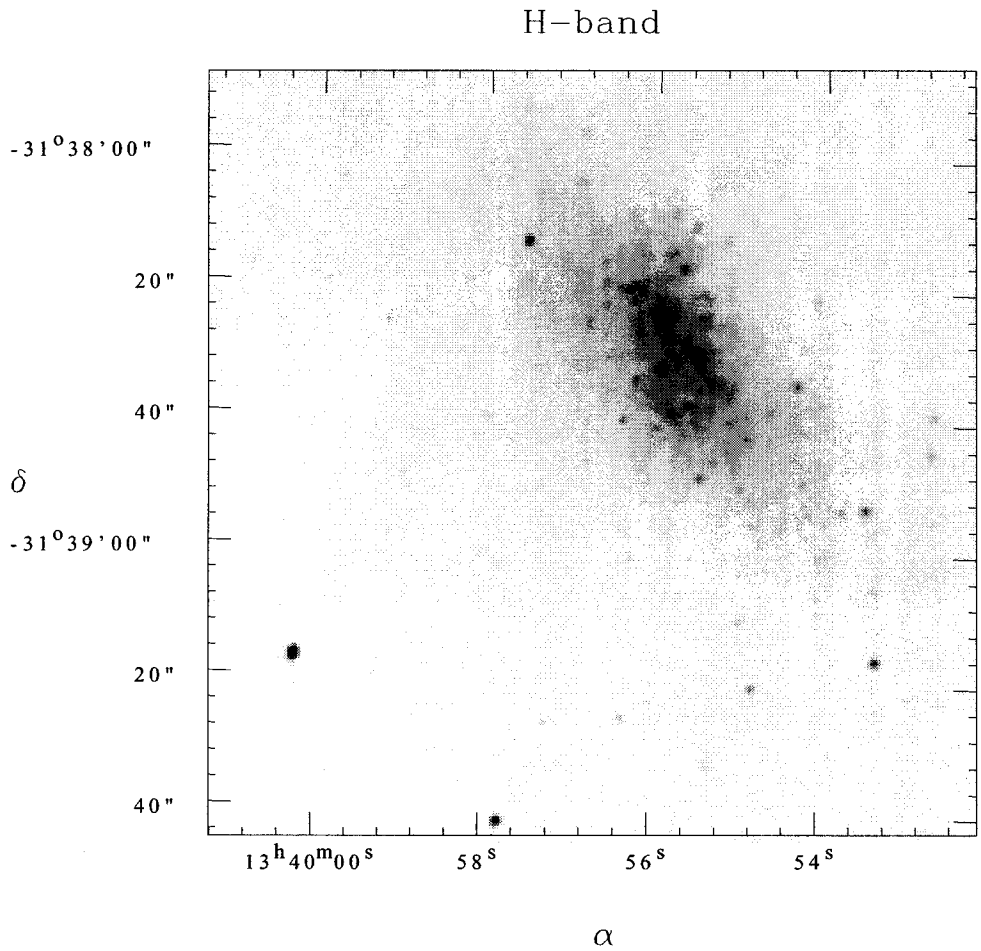

Figure 2.15: H-band image of NGC 5253.

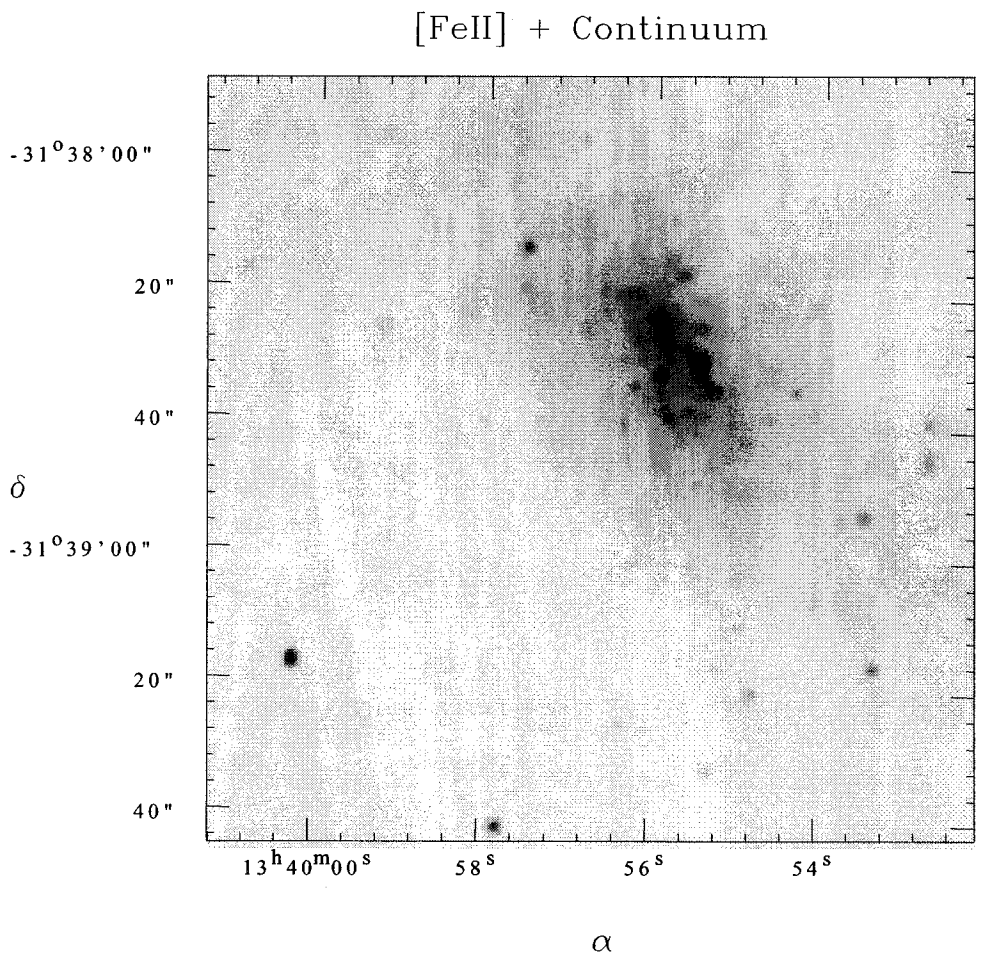

Figure 2.16: [Fe II] λ1.644 μm narrow-band image of NGC 5253.

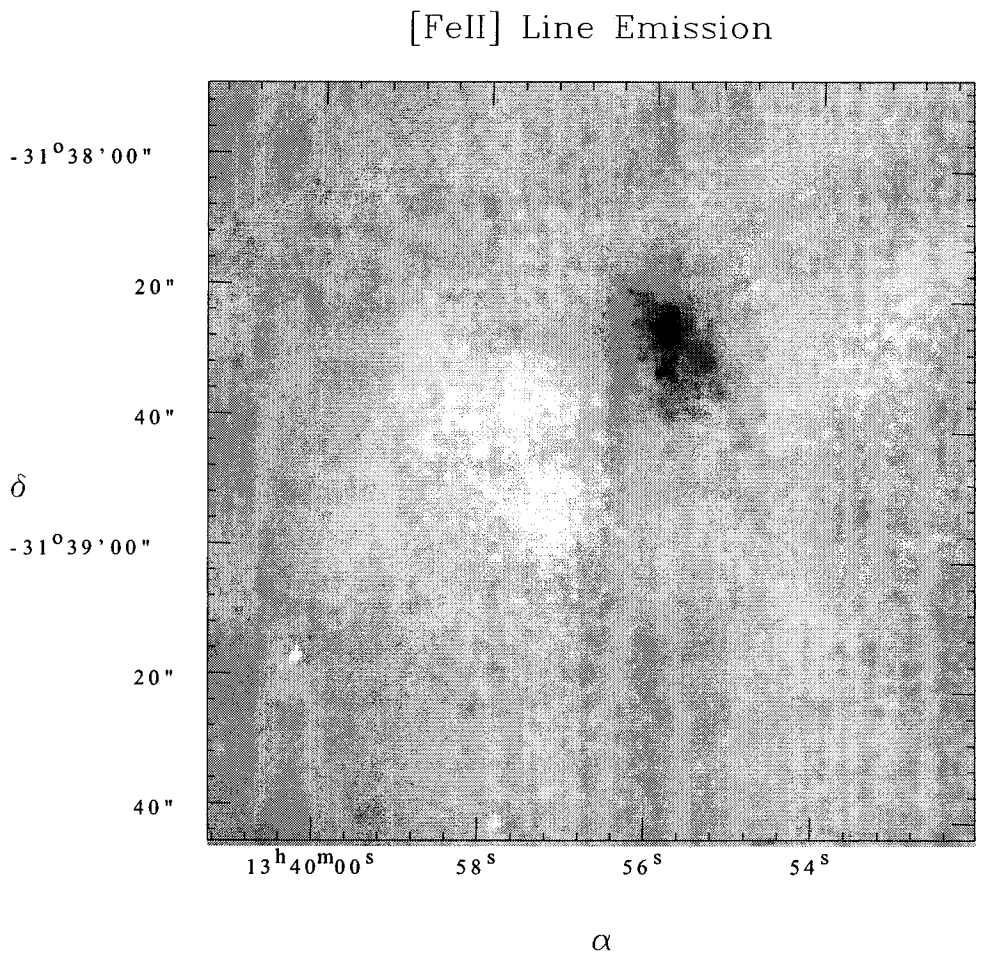

Figure 2.17: [Fe II] λ1.644 μm emission line image of NGC 5253.

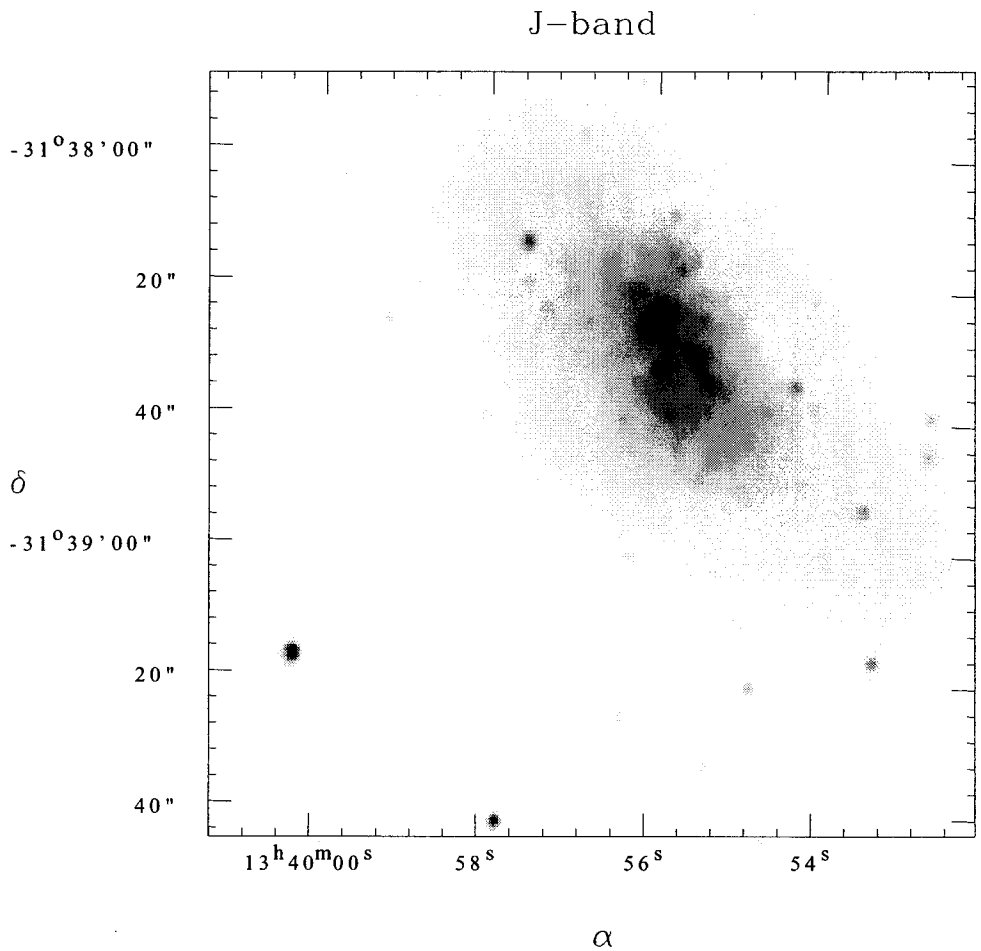

Figure 2.18: J-band image of NGC 5253.

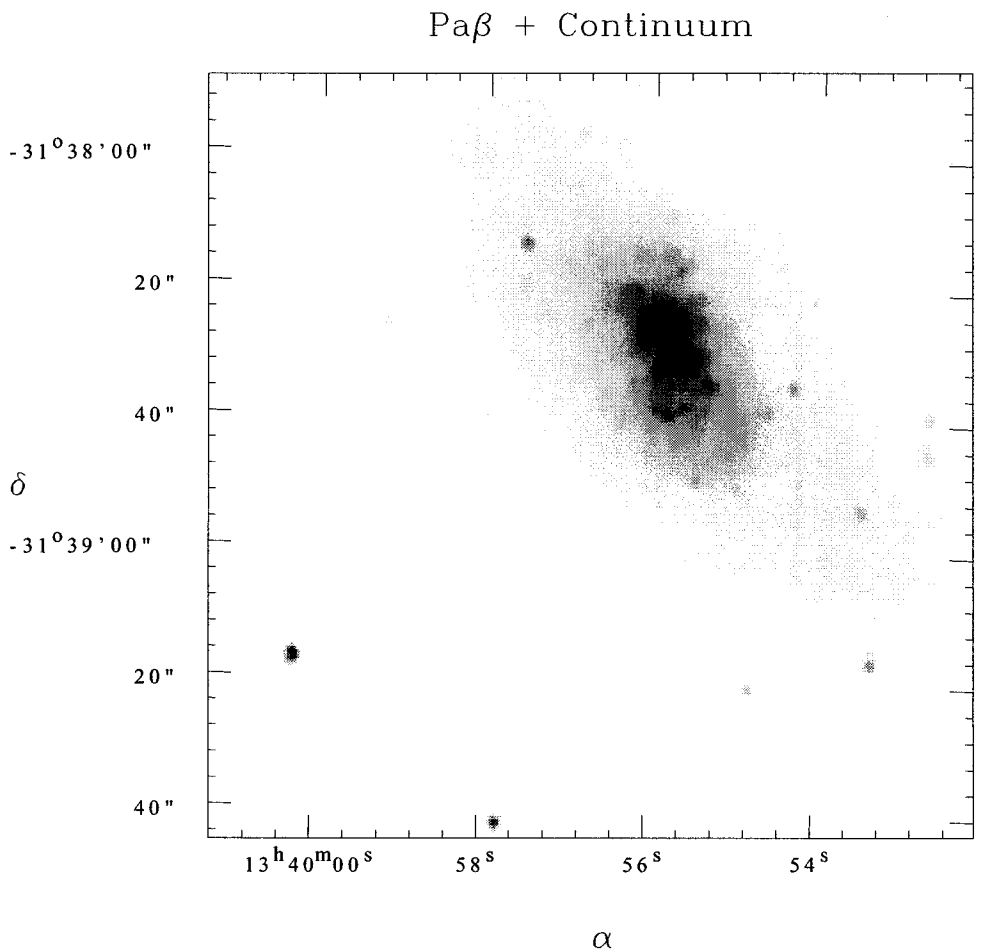

Figure 2.19: Paβ λ1.282 μm narrow-band image of NGC 5253.

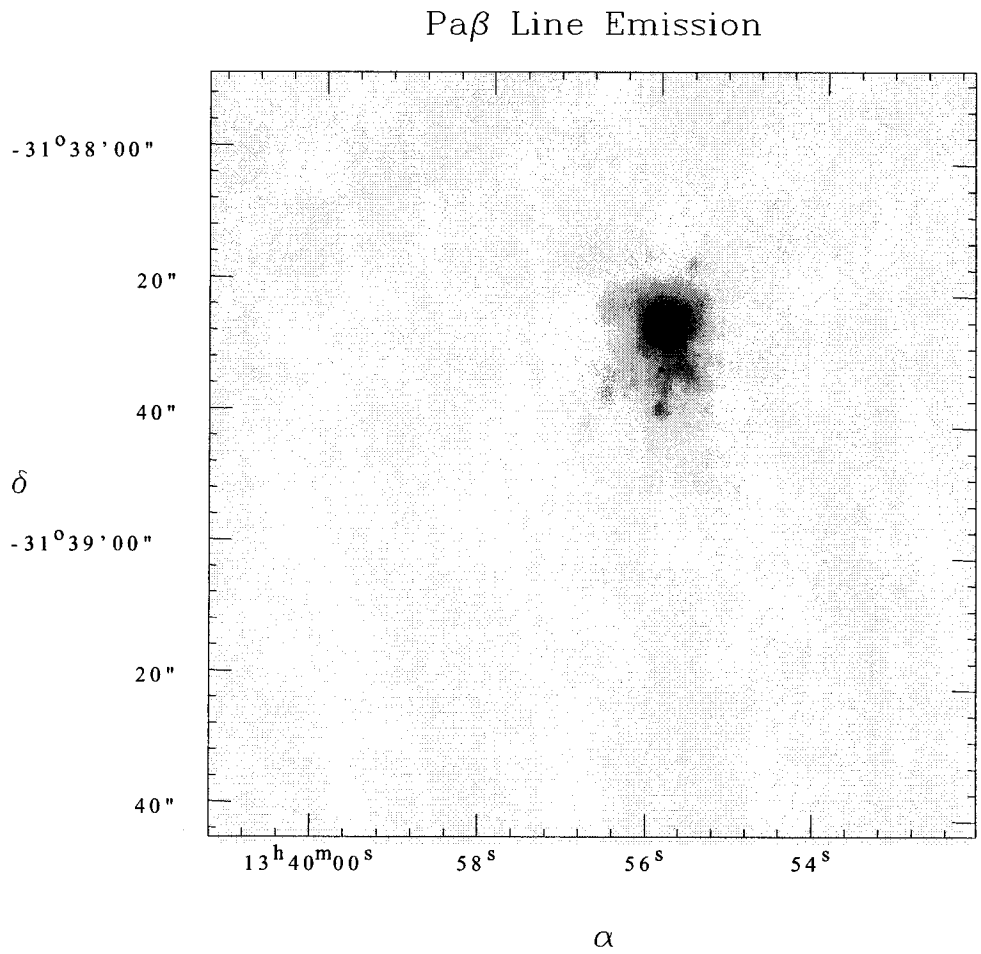

Figure 2.20: Paβ λ1.282 μm emission line image of NGC 5253.

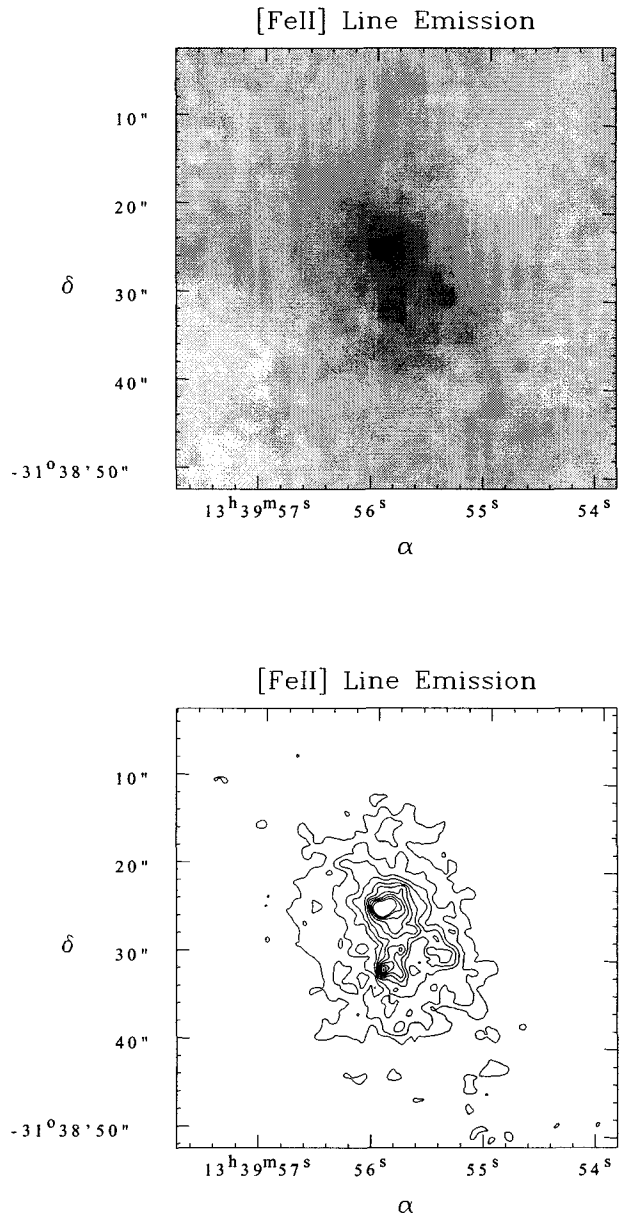

Figure 2.21: Contour plot of the [Fe II] $\lambda 1.644$ μm line emission in the nuclear starburst of NGC 5253. The contours are drawn from the 3σ level to 30σ, by steps of 3σ ($1\sigma = 4$ ADU).

Table 2.5: Standard stars. The stars were selected from the UKIRT Faint Standards (Hawarden et al., 2001). Magnitudes are in the IRCAM3 System

ID	RA J2000	Dec J2000	Other Name	Spectral Type	K (+/−)	J-H (+/−)	H-K (+/−)
FS12	05 52 27.66	+15 53 14.3	GD71	sdO	13.916	−0.115	−0.094
					(0.006)	(0.003)	(0.005)
FS13	05 57 07.59	+00 01 11.4	SA97-249	G4V	10.140	0.313	0.048
					(0.002)	(0.002)	(0.001)
FS21	11 37 05.15	+29 47 58.4	GD140	DA3	13.147	−0.069	−0.090
					(0.002)	(0.004)	(0.004)
FS24[a]	14 40 06.9	+00 01 45.0	SA106-1024		10.753	0.132	0.019
					(0.008)	(0.010)	(0.004)

[a] Data taken from the original UKIRT Faint Standard List that was published on the UKIRT website at the time of the observations. FS24 is no longer on the Fundamental List (see text).

2.3 Photometric Calibration

With the exception of the standard star observations taken at the very end of the second night, all observations were obtained under photometric conditions. The standard stars observed were selected out of the UKIRT Faint Standards List (Hawarden et al., 2001, and UKIRT website for FS24). The properties of the four standard stars, FS12, FS13, FS21 and FS24, are presented in Table 2.5. Since the time of the observations, FS24 has been removed from the Fundamental List. FS24 (SA106-1024) is a δ Scuti variable (Landolt, 1990) which exhibits occasional excursions in the near-IR. Despite this flaw, it appears that, at the time of the observations, FS24 was well behaved, as shown by its agreement with the other stars in the derivation of the colour terms (Figure 2.22, $(J-H)_{\mathrm{FS24}} = 0.132$). (The properties of FS24 are not published; they were once found on the UKIRT website, but not anymore.) A summary of the standard star observations is given in Table 2.6.

Table 2.6: Summary of the standard star observations: date of the observations, star ID, average airmass, filter, total exposure time.

Date	Star	⟨Airmass⟩	Filter	Exp.time (s)
Jan 29, 1998	FS12	1.243	J-band	90.
		1.220	H-band	60.
		1.147	Paβ λ1.282 μm	270.
		1.173	[Fe II] λ1.644 μm	240.
	FS13	1.177	J-band	20.
		1.156	H-band	6.
		1.130	Paβ λ1.282 μm	150.
		1.141	[Fe II] λ1.644 μm	90.
	FS21	1.175	J-band	60.
		1.188	H-band	60.
		1.235	Paβ λ1.282 μm	240.
		1.208	[Fe II] λ1.644 μm	240.
Jan 30, 1998	FS13	1.349	J-band	8.
		1.337	H-band	2.
		1.255	Paβ λ1.282 μm	90.
		1.291	[Fe II] λ1.644 μm	120.
	FS21	1.267	J-band	30.
		1.291	H-band	60.
		1.334	Paβ λ1.282 μm	120.
		1.312	[Fe II] λ1.644 μm	120.
Jan 31, 1998	FS13	1.392	J-band	15.
		1.336	H-band	7.
		1.263	Paβ λ1.282 μm	60.
		1.290	[Fe II] λ1.644 μm	105.
	FS24	1.069	J-band	16.
		1.067	H-band	16.
		1.063	Paβ λ1.282 μm	240.
		1.064	[Fe II] λ1.644 μm	240.

The instrumental magnitudes were converted to true magnitudes through the following transformation equations, where instrumental and true magnitudes are written in lower and upper cases, respectively:

$$\begin{aligned}
(J-H) &= (0.872 \pm 0.059)(j-h) + (0.321 \pm 0.027) \\
H &= h + (0.169 \pm 0.058)(J-H) - (2.922 \pm 0.023) \\
J &= j + (0.026 \pm 0.044)(J-H) - (2.554 \pm 0.017) \\
H_{[feii]} &= [feii] + (0.125 \pm 0.016)(J-H) - (5.874 \pm 0.007) \\
J_{pa\beta} &= pa\beta + (0.462 \pm 0.066)(J-H) - (5.682 \pm 0.026)
\end{aligned} \tag{2.1}$$

The colour terms and the zero-point corrections for the above transformation equations were obtained from least-square fits on the data (Figure 2.22). Except for the colour-colour transformation equation, the observations of FS21 obtained at the end of the second night were discarded, as the atmospheric conditions were no longer photometric. The airmass coverage was not sufficient to allow for the derivation of reliable atmospheric extinction corrections. Since the airmass dependence seemed to be very weak, no extinction corrections were added to the transformation equations.

Narrow-band true magnitudes are not available for the standard stars as flux units are usually preferred for such filters. The transformation equations for the narrow-band filters give a magnitude that is calibrated to their respective broad-band filters. As explained earlier, the narrow-band filters are close to the centre of the broad-band filter bandpasses. Hence it is possible to estimate the broad-band fluxes of continuum objects from narrow-band magnitudes.

The transformation to absolute flux measurements for a given source takes the form:

$$F_{\rm line}^{\rm obj} = \left(\frac{F_{\rm line}^{\rm std}}{f_{\rm line}^{\rm std}}\right) f_{\rm line}^{\rm obj} \tag{2.2}$$

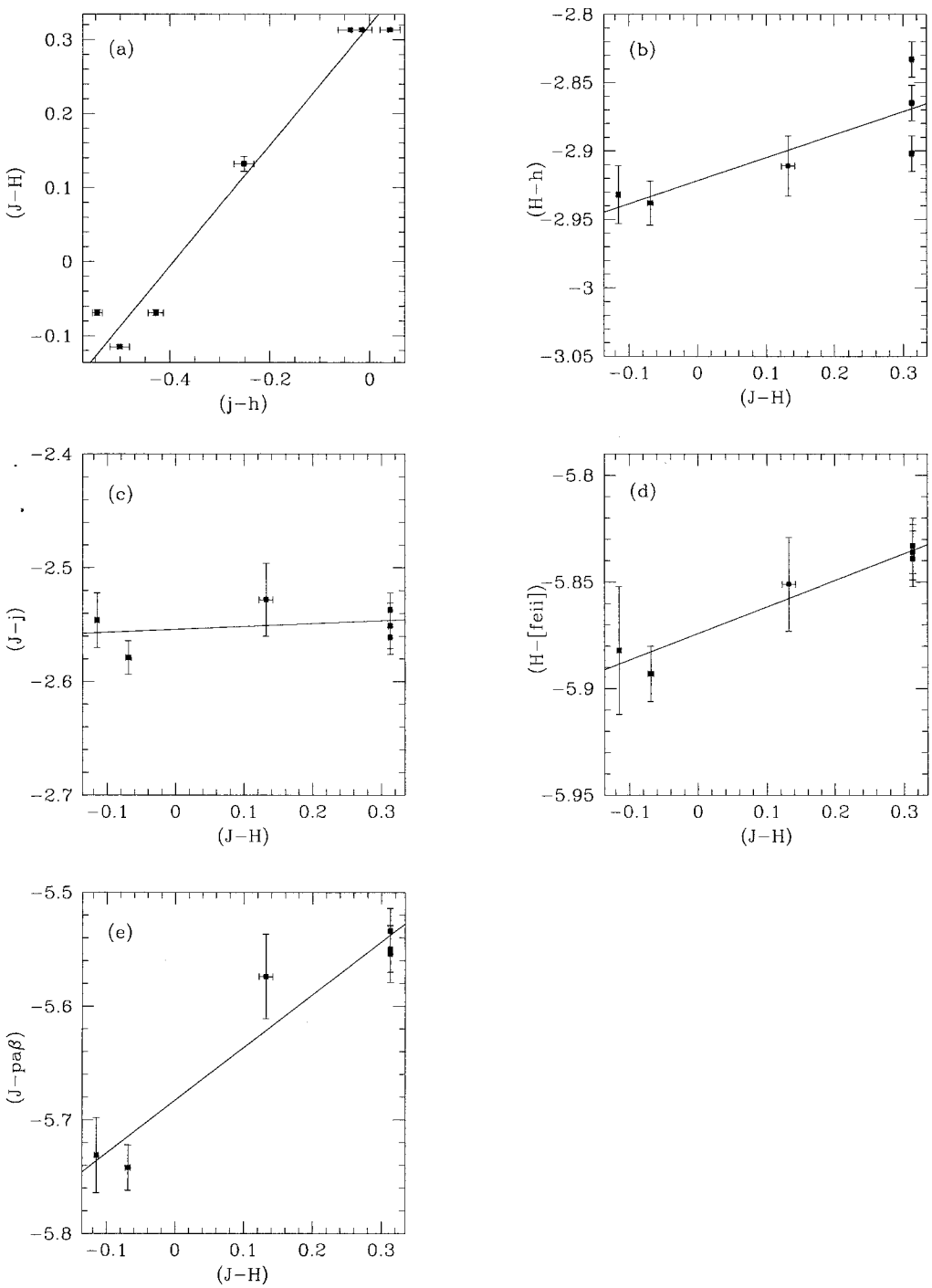

Figure 2.22: Solution to colour terms and zero-points.

where, $F_{\rm line}$ and $f_{\rm line}$ refer to absolute and instrumental line flux, respectively, and *obj* and *std* stand for *object* and *standard*. For the two narrow-band filters the $F^{\rm std}_{\rm line}/f^{\rm std}_{\rm line}$ ratios, averaged over all the standard star observations, were found to be

$$\begin{aligned} (F^{\rm std}_{\rm [FeII]}/f^{\rm std}_{\rm [FeII]}) &= (3.860 \pm 0.036) \times 10^{-19}\,{\rm Wm^{-2}\,ADU^{-1}} \\ (F^{\rm std}_{\rm Pa\beta}/f^{\rm std}_{\rm Pa\beta}) &= (5.639 \pm 0.198) \times 10^{-19}\,{\rm Wm^{-2}\,ADU^{-1}} \end{aligned} \tag{2.3}$$

The absolute line flux of a standard stars is given by

$$F^{\rm std}_{\rm line} = F_{\rm line,0}\ 10^{-0.4\,M^{\rm std}_{\rm line}} \tag{2.4}$$

where $M_{\rm line}$ is the broad-band calibrated magnitude obtained from the [Fe II] and Paβ transformation equations (Equation 2.1), and the subscript "0" refers to the line flux from a continuum source with an apparent magnitude of 0.

To find the line flux of a 0-magnitude star, the absolute calibration of the narrow-band filters is required. The 0-magnitude flux is given by $F_{\rm 0\text{-}mag} = \int S(\lambda)\,B(\lambda,T)d\lambda$, where $S(\lambda)$ is the transmission curve of the filter, and $B(\lambda,T)$ is a blackbody curve calibrated to the star Vega.

Bersanelli et al. (1991) compared a number of independent absolute calibrations of near-IR photometry to a blackbody curve. A blackbody, normalized to the flux of Vega at $\lambda = 5550\,$Å, $F(\lambda = 5550\,{\rm Å}) = 3.44 \times 10^{-8}\,{\rm Wm^{-2}}\,\mu{\rm m}^{-1}$ (Hayes and Latham, 1975), with a temperature $T = 11\,200$ K, gives the best overall agreement with the calibration points. The authors claim an uncertainty of 4% for the absolute calibration.

Observations in the near-infrared domain are particularly sensitive to the temperature of the components along the optical path. The REDEYE camera, like most CCD cameras, must be cooled to the temperature of liquid nitrogen to reduce dark current caused by the electronics. A peculiarity of the near-IR camera design is that the filters are also cooled down to the same temperature. The transmission curve of a filter depends on its temperature. In order to properly calibrate the flux observations, the transmission curve at the operating temperature is required. Unfortunately,

CFHT does not possess cool scans for the REDEYE filter set; only warm (20 °C) scans are available.

Therefore, the warm scans were converted to cool scans using the approximation provided by CFHT which includes a blueward shift of the transmission curve of 0.004% per degree Kelvin. The warm scans being representative of the transmission at 293 K, and the REDEYE camera operating at 77 K, the total wavelength shift came to 0.864%. Other than being shifted in wavelength, the transmission curves were not otherwise modified. The warm and approximated cool transmission curves for the two narrow-band filters, [Fe II] λ1.644 μm and Paβ, and the two broad-band filters, J and H, are presented in Appendix B.

The 0-mag fluxes for the [Fe II] and Paβ filters, warm and cold, are given in Table 2.3. The 0-mag fluxes from the cold scans were used in the photometric measurements presented in the next chapter. Uncertainties are estimated as $\pm$4% from the absolute calibration, with an additional $\pm$2% from the warm-to-cold approximation.

2.4 Astrometry

The astrometric solutions for the images were based on the coordinates of guide stars taken from the USNO[5] Guide Star Catalogue Version A.2. For NGC 1569, a number of guide stars were found in both fields (Figures 2.23 (a) and (b)). For NGC 3738 and NGC 5253, however, just a few stars from the USNO Catalogue were visible in the field of view. To improve on the astrometry, registered Digitized Sky Survey images of the NGC 3738 and NGC 5253 fields were loaded into the *ESO SkyCat Tool*[6] from which the coordinates of a few more stars were read off. The stars selected are labeled on Figures 2.23 (c) and (d). The USNO stars are circled while

[5]US Naval Observatory
[6]Developed by the European Southern Observatory

the stars measured with SkyCat are identified by a square.

The astrometric solutions were calculated with the *imcoords* package in IRAF. The precision of the astrometric solutions is estimated as $\pm 0.5''$.

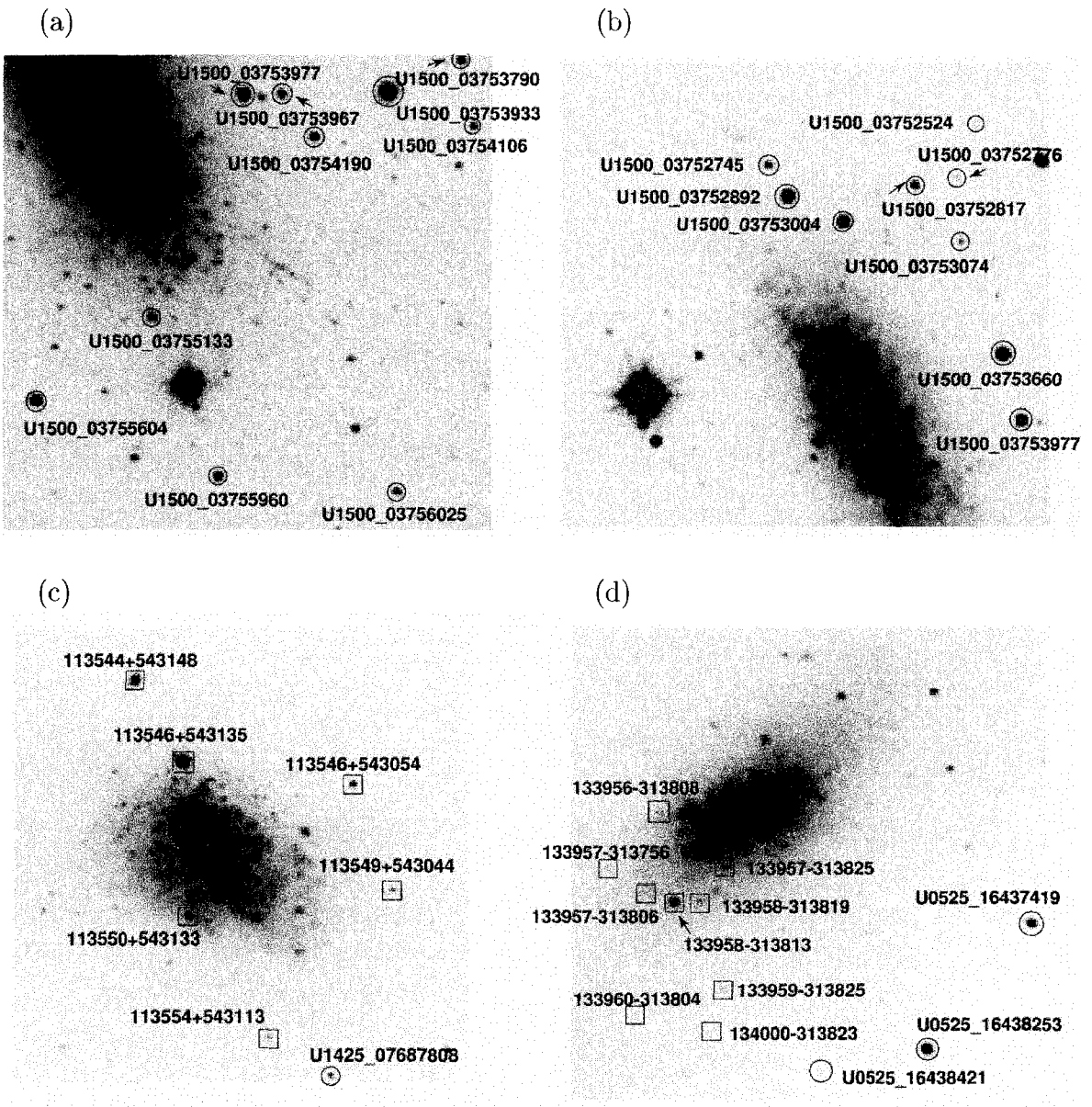

Figure 2.23: Astrometric Stars. The stars identified with a circle are guide stars from the *USNO Guide Star Catalogue vA.2*. The coordinates of the stars identified with a square were obtained from the *ESO SkyCat Tool* and registered *Digitized Sky Survey* images. The stars are labeled with either their identification from the USNO catalogue or with their coordinates. **(a)** NGC 1569 Field 1; **(b)** NGC 1569 Field 2; **(c)** NGC 3738; **(d)** NGC 5253 Field 1.

Chapter 3

Observed [Fe II] and Paβ Line Emission

In this chapter, we present the measurements of the compact sources and the diffuse[1] emission detected in the [Fe II] line emission images. We use the [Fe II]/Paβ line ratio, the morphology of the [Fe II] and Paβ line emissions, and the spatial coincidence with continuum sources to address the nature of the [Fe II] emitters.

A number of compact sources are observed in NGC 1569 and NGC 5253. Among what we refer to as *compact sources*, we include supernova remnant candidates, known star clusters, and other slightly more extended [Fe II] emitting regions. Detailed description and discussion is offered for each compact source.

Measurements of the global, extended line emission from each galaxy are also presented and briefly discussed. A more detailed analysis of the diffuse [Fe II] line emission can be found in Chapter 4. The present chapter is divided into four sections. In the first section, we address issues regarding the photometry and the uncertainties in the measurements. In the next three sections, one for each galaxy, we present and dis-

[1]The term *diffuse* is used liberally to identify any emission not easily identified with a well defined source, be it true diffuse emission or simply unresolved sources. The actual nature of the observed diffuse emission is addressed in Chapter 4.

cuss the various observations and measurements (NGC 1569, Section 3.2; NGC 3738, Section 3.3; NGC 5253, Section 3.4).

3.1 Photometry and Uncertainties

A simple aperture photometry technique was used to obtain the flux measurements. For most sources, a simple circular aperture was adequate. However, for some sources, an elliptical aperture was used. The size and shape of the aperture were set according to the extent of the [Fe II] emitter. The same aperture was used for both the [Fe II] and the Paβ flux measurements. The instrumental flux of the source in ADU, f, was obtained from :

$$f = f_{ap} - f_{sky}\, n_{pix} \tag{3.1}$$

where f_{ap} is the total flux, in ADU, within the aperture, n_{pix} is the aperture's area in pixels, and f_{sky} is the average sky background flux in ADU per pixel.

The sky background was measured from an annulus surrounding the aperture. The shape of the annulus was the same as the shape of the aperture. The sky background annuli were typically 5-pixels wide. Sigma-clipping on the sky annulus pixel values ensured that the average sky background estimate was not affected by local variations due, for example, to a nearby source.

The statistical uncertainties on the instrumental flux in ADU, σ_f, were obtained from :

$$\sigma_f = \sqrt{\frac{f}{g} + n_{pix}\,\sigma_{sky}^2 + \frac{n_{pix}^2\,\sigma_{sky}^2}{n_{skypix}}} \tag{3.2}$$

where g is the gain of the instrument in e^-/ADU (Table 2.2), σ_{sky} is the standard deviation within the sky annulus, and n_{skypix} is the number of sky pixels used.

Great care was taken in the selection of the apertures and sky annuli. For each source, the flux was measured within a series of increasing aperture sizes to select the aperture at which all the flux from the source was included. The varying aperture

measurements showed that the statistical uncertainties (Equation 3.2) were underestimating the true uncertainties in the flux measurements. This was because the sources were often found in crowded areas, leading to possible contamination from nearby emission features. The final uncertainties were therefore estimated from the effect of a slight change in aperture size on the flux measurements. Typical uncertainties on the instrumental flux are $\sim$10%, about a 5% increase over the statistical uncertainties.

Using bright stellar objects in the field of view, we attempted to quantify the systematic uncertainties associated with the continuum subtraction. Stars are not [Fe II] or Paβ emitters. Therefore, no flux should remain at the stars' positions after the removal of the continuum emission. To test this, aperture photometry was done on the continuum subtracted images, and the average of the residual flux of each star was taken as representing the systematic uncertainties.

The systematic uncertainties for each field are presented in Table 3.1. For almost all the sources discussed in this chapter, the systematic uncertainties are smaller than the photometric uncertainites given in Tables 3.3, 3.6 and 3.9. Only three sources, N1569-S001, N5253-S001 and N5253-C006, are afflicted by systematic uncertainties larger than the photometric uncertainties, the most "extreme" case being for the [Fe II] line emission measurement of N1569-S001: $4.5 \times 10^{-19}\,\mathrm{Wm}^{-2}$ (systematic) versus $3.1 \times 10^{-19}\,\mathrm{Wm}^{-2}$ (photometric) (Table 3.3).

3.2 NGC 1569

NGC 1569 is a Magellanic type irregular galaxy. It is the closest starburst galaxy known. This galaxy is famous for its two super star clusters, SSCs A and B (Arp and Sandage, 1985; Ho and Filippenko, 1996). The mass of this galaxy has been estimated as $M \simeq 3.3 \times 10^8\,\mathrm{M}_\odot$, with a mass in hydrogen of $M_H \simeq 1.3 \times 10^8\,\mathrm{M}_\odot$

Table 3.1: Systematic uncertainties introduced by the continuum subtraction.

Galaxy (1)	Field (2)	[Fe II] (3)	Paβ (4)
NGC 1569	Field 1	0.09	0.06
	Field 2	0.03	0.10
	Central	0.06	0.10
NGC 3738	Field 1	0.02	0.03
NGC 5253	Field 1	0.03	0.08

Col. (3)-(4).— $10^{-19}\,\mathrm{Wm}^{-2}$ per pixel

(Israel, 1988). The oxygen abundance has been measured by a number of authors. The range observed is very narrow with an average $12 + \log(\mathrm{O/H}) \simeq 8.25$ (Calzetti et al., 1994; Devost et al., 1997; González-Delgado et al., 1997). NGC 1569 shows no significant evidence for chemical inhomogeneities (Devost et al., 1997; Kobulnicky and Skillman, 1997). Using the average oxygen abundance, a metallicity of $Z \approx 0.25\,\mathrm{Z}_{\odot}$ is derived[2]. The galaxy has recently undergone a global burst of star formation that lasted at least 100 Myr, ending ~5 to 10 Myr ago (Greggio et al., 1998). Assuming a Salpeter IMF, it is estimated that the star formation rate was about $0.5\,\mathrm{M}_{\odot}/\mathrm{yr}$ during that starburst episode. Although usually regarded as a post-starburst galaxy, the presence of bright H II regions indicates that the galaxy still has substantial ongoing star formation. A hole in the H I distribution is observed, centred on SSC A (Israel and van Driel, 1990). A trough is also observed in Hα (Devost et al., 1997). Stellar winds and SNRs from SSC A are likely candidates to explain this trough. Giant molecular clouds are observed just outside the western edge of the H I hole (Taylor et al., 1999). Recent MERLIN radio observations at 1.4 and 5 GHz by Greve et al. (2002) revealed a few non-thermal sources that they associate with radio supernovae and SNRs. Their observations focused on the region around the two SSCs. They

[2]An abundance ratio of [O/Fe]=0.0 is assumed. This is likely a lower limit as Type II supernovae, which appear shortly after the onset of star formation, produce a higher abundance of oxygen relative to iron (Woosley and Weaver, 1986).

found that the surroundings of SSCs A and B are more or less devoid of non-thermal sources, possibly because the SSCs create an environment that is too disturbed for the survival of supernova remnants.

3.2.1 Data Analysis Issues

Reddening

The intrinsic flux of a source, F_i, is recovered by applying the effective absorption, at the wavelength of observation, $A(\lambda)$, to the observed flux, F_o:

$$F_i(\lambda) = F_o(\lambda)\, 10^{0.4\, E(B-V)\, k(\lambda)} \tag{3.3}$$

where $E(B-V)$ is the color excess and $k(\lambda) = A(\lambda)/E(B-V)$ is the effective extinction law. For a galaxy, the total absorption is a combination of the foreground extinction, due to the Milky Way, and of the absorption intrinsic to the galaxy itself. The extinction law of the galaxy is not necessarily the same as the extinction law observed for the Milky Way. This is particularly true for starburst galaxies (e.g. Calzetti et al. 2000).

To correct for foreground absorption, we used the infrared extinction law of Cardelli et al. (1989):

$$k(\lambda) = R_V\, [\, a(x) + b(x)/R_V\,] \tag{3.4}$$

where $x \equiv 1/\lambda\ \mu\mathrm{m}^{-1}$, $R_V \equiv A_V/E(B-V)$, and the infrared solution for $a(x)$ and $b(x)$ is :

$$a(x) = 0.574\, x^{1.61}\ ; \tag{3.5}$$

$$b(x) = -0.527\, x^{1.61}\ , \tag{3.6}$$

$$\text{for } 0.3\,\mu\mathrm{m}^{-1} \leq x \leq 1.1\,\mu\mathrm{m}^{-1}.$$

For the Galactic diffuse interstellar medium, $R_V = 3.1$.

A reddening curve derived for starburst galaxies (Calzetti et al., 2000, and references therein) is used for the intrinsic absorption correction. It is expressed as:

$$k'(\lambda) = 2.659(-1.857 + 1.040/\lambda) + R'_V\ , \qquad 0.63\,\mu\mathrm{m} \leq \lambda \leq 2.20\,\mu\mathrm{m}\,, \qquad (3.7)$$

where the value of the parameter of the starburst reddening curve, R'_V, is equal to 4.05.

At a galactic latitude of $b = 11°.2$ (Clements, 1983), most of the extinction suffered by NGC 1569 occurs in the Milky Way. Using the H I column density, Burstein and Heiles (1984) derived a Galactic component to the extinction in the direction of NGC 1569 equivalent to a color excess of $E(B-V)_f = 0.51$.

The intrinsic absorption in NGC 1569 varies across the galaxy but remains small. Indeed, Kobulnicky and Skillman (1997) found that the range in total color excess, $E(B-V)_t$, is 0.56–0.71 (for $R_V = 3.1$). Of these total color excess estimates, 0.51 is due to foreground Galactic reddening. The Paβ image shows that the distribution of ionized gas is not uniform; the neutral gas and the dust are probably also nonuniform. This will affect the intrinsic absorption; for example a source embedded in a H II region is likely to suffer more extinction than a source in a lower density area.

Hunter et al. (2000) catalogued star clusters in NGC 1569. To better account for the variation in the intrinsic extinction, they classified the clusters in three extinction bins depending on how much ionized gas was present in the immediate vicinity of the cluster. Since the clusters are distributed throughout the galaxy, we used their color excess estimates to "map" the internal reddening in NGC 1569. For each one of our sources, we used the intrinsic color excess estimate, $E(B-V)_i$, of the closest star cluster. The $E(B-V)_i$ in Hunter et al. are based on $R_V = 3.1$. We converted the $E(B-V)_i$ values to $R_V = 4.05$, following Calzetti et al. (2000). The color excess values used for each source are listed in Table 3.2.

Distance

O'Connell et al. (1994) used color-magnitude diagrams from HST/WFPC1 observations of NGC 1569 to obtain a distance estimate from the distribution of stars with $(V-I) < 1.5$. Assuming a $E(B-V)_t$ of 0.56 from Israel (1988) they calculated a distance to NGC 1569 of 2.5 ± 0.5 Mpc. An earlier estimate from Israel (1988) suggests a distance of 2.2 ± 0.6 Mpc. In this dissertation a distance of 2.5 ± 0.5 Mpc will be adopted for NGC 1569.

3.2.2 Comments on Compact [Fe II] Sources

Here we comment on the sources identified in the [Fe II] line emission image of NGC 1569. Under *SNR Candidates* we have collected all the small, well defined [Fe II] sources. Whether they should be retained as SNR candidates is discussed below. The sources found under the label *Other Sources* are [Fe II] areas more extended than the SNR candidates, and sometimes show substructure.

The coordinates of the [Fe II] sources, along with the foreground and intrinsic color excesses, are listed in Table 3.2. The measured line properties of the sources are presented in Tables 3.3 and 3.4.

Supernova remnant candidates

N1569-S001 [Figure C.1] With a diameter of 3″, this strong [Fe II] source is resolved on our image. At a distance of 2.5 Mpc its physical diameter is estimated as 36 parsecs. No continuum emission is associated with the object. Also, there are no strong hydrogen emission sources at this candidate's location. The source is not coincident with any of the nearby H II regions (Sources 6, 7 and 9, from Waller (1991)), nor is it coincident with the H II complex observed by Seaquist

Table 3.2: Coordinates of the sources in NGC 1569

ID (1)	RA (2)	Dec (3)	$E(B-V)_f$ (4)	$E(B-V)_i$ (5)
SNR Candidates				
N1569-S001	04:30:54.05	+64:50:43.0	0.51	0.04
N1569-S002	04:30:51.59	+64:50:50.1	0.51	0.09
N1569-S003	04:30:49.85	+64:50:49.9	0.51	0.04
N1569-S004	04:30:49.62	+64:50:51.0	0.51	0.04
N1569-S005	04:30:48.89	+64:50:56.4	0.51	0.04
N1569-S006	04:30:49.02	+64:50:57.9	0.51	0.04
N1569-S007	04:30:47.98	+64:50:55.1	0.51	0.04
N1569-S008	04:30:49.53	+64:50:58.8	0.51	0.04
N1569-S009	04:30:47.04	+64:51:07.2	0.51	0.09
N1569-S010	04:30:46.31	+64:51:09.0	0.51	0.04
N1569-S011	04:30:46.57	+64:51:00.4	0.51	0.09
Other Sources				
N1569-O001	04:30:51.58	+64:50:48.6	0.51	0.09
N1569-O002	04:30:48.70	+64:50:58.4	0.51	0.04
N1569-O003	04:30:48.29	+64:50:53.3	0.51	0.04
N1569-O004	04:30:46.42	+64:51:01.5	0.51	0.09
Whole Galaxy				
[Fe II]	04:30:46.44	+64:51:02.24	0.51	0.04
Paβ	04:30:45.59	+64:51:08.08	0.51	0.04

Col. (2)-(3).— Equatorial coordinates. Epoch *J2000*. The coordinates refer to the centre of the aperture used in the flux measurements. For the SNR candidates, they also correspond to the centre of the source with an accurary of 0.5″.

Col. (4).— Foreground color excess from Burstein and Heiles (1984). $R_V = 3.1$.

Col. (5).— Intrinsic color excess from Hunter et al. (2000). $R_V = 4.05$.

Table 3.3: Line emission measurements for NGC 1569.

ID	Aperture	$\mathcal{F}_{[\text{Fe II}]}$	$\mathcal{F}_{[\text{Fe II}],\text{dered}}$	$\mathcal{F}_{\text{Pa}\beta}$	$\mathcal{F}_{\text{Pa}\beta,\text{dered}}$
N1569-	(″)	($\times 10^{-19}$ Wm^{-2})		($\times 10^{-19}$ Wm^{-2})	
(1)	(2)	(3)	(4)	(5)	(6)
SNR Candidates					
S001	4.0	30.2 ± 3.1	40.5 ± 4.9	24.8 ± 3.2	38.5 ± 6.0
S002	1.0	2.97 ± 0.38	4.13 ± 0.64	<9.7 ± 1.2	16.0 ± 2.7
S003	(3×2), 47°	6.95 ± 0.90	9.32 ± 1.40	7.3 ± 2.0	11.4 ± 3.5
S004	2.0	3.01 ± 0.83	4.0 ± 1.2	2.3 ± 1.3	3.6 ± 2.1
S005	2.0	3.40 ± 0.86	4.6 ± 1.2	4.1 ± 1.3	6.3 ± 2.1
S006	2.0	3.24 ± 0.91	4.3 ± 1.3	2.3 ± 1.8	3.6 ± 2.8
S007	2.0	9.92 ± 0.82	13.3 ± 1.4	41.7 ± 2.8	64.8 ± 6.3
S008	(2×0.5), 2°	2.78 ± 0.56	3.73 ± 0.83	19.3 ± 1.6	30.6 ± 3.5
S009	2.0	10.0 ± 1.0	13.9 ± 1.8	7.6 ± 1.7	12.7 ± 3.3
S010	1.5	6.33 ± 0.64	8.5 ± 1.0	20.1 ± 2.6	31.8 ± 5.0
S011	2.0	5.44 ± 0.80	7.6 ± 1.3	122. ± 21.	205. ± 44.
Other Sources					
O001	(5×3.5), 2°	18.6 ± 1.9	25.9 ± 3.3	<137. ± 17.	225. ± 38.
O002	(4×1.5), 2°	14.4 ± 1.5	19.3 ± 2.3	15.0 ± 1.9	23.3 ± 3.7
O003	(4×3), 354°	31.3 ± 2.6	42.0 ± 4.3	86.0 ± 9.5	134. ± 19.
O004	(7.5×6), 49°	29.0 ± 2.9	40.4 ± 5.2	1050. ± 134.	1765. ± 300.
Whole Galaxy					
[FeII]	(31×13.5), 296°	1234 ± 68	1660 ± 120	1033 ± 840	16 300 ± 1800
Paβ	(52×21), 296°				

Col. (2).— Size and position angle of the aperture used in the flux measurements.

Col. (3)-(4).— Observed and extinction corrected [Fe II] λ1.644 μm fluxes.

Col. (5)-(6).— Observed and extinction corrected Paβ λ1.282 μm fluxes.

Table 3.4: Line ratio and luminosity of the sources in NGC 1569.

ID N1569-	[Fe II]/Paβ	$L_{[\mathrm{Fe\ II}]}$	$L_{\mathrm{Pa}\beta}$
		($L_\odot$)	
(1)	(2)	(3)	(4)
SNR Candidates			
S001	1.05 ± 0.21	780. ± 340.	740. ± 330.
S002	0.259 ± 0.060	78. ± 35.	307. ± 140
S003	0.82 ± 0.28	179. ± 79.	220. ± 110.
S004	1.12 ± 0.72	77. ± 39.	69. ± 48.
S005	0.72 ± 0.32	87. ± 43.	122. ± 65.
S006	1.2 ± 1.0	83. ± 42.	69. ± 61.
S007	0.205 ± 0.029	255. ± 110.	1240. ± 540.
S008	0.122 ± 0.030	72. ± 33.	587. ± 257.
S009	1.09 ± 0.32	266. ± 117.	244. ± 121.
S010	0.267 ± 0.053	163. ± 70.	610. ± 275.
S011	0.037 ± 0.010	145. ± 66.	3930. ± 1880.
Other Sources			
O001	0.115 ± 0.024	500. ± 125.	4300. ± 1200.
O002	0.83 ± 0.16	370. ± 90.	450. ± 120.
O003	0.314 ± 0.054	805. ± 190.	2560. ± 660.
O004	0.023 ± 0.005	775. ± 340.	$(3.4 \pm 1.7)\times10^4$
Whole Galaxy			
	0.101 ± 0.014	$(3.2 \pm 1.3)\times10^4$	$(31. \pm 14.)\times10^4$

Col. (2).— Extinction corrected [Fe II] λ1.644 μm /Paβ line ratio.
Col. (3)-(4).— Extinction corrected luminosity. $D = 2.5 \pm 0.5$ Mpc.

and Bignell (1976). We measure a [Fe II]/Paβ line ratio of 1.22 for this source, which agrees with ratios found in SNRs in M33 and M82 (Lumsden and Puxley, 1995; Greenhouse et al., 1997; Alonso-Herrero et al., 2001). Also, the line ratio is a few orders of magnitude larger than for typical H II regions, as expected for SNRs. The [Fe II] luminosity is similar to the largest luminosities observed in SNRs in M33 (Morel et al., 2002). On the [Fe II] image, the source is resolved and circular, and shows some substructure. The source has been detected in the radio with MERLIN (Greve et al., 2002, their source M-6). The source displays a non-thermal spectrum, with $\alpha = -0.55 \pm 0.02$. Therefore, we are very confident that this source is indeed a supernova remnant.

N1569-S002 [Figure C.2] This compact, high surface brightness source lies on the edge of Waller 7, a bright H II region (Waller, 1991). Although a fair amount of Paβ emission is detected within the source's aperture, no Paβ knot, or enhancement, can be detected. It is quite possible that the Paβ emission measured is not actually associated with the [Fe II] source. Therefore, the [Fe II]/Paβ line ratio, observed to be 0.259, which is more typical of starburst galaxies than of supernova remnants, should be taken as a lower limit. At $56\,L_{\odot}$, the [Fe II] luminosity corresponds to the low-end of the luminosity distribution of SNRs. Finally, no continuum counterpart is detected. We conclude that this source is most likely a supernova remnant.

N1569-S003 [Figure C.3] On the [Fe II] image, the source shows up as a small crescent. It is coincident with Star Cluster 35 of Hunter et al. (2000), extending to the South of the cluster. Some Paβ emission, with a morphology similar to the [Fe II] emission, seems to be associated with the source. Yet, the [Fe II]/Paβ line ratio is observed to be 0.82, and the [Fe II] luminosity to be $179\,L_{\odot}$. Both values are typical of SNRs. This source is likely a supernova remnant.

N1569-S004 [Figure C.4] The source lies between Star Clusters 35 and 31 of Hunter et al. (2000). Some Paβ emission might be associated with the source. The measurements and their interpretation are made difficult by the source's proximity to the masked out area corresponding to the saturated SSC B. The [Fe II] luminosity is quite low, but the [Fe II]/Paβ line ratio is large, at 1.12. The extent of the [Fe II] source is approximatively 1.5″, or 18 pc at the distance of NGC 1569. We conclude that this source is probably a SNR, but better observations are recommended for a firmer identification.

N1569-S005 [Figure C.5] This source lies between Star Cluster 29 (Hunter et al., 2000) and SSC B. Continuum flux, possibly a small association of stars, is spatially coincident with the source. Faint, extended Paβ emission is also seen at the source's position. The source is located near the masked out areas of the saturated SSCs A and B. The region is crowded and the source is quite faint, but the [Fe H]/Paβ line ratio is large enough to suggest a SNR. This is probably a SNR, but better observations are recommended for a firmer identification.

N1569-S006 [Figure C.6] This faint source, to the East of Star Cluster 29 (Hunter et al., 2000), lies near the edge of a faint H II region. No continuum emission can be associated with the source. The large measurement uncertainties, both in [Fe II] and Paβ, come from the measurement of the surrounding background. The source is located in a crowded area, and it is near the masked out areas of SSCs A and B. The [Fe II]/Paβ line ratio is typical of SNRs. This source is probably a SNR, but better observations are recommended for a firmer conclusion.

N1569-S007 [Figure C.7] This source is slightly offset from a compact continuum source. The source is also coincident with a strong compact Paβ source. The

Paβ knot might be associated with the surrounding intense emission that seems to come from a large H II region in that area. The source lies near the SSC A masked out area, but the whole source is visible. The [Fe II]/Paβ line ratio, observed to be 0.205, is more typical of starburst galaxies than of SNRs. The presence of a very bright Paβ knot and of a continuum source at the candidate's location could suggest a blackbody photoionization origin for the [Fe II] emission. However, the line ratio seems too high. Indeed, the line ratio for the blackbody photoionization [Fe II] source N5253-C005, in NGC 5253, is an order of magnitude lower (Section 3.4). N1569-S007 is probably a SNR associated with a small star-forming cluster.

N1569-S008 [Figure C.8] This faint [Fe II] emitter is located about 0.5″ East of a H II region (aperture number 9 of Devost et al. (1997)). The [Fe II] emission is elongated along the edge of the H II region and spans approximatively 24 pc. No continuum emission can be clearly associated with the source. This source is located near the masked out area around the saturated Star Cluster 30 (Hunter et al., 2000). In Paβ, it is not clear whether the flux measured is actually associated with the [Fe II] emitter or with the H II region. Therefore, the Paβ flux is taken as an upper limit, leading to a lower limit of 0.122 for the observed [Fe II]/Paβ line ratio. The source has been confirmed to be mostly non-thermal, with some thermal emission (Greve et al., 2002, Source M-5). Given these observations it seems plausible that we have in fact detected a SNR in interaction with a molecular cloud.

N1569-S009 [Figure C.9] This high surface brightness [Fe II] source is located just ($\sim$ 0.25″) West of Star Cluster 8 (Hunter et al., 2000). The source is about 5″ North of the Waller 2-3 H II complex that, in Paβ, outshines everything else in

this area. Efforts were made to remove the Paβ flux associated with Waller 2. On the resulting image, a faint Paβ knot can be seen near the position of the SNR candidate. Based on the FWHM, the source is marginally resolved and has a diameter of 2″ or 24 pc. The [Fe II]/Paβ line ratio is observed to be 1.09, well within the SNR regime. In addition, the source has been confirmed to be non-thermal, with a spectral index of -0.58 (Greve et al., 2002, Source M-3). We can conclude that this source is a strong SNR candidate.

N1569-S010 [Figure C.10] This is another high surface brightness [Fe II] source. It is located 0.5″ to the West of Star Cluster 3 (Hunter et al., 2000). It is also spatially coincident with a bright Paβ knot. Whether the Paβ emission is associated with the cluster or with the [Fe II] emitter is impossible to tell at this spatial resolution. The [Fe II]/Paβ line ratio is more typical of starburst galaxies than SNRs, while the [Fe II] luminosity is typical for a SNR. With the information at hand, we suggest that the [Fe II] emitter is a SNR within a star-bursting cluster. The strong Paβ emission coincident with the cluster does suggest that star formation is occurring. The low line ratio is likely due to Paβ contamination from the H II region.

N1569-S011 [Figure C.11] This source is actually a bright knot in a much larger [Fe II] feature (see N1569-O004). The feature is spatially coincident with a large H II complex, of which Waller 2 and 3 are the main components. The peak in the [Fe II] emission has Waller 2 as its Paβ counterpart. It should be noted that, while Waller 2 is the strongest Hα emitter, it is not so in Paβ. The Paβ peak is more or less coincident with Waller 3. Relative to the star clusters in the vicinity, the [Fe II] source is located halfway between Clusters 4 and 6 (Hunter et al., 2000). The visible-band HST image shows a large stellar association in

that area. The [Fe II]/Paβ line ratio is low and similar to the ratio observed in the Orion H II region. It seems that we see here a case where the [Fe II] emission is produced through blackbody photoionization by massive, young stars. This source is probably *not* a SNR. Better resolution images would help confirm our conclusion.

Star clusters

Originally, the project was not involved with the super star clusters of NGC 1569, since the goal was to obtain deep images of the galaxy. In the process of obtaining the deep images, the bright star clusters ended up saturating the detector. Therefore no measurements could be made for the star clusters.

As part of another project, near-IR [Fe II] adaptive optics observations of the two SSCs in NGC 1569 were obtained at CFHT. Since no proper guide stars were in range the wave front corrections were done using SSC A as "guide star". This caused a number of complications that resulted in a somewhat limited improvement on the Strehl ratio, and in a disappointing continuum flux subtraction at the position of the star clusters. Nevertheless, the data indicates that the SSCs in NGC 1569 do not exhibit strong [Fe II] line emission, certainly not as strong as what is observed in the young super star cluster in NGC 5253 (N5253-C005, Section 3.4.2).

Previous [Fe II] line emission measurements of NGC 1569 were obtained by Vanzi and Rieke (1997) from long-slit spectroscopy. Their slit aperture was centred on SSC A. They found a flux equal to $(1.7 \pm 0.3)\times10^{-18}\,\mathrm{Wm}^{-2}$. Unfortunately, the area covered by the slit is saturated in our images. However, we can see that the flux measured by Vanzi and Rieke for SSC A is about 100 times lower than the flux we measured for the whole galaxy.

Other sources

N1569-O001 [Figure C.12] This extended source lies on the Western edge of a bright H II region (Waller 7). Substructure is visible. The [Fe II]/Paβ line ratio is more typical of starburst galaxies than SNRs, but one has to keep in mind that the Paβ flux is not exactly spatially coincident with the [Fe II] emission. The Paβ emission within the aperture might not be associated to the [Fe II] region, making the line ratio a lower limit. On the other hand, a physical connection between the H II region and the [Fe II] region is possible as they are separated by a projected distance of only $\sim 18\,\mathrm{pc}$. The [Fe II] luminosity is observed to be $500\,L_{\odot}$. This value includes the compact source N1569-S002, itself with a luminosity of $78\,L_{\odot}$. This leaves about $422\,L_{\odot}$ to be accounted for. The average [Fe II] luminosity of the SNR candidates detected in NGC 1569 is $\sim 200\,L_{\odot}$. Two or three unresolved remnants can account for the [Fe II] emission in this area. Of course, since this average luminosity is obtained from the brightest SNRs, a few more remnants could be necessary to explain the measured flux .

N1569-O002 [Figure C.13] The source is partially masked out due to the saturation of SSC A, yet significant emission is observed. The source coincides with the Eastern part of a strong continuum source, Star Cluster 29 (Hunter et al., 2000). Compact Paβ emission is also spatially coincident. Although the [Fe II]/Paβ ratio (0.828) would suggest SN activity, the proximity to the saturated SSC A make us cautious: this source might be an artifact caused by the PSF matching of the broad-band image to the narrow-band image.

N1569-O003 [Figure C.14] Although the source is near the SSC A masked-out area, it is entirely visible. An extended Paβ feature is spatially coincident with the [Fe II] source. No continuum source can be associated with the [Fe II] emission.

The [Fe II]/Paβ line ratio is a little low for a SNR but is typical of a starburst. The [Fe II] luminosity is sufficiently large to account for 3 to 4 SNRs (with $\langle L_{SNR} \rangle \sim 200\,L_{\odot}$, see discussion of N1569-O001).

N1569-O004 [Figure C.15] The morphology of this extended [Fe II] source is quite interesting. The [Fe II] emission seems to define an arc with a large patch of emission to the West. The strongest emission comes from a knot identified above as N1569-S011. The whole feature is not exactly spatially coincident with the large H II complex formed by Waller 2 and 3. Rather, it is offset to the West. The continuum emission does not display this morphology. Although quite large, the feature has a low total [Fe II] luminosity, most of which actually comes from the compact source (N1569-S011). The [Fe II]/Paβ line ratio is very low, similar to the Orion H II region. An important factor to consider is the presence of a giant molecular cloud (GMC) in the vicinity. The [Fe II] feature is in fact coincident with the Northern section of GMC-3 detected by Taylor et al. (1999) from CO emission. It is possible that the [Fe II] emission maps the interaction of SNRs, or a SNR blown bubble, with the high density cloud. A blackbody photoionization origin for the [Fe II] cannot be rejected, although this mechanism could not explain the Northern branch of the feature which is not coincident with the Paβ complex.

3.2.3 Comments on the Extended [Fe II] Emission

Although quite a few compact sources can be distinguished, most of the [Fe II] emission appears as extended emission. Whether the emission is true diffuse and unstructured emission, or simply a large contingent of unresolved and mingled SNRs, will be addressed in Chapter 4. *Note that the compact sources detected (SNR candidates and other sources) account for only 14% of the total [Fe II] luminosity.* Using

the average [Fe II] luminosity of the sources listed as SNR candidates as the typical luminosity of the SNR in NGC 1569, i.e. $\sim 200\,L_{\odot}$, one finds that the number of SNRs needed to account for the integrated [Fe II] luminosity is $\sim$160. At first glance this number surprises us as being quite low. However one must keep in mind that the [Fe II] emitting phase is limited to the radiative stage of a SNR's evolution. As explained in Waller (1991), when scaled to the Milky Way, the current ionizing star formation rate in NGC 1569 suggests the explosion of about 4000 SNe/Myr. Assuming that the radiative phase of the evolution, and therefore the [Fe II] emitting phase, lasts at most 10^5 yrs, the number of emitting remnants should be <400.

3.3 NGC 3738

Unlike the cases of NGC 1569 and NGC 5253, NGC 3738 has not been the subject of intense scrutiny. The information available on this galaxy is fairly limited. NGC 3738 is classified as a Magellanic irregular (de Vaucouleurs et al., 1991) displaying nuclear H II activity (e.g. Böker et al. (1999)). The light profile is described as a bright central light excess above a pure exponential. The excess is also bluer, suggesting ongoing star formation (Bremnes et al., 2000). In the central region, the star formation rate per unit area has been estimated as $\log SFR/Area = -2.26\,M_{\odot}\,yr^{-1}\,kpc^{-2}$ from the Hα luminosity (Roye and Hunter, 2000). The line profile of the weak CO emission detected at the centre of the galaxy gives a dynamical mass of $M_{dyn} = 2.4 \times 10^8\,M_{\odot}$ and a hydrogen mass of $M_{HI} = 1.6 \times 10^6\,M_{\odot}$ (Tacconi and Young, 1985). The average electron density, n_e, is measured to be $52^{+11}_{-21}\,cm^{-3}$ from [SII] line ratio (Martin, 1997). Hunter (1984) found areas with high oxygen ratios, suggestive of the presence of shocks throughout the galaxy.

3.3.1 Data Analysis Issues

Reddening

The foreground Galactic extinction in the direction of NGC 3738 is negligible, $E(B-V)_f = 0.0$ (Burstein and Heiles, 1984). The intrinsic reddening has been estimated as $E(B-V)_i = 0.22$ from emission line spectroscopy of H II regions in the centre of the galaxy (Hunter and Hoffman, 1999). We applied the same intrinsic reddening law to the flux and luminosity measurements as we did for NGC 1569 (Section 3.2.1).

Distance

Widely different distance estimates for this galaxy are used in the literature. However, most of these distances are derived from the radial velocity of the galaxy, assuming some value for the Hubble constant. These estimates range from 4 to 5.4 Mpc (Hunter, 1982; Hunter et al., 1982; Hunter and Hoffman, 1999). For nearby galaxies, such distance estimates are plagued not only by the uncertainties in the Hubble constant, but also by the peculiar velocities of the galaxies. Recently, good photometric measurements of the brightest stars in NGC 3738 led to a distance of 3.52 ± 0.44 Mpc (Georgiev et al., 1997). We consider this distance estimate more reliable than the ones obtained from the Hubble law. Georgiev et al. did not provide an uncertainty for the distance. The uncertainty quoted above comes from the spread in the magnitudes of the three brightest stars that were used in the distance calculation. In this work, a distance of 3.52 ± 0.44 Mpc will be adopted for NGC 3738.

3.3.2 Comments on Compact [Fe II] Sources

No compact [Fe II] sources can be identified in NGC 3738. The [Fe II] 1σ detection level, for one pixel, is estimated as $2.2\,L_\odot$ ($D = 3.52$ Mpc). If supernova remnants

Table 3.5: Coordinates of the sources in NGC 3738

ID	RA	Dec	$E(B\text{-}V)_f$	$E(B\text{-}V)_i$
(1)	(2)	(3)	(4)	(5)
SNR Candidates				
No SNR candidates can be identified				
Whole Galaxy				
[Fe II]	11:35:48.70	+54:31:27.2	0.00	0.22
Paβ	11:35:48.70	+54:31:27.2	0.00	0.22

Col. (2)-(3).— Equatorial coordinates. Epoch *J2000.* The coordinates refer to the centre of the aperture used in the flux measurements.

Col. (4).— Foreground color excess from Burstein and Heiles (1984).

Col. (5).— Intrinsic color excess from Hunter and Hoffman (1999).

Table 3.6: Line emission measurements for NGC 3738.

ID	Aperture	$\mathcal{F}_{[\text{Fe II}]}$	$\mathcal{F}_{[\text{Fe II}],\text{dered}}$	$\mathcal{F}_{\text{Pa}\beta}$	$\mathcal{F}_{\text{Pa}\beta,\text{dered}}$
	($''$)	($\times 10^{-19}$ Wm^{-2})		($\times 10^{-19}$ Wm^{-2})	
(1)	(2)	(3)	(4)	(5)	(6)
SNR Candidates					
No SNR candidates can be identified					
Whole Galaxy					
	(17.5×13.5), 301°	142 ± 14	167 ± 22	841 ± 45	1088 ± 114

Col. (2).— Size and position angle of the aperture used in the flux measurements.

Col. (3)-(4).— Observed and extinction corrected [Fe II] λ1.644 μm fluxes.

Col. (5)-(6).— Observed and extinction corrected Paβ λ1.282 μm fluxes.

Table 3.7: Line ratio and luminosity of the sources in NGC 3738.

ID	[Fe II]/Paβ	$L_{[\mathrm{Fe\ II}]}$ ($L_\odot$)	$L_{\mathrm{Pa}\beta}$
(1)	(2)	(3)	(4)
SNR Candidates			
	No SNR candidates can be identified		
Whole Galaxy			
	0.153 ± 0.026	(0.634 ± 0.192)×10^4	(4.136 ± 1.271)×10^4

Col. (2).– Extinction corrected [Fe II] λ1.644 μm /Paβ line ratio.
Col. (3)-(4).– Extinction corrected luminosity. $D = 3.52 \pm 0.44$ Mpc.

similar to the ones observed in the other two galaxies were present, we would have detected them. The electron density in NGC 3738 is lower than what is observed in the central parts of NGC 1569 and NGC 5253, where we detect a number of SNR candidates (Martin, 1997). Indeed, the electron density in NGC 3738 is more similar to the density measured in the outer regions of the other two galaxies where, with the exception of N1569-S001, no compact [Fe II] sources are detected.

3.3.3 Comments on the Extended [Fe II] Emission

A faint [Fe II] glow, coincident with the core of galaxy, remains after the continuum subtraction. For such a weak detection, residual flux from the continuum subtraction could be significant. The [Fe II] flux and luminosity are quoted in Tables 3.6 and 3.7, respectively. The coordinates of centre of the photometric apertures are given in Table 3.5. The [Fe II] measurements must be taken as upper limits, as it is unclear what fraction of the flux is due to artifacts left over from the continuum subtraction.

Star formation, and the supernova activity that comes along with it, are expected to create regions of shock-heated gas (e.g. McKee and Hollenbach, 1980). Hα loops

from expanding shells of ionized gas (Martin, 1998), and high [O II]λ3727/[O III]λ5007 line ratios (Hunter, 1984) — the latter often seen in association with SNRs (e.g. Dopita et al., 1980) — have been observed in NGC 3738. Hence, the absence of [Fe II] line emission is somewhat unexpected.

However, in Hunter (1984), it was found that the region with the highest [O II]λ3727/[O III]λ5007 line ratio did not agree with standard shock models. This conclusion is supported by the weakness of the [Fe II] emission in our images, which argues against a significantly shocked environment.

Martin (1998) used long-slit echelle spectroscopy of the Hα emission to identify expanding shells of ionized gas in NGC 3738. The maximum shell expansion velocity observed is 37 km/s. This is too slow to generate near-IR [Fe II] emission from shock heating (Mouri et al., 2000). The shells are found very close to the center of the galaxies, near the H II regions. This contrasts with the shells in NGC 1569 and NGC 5253, which are predominantly found around the core rather than directly where the star formation activity is occurring. It is possible that the expanding bubbles in NGC 3738 prevent the survival of the extensive partially ionized zones essential to the [Fe II] line emission. A parallel can be made with the Hα shell surrounding the super-star clusters A and B in NGC 1569, a bubble within which little SNR activity has been detected (Devost et al., 1997; Greve et al., 2002).

The star formation rate in NGC 3738 is an order of magnitude lower than the rates derived for NGC 1569 and NGC 5253 (Martin, 1998); it is reasonable to assume that the supernova rate will also be about an order of magnitude lower. If the integrated [Fe II] luminosity of a galaxy scales with the SN rate, then we would expect a luminosity of about $4 \times 10^3\,L_\odot$, scaling from the [Fe II] luminosity we observe in NGC 1569 and NGC 5253. This agrees with our upper limit of $< 6 \times 10^3\,L_\odot$ for the total [Fe II] luminosity of NGC 3738.

In conclusion, a low integrated [Fe II] luminosity for NGC 3738 can be explained from star formation rate arguments. However, the absence of compact [Fe II] sources is puzzling.

3.4 NGC 5253

NGC 5253 is a metal-poor dwarf galaxy member of the Centaurus Group. The galaxy harbours an extremely young starburst in its core that may have been triggered by an encounter with the "grand design" galaxy M83. A wealth of information, from X-ray to radio, has been published on this prototype starburst galaxy. As is the case for NGC 1569, the proximity of the galaxy makes it an excellent laboratory for the study of the starburst phenomenon.

A metallicity of $\frac{1}{5}Z_{\odot}$, mostly uniform across the galaxy, has been measured for NGC 5253 (Kobulnicky et al., 1999). The metallicity uniformity is broken only in a few areas where an enhanced nitrogen abundance is observed (Walsh and Roy, 1989; Kobulnicky et al., 1997).

The most prominent feature of NGC 5253 is an intense, ongoing burst of star formation more or less coincident with the geometric centre of the galaxy. An encounter, 1–2 Gyr ago, with the neighbouring galaxy M83 has been suggested as the triggering event for the current burst (van den Bergh, 1980), an argument based, in particular, on the warping of the H I disk of M83 (Rogstad et al., 1974). A dozen young, UV-bright star clusters are detected in the central 20″ (Meurer et al., 1995). The galaxy is very blue except where dust causes patchy and heavy obscuration (Calzetti et al., 1997). Indeed, radio observations indicate that a large fraction of the most recent star formation is hidden by dust (Turner et al., 1998).

Thermal free-free emission from ionized gas in the starburst core dominates the radio continuum (e.g. Turner et al., 1998). So strong is the thermal component that Beck, Turner and Ho (1996) were forced to conclude that there was no evidence for

synchrotron emission from supernova remnants, a rather unusual result for a starburst galaxy. More recently, the authors revisited NGC 5253 with higher resolution radio observations. They did find regions of diffuse non-thermal synchrotron emission, as well as probable SNRs around the central radio source (Turner et al., 1998). We will see below that several SNR candidates were detected in our [Fe II] line emission images (Section 3.4.2).

3.4.1 Data Analysis Issues

Reddening

We used the same foreground and intrinsic reddening laws as the ones we used before for NGC 1569 (Section 3.2.1). NGC 5253 suffers from very little foreground reddening. Burstein & Heiles (1984) derived a Galactic extinction in the direction of NGC 5253 equivalent to a color excess of $E(B-V)_f = 0.05$.

The obscuration intrinsic to NGC 5253 is not uniform. In particular, a large dust lane crosses the galaxy along the East-West axis. To improve on the reddening correction we used $E(B-V)_i$ estimates for star clusters from Tremonti et al. (2001) and Calzetti et al. (1997). The color excess values of Tremonti et al. were derived using the starburst reddening curve of Calzetti et al. (2000). The intrinsic absorption obtained from Calzetti et al. had to be converted to a color excess. $R_V = 4.05$ (Calzetti et al., 2000) was used in the correction. As we did for the sources in NGC 1569, we assigned to our sources the $E(B-V)_i$ value of the closest star cluster.

Distance

Observations of Cepheid variables in NGC 5253 by the *Hubble Space Telescope* Key Project team indicate a distance of 4 Mpc and 4.1 Mpc (Sandage et al., 1994; Saha et al., 1995, respectively). However, a recent recalibration of the existing HST Key Project data by Gibson et al. (2000) has produced an improved distance estimate

to the galaxy of 3.33 ± 0.29 Mpc. In this work, a distance of 3.33 ± 0.29 Mpc will be adopted for NGC 5253.

3.4.2 Comments on Compact [Fe II] Sources

Here we comment on the sources identified in our [Fe II] line emission image of NGC 5253. Under the *SNR Candidates* label, we have collected all the small, well defined [Fe II] sources. Whether or not they should be retained as SNR candidates is discussed below. The sources found under the label *Other Sources* are [Fe II] areas more extended than the SNR candidates, and sometimes show substructure. Also, six of the largest star clusters were considered, regardless of the strength of the [Fe II] emission.

The coordinates of the [Fe II] sources, along with the foreground and intrinsic color excess, are listed in Table 3.8. The measured line properties of the sources are presented in Tables 3.9 and 3.10.

Supernova remnant candidates

N5253-S001 [Figure C.16] This strong and large [Fe II] source lies near the centre of what appears to be a trough in the Paβ emission. The star clusters 2 and 3 (following the identification scheme by Calzetti et al. (1997)) are also located close to the centre of that void. The source has a diameter of 3″ which corresponds to 48 pc at the distance of NGC 5253. It exhibits a circular symmetry with well defined edges. The source is not spatially coincident with any continuum sources. The large [Fe II]/Paβ line ratio of 3.1 strongly support a SNR origin for the [Fe II] emission. The [Fe II] luminosity of 331 $L_\odot$ of this SNR candidate is similar the luminosity of the SNRs observed in M33 (Morel et al., 2002).

Table 3.8: Coordinates of the sources in NGC 5253

ID (1)	RA (2)	Dec (3)	$E(B-V)_f$ (4)	$E(B-V)_i$ (5)
SNR Candidates				
N5253-S001	13:39:55.37	-31:38:29.9	0.05	0.15
N5253-S002	13:39:55.47	-31:38:27.7	0.05	0.15
N5253-S003	13:39:55.67	-31:38:27.0	0.05	0.11
N5253-S004	13:39:55.76	-31:38:32.0	0.05	0.0
N5253-S005	13:39:55.76	-31:38:29.3	0.05	0.54
N5253-S006	13:39:55.86	-31:38:29.6	0.05	0.54
N5253-S007	13:39:55.76	-31:38:22.5	0.05	0.11
Star Clusters				
N5253-C001	13:39:55.92	-31:38:31.6	0.05	0.0
N5253-C002-3	13:39:55.51	-31:38:29.4	0.05	0.15
N5253-C004	13:39:55.83	-31:38:27.1	0.05	0.11
N5253-C005	13:39:55.93	-31:38:24.6	0.05	0.42
N5253-C006	13:39:55.32	-31:38:33.6	0.05	0.0
Other Sources				
N5253-O001	13:39:55.91	-31:38:24.3	0.05	0.42
Whole Galaxy				
	13:39:55.94	-31:38:28.4	0.05	0.09

Col. (2)-(3).— Equatorial coordinates. Epoch *J2000*. The coordinates refer to the centre of the aperture used in the flux measurements. For the SNR candidates, they also correspond to the centre of the source with an accurary of 0.5″.

Col. (4).— Foreground color excess from Burstein and Heiles (1984). $R_V = 3.1$.

Col. (5).— Intrinsic color excess from Tremonti et al. (2001) and Calzetti et al. (1997). $R_V = 4.05$.

Table 3.9: Line emission measurements for NGC 5253.

ID N5253- (1)	Aperture (″) (2)	$\mathcal{F}_{[\mathrm{Fe\ II}]}$ ($\times 10^{-19}$ Wm^{-2}) (3)	$\mathcal{F}_{[\mathrm{Fe\ II}],\mathrm{dered}}$ ($\times 10^{-19}$ Wm^{-2}) (4)	$\mathcal{F}_{\mathrm{Pa}\beta}$ ($\times 10^{-19}$ Wm^{-2}) (5)	$\mathcal{F}_{\mathrm{Pa}\beta,\mathrm{dered}}$ ($\times 10^{-19}$ Wm^{-2}) (6)
SNR Candidates					
S001	3.0	8.49 ± 0.71	9.7 ± 1.0	2.5 ± 1.4	3.1 ± 1.8
S002	2.0	3.63 ± 0.54	4.16 ± 0.71	<0.73	<0.908 ± 0.034
S003	1.0	0.93 ± 0.18	1.03 ± 0.22	<0.90	<1.07 ± 0.03
S004	(2×1.5), 1°	5.10 ± 0.50	5.23 ± 0.53	<1.15	<1.197 ± 0.002
S005	1.5	2.28 ± 0.90	3.47 ± 1.65	<5.70	<11.1 ± 6.6
S006	1.0	1.33 ± 0.48	2.03 ± 0.89	<1.64 ± 0.84	<3.2 ± 2.1
S007	2.0	4.32 ± 0.72	4.81 ± 0.88	50.0 ± 3.7	98. ± 20.
Star Clusters					
C001	(2×1.5), 301°	11.5 ± 1.2	11.8 ± 1.2	11.4 ± 3.0	11.8 ± 3.2
C002-3	1.0	1.47 ± 0.28	1.68 ± 0.38	2.65 ± 0.83	3.28 ± 1.18
C004	(3×2.2), 291°	5.13 ± 0.99	5.7 ± 1.2	86.7 ± 11.0	103. ± 16.
C005	2.0	13.55 ± 0.75	18.9 ± 2.2	311. ± 17.	528. ± 81.
C006	2.0	-0.31 ± 0.36	–.– ± –.–	4.91 ± 0.85	5.10 ± 0.89
Other Sources					
O001	(2×1.5), 288°	36.7 ± 1.7	50.8 ± 5.5	705. ± 90.	1220. ± 280.
Whole Galaxy					
	(45×35), 23°	1406 ± 78	1540 ± 130	6830 ± 550	7900 ± 1000

Col. (2).— Size and position angle of the aperture used in the flux measurements.

Col. (3)-(4).— Observed and extinction corrected [Fe II] λ1.644 μm fluxes.

Col. (5)-(6).— Observed and extinction corrected Paβ λ1.282 μm fluxes.

Table 3.10: Line ratio and luminosity of the sources in NGC 5253.

ID N5253-	[Fe II]/Paβ	$L_{[\mathrm{Fe\ II}]}$	$L_{\mathrm{Pa}\beta}$
		($L_\odot$)	
(1)	(2)	(3)	(4)
SNR Candidates			
S001	3.1 ± 1.8	331. ± 72.	107. ± 65.
S002	>4.58 ± 0.80	141. ± 36.	<31. ± 7.
S003	>0.97 ± 0.21	35.0 ± 9.7	<36.3 ± 7.3
S004	>4.37 ± 0.44	178. ± 36.	<40.8 ± 7.2
S005	>0.31 ± 0.24	188. ± 61.	<380. ± 235.
S006	>0.64 ± 0.50	69. ± 33.	<110. ± 73.
S007	0.049 ± 0.013	164. ± 42.	3300. ± 1050.
Star Clusters			
C001	1.00 ± 0.29	402. ± 82.	403. ± 130.
C002-3	0.51 ± 0.22	57. ± 17.	112. ± 45.
C004	0.056 ± 0.015	194. ± 54.	3490. ± 850.
C005	0.036 ± 0.007	640. ± 160.	$(18 \pm 5)\times10^3$
C006	–.– ± –.–	–.– ± –.–	174. ± 43.
Other Sources			
O001	0.041 ± 0.010	1740. ± 420.	$(42 \pm 12)\times10^3$
Whole Galaxy			
	0.195 ± 0.041	$(5.2 \pm 1.1)\times10^4$	$(26.8 \pm 6.4)\times10^4$

Col. (2).— Extinction corrected [Fe II] λ1.644 μm /Paβ line ratio.
Col. (3)-(4).— Extinction corrected luminosity. $D = 3.33 \pm 0.29$ Mpc.

N5253-S002 [Figure C.17] This source lies at the centre of a void in the Paβ emission, along with N5253-S001 and Star Clusters 2 and 3. No Paβ emission is detected at the candidate's location. The Paβ detection level is estimated as $0.733 \times 10^{-19}\,\mathrm{Wm}^{-2}$, which leads to a lower limit of 4.58 on the [Fe II]/Paβ line ratio, typical of SNRs. The source is marginally resolved with a diameter of 1.5″ (24 pc). It exhibits a circular symmetry and it is not coincident with any continuum sources. We conclude that this [Fe II] source is a strong SNR candidate.

N5253-S003 [Figure C.18] The source lies in a Paβ trough connected to the void in which N5253-S002 is found. No Paβ emission appears to be associated with the [Fe II] source. The Paβ detection threshold is estimated as $0.9 \times 10^{-19}\,\mathrm{Wm}^{-2}$. The [Fe II]/Paβ line ratio is found to be greater than 0.97, in agreement with a SNR interpretation. The source is small and unresolved with a diameter < 18 pc. No continuum source is observed at the candidate's location. The [Fe II] luminosity is very low, however. Nevertheless, we conclude that this source is likely a SNR.

N5253-S004 [Figure C.19] This source lies South-East of a H II region, and it is a significant distance away from N5253-C001. The [Fe II] emission is more extended along the North-South axis, spanning over 2″. No Paβ emission appears to be associated with the [Fe II] source. No continuum source is detected at the candidate's position. The [Fe II]/Paβ line ratio is particularly large, 4.37, and since no Paβ emission was actually detected, this ratio is a lower limit. We conclude that this source is most likely a SNR.

N5253-S005 [Figure C.20] This unresolved [Fe II] source lies in the East-West dust lane (e.g. Calzetti et al., 1997). The source is located just West of a continuum

source, but it is not spatially coincident with it. We detect Paβ emission at this location. However, whether this emission is actually associated or not with the [Fe II] source is far from clear. The Paβ emission looks more like diffuse emission emanating from the intense Paβ source that is associated with N5253-C005. We attempted to remove the diffuse Paβ emission to see if any knot would surface, but the resulting image was too noisy in that area. Therefore, the Paβ flux measurement should be considered an upper limit, and the [Fe II]/Paβ line ratio of 0.31 a lower limit. Even so, the ratio favours a SNR origin for the [Fe II] emission. And because of the compactness of the [Fe II] source, we conclude that the source is a likely SNR candidate.

N5253-S006 [Figure C.21] This small, low surface brightness [Fe II] source is also located in the East-West dust lane of NGC 5253. Within alignment uncertainties, the source is spatially coincident with a continuum source. After removal of the diffuse Paβ emission, no Paβ feature is detected at the [Fe II] source's location. With a [Fe II]/Paβ line ratio >0.64 this source is probably of SNR origin.

N5253-S007 [Figure C.22] This [Fe II] source is located 3″ North-West of the super star cluster N5253-C005 (SSC-5). The flux measurements were made difficult by the strong [Fe II] and Paβ emission associated with SSC-5. To improve on the accuracy of the measurements, most of the flux emitted by SSC-5 was first removed. The morphology of the fainter features were revealed. In particular, the Paβ emission in the vicinity of SSC-5 is quite complex and displays several knots. The [Fe II] source is coincident with an unresolved continuum source. As for the Paβ flux measured within the [Fe II] source's aperture, it is not clear whether it is associated with the [Fe II] emitter: the nearest Paβ knot

is 1″ South of the [Fe II] source. The low [Fe II]/Paβ line ratio is similar to the ratio observed in the Orion H II region. However, we detect no H II region spatially coincident with the [Fe II] source. The [Fe II] source itself is sharp, and well above the detection threshold. Contamination from the surrounding H II complex could explain the inflated Paβ luminosity. With all these considerations in mind, the [Fe II] source could still be a SNR, despite the low ratio. A definitive conclusion regarding the nature of this source is not possible from our data, but a SNR origin for the [Fe II] emission is a reasonable conclusion.

Star clusters

N5253-C001 [Figure C.23] The [Fe II] emission is fairly compact but extends a little ($\sim$1″) to the West of the cluster. The peak is coincident with the cluster, within alignment uncertainties. The Paβ emission is limited to the centre of the cluster, and it does not exhibit the oval shape observed in [Fe II]. The [Fe II]/Paβ line ratio is consistent with SNR excitation. The [Fe II] luminosity of the cluster is 402 $L_\odot$ which allows for 1 bright SNR, or 2–3 average remnants. The emission extending to the West could be one of these.

N5253-C002-3 [Figure C.24] The two clusters are too close to each other to be spatially resolved by our observations. The faint [Fe II] emission is very compact and limited to the clusters' position. The Paβ emission is also weak. The [Fe II]/Paβ line ratio is typical of starburst galaxies. Both the low luminosity and the compactness of the [Fe II] emission limit the number of SNR in these clusters to one.

N5253-C004 [Figure C.25] The proximity of this cluster to SSC-5 required the removal of the large scale emission gradient in both emission line images in order

to improve on the accuracy of the flux measurements. The [Fe II] emission is extended with a diameter of $\sim 2''$. The peak of the Paβ emission is located $0.5''$ to the East of the centre of the [Fe II] region. The Paβ region is not limited to the cluster itself, but extends $3''$ to the South-East. The Paβ region is more extended than the [Fe II] region. The [Fe II]/Paβ line ratio is 0.056, similar to the ratio observed in the Orion H II region. Blackbody photoionization would be a valid [Fe II] excitation mode in this young star-forming cluster. However, the [Fe II] emission does not display the same morphology as the Paβ emission. Considering the circular symmetry of the [Fe II] emission and a total [Fe II] luminosity similar to the luminosity of a SNR in this galaxy, we cannot rule out a SNR origin for the [Fe II] flux observed.

N5253-C005 [Figure C.26] This unusual super star cluster is the strongest source of [Fe II] and Paβ emission in NGC 5253. The emission at both wavelengths extends well beyond the cluster itself, despite the evidence from HST images that the size of the cluster is less than $0.5''$ (Calzetti et al., 1997). To isolate the flux originating in the cluster, the photometric aperture was centred on the cluster and kept fairly small. The FWHM of a point source in our line emission data is ~ 2.5 pixels ($\sim 1.25''$). Almost all the flux is contained within a 2 pixel radius. The radius of the aperture was set to 2 pixels. A larger aperture would have included a greater portion of the emission from the surroundings of the cluster; a smaller aperture would have excluded a significant amount of flux directly associated with the cluster itself. In both narrow-band images, a strong compact source is found spatially coincident with the peak in the continuum emission, i.e. the star cluster itself. The [Fe II]/Paβ line ratio is very low, similar to what is observed for the Orion H II region. This ratio is also similar to the ratio observed in N5253-C004. Numerous studies have shown that N5253-C005 is one of the youngest super star clusters observed to date (Tremonti et al.,

2001; Calzetti et al., 1997; Turner et al., 1998). The radio continuum from this region of the galaxy has been observed to be almost purely thermal (Beck et al., 1996; Turner et al., 1998). The large flux of ionizing photons from the young SSC favours a blackbody photoionization origin for the [Fe II] emission.

N5253-C006 [Figure C.27] This star cluster exhibits no [Fe II] emission. Some Paβ emission can be detected but the luminosity is less than 175 $L_\odot$. There might be some [Fe II] emission to the West of the cluster but the emission is faint and diffuse. Calzetti et al. (1997) estimate the age of N5253-C006 to be 10–17 Myr. This cluster is therefore much older than clusters 1, 4, and 5. It is possible that the impact of the starburst on the ISM has had time to fade away, especially if the starburst for this cluster was instantaneous.

Other sources

N5253-O001 [Figure C.28] The whole area around N5253-C005 is very active. The emission, in both Paβ and [Fe II], is more intense in this area than anywhere else in the galaxy, and it displays a complex morphology. Several H II regions are seen around the star cluster. The bulk of the [Fe II] emission comes from two large lobes separated by about 1″, with the Eastern lobe coincident with N5253-C005. The flux measurements correspond to an aperture that includes the two [Fe II] lobes and the bulk of the Paβ emission. The [Fe II]/Paβ line ratio is small and similar to the Orion H II region. It is also similar to the line ratio measured for N5253-C004 and N5253-C005. With the exception of the peak of the emission, spatially coincident with N5253-C005, the [Fe II] emission does not follow the Paβ emission. The [Fe II] emission extends over many parsecs and it is not clear if blackbody photoionization would be sufficient to explain the [Fe II] emission. Shock excitation from SNRs, or perhaps stellar winds, could be present. The [Fe II] luminosity within the aperture is over a 1000 $L_\odot$, even

when the luminosity of N5253-C005 is removed. Up to ~7 SNRs could account for the [Fe II] luminosity (with an average of 150 $L_\odot$ per SNR).

3.4.3 Comments on the Extended [Fe II] Emission

The [Fe II]/Paβ line ratio for the whole galaxy is 0.195, typical of starburst galaxies. The line ratio observed is higher than previous measurements ([Fe II]/Paβ = 0.105, derived by Mouri et al. (2000) from the [Fe II] λ1.644 μm /Brγ line ratio measured by Kawara et al. (1988)). However, these measurements were based on spectroscopic observations of a smaller area centered on cluster N5253-C005. The integrated [Fe II] luminosity is observed to be $5.2 \times 10^4\,L_\odot$. The average [Fe II] luminosity of the detected SNR candidates in NGC 5253 is about 150 $L_\odot$. Nearly 350 such SNRs would be needed to account for the total [Fe II] flux, assuming the dominant excitation mechanism is shock-heating ionization from supernova remnants. Although there is strong evidence that [Fe II] emission from blackbody ionization is present in two of the clusters, this emission is negligible compared to the total flux. Indeed, the compact sources we detected account for a little less than 7%[3] of the total [Fe II] flux. The overall morphology of the [Fe II] emission is quite different from the morphology of the Paβ emission, except at the location of Star Clusters 4 and 5. Finally, based on the line ratios, the presence of an AGN is very unlikely.

3.4.4 Comparison to Previous Measurements

Previous long-slit spectroscopic [Fe II] observations of NGC 5253 have been published (Vanzi and Rieke, 1997; Kawara et al., 1988). Using a small $1'' \times 3''$ slit aperture centred on N5253-C005 (orientation unknown), Vanzi and Rieke (1997) measured a [Fe II] line flux of $\mathcal{F}_{[\mathrm{Fe\,II}]} = (15 \pm 3) \times 10^{-18}\,\mathrm{Wm}^{-2}$. As mentioned in their paper, the presence of many stellar absorption features in their low resolution spectrum made

[3]Including the flux from the star clusters.

the choice of the continuum level difficult. Indeed, looking at the published spectrum, the systematic uncertainties due to continuum subtraction could be as large as ~15%. Vanzi and Rieke's measurement then becomes $\mathcal{F}_{[\mathrm{Fe\ II}]} = (15 \pm 3 \pm 2.5) \times 10^{-18}\,\mathrm{Wm}^{-2}$.

Using a synthetic $1'' \times 3''$ aperture centred on N5253-C005, we measured the flux in our [Fe II] line image. Since the orientation of the slit is not known, we tried both a North–South and a East–West slit. We measured $\mathcal{F}_{[\mathrm{Fe\ II}]} = 3.0 \times 10^{-18}\,\mathrm{Wm}^{-2}$ and $\mathcal{F}_{[\mathrm{Fe\ II}]} = 3.3 \times 10^{-18}\,\mathrm{Wm}^{-2}$, respectively. The photometric uncertainties are estimated as ~10%. Errors on the slit alignment are not included. Our measurements are significantly lower than the measurement by Vanzi and Rieke. It is unclear why there is such a discrepancy. A possible explanation could be in the complex spatial distribution of the [Fe II] emission in this area, combined with the small aperture of the slit. These would make the exact positioning of synthetic slit critical. Also, seeing effects could take some of the flux out of the slit aperture. Increasing the East–West synthetic slit width by $0.5''$ ($1.5'' \times 3''$ instead of $1'' \times 3''$) led to a [Fe II] flux of $4.6 \times 10^{-18}\,\mathrm{Wm}^{-2}$, a 40% increase on the flux from the original aperture. Seeing effects are, we believe, the most likely explanation.

Kawara et al. (1988) used a much larger slit ($10'' \times 21''$), presumably centred on N5253-C005. Although the orientation is not specified, it would be logical to align such a slit to the major axis of the galaxy. The slit covers a good fraction of the [Fe II]-emitting area. The [Fe II] flux measurement with the larger slit should be less sensitive than the Vanzi and Rieke measurement to positioning and seeing issues. Kawara et al. obtained $\mathcal{F}_{[\mathrm{Fe\ II}]} = (9.7 \pm 2.0) \times 10^{-17}\,\mathrm{Wm}^{-2}$.

We measured the [Fe II] flux within a synthetic slit with the same characteristics as the Kawara et al. aperture. We obtained a flux of $\mathcal{F}_{[\mathrm{Fe\ II}]} = 6.3 \times 10^{-17}\,\mathrm{Wm}^{-2}$ with a photometric uncertainties of ~10%, and another ~10% due to slit alignment uncertainties. Given the quoted uncertainties, our measurement is in a marginal agreement with the Kawara et al. flux measurement.

Chapter 4

Near-IR [Fe II] Emission and Supernova Remnant Activity

It is now well recognized that near-IR [Fe II] emission is linked to supernova remnant interactions with the ISM in normal and starburst galaxies. The [Fe II] emission is believed to arise from the partially-ionized zone behind the shock front of a radiative supernova remnant. [Fe II] emission is also observed in active galactic nuclei but the emission mechanism is understood to be power-law photoionization (Mouri et al., 2000). The supernova rate in a galaxy or a star cluster depends on the star formation history. Therefore using the near-IR [Fe II] emission as a tracer of supernova remnants, themselves long-lived tracers of supernova activity, can give insight into the properties of star formation episodes.

We have presented in the previous chapter our sample of [Fe II] sources. Each galaxy will be discussed individually below but a common characteristic to all three is the small number of individual SNRs detected. A priori this observation is rather surprising as one would expect a considerable number of supernova explosions in actively star forming galaxies. With the exception of NGC 3738, for which no [Fe II] emission can be detected, the morphology of the [Fe II] emission is characterized

by a somewhat textured veil of [Fe II] emission around the starburst core with a few compact sources, sometimes spatially coincident with a star cluster. Another characteristic is the absence, with one exception (N1569-S001), of SNRs away from the starburst core. This can be explained, simply on statistical grounds, if the SN rate depends on the stellar mass. But we will see in this chapter that the ambient density also plays an important role.

The purpose of this chapter is to better understand the supernova remnant population in our sample of starburst galaxies and its link to the morphology of the [Fe II] emission. In Section 4.1 we will discuss and compare the properties of the SNRs candidates in NGC 1569 and NGC 5253 to those of Galactic SNRs and SNRs observed in other galaxies. Then, in Section 4.2.1, we will describe the model used to simulate the [Fe II] emission morphology expected for a supernova remnant population. Using this model, we will attempt to simulate the observed [Fe II] emission morphology of our starburst galaxies and to draw conclusions regarding the recent supernova activity and the origin of the near-IR [Fe II] emission in these galaxies (Section 4.2.2).

4.1 Comparative Study of the SNR Candidates

Although the [Fe II] line emission has been used as a diagnostic probe of global supernova activity in starburst galaxies, very few resolved and confirmed SNRs have been systematically surveyed for their [Fe II] emission. Because of their proximity, Galactic supernova remnants are generally too large for the limited field of view of current near-IR camera. Indeed, in most cases the [Fe II] emission is measured only for a small section of the remnant, forcing an extrapolation of the flux for the whole remnant and leading to large uncertainties. Also, the poor distance estimates and extinction corrections for the Galactic SNRs add to the uncertainties in the total [Fe II] luminosity. A few Magellanic Cloud remnants do have [Fe II] measurements, and a number of very luminous [Fe II] sources have been detected in M82 and NGC 253. By

far the most useful sample to date comes from a recent paper by Morel et al. (2002) on a [Fe II] line-imaging survey of known SNRs in M33.

Table 4.1: Properties of SNRs in other galaxies.

Galaxy	ID	D (kpc)	d (pc)	$L_{[\mathrm{Fe\ II}]}$ ($L_\odot$)	[Fe II]/Paβ	References
(1)	(2)	(3)	(4)	(5)	(6)	(7)
Milky Way	Kepler	4 ± 1	4	0.7 ± 0.4	> 1.9	1,2
	RCW 103	6 ± 3	13	170 ± 195	10	1,2
	3C 391:BML	7.2 ± 1.5	12	40 ± 20		3,4,5
LMC	N49	52 ± 3.5	16	720 ± 97	> 2.9	1,6,7
	N63 A	52 ± 3.5	6.3	240 ± 32	> 2.8	1,6,7
	N103 B	52 ± 3.5	6.3	26 ± 3.5		1,6,7
M33	9	840	18	59.9 ± 37.2		8,9,10
	15	840	48	37.3 ± 12.2	1.3 ± 0.6	8,9,10,11
	25	840	27	70.6 ± 28.6		8,9,10
	28	840	11	475 ± 105	4.7 ± 2.2	8,9,10,11
	31	840	39	671 ± 208	4.6 ± 1.6	8,9,10,11
	35	840	32	695 ± 217	1.1 ± 0.4	8,9,10,11
	55	840	18	280 ± 98	1.5 ± 0.6	8,9,10,11
	58	840	17	13.0 ± 4.3		8,9,10,11
	73	840	17	303 ± 93	2.9 ± 1.2	8,9,10,11
	94	840	11	189 ± 51		8,9,10
M82	Fe1	$(3.9 \pm 0.6) \cdot 10^3$	52	$(232 \pm 71) \cdot 10^3$	0.263	12,13
	Fe2	$(3.9 \pm 0.6) \cdot 10^3$	45	$(156 \pm 48) \cdot 10^3$	0.227	12,13
	Fe3	$(3.9 \pm 0.6) \cdot 10^3$	< 27	$(31.2 \pm 9.5) \cdot 10^3$	0.169	12,13
	Fe4	$(3.9 \pm 0.6) \cdot 10^3$	37	$(126 \pm 26) \cdot 10^3$	0.180	12,13
	Fe5	$(3.9 \pm 0.6) \cdot 10^3$	< 27	$(7.3 \pm 2.2) \cdot 10^3$	0.750	12,13
	Fe6	$(3.9 \pm 0.6) \cdot 10^3$	< 27	$(7.2 \pm 2.2) \cdot 10^3$	0.642	12,13
Bin 1: 14 sources		$(3.9 \pm 0.6) \cdot 10^3$		956–6950		13,14
Bin 2: 22 sources		$(3.9 \pm 0.6) \cdot 10^3$		$(7.0\text{–}13.9) \cdot 10^3$		13,14
Bin 3: 26 sources		$(3.9 \pm 0.6) \cdot 10^3$		$(13.9\text{–}20.9) \cdot 10^3$		13,14
Bin 4: 16 sources		$(3.9 \pm 0.6) \cdot 10^3$		$(20.9\text{–}27.8) \cdot 10^3$		13,14
Bin 5: 11 sources		$(3.9 \pm 0.6) \cdot 10^3$		$(27.8\text{–}34.8) \cdot 10^3$		13,14
Bin 6: 9 sources		$(3.9 \pm 0.6) \cdot 10^3$		$(34.8\text{–}41.7) \cdot 10^3$		13,14
Bin 7: 13 sources		$(3.9 \pm 0.6) \cdot 10^3$		$(41.7\text{–}48.7) \cdot 10^3$		13,14
Bin 8: 5 sources		$(3.9 \pm 0.6) \cdot 10^3$		$(48.7\text{–}55.6) \cdot 10^3$		13,14
Bin 9: 6 sources		$(3.9 \pm 0.6) \cdot 10^3$		$(55.6\text{–}62.6) \cdot 10^3$		13,14
Bin 10: 1 sources		$(3.9 \pm 0.6) \cdot 10^3$		$70.0 \cdot 10^3$		13,14

Table 4.1: *continued.*

Galaxy	ID	D (kpc)	d (pc)	$L_{[\mathrm{Fe\ II}]}$ ($L_\odot$)	[Fe II]/Paβ	References
(1)	(2)	(3)	(4)	(5)	(6)	(7)
NGC 253	Nucleus	$(2.5 \pm 0.5) \cdot 10^3$	< 24	$6.3 \cdot 10^3$	0.18	15,16
	A	$(2.5 \pm 0.5) \cdot 10^3$	< 24	$10.3 \cdot 10^3$	0.38	15,16
	B	$(2.5 \pm 0.5) \cdot 10^3$	< 24	$15.0 \cdot 10^3$	1.0	15,16
NGC 1808	Nucleus	$16.4 \cdot 10^3$		$138 \cdot 10^3$	0.533	17,18
	1	$16.4 \cdot 10^3$	< 80	$31.2 \cdot 10^3$	0.689	17,18
	2	$16.4 \cdot 10^3$	< 80	$14.3 \cdot 10^3$	0.160	17,18
	3	$16.4 \cdot 10^3$	< 80	$23.1 \cdot 10^3$	0.201	17,18
	4	$16.4 \cdot 10^3$	< 80	$49.6 \cdot 10^3$	0.314	17,18
	5	$16.4 \cdot 10^3$	< 80	$39.7 \cdot 10^3$	0.154	17,18
	6	$16.4 \cdot 10^3$	< 80	$23.9 \cdot 10^3$	0.132	17,18
	7	$16.4 \cdot 10^3$	< 80	$43.7 \cdot 10^3$	0.152	17,18
	8	$16.4 \cdot 10^3$	< 80	$15.8 \cdot 10^3$	0.139	17,18
	9	$16.4 \cdot 10^3$	< 80	$35.7 \cdot 10^3$	0.149	17,18
	10	$16.4 \cdot 10^3$	< 80	$29.8 \cdot 10^3$	0.235	17,18

Col. (2).— Remnant's identification. M33: *Ref. 9*; M82: *Ref. 12*; NGC 253: *Ref. 15*; NGC 1808: *Ref. 17.*
Col. (3).— Distance to the remnant.
Col. (4).— Diameter of the remnant.
Col. (5).— [Fe II] λ1.644 μm line luminosity.
Col. (6).— [Fe II] λ1.644 μm /Paβ line ratio.

References:

1 – Oliva, Moorwood and Danziger, 1989
2 – Berkhuijsen, 1986
3 – Reach et al., 2002
4 – Reynolds and Moffett, 1993
5 – Wilner et al., 1998
6 – Mathewson et al., 1983
7 – Benedict et al., 2002
8 – Morel et al., 2002
9 – Gordon et al., 1998
10 – Freedman et al., 1991
11 – Lumsden and Puxley, 1995
12 – Greenhouse et al., 1997
13 – Sakai and Madore, 1999
14 – Alonso-Herrero et al., 2001
15 – Forbes et al., 1993
16 – Davidge et al., 1991
17 – Kotilainen et al., 1996
18 – Sandage and Tammann et al., 1987

4.1.1 Results

Our study has led to the detection of 11 compact [Fe II] sources in NGC 1569, 10 of which are considered SNR candidates, and 7 compact sources in NGC 5253, all considered to be SNR candidates (Chapter 3). The [Fe II] luminosity of the SNRs is found to be similar to the luminosity of the SNRs in the M33 sample, and to

the luminosity of the Galactic and Magellanic SNRs (Table 4.1). We will return to the strikingly large luminosity of [Fe II] sources observed in M82 and NGC 253 in a moment.

SNRs in Quiescent Galaxies

When we compare the distribution in luminosity of our detections to the [Fe II]-emitting SNRs in M33 (Figure 4.1), we see that the three samples do agree quite well with each other, keeping in mind the small number of events. In Figure 4.2 we compare the luminosity and diameter of our candidates to the M33, LMC and Galactic remnants. Despite the different properties of the five host galaxies, the luminosities and diameters are in a reasonable agreement; in other words the SNRs in NGC 1569 and NGC 5253 appear to be quite "normal" and do not show the particularly large luminosities that are expected in starburst galaxies. The spread in luminosity can be explained by a spread in the electron density of each remnant, which in turn reflects a variation of the ambient densities. Morel et al. (2002) confirmed a result by Lumsden and Puxley (1995) which showed that the [Fe II] luminosity of a supernova remnant does not correlate well with its diameter. Rather, Morel et al. found that the [Fe II] luminosity is proportional to the electron density measured in the line emitting region of a supernova remnant:

$$L_{[\mathrm{Fe\ II}]} = (1.1 \pm 0.3)\left(\frac{n_e}{\mathrm{cm}^{-3}}\right) \mathrm{L}_{\odot} \tag{4.1}$$

where n_e is derived from the [S II] emission line ratio. This empirical relation applies to radiative SNRs. It should be kept in mind that this relation has been derived on the basis of a few detections that sample only a limited density regime.

In Figure 4.2, we investigate the relation between the [Fe II] luminosity and the diameter of the remnant. It should be noted that the large error bars afflicting the luminosity measurements are dominated by uncertainties in distance estimates to the SNRs or to their host galaxies. Looking at the $L_{[\mathrm{Fe\ II}]}$–diameter plot, one may be

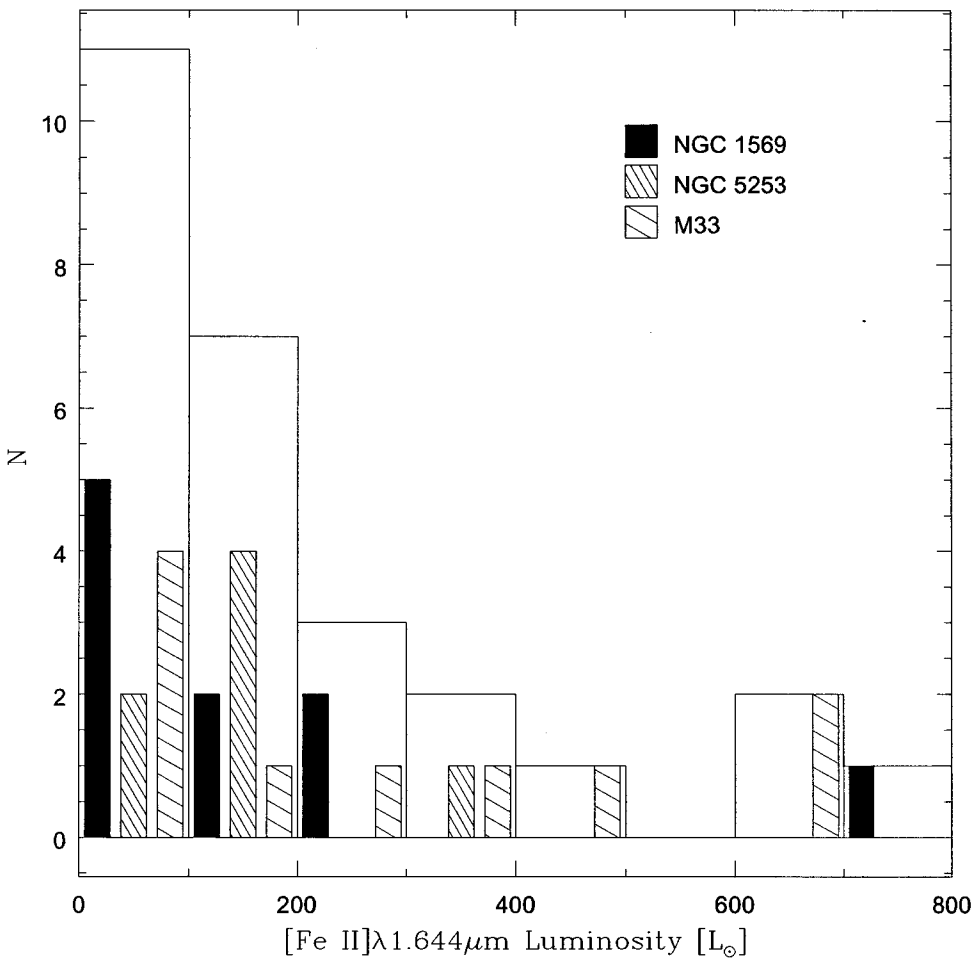

Figure 4.1: The comparative [Fe II] λ1.644 μm luminosity distribution of SNRs in M33 and of SNR candidates in NGC 1569 and NGC 5253. The large histogram represents the sum of all the remnants in each bin. (M33 data from Morel et al. (2002))

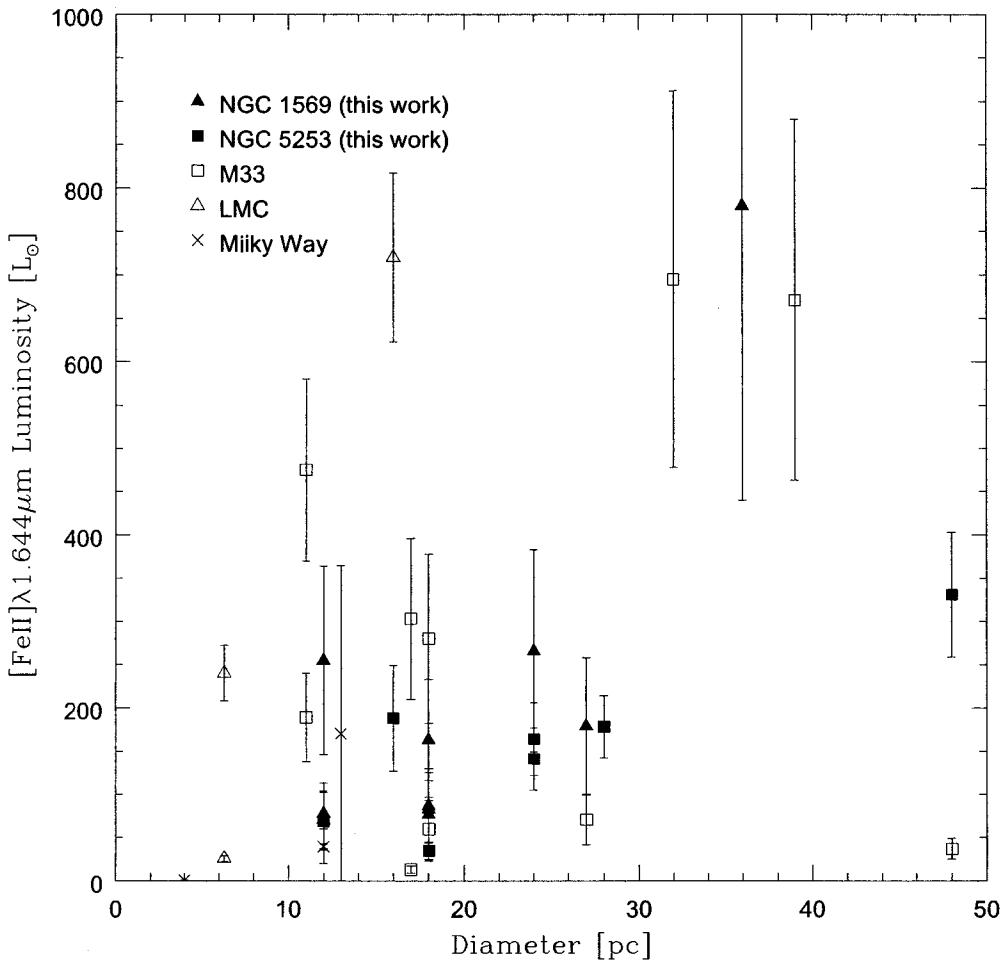

Figure 4.2: [Fe II] λ1.644 μm Luminosity-diameter relation for supernova remnants. All SNR candidates detected in NGC 1569 and NGC 5253, with the exception of N1569-S011, are included. Also shown are SNRs in M33, in the LMC and in the Milky Way (see Table 4.1 for complete references). Despite the different properties of the host galaxies, the luminosities are in a reasonable agreement.

tempted to see a rise in luminosity around 35 pc followed by a sharp decline at larger diameters. However, considering the large uncertainties and the small number of detections at large diameters this pattern is more likely coincidental and we argue that the variation in luminosity is more likely due to variation in local density. Indeed, the 48-pc wide M33 remnant in the lower-right corner of the plot displays a very low post-shock electron density (Gordon et al., 1998). Unfortunately, n_e measurements for our SNR candidates are not currently available, and obtaining such measurements would be a challenging task involving high-spatial resolution adaptive optics spectroscopy on a large telescope.

Although difficult to obtain, n_e measurements on [Fe II] emitters are probably the key to a better understanding of the [Fe II] emission in SNRs. For example, it would be interesting to see if, for a constant n_e, the diameter, which is linked to the age of the remnant, influences the [Fe II] luminosity. Also, the [Fe II]-emitting lifetime of a SNR is poorly constrained and the influence of the ambient density on that parameter, obviously an important factor, is simply not known. It is currently believed that the [Fe II]-emitting lifetime is of the order of 10^4 yrs (Condon and Yin, 1990; Lumsden and Puxley, 1995; Morel et al., 2002). Although a reasonable estimate, it should be remarked that this number is derived, in particular, from observations in M82, an extreme starburst galaxy, with high densities and an enormous amount dust. As a matter of fact, we have indications that the [Fe II]–emitting lifetime of a supernova remnant could be much longer. We must postpone this discussion for now but we will return to this issue once we have addressed the case of the SNRs in M82.

Impact of SNRs on the interstellar medium in NGC 1569 and NGC 5253

The luminosity of the SNRs candidates varies from 72 to 780 $L_\odot$ and 69 to 331 $L_\odot$ for NGC 1569 and NGC 5253, respectively. Following the $L_{[\mathrm{Fe\ II}]}$–n_e relation given above (Equation 4.1), to account for the [Fe II] luminosities observed, the *post-shock*

electron density at the remnants' location should be in the 60 to 700 cm^{-3} range. That range is conspicuously similar to the ISM electron density observed in the two galaxies: $n_e \sim 50-300\,\mathrm{cm}^{-3}$, peaking at the position of the SSCs for NGC 1569 (Kobulnicky and Skillman, 1997) and $n_e \sim 100-250\,\mathrm{cm}^{-3}$ for the general nuclear region of NGC 5253 (Kobulnicky et al., 1999; Martin, 1997; Walsh and Roy, 1989; Crowther et al., 1999). Higher electron densities are observed in NGC 5253 but are limited to the close vicinity of the young, ionizing SSC at the centre of the galaxy (N5253-C005) (Crowther et al., 1999; Mohan et al., 2001; Turner et al., 1998).

If we assume a compression ratio of 30, a typical average for SNRs, our [Fe II] luminosity measurements indicates that the expected *pre-shock* densities at the SNRs' position should be between 2 and 20 cm^{-3}. This is much smaller than the ISM electron density ranges actually observed in NGC 1569 and NGC 5253 ($n_e \sim 100\,\mathrm{cm}^{-3}$). It is very unlikely that the SNRs detected should be found only in low density pockets, which would have to be the case if the measured ISM electron density in the galaxies is taken to be the average pre-shock density. Rather, the opposite effect, that is, the SNRs being predominantly detected in high density pockets, should be expected as higher densities lead to higher luminosities. This argues that the average unshocked ISM density should be at most 2 cm^{-3}. Therefore, some mechanism must be brought forward to explain the observed high density of the ISM. Shock compression from supernova remnants is a viable mechanism. *The similarity between the SNRs luminosity and the ISM electron density suggests that a good fraction of the ISM is being compressed by shocks.* As we will see in Section 4.2, the analysis of the extended [Fe II] emission brings additional support for a predominantly shocked ISM in NGC 1569 and NGC 5253.

Larger starburst galaxies

Now let us turn our attention to the very bright [Fe II] sources observed in M82 and NGC 253. Part of the solution to reconcile the M82 measurements with what is observed in the galaxies discussed above was recently provided in a short paper by Alonso-Herrero et al. (2001). Before that work, only six powerful sources (the *"Fe"* sources in Table 4.1) had been measured in M82 and were associated with SNR activity (Greenhouse et al., 1997). These sources are three to four orders of magnitude more luminous that other SNRs in quiescent galaxies. Since the sources have small diameters, similar to single radiative SNRs, it seemed at the time reasonable to conclude that each [Fe II] source was an individual, very luminous, SNR, the unusual luminosity being somehow caused by the intense starburst activity observed to be in progress in M82. Further detections of [Fe II] sources in other starburst galaxies (e.g. NGC 253 and NGC 1808), also showing large luminosities, suggesting a dichotomy between SNRs in quiescent and starburst galaxies, but without a real understanding of how a SNR could reach such an enormous [Fe II] luminosity.

Our results contradict the quiescent – starburst dichotomy hypothesis. NGC 1569 and NGC 5253 are starburst galaxies. Yet we surely do not detect any super luminous [Fe II] sources in these galaxies. Even the brightest [Fe II] source, N5253-C005, associated with the very young super-star cluster at the centre of NGC 5253, reaches only $\approx 10^3\,L_\odot$.

As discussed above, the study by Morel et al. (2002) linked the [Fe II] luminosity of radiative SNRs to the post-shock electron density (recall Equation 4.1). Considering that the M82's ISM electron density is estimated to vary from 50 to 500 cm^{-3} (Förster Schreiber et al., 2001), Morel et al. tried to conceive a realistic scenario where density effects alone could account for the high luminosities observed in the Greenhouse et al. sources; they could not. Indeed, even using the highest density as pre-shock density, one can reach [Fe II] luminosities of only about $10^4\,L_\odot$, well below

the $10^5\,L_\odot$ observed. Without invoking very large, and not well understood, dust or metallicity effects, ultra-high densities or exceptionally large shock compression factors, it follows that the simplest explanation would be that each source is composed of several small SNRs clustered in a very small volume, a volume equivalent to the average volume of individual SNRs observed elsewhere.

In a high density environment, kinetic arguments restrain the expansion of a SNR. Also a remnant is predicted to evolve much faster and reach the radiative stage at a much earlier time; therefore the average diameter of radiative SNRs in dense environment can be well below 10 pc.

From HST NICMOS3 observations of the [Fe II] $\lambda 1.644\ \mu$m emission line in M82, this is exactly what Alonso-Herrero et al. (2001) found. The NICMOS3 observations offered a high spatial resolution of 0.35″, compared to the 1.3″ achieved by Greenhouse et al. (1997). They found as many as 123 compact [Fe II] emitters in the disc of the galaxy. The luminosity of the sources range roughly from $950\,L_\odot$ to $70\,000\,L_\odot$, assuming a distance to M82 of 3.9 Mpc (Table 4.1). It is unfortunate that the data regarding the diameter and luminosity of each source has not been published. This range of luminosity is more easily explained than the range observed in the Greenhouse et al. sources. Let us consider a few examples. With ambient densities in the range quoted above and a typical compression ratio of 30, we can easily reach luminosity of 1500 to $15\,000\,L_\odot$. For the most luminous events, a larger compression ratio can be invoked. Compression ratios as large as 100 can be achieved at the onset of the radiative phase (Blondin et al., 1998; McKee and Hollenbach, 1980; Thornton et al., 1998). Although short-lived, with a supernova rate as large as $0.11\,yr^{-1}$, it is almost guaranteed that, at any given time, a few SNRs will be in that high compression regime. This is especially true in the high density environment where the evolution of the SNRs is more rapid. Combining the high end of the density range ($\sim 500\,cm^{-3}$) with a compression ratio of 100, SNRs with [Fe II] luminosities around $50\,000\,L_\odot$ can readily be explained from density arguments alone.

Impact of SNRs on the interstellar medium in M82

While the luminosity of the SNRs in M82 can now be reasonably explained from density arguments, and no longer appears so fundamentally different from the luminosity of SNRs in other galaxies, a new problem surfaces. As mentioned above the ISM electron density of M82 ranges from 50 to 500 cm^{-3}. To explain the high luminosities of the remnants we had to assume that the ISM electron density corresponded to the *pre-shock* density. This contrasts with what we concluded above regarding the ISM in NGC 1569 and NGC 5253: to explain the luminosity of the remnants, the ISM had to be mostly shock-excited. Indeed, the range in n_e measured in M82 is practically the same as the range observed in NGC 1569 and NGC 5253, yet the average [Fe II] luminosities of the SNRs are dramatically different. This raises an interesting question: why is the impact of the SN activity on the ISM so different in NGC 1569 and NGC 5253 compared to M82? Given that the supernova rate in M82 is very high, is it so unreasonable to expect a large impact of the SNRs on the ISM?

In a nutshell, NGC 1569 and NGC 5253 are small, metal poor dwarf galaxies with a low dust content and, we argue, low pre-shock densities. M82 is a massive irregular galaxy, extremely dusty, that displays large density enhancements throughout the core region. Given that the galaxies are so different, a number of factors can potentially affect the level and the type of feedback from the SN activity. Nearly half the SNRs found in M82 have luminosities between 5 000 $\mathrm{L}_{\odot}$ and 20 000 $\mathrm{L}_{\odot}$. With a compression ratio of 30, this implies pre-shock densities, at the remnants' position, ranging approximately from 150 to 650 cm^{-3}, the high end of the galaxy's ISM electron density measurements. *This suggests that the SNRs in M82 are preferably found in density enhanced regions.*

The tendency of the SNRs in M82 to be found in densely packed groups, combined with the evidence suggesting that the ISM is mostly in pre-shock state, could be taken

as an indication that the high density regions hosting the SNe absorb most of the energy of the shock fronts, shielding the surrounding, less dense ISM from extensive impact from the SNR shocks. Effectively, the organized SNR shock fronts would have dissipated by the time they reached the lower density ISM.

With so few high spatial resolution studies of the [Fe II] line emission in nearby starburst galaxies it is impossible to tell whether we have evidence for two families of starburst galaxies, or if M82 is simply a rare and exceptional individual drawn from a single family. As suggested many times before by various authors, we also feel that a systematic [Fe II] line emission survey of nearby galaxies in various stages of starburst evolution is desirable at this point.

4.1.2 Discussion

Implications for the ν_{SN}–$L_{[Fe\ II]}$ relation

This whole issue has implications on the supernova rate, ν_{SN}, estimated from the global [Fe II] luminosity of a galaxy. Without the ability to spatially resolve the SNRs in a galaxy, it is not possible to know whether the n_e measured from [S II] line ratios corresponds to the density of the pre-shocked or post-shocked gas. It then becomes impossible to calculate the actual average SNR [Fe II] luminosity for that galaxy. Moreover, most if not all the ν_{SN}– $L_{[Fe\ II]}$ relations published in the scientific literature have been derived using, at some point or another, [Fe II] luminosities from SNRs in M82. In the light of the average luminosity of the SNRs observed in NGC 1569 and NGC 5253, we argue that the use of M82 to scale a ν_{SN}–$L_{[Fe\ II]}$ relation is ill-advised. *The average luminosity of the SNRs in M82 is high not because the supernova rate is high but because the pre-shock density is large.* These relations gravely underestimate the supernova rate in galaxies with fainter SNRs and lower pre-shock densities, like NGC 1569 and NGC 5253. Understanding the importance of the density on the [Fe II] luminosity of supernova remnants, Morel et al. (2002) derived a

relation for the supernova rate as a function of the global [Fe II] luminosity of a galaxy and the average post-shock electron density obtained from the [S II] line ratio. This expression is a much better representation of the physics involved; however, without the ability to know whether the electron density measured corresponds to the pre-shock density as in M82, or the post-shock density as in NGC 1569 and NGC 5253, it cannot be used with confidence.

One of the appeals of a $\nu_{\rm SN}$– $L_{\rm [Fe\,II]}$ relation is its use to quickly measure the current supernova rate in more distant galaxies. Clearly, following the discussion above, a simple [Fe II] luminosity measurement would not be sufficient. Even adding a [S II] line ratio n_e measurement would not suffice. But the situation is not hopeless. The solution lies in the ability to measure the electron density in the post-shock regions, and *only* the post-shock regions. This is possible if [Fe II] line ratios are used instead of the [S II] line ratio. The [Fe II] line-emission originates in those regions that have been swept up by a supernova remnant shock front. The [Fe II] line ratios would then ensure that the measured n_e indeed corresponds to the density of the shocked gas. This proposed technique also has the advantage of limiting the observations to the near-IR domain, rather than requiring additional optical spectroscopy to obtain the [S II] line ratio. However, a major difficulty arises from the faintness of the [Fe II] lines other than the ones at $1.257\,\mu$m and $1.644\,\mu$m. The two brightest lines cannot be used to measure the electron density, as they originate from the same upper level. Possible line ratios include [Fe II]$\lambda 1.5995\mu$m$/\lambda 1.644\mu$m (cf. Oliva et al., 1989) or [Fe II]$\lambda 1.533\mu$m$/\lambda 1.644\mu$m (cf. Pradhan.Zhang.1993). Both ratios are relatively temperature independent in the relevant density range. However, it should be noted that these diagnostics have limited use in the low electron density regime ($n_e < 100\,{\rm cm}^{-3}$).

Grain destruction

It has been suggested that the increase in [Fe II] line emission in supernova remnants is the result of an increase in gas phase iron abundance from grain sputtering caused by the shock front. In recent years, this theory has somewhat faded away in favour of a purely radiative process in a partially ionized shock-heated medium. Our observations also support the hypothesis that grain sputtering in not an important factor in the [Fe II] emission from supernova remnants. Two of the SNRs detected occurred in the East-West dust lane of NGC 5253 (N5253-S005 and N5253-S006). These two remnants do not show a particularly large [Fe II] luminosity, which would be expected if grain destruction had a significant effect on the luminosity. That being said, we should keep in mind that the metallicity of NGC 5253 is quite low. It could well be that even if grain sputtering occurs at a significant level, there is not enough iron to return to the gas phase to make an observable difference in the [Fe II] luminosity of the remnants.

[Fe II]–emitting lifetime

Before moving on to the analysis of the extended [Fe II] emission, one last issue we wish to address here concerns the duration of the [Fe II] emission phase. The [Fe II] emitting lifetime has been estimated as 10^4 yrs from [Fe II] and radio observations of M82 and NGC 253 (Lumsden and Puxley, 1995; Morel et al., 2002). In the light of our new observations and the above discussion, it seems advisable to revisit this estimate. In low density environments SNRs can remain in the radiative phase for as long as 10^5 yrs (e.g. Thornton et al., 1998). The duration of the radiative phase and the strength of the [Fe II] emission both depend on the ambient density. We can infer that the [Fe II] emitting lifetime would also depend on the ambient density.

The two largest SNRs detected in our observations, N1569-S001 and N5253-S001, are evidence that this is indeed the case. These two SNRs are definitely strong [Fe II]

emitters, yet their size suggests that they are old remnants. The time since the explosion, or the age of a radiative remnant, can be obtained from Equation 1.7 given the current diameter, and the age and diameter of the remnant at the adiabatic-radiative transition (D_{PDS}, Equation 1.5; t_{PDS}, Equation 1.4). Both D_{PDS} and t_{PDS} depend on the metallicity and the ambient density.

Using the [Fe II] luminosity – n_e relation (Equation 4.1) and a compression ratio of 30, we can estimate the ambient density at the remnant's position. For N1569-S001, we then obtain a t_{PDS} of 3550 yrs, and a D_{PDS} of 8.7 pc. With an estimated diameter of 36 pc for N1569-S001, one calculates an age of $t_{\text{N1569-S001}} \approx 3 \times 10^5$ yrs. A similar calculation for N5253-S001 leads to an age of $t_{\text{N5253-S001}} \approx 3.7 \times 10^5$ yrs.

Since the [Fe II] emission phase begins at the onset of the radiative stage, our 10^5yr-old emitters, which have entered the radiative phase when they were at most 10^4yr-old, have evidently been emitting [Fe II] photons for much longer than 10^4 yrs!

The new observations do not invalidate the [Fe II] emitting lifetime for the SNRs in M82. Indeed, we can use the same arguments we used for N1569-S001 and N5253-S001 to show[1] that the age of a typical SNR in M82 is of order 10^4 yrs, a fact that probably explains the short [Fe II] emitting lifetime measured in M82.

Again, based on our new observations, we must caution against the indiscriminate use of the average properties of the SNRs in M82 to generalize to other galaxies.

Finally, we conclude that the [Fe II] emitting lifetime is limited only by the duration of the radiative phase and is dependent on the ambient density at the supernova remnant's location.

[1]Let us take the average [Fe II] luminosity of the SNRs in M82 to be $10^4\,L_\odot$. This requires $n_0 = 300\,\text{cm}^{-3}$. We find t_{PDS} and D_{PDS} equal to 510 yr and 2.5 pc, respectively. Assuming $D = 10$ pc (Alonso-Herrero et al., 2001), this leads to an age $\approx 4 \times 10^4$ yr.

Metallicity

In the above, we have not considered metallicity effects, primarily because our data does not allow us to draw any conclusions regarding this parameter. The [Fe II] emission is expected to scale with metallicity (cf. Morel et al., 2002), as cooling is more efficient in high metallicity environments. As mentioned before, NGC 1569 and NGC 5253 have relatively low metallicities (0.25 and 0.2 $Z_{\odot}$, respectively). Metallicity effects could explain the scatter in the $L_{[\mathrm{Fe\ II}]}$– n_e relation but it has not yet been shown to be a dominant parameter, at least when compared to electron density.

4.1.3 Summary

To summarize, we refute the previously claimed dichotomy between quiescent and starburst galaxies regarding the [Fe II] luminosity of SNRs. Indeed, we have found that the SNRs in the starburst galaxies NGC 1569 and NGC 5253 have properties similar to supernova remnants in quiescent spiral galaxies and in Magellanic irregulars.

When the high density environment of M82 is taken into account, the [Fe II] properties of the SNRs are in agreement with what is observed in lower density galaxies. There seems to be no need for grain destruction enhanced [Fe II] abundances, or other special conditions, to explain the high luminosity of the M82 SNRs.

Instead of a dichotomy in SNR properties, we raise a possible dichotomy regarding the *impact* of the SNRs on the ISM. For NGC 1569 and NGC 5253, we suggest that a significant fraction of the ISM is under the influence of SNRs. This does not seem to be the case in M82, where the impact of the SNRs is limited to the high density knots.

Finally, we caution against the blind usage of SN rate–$L_{[\mathrm{Fe\ II}]}$ relations derived from average properties of SNRs in extreme starburst galaxies like M82. This is due to the fact that in M82 the average [Fe II] luminosity of the SNRs is exceptionally large, and the [Fe II]–emitting lifetime is also not representative of SNRs in all starburst

galaxies.

4.2 The Extended [Fe II] Emission

The compact [Fe II] sources detected in NGC 1569 and NGC 5253 account for only 14% and 7%[2], respectively, of the total [Fe II] line emission observed. In this section we will examine the possibility that the extended [Fe II] line emission results from unresolved SNRs. We will also place limits on the pre-shock density, supernova rate and current number of [Fe II]–emitting SNRs in NGC 1569 and NGC 5253.

4.2.1 Modeling

To investigate the origin of the [Fe II] line emission we will attempt to reproduce our [Fe II] observations under the assumption that the [Fe II] line emission is produced in radiative supernova remnants. Populations of [Fe II]-emitting SNRs will be generated and added to artificial images with noise characteristics similar to the real images.

The essential astrophysical ingredients for the simulation of [Fe II] emission from a SNR population are models for the spatial distribution of the SNRs, for their distribution in diameter, and for the SNR [Fe II] surface brightness distribution. There are also instrumental issues — for example pixel scale, absolute flux calibration, noise level — all details that are necessary for the creation of artificial images which have similar characteristics to the real images.

Below we discuss the physics, and the assumptions, on which the model is built. The input parameters and the algorithms for the SNR population and the artificial image creation are outlined in Appendix D for reference.

[2]Including the flux from the star clusters.

Spatial distribution

The positions of the SNRs relative to the centre of the galaxy were defined from random deviates drawn from a 2-dimensional Gaussian distribution. The ellipticity, the position angle and the scale radius (effectively the standard deviation along the major axis of the Gaussian distribution) of the distribution were set to best represent the shape and the extent of the [Fe II] emission in the real galaxies. The ellipticity and position angle of the distribution were evaluated from isophotal fitting to the [Fe II] emission in both galaxies. The approximate centre of the SNR distribution was also obtained from the isophotes. For each galaxy, the scale radius was set, by hand, to a value that reproduced the extent of the [Fe II] emission.

Although the spatial distribution of the SNRs is probably not Gaussian and most likely depends on distribution of the stars and gas across the galaxy, the resulting images show that it is a reasonable compromise. It will not significantly affect the final results, since it is the same for all the points in the $[N_{SNR}$–ν_{SN}–$n_0]$ parameter grid we will later explore. The effect of this distribution of sources is mostly to increase the minimum achievable goodness-of-fit statistic.

Diameter distribution

The physical conditions particular to each evolutionary phase of a SNR dictate its expansion into the ISM. The number of SNRs at a given diameter will depend on the average evolutionary phase of the population, the time at which each phase is entered being governed mostly by the ambient ISM density.

In the simple four-stage evolutionary model, the transition from the first stage, the free expansion phase, and the second, the Sedov-Taylor expansion phase, is expected to occur when the mass of swept-up ISM is equal to the ejected mass (Equation 1.1). For a range of interstellar densities typical of starburst galaxies, $n_0 \approx 1 - 100\,\mathrm{cm}^{-3}$, and for typical ejecta masses, $M_E \approx 1 - 10\,M_\odot$, the transition

radius ranges from 0.5 to 5 pc. This small transition radius, combined with the very high expansion velocity characteristic of the free expansion phase, means that the Sedov-Taylor (adiabatic) expansion phase will be reached very early ($\sim 10^2$ yrs). It is therefore very unlikely that a SNR population in a starburst core could be caught in its short first stage of evolution.

The next transition occurs when the shock front becomes radiative. The diameter of the remnant at the transition depends on the ambient density, the initial SNR energy and the metallicity of the environment (Equation 1.5). Using the same range in density as above, an initial SNR mechanical energy of 10^{51} ergs, and a metallicity 1/4 solar, typical of the metallicity of the galaxies studied in this work, one finds an adiabatic to radiative transition radius ranging from $\sim$2.5 to 17 parsecs.

Because of the rapid evolution caused by the high densities found in starburst core, the diameter distribution of the radiative SNR population model is expected to better reproduce the observations.

Our observations seem to support this assumption as the SNRs observed have radii of the order of 10 parsecs. Based on the above calculations, the SNRs observed should have recently entered the radiative phase of their evolution. We will therefore concentrate our efforts on modeling a population of radiative SNRs.

A useful way to express the distribution in diameter of the SNRs is the cumulative number-diameter relation, $N(< D)$. It is defined as the number of SNRs smaller than a given diameter, and is equal to the ratio of the age of the remnant, $t(D)$, to the average time, τ, between the creation of SNRs, i.e. the inverse of the supernova rate, ν_{SN}:

$$N(< D) = \frac{t(D)}{\tau} \tag{4.2}$$

We have seen in the introduction that during the pressure-snowplow radiative phase the diameter of a remnant evolves as $t^{3/10}$ (Equation 1.6). The cumulative

number-diameter relation then becomes

$$N(< D) = \frac{3}{4}\left[\left(\frac{D}{D_{PDS}}\right)^{10/3} + \frac{1}{3}\right] \frac{t_{PDS}}{\tau} \tag{4.3}$$

where t_{PDS} and D_{PDS} are, respectively, the age and the diameter of a remnant when it enters the radiative phase (Equations 1.4 and 1.5). The generation of random distributions respecting the above number-diameter relation is based on the *rejection method* (Press et al., 1992, and references therein).

The diameter assigned to a SNR is completely independent of its position relative to the centre of the galaxy, which is equivalent to saying that we assume a uniform ambient density across the galaxy. (This is discussed below.)

Surface Brightness Distribution

The next ingredient in our model is the supernova remnant [Fe II] λ1.644 μm surface brightness distribution. As explained at the beginning of Section 4.1, relatively few confirmed supernova remnants have been surveyed for near-infrared [Fe II] emission. In such conditions a solid comparison between intrinsic [Fe II] properties of the remnants becomes rather difficult, as has been demonstrated in Section 4.1.

We can improve this situation by using line-imaging observations of SNRs in nearby galaxies; the ability to observe whole SNRs, at about the same distance, suffering more or less the same amount of extinction, would lead to a more homogeneous sample. The nearby spiral galaxy M33 has the best studied extragalactic SNR population. The latest catalogue of optically-selected SNR candidates comprises 98 objects (Gordon et al., 1998). As mentioned before, a sample of 42 SNRs drawn from the Gordon et al. catalogue was systematically surveyed for near-infrared [Fe II] λ1.644 μm emission (Morel et al., 2002). This line-imaging program led to the firm detection of 7 SNRs and set 3σ upper limits on the [Fe II] luminosity for the remaining remnants. Combined with observations by Lumsden and Puxley (1995), a total of 10 SNRs, out of the 42 in the Morel et al. sample, have a measured [Fe II] luminosity.

If the [Fe II] emission arises from *radiative* SNRs, the small number of detections is not that unexpected. Using the cumulative number-diameter relation, Gordon et al. (1998) showed that the SNR population in M33 is mostly adiabatic. Therefore, only the remnants evolved enough to have reached the radiative stage would be [Fe II] emitters. Those remnants are the radiative *tip* of the adiabatic population. The larger remnants are usually older and have had time to reach the radiative stage, while the remnants in a denser environment went through a faster than average evolution.

In Figure 4.3, we compare the diameter of the 42 remnants to the threshold diameter at which a SNR become radiative (Equation 1.5). The ambient number density was calculated from the electronic density of each remnant using a range of compression factor, 10 to 50, illustrated by the error bars. The data points correspond to a compression factor of 30, typical for supernova remnants. Although approximate, the plot does show the tendency of the detected SNRs to have a diameter larger than the adiabatic-to-radiative transition diameter.

From their sample of SNRs in M33, Morel et al. (2002) found a correlation between the [Fe II] $\lambda 1.644$ μm luminosity of the SNRs and the electron post-shock density, n_e, derived from the [S II] line emission (Equation 4.1). We have used this relation to model the luminosity of the remnants in our artificial population as it can be scaled to the physical conditions of the ISM, which, we established in Section 4.1, varies considerably from galaxy to galaxy. By varying the ambient density of the ISM in our models we will be able to estimate the ambient density required to reproduce the [Fe II] emission morphology and intensity observed in NGC 1569 and NGC 5253.

The distributions in luminosity of the SNRs are generated from random Gaussian deviates about the proportionality factor between n_e and $L_{[\mathrm{Fe\ II}]}$. The electron density is obtained from the input ambient density and a compression ratio taken to be 30. The diameter of each remnant is compared to the PDS transition diameter to see if it has reached the radiative phase. If it has not, it is assigned an [Fe II] surface brightness of zero. Otherwise a spatially uniform surface brightness is assigned across

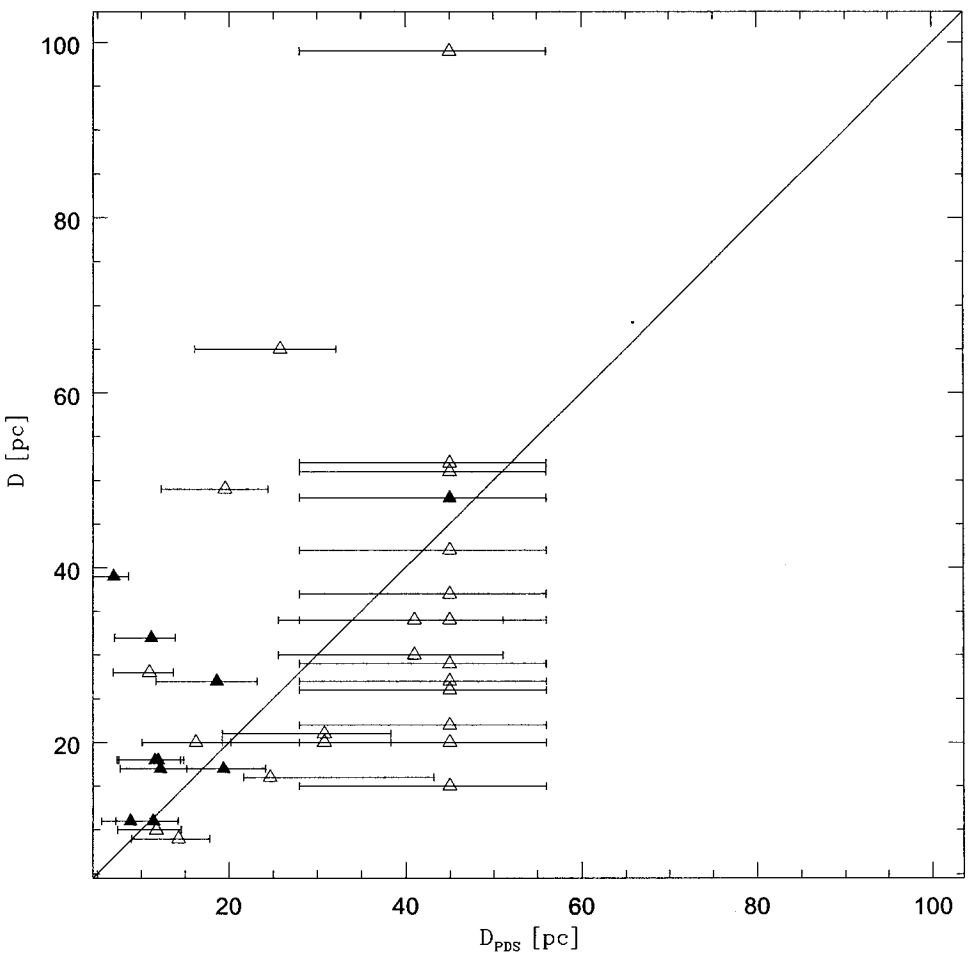

Figure 4.3: Diameter of the supernova remnants in M33 compared to the adiabatic-to-radiative transition diameter. *Solid triangles*: detected in [Fe II] . *Open triangles*: not detected. Data from Morel et al. (2002)

the remnant.

In our model, the luminosity distribution is completely independent of the SNR's location in the galaxy. This is equivalent to saying that there is a uniform ambient density across the galaxy, and there is no preference for bright SNRs to be found, for example, closer to the centre. It is likely that the density in the outskirt of the galaxy is significantly lower than in the starburst core. However, since our observations show that the SNR activity is limited to the small area around the core, we do not have to be overly concerned about a large scale density gradient, as long as the simulated spatial distribution is also limited to the nuclear region. Indeed, Kobulnicky and Skillman (1997) showed that the density in the starburst area of NGC 1569 is relatively constant with the exception of a few localized density enhancements. Fluctuations in the [Fe II] luminosity, caused by small scale variations in the ambient density, are introduced in a random fashion using a Gaussian distribution about the average luminosity for the given average ambient density.

The luminosity distribution is also independent of the SNR's diameter once it has reached the adiabatic-to-radiative transition diameter. We assume that the [Fe II] luminosity is constant throughout the radiative phase of the evolution. Although likely not to be the case, the dependence of the [Fe II] emission on the age of the remnant is still unknown. The presence of radiative SNRs among the predominantly adiabatic population of M33, and the small radii of the remnants we have detected, suggests, at the very least, that the [Fe II] emission is strong in the early times of the radiative phase. But how long it lasts is still of a matter for debate, as discussed in Section 4.1. Indeed, we have observed that some large and old remnants can still be strong [Fe II] sources.

Artificial Image Creation

Here we present a summary of the procedure followed to generate the artificial images. (Details can be found in Appendix D.) Given a SNR population, an artificial image is created that will mimic the characteristics of the real image. The real image was obtained from the combination of a number of short exposure images. To ensure that the noise properties of the final artificial image are similar to what is observed in the real image, we generate a series of short exposure intermediate images that are later combined the same way that the real short exposure images were combined.

Each intermediate image is created as follows: First, the input properties of the SNRs are scaled to the distance of the galaxy being modeled. The pixel scale and the absolute-to-instrumental flux calibration found in Chapter 2 are used to convert the physical properties of the SNRs to instrumental properties. The sky background is included as a constant value added to each pixel. The background and SNR flux are scaled to the exposure time. The image is then convolved with a Moffat profile of width similar to the seeing observed in the real images. Finally, read noise and Poisson noise are applied to each pixel. Since the line emission is obtained from narrow-band images containing continuum emission, the Poisson noise applied to a pixel is actually calculated from the flux of a real narrow-band image. Ignoring the continuum flux as a source of noise would gravely underestimate the Poisson noise.

Additional Gaussian noise can be added to represent noise generated in the various data reduction steps (dark frames, flats, etc.).

Limitations of the model

The most important limitation of the model is regarding the late evolution of the supernova remnants. The moment at which a remnant enters the radiative phase and commences [Fe II] emission is relatively easy to identify; the moment at which it stops emitting is much harder to define. Also, the late time morphology of the [Fe II]

line emission is likely not to be uniform across the remnant, but instead will be more shell-like. And, there is the issue of the supernova-driven galactic winds often seen in starburst galaxies (e.g. Heckman et al., 1990; Taniguchi et al., 1988): when and how the supernova remnant bubbles merge and join the galactic wind is not well defined.

Our model allows us to arbitrarily set the maximum age of an [Fe II] emitting supernova remnant. However, the late time evolution issues should be kept in mind in the following analysis, since old SNR populations possess a significant fraction of remnants older than 10^5 yrs.

4.2.2 Density and Supernova Activity

We will now use our computer model to simulate a number of SNR populations in different ambient densities. This will allow us to determine the physical conditions required to reproduce the extended [Fe II] line emission observed in our galaxies.

In the following, we consider two scenarios. In the first scenario, once a SNR is turned on, it simply fades away as the constant luminosity is spread across an ever larger area. This model mimics — although not rigorously — a scenario in which the large and old SNRs join to generate shocks on a galactic scale. In the second scenario, the SNRs are given a limited [Fe II] emitting lifetime. As we have discussed before, the [Fe II] emitting lifetime of a SNR is uncertain. While many authors claim a lifetime of order 10^4 yrs, we have detected [Fe II] emitting SNRs much older than that (Section 4.1.2). Therefore, in this second scenario, the maximum age of a [Fe II] emitting SNR is set to 10^5 yrs based on our observation of $\sim 10^5$ yr-old SNRs in NGC 1569 and NGC 5253.

The parameter space explored is defined by a $5 \times 10 \times 10$ grid of ambient density, n_0, number of supernova remnants, N_{SNR}, and supernova rate, ν_{SN}. The grid covers densities from 0.5 to 10 cm^{-3}, numbers of SNRs from 50 to 2500, and SN rates from 0.0005 to 0.1 yr^{-1}.

Goodness-of-fit statistics

For each point in the parameter grid, a SNR population is created and an artificial image of that population is generated. Then the simulated image is compared to the real image of the galaxy. A goodness-of-fit statistic is defined from two measured properties of the [Fe II] line emission. The first observable is the total flux, f, within an elliptical aperture encompassing the [Fe II]-emitting region of the galaxy. The second property is the standard deviation in the values of the pixels inside the aperture, s. This property is taken as a measure of the spatial smoothness of the [Fe II] line emission produced by the SNR population. This indicator is sensitive to the ratio of compact sources versus unresolved [Fe II] sources. For example, an image containing mostly unresolved remnants will have a very smooth appearance, and therefore, the standard deviation within the aperture will be small.

The goodness-of-fit statistic is calculated at each point along the grid:

$$\Gamma = \frac{(f_{model} - f_{real})^2}{w_f^2} + \frac{(s_{model} - s_{real})^2}{w_s^2} \tag{4.4}$$

where w_f^2 and w_s^2 are effectively weighting factors balancing the relative importance of the smoothness indicator to the total flux indicator.

For the flux term, w_f^2 is defined as the quadratic sum of the uncertainties in the aperture flux measurement, in the model and the real images: $w_f^2 = \Delta f_{model}^2 + \Delta f_{real}^2$. Since the smoothness indicator is the standard deviation within the aperture, the uncertainty in this value cannot rigorously be calculated. For the smoothness term of the goodness-of-fit statistic, we defined the weighting factor as $w_s^2 = \Delta s_{model}^2 + \Delta s_{real}^2$, where Δs is some conceptual uncertainty for the smoothness indicator. We set Δs to 5% of the standard deviation measured within the aperture. We settled on 5% after some experimentation aiming at balancing the relative importance of the smoothness term to the flux term in the goodness-of-fit statistic.

In this way, a 3-D map of the goodness-of-fit statistic of the [n_0–N_{SNR}–ν_{SN}] parameter space is created. For a given galaxy, this process was repeated a 100 times. The

goodness-of-fit maps generated were then averaged to create the final goodness-of-fit map used in the analysis.

It should be noted that the goodness-of-fit statistic becomes insensitive to the total number of supernova remnants when the SNR population becomes older than any restriction on the emitting lifetime. For a given SN rate, and a fixed emitting lifetime, there is a limit to the maximum number of [Fe II]-emitting SNRs at any given time. In other words, when the age of a population reaches the maximum allowed age for [Fe II] emission, for each SNR that is turned off, statistically, a new one is turned on.

A brief outline of the algorithm for the goodness-of-fit routine is presented in Appendix D. Below, the results for NGC 1569 and NGC 5253 are presented (Sections 4.2.3 and 4.2.4, respectively). A summary can be found in Table 4.2.

4.2.3 NGC 1569

The overexposed regions around the SSCs have been masked out, both in the real and the synthetic images. These pixels are not used in the flux and standard deviation measurements. AOBIR[3] observations near the SSCs obtained as part of a different project show little or no [Fe II] emission. It is well known that a bubble has created a Hα void around SSC A (e.g. Devost et al., 1997). Since the strength of the [Fe II] emission depends on the ambient density, we should expect any SNRs in that area to be weak [Fe II] emitters. But it could well be that no SNRs are present in the area, an hypothesis supported by the absence of radio SNRs around the NGC 1569 SSC A and B (Greve et al., 2002). Ignoring these regions probably does not have a serious impact on the best-fit parameters.

To help in the accuracy of the fit, the 11 compact sources we detected were reproduced from their observed properties and added to the artificial SNR populations.

[3]CFHT's Adaptive Optic Bonnette near-IR Imager

In this way the goodness-of-fit statistic is more sensitive to the unresolved emission, which is after all the main interest of the present analysis.

The results of the fit for NGC 1569 are illustrated in Figures 4.4 and 4.10, for the unlimited lifetime and the 10^5 yrs lifetime scenarios, respectively. For each of the 5 ambient densities tested, a ν_{SN}–N_{SNR} goodness-of-fit map is presented. The dashed lines indicate the age of the SNR populations. The older a model is, the more potentially unrealistic it becomes due the limitations of the model regarding the [Fe II]-emitting lifetime and the morphology of the remnants at late times, especially beyond 10^5 yrs (see Section 4.2.1).

The most striking result is how strongly the high density models are rejected. For a pre-shock density of $10\,cm^{-3}$ most of the models are rejected, in both scenarios, at a very high level from the goodness-of-fit test (Figure 4.4 (e) and 4.10 (e)). Typical synthetic images corresponding to goodness-of-fit test minima are presented in Figure 4.9. Under high densities, the remnants are considerably more luminous than the average luminosity actually observed for the SNRs we detected. Also, the high density keeps the diameter of the remnants quite small. No extended [Fe II] line emission is produced unless the number of SNRs is increased beyond what is allowed from the total [Fe II] flux.

Here it should be noted that the analysis of the goodness-of-fit test maps must be complemented by the examination of the synthetic images. The goodness-of-fit test we designed does not count the number of resolved SNRs, and it is not directly sensitive to their average luminosity. While the standard deviation, within the aperture, does give an idea of the smoothness of the [Fe II] emission, it can cause an isolated low in the goodness-of-fit map when the supernova remnants are few and small, which is more likely to happen in high density models.

The extended [Fe II] emission is more easily reproduced when the density is kept low. But too low a density fails to produce bright [Fe II] sources like the ones we detected. Also, to accumulate enough flux to match the total flux of the real image,

Table 4.2: Best-fit ranges for the pre-shock density, the supernova rate, and number of [Fe II]-emitting supernova remnants, as derived from the modeling of the [Fe II] emission.

Galaxy	[Fe II] Lifetime	n_0 (cm^{-3})	ν_{SN} (SN/yr)	$N_{emitter}$
(1)	(2)	(3)	(4)	(5)
NGC 1569	unlimited	1–2	0.004–0.01	250–500
	10^5 yrs	1–2	0.002–0.008	250–500
	$\Rightarrow$	**1–2**	**0.004–0.008**	**250–500**
NGC 5253	unlimited	1–2	0.001–0.008	500–1000
	10^5 yrs	1–2	0.003–0.01	300–1000
	$\Rightarrow$	**1–2**	**0.003–0.008**	**500–1000**

Col. (3). – Pre-shock densities.
Col. (4). – Supernova rates.
Col. (5). – Number of [Fe II]-emitting supernova remnants.

a very large number of SNRs, with unrealistically large sizes, are required. Note the $0.5\,cm^{-3}$ goodness-of-fit map (Figure 4.4 (a)): the local minimum occurs mostly for very old SNR populations. When the old SNRs are prevented from emitting [Fe II] after they have reached a certain age, it is not possible to reproduce the total flux observed (Figures 4.5 and 4.11).

Using, in concert, the contour plots and the synthetic images, for both the unlimited and the 10^5 yrs [Fe II]-emitting lifetime scenarios, we narrowed down the ranges of acceptable values for the three parameters, n_0, ν_{SN} and N_{SNR} (Table 4.2). Our analysis shows that a good agreement between the model and the observations is obtained when the average pre-shock density in NGC 1569 is $1–2\,cm^{-3}$, with 250 to 500 [Fe II]-emitting SNRs, and when the supernova rate is set to 0.004 to 0.008 SN/yr. We conclude that, for NGC 1569, in both lifetime scenarios, n_0=$1.5\,cm^{-3}$, ν_{SN}=0.006 SN/yr, and about 400 [Fe II]-emitting SNRs are present.

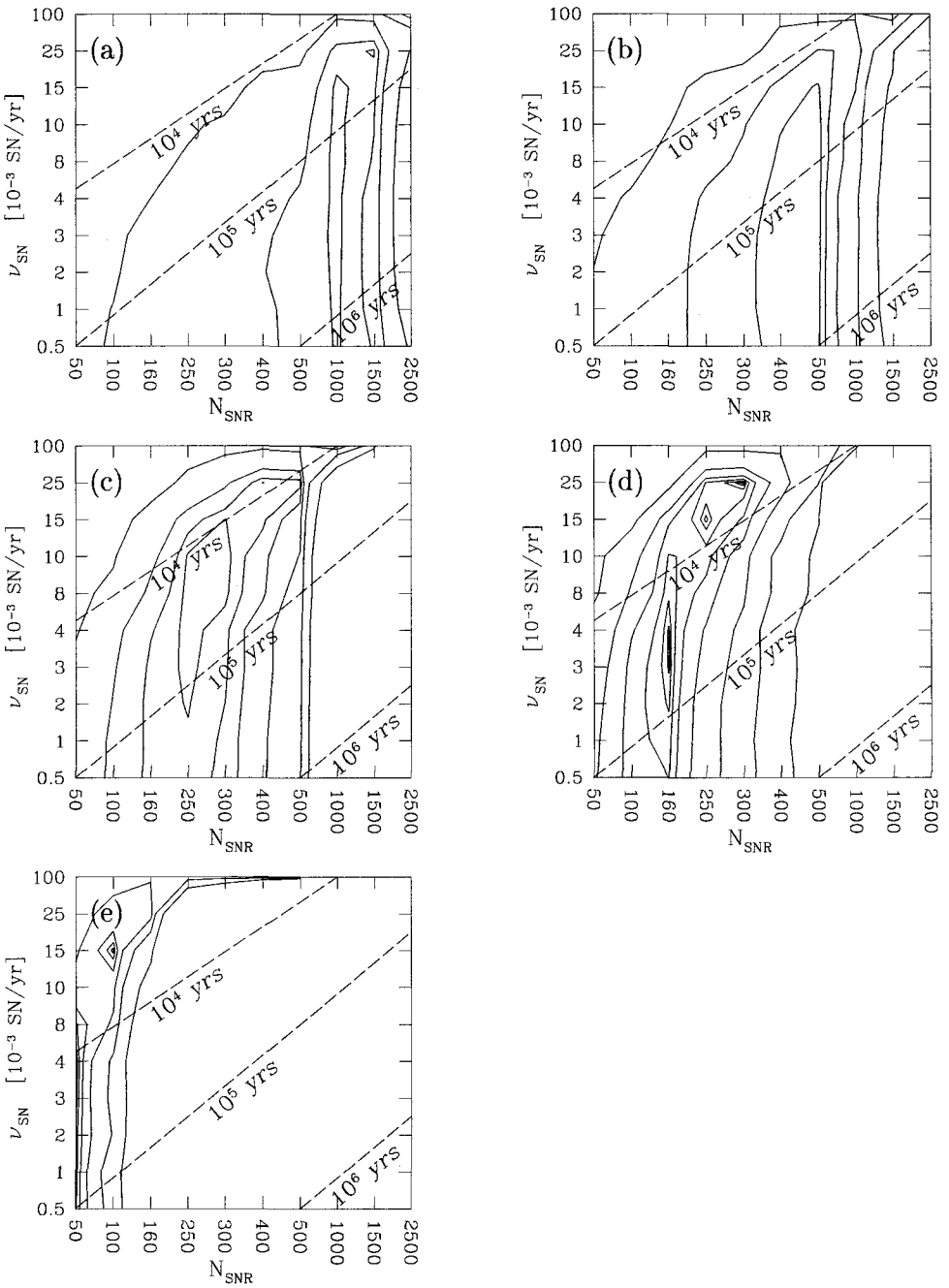

Figure 4.4: Results from the goodness-of-fit tests on the images of the simulated SNR populations of NGC 1569. No limits on the [Fe II]-emitting lifetime of the remnants were applied on these models. Shown are five ν_{SN}–N_{SNR} slices of the parameter space: **(a)** $n_0 = 0.5\,\mathrm{cm}^{-3}$, **(b)** $n_0 = 1\,\mathrm{cm}^{-3}$, **(c)** $n_0 = 2\,\mathrm{cm}^{-3}$, **(d)** $n_0 = 3\,\mathrm{cm}^{-3}$, **(e)** $n_0 = 10\,\mathrm{cm}^{-3}$. The dashed lines indicate the age of the SNR populations; populations older than 10^5 yrs are more affected by the limitations of the model (see Section 4.2.1).

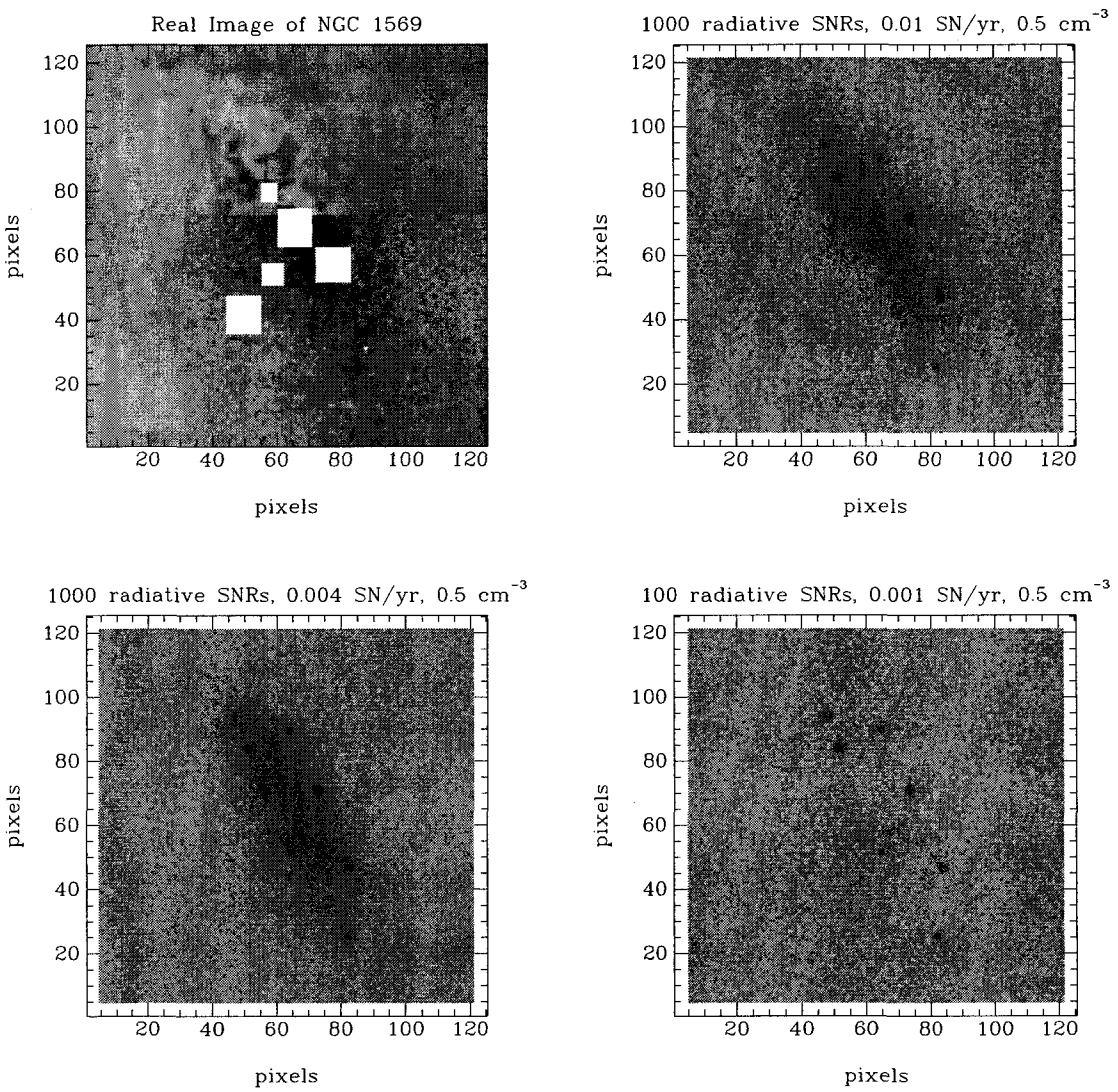

Figure 4.5: Examples of synthetic [Fe II] line emission images compared to the real image of NGC 1569, for a pre-shock density of 0.5 cm $^{-3}$ and no limits on the emission lifetime of the remnants. The real image is shown in the upper left corner.

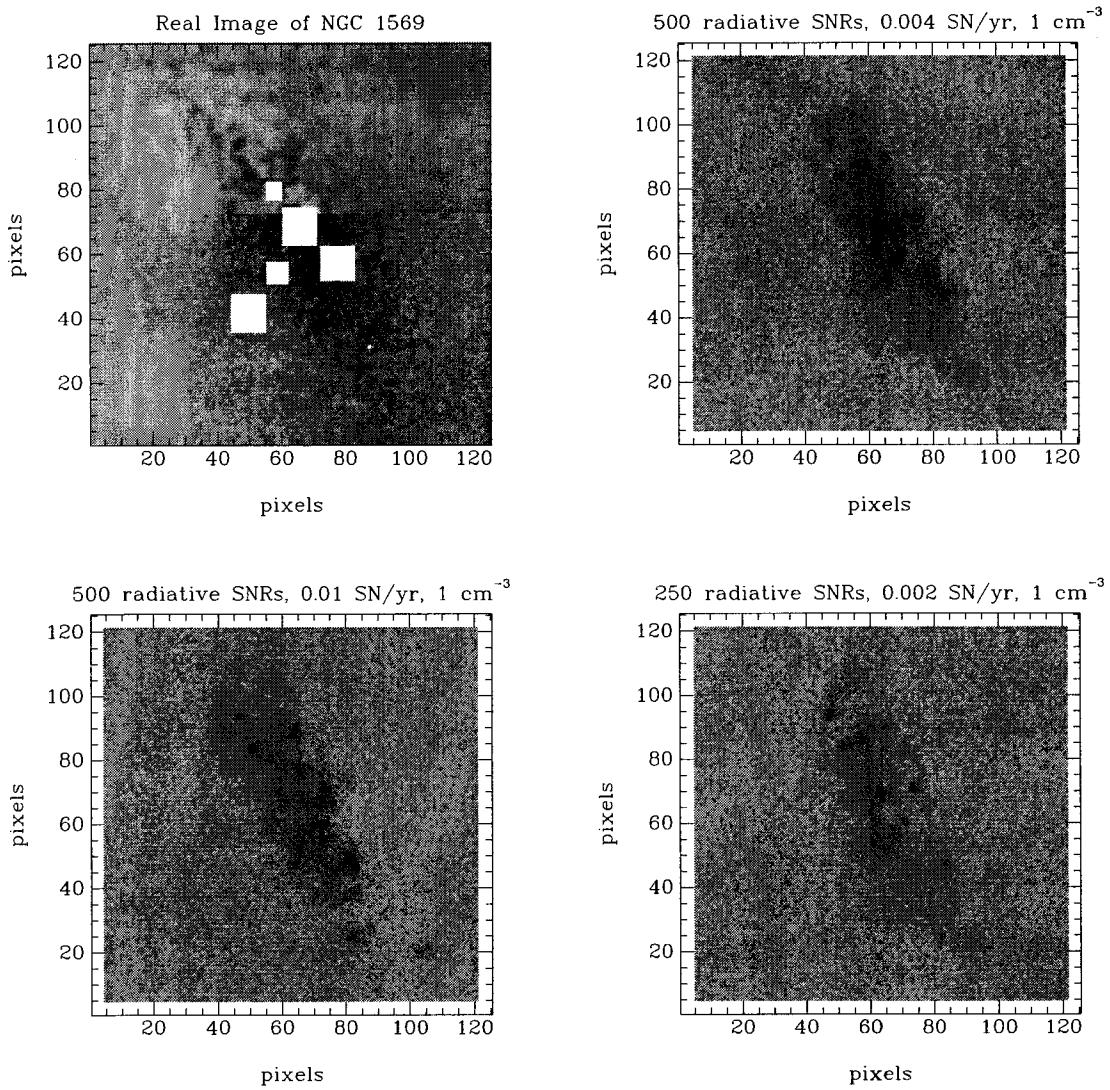

Figure 4.6: Examples of synthetic [Fe II] line emission images compared to the real image of NGC 1569, for a pre-shock density of $1\,\mathrm{cm}^{-3}$ and no limits on the emission lifetime of the remnants. The real image is shown in the upper left corner.

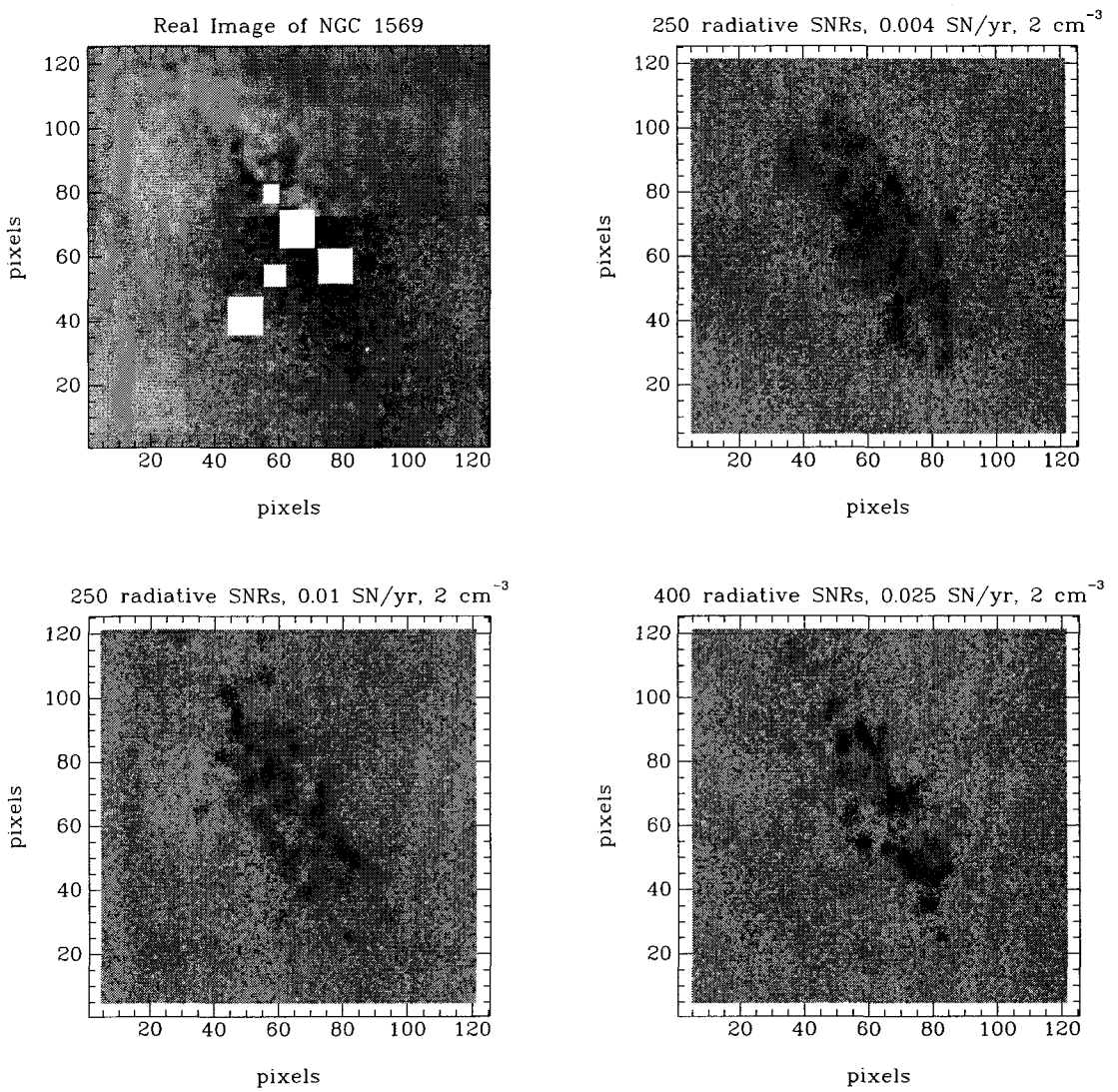

Figure 4.7: Examples of synthetic [Fe II] line emission images compared to the real image of NGC 1569, for a pre-shock density of $2\,\mathrm{cm}^{-3}$ and no limits on the emission lifetime of the remnants. The real image is shown in the upper left corner.

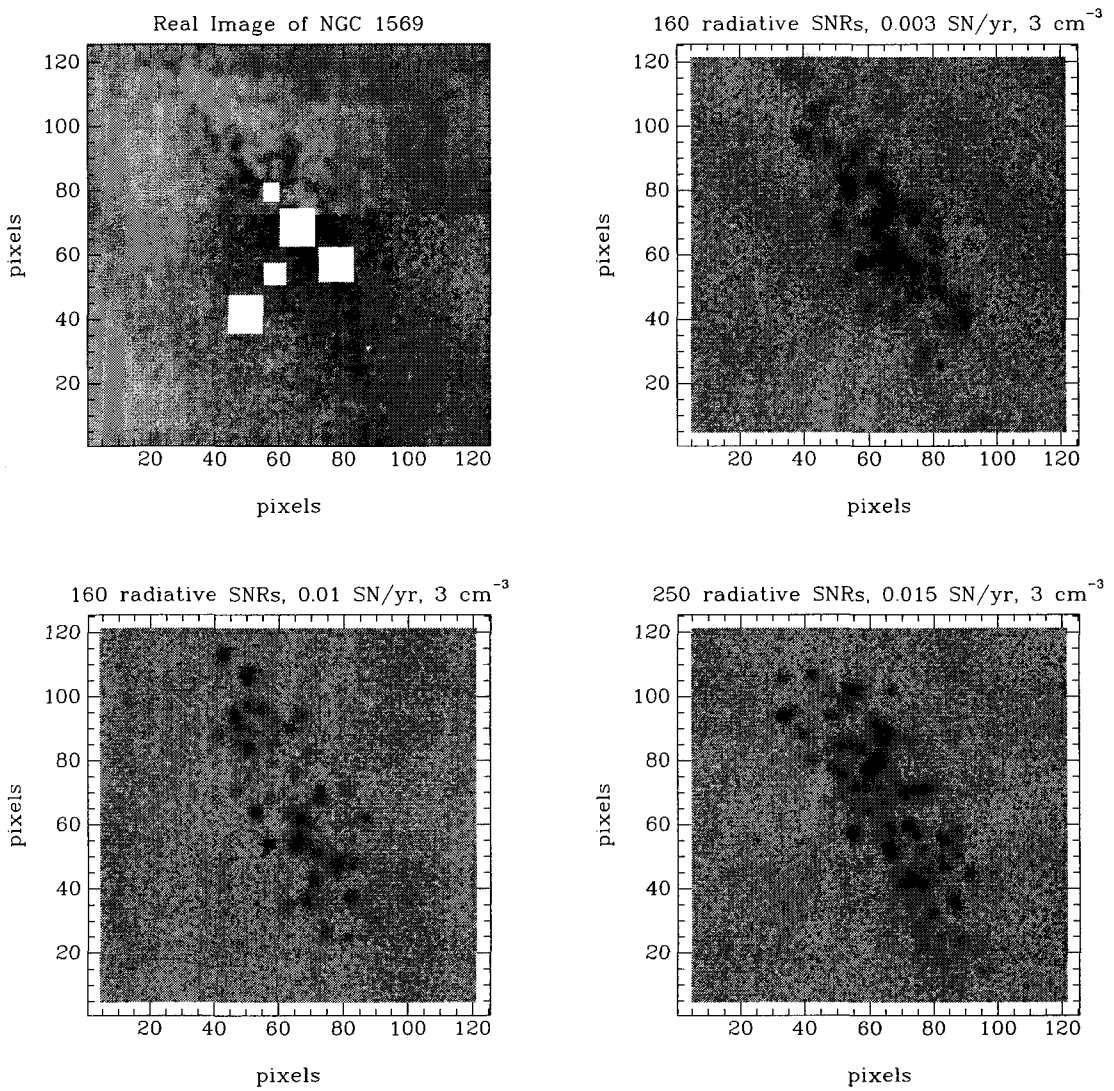

Figure 4.8: Examples of synthetic [Fe II] line emission images compared to the real image of NGC 1569, for a pre-shock density of $3\,\mathrm{cm}^{-3}$ and no limits on the emission lifetime of the remnants. The real image is shown in the upper left corner.

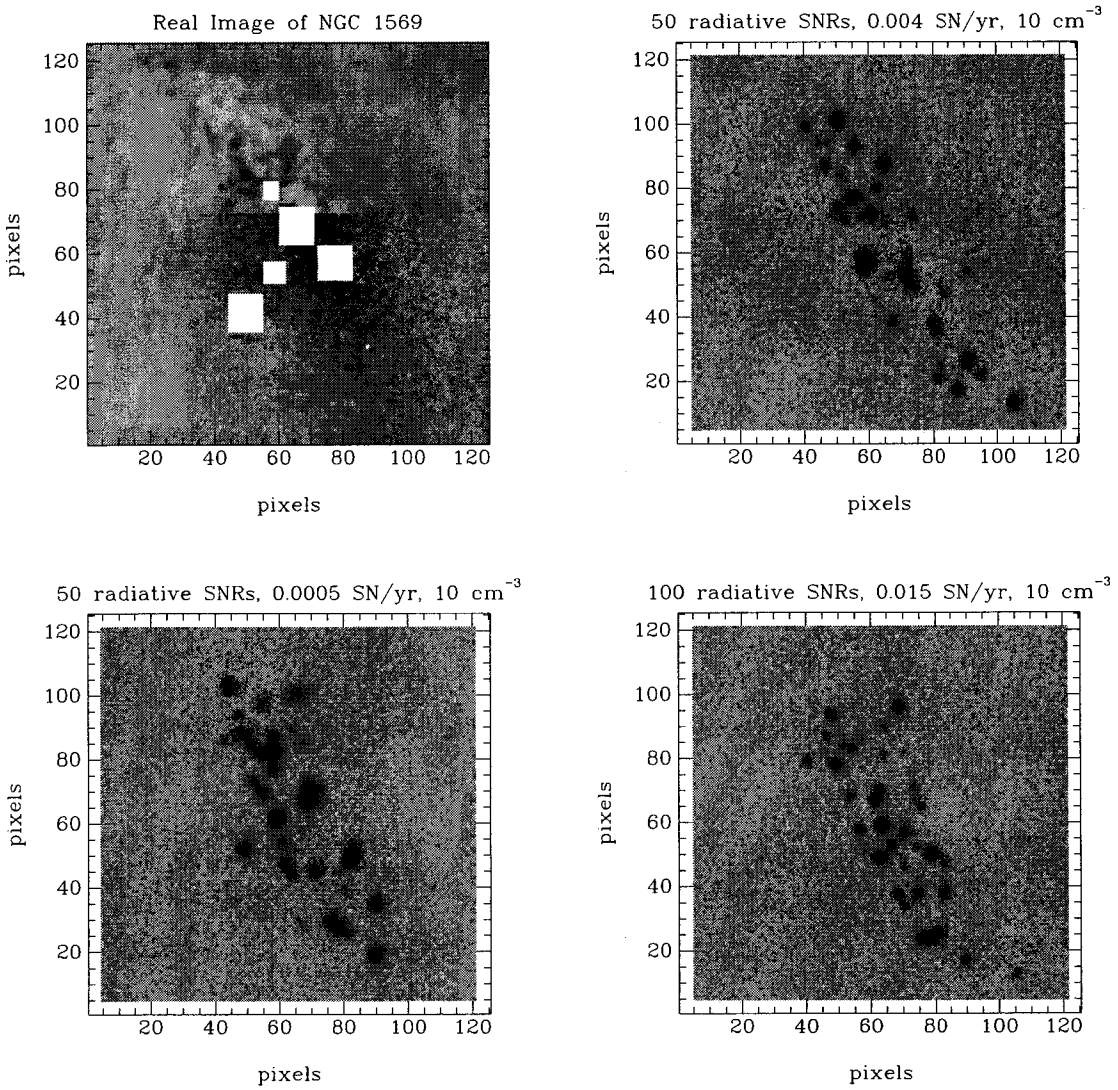

Figure 4.9: Examples of synthetic [Fe II] line emission images compared to the real image of NGC 1569, for a pre-shock density of 10 cm $^{-3}$ and no limits on the emission lifetime of the remnants. The real image is shown in the upper left corner.

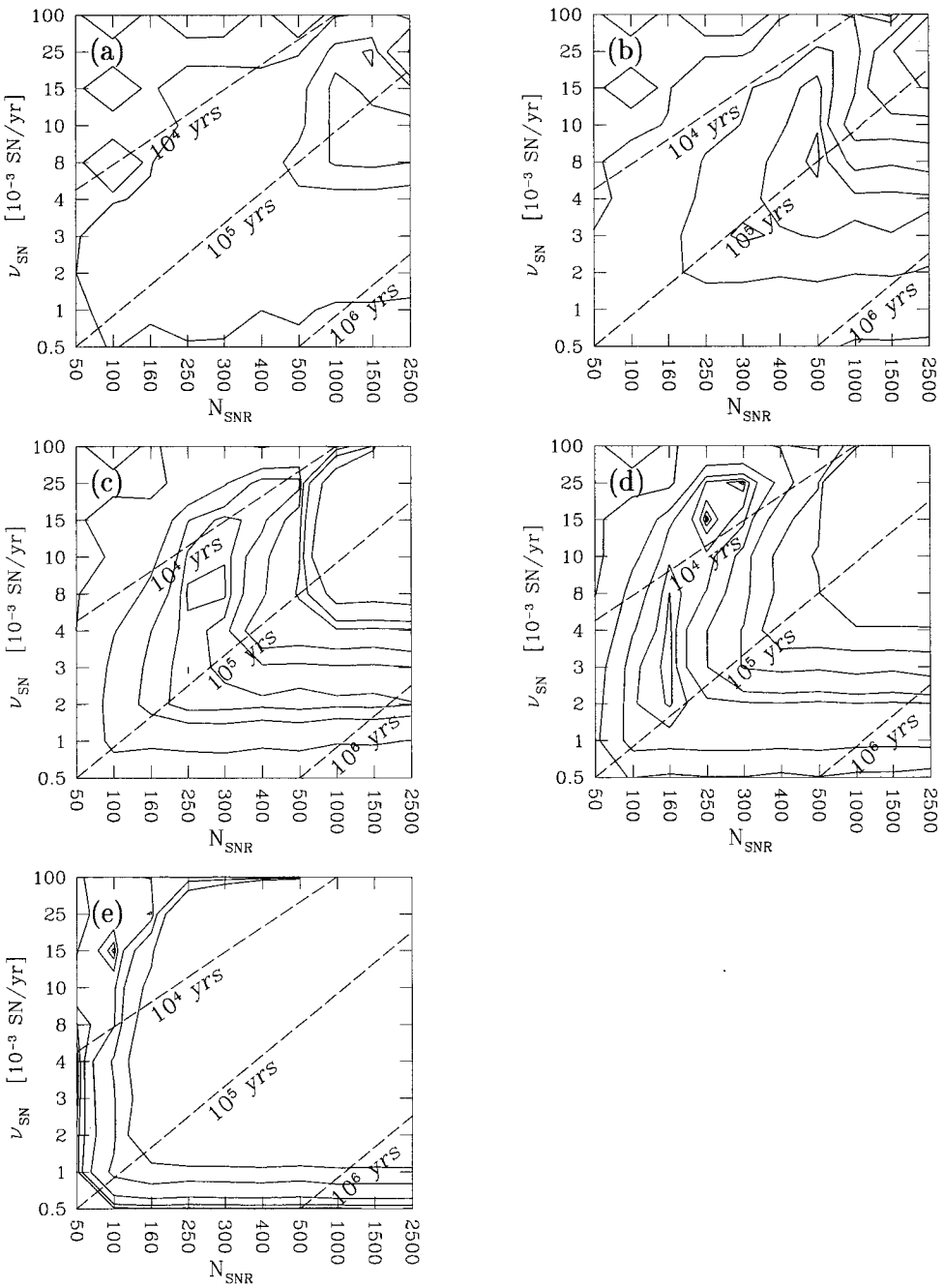

Figure 4.10: Results from the goodness-of-fit tests on the images of the simulated SNR populations of NGC 1569. Shown are five ν_{SN}–N_{SNR} slices of the parameter space: **(a)** $n_0 = 0.5\,\mathrm{cm}^{-3}$, **(b)** $n_0 = 1\,\mathrm{cm}^{-3}$, **(c)** $n_0 = 2\,\mathrm{cm}^{-3}$, **(d)** $n_0 = 3\,\mathrm{cm}^{-3}$, **(e)** $n_0 = 10\,\mathrm{cm}^{-3}$. The dashed lines indicate the age of the SNR populations. For models with a SNR population older than 10^5 yrs, the goodness-of-fit statistic is no longer sensitive to the total number of SNRs (see Section 4.2.2).

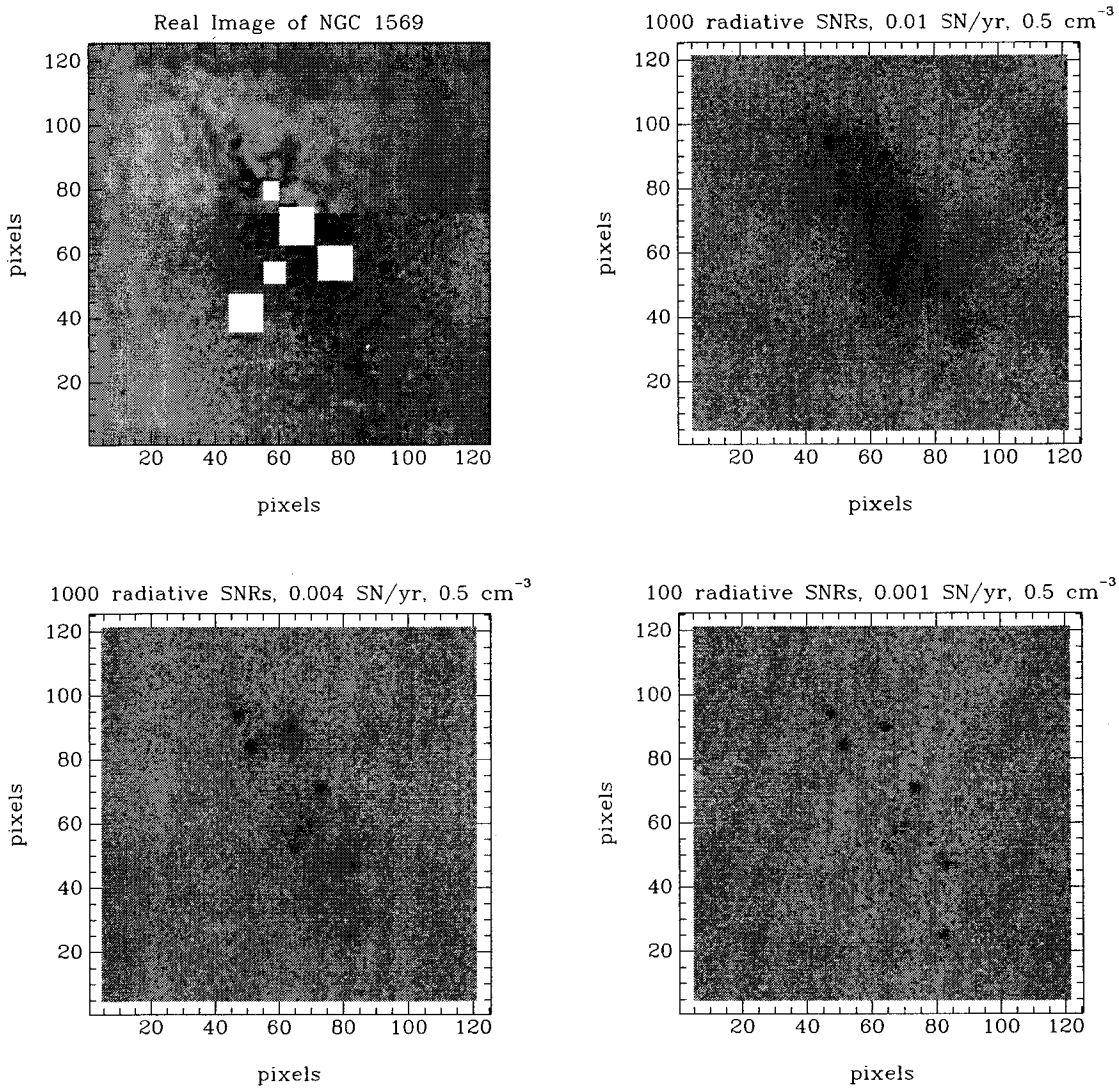

Figure 4.11: Examples of synthetic [Fe II] line emission images compared to the real image of NGC 1569, for a pre-shock density of $0.5\,\mathrm{cm}^{-3}$ and an emission lifetime of 10^5 yrs. The real image is shown in the upper left corner.

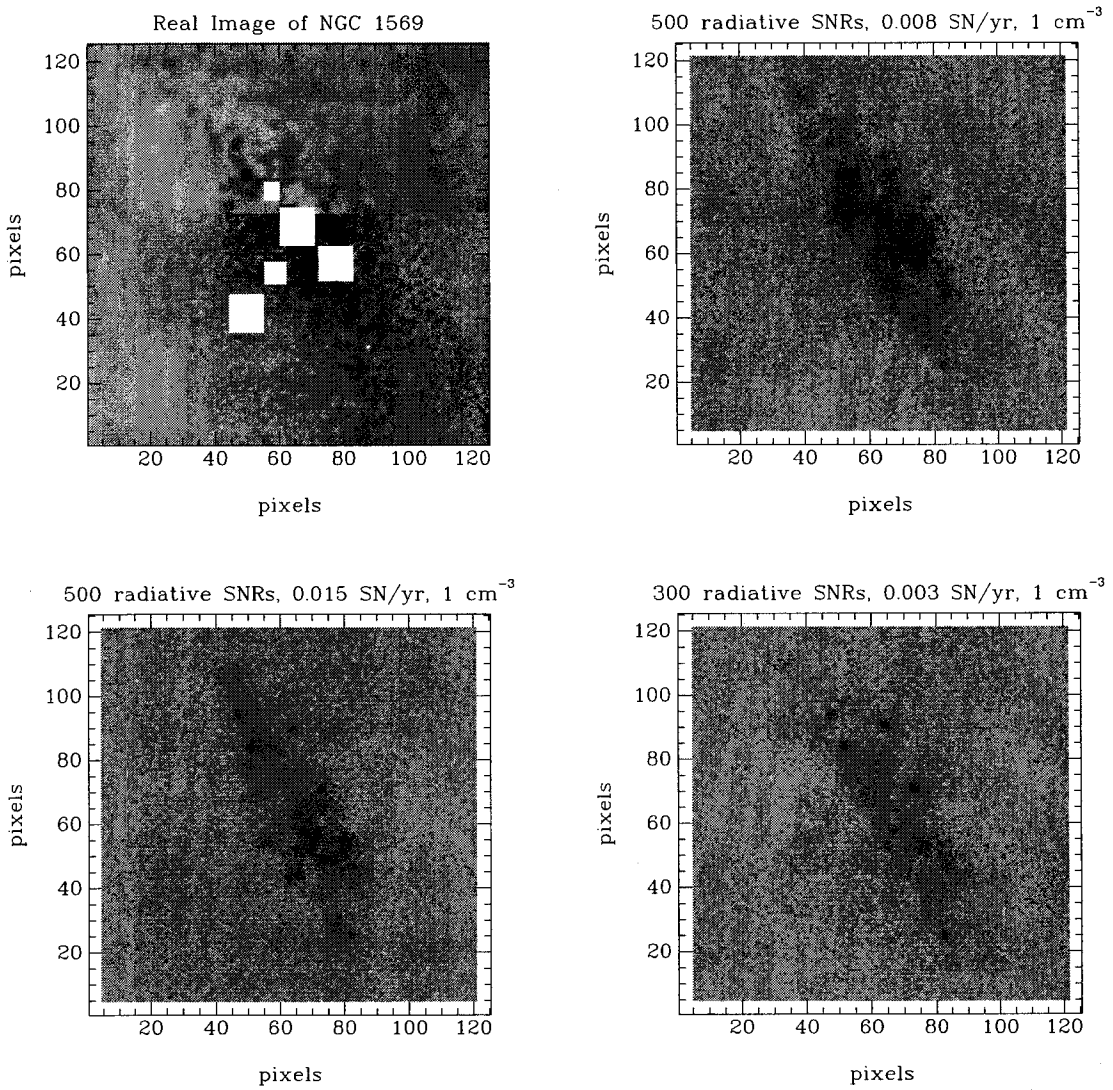

Figure 4.12: Examples of synthetic [Fe II] line emission images compared to the real image of NGC 1569, for a pre-shock density of $1\,\mathrm{cm}^{-3}$ and an emission lifetime of 10^5 yrs. The real image is shown in the upper left corner.

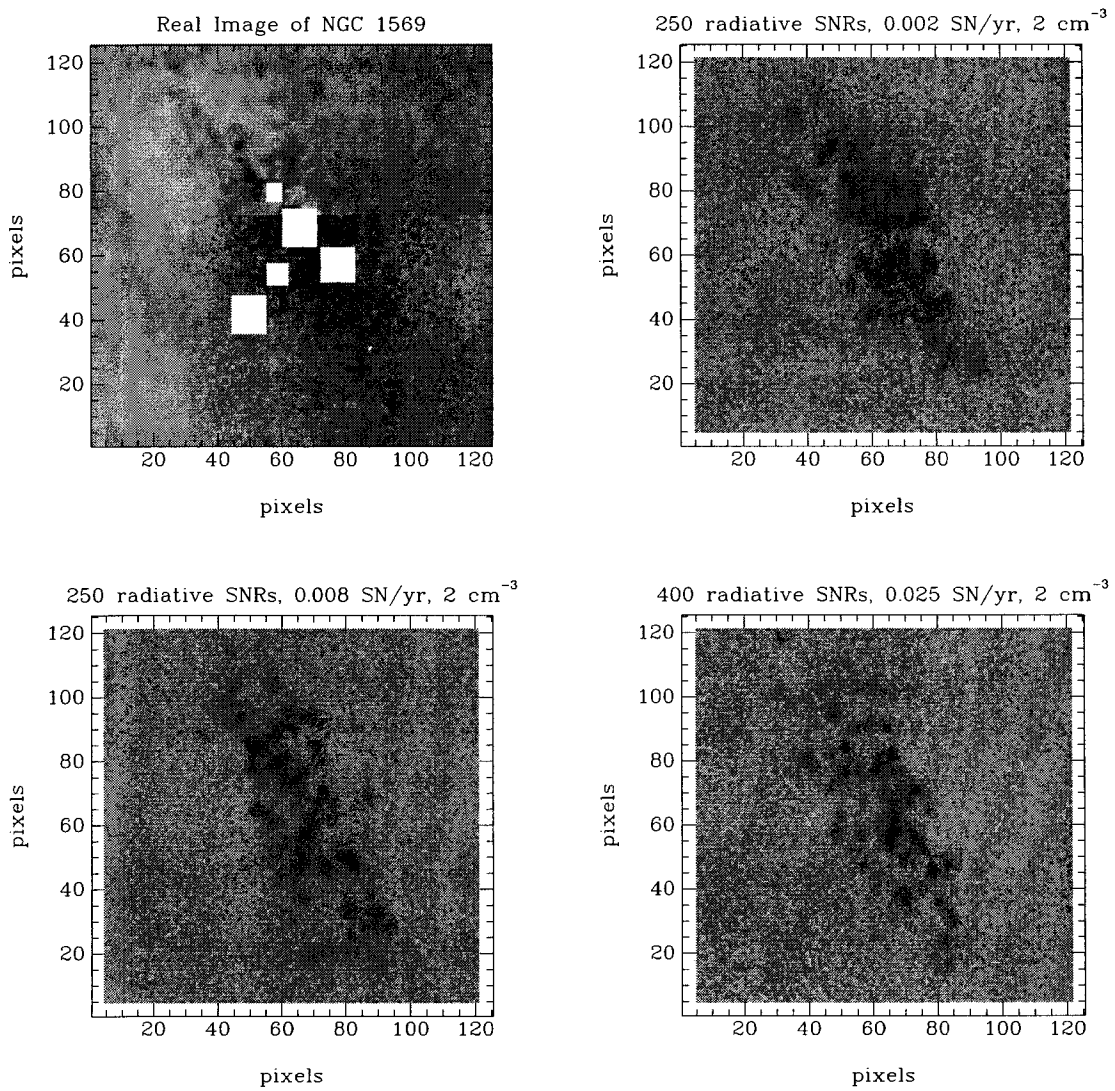

Figure 4.13: Examples of synthetic [Fe II] line emission images compared to the real image of NGC 1569, for a pre-shock density of $2\,\mathrm{cm}^{-3}$ and an emission lifetime of 10^5 yrs. The real image is shown in the upper left corner.

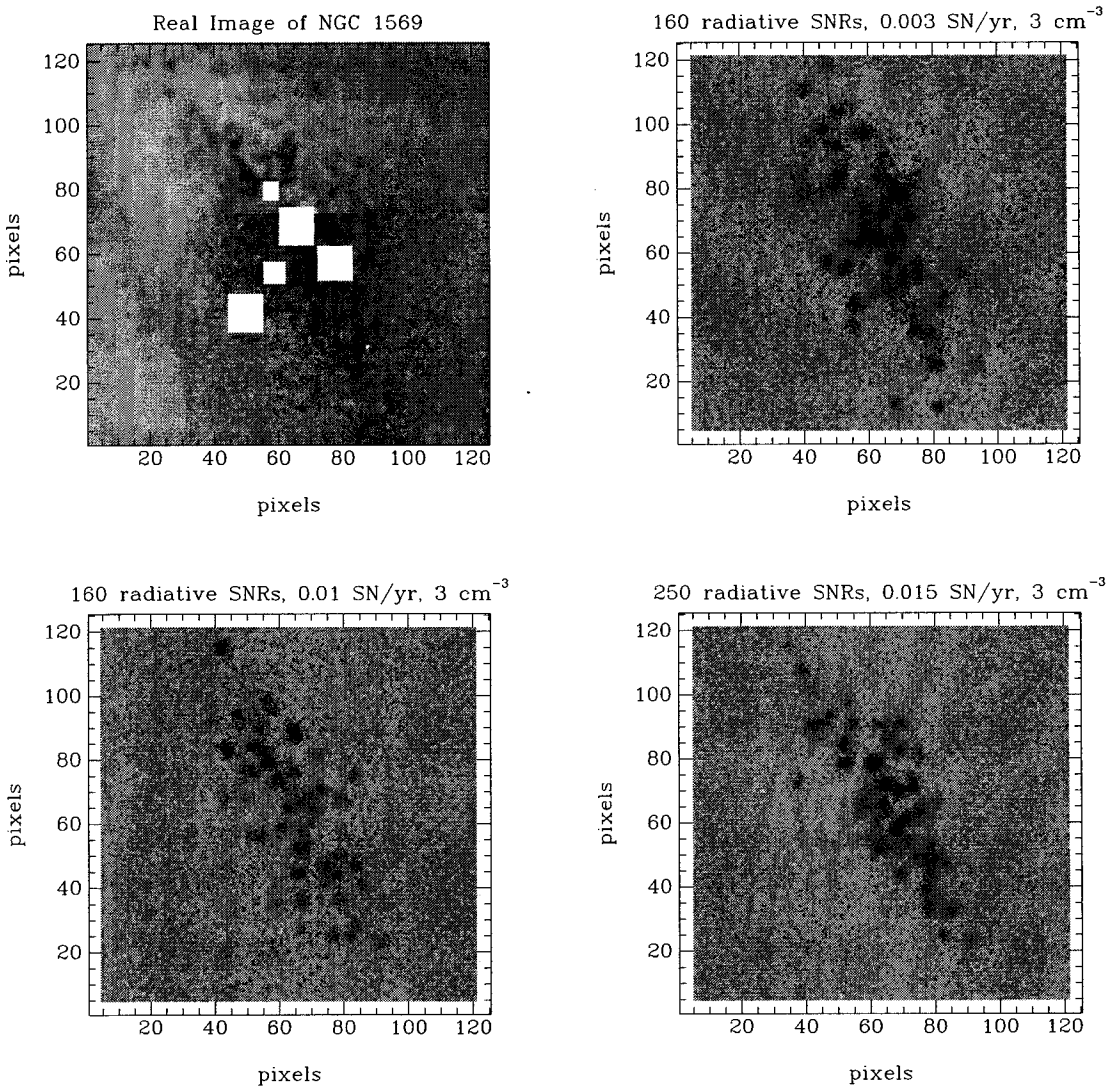

Figure 4.14: Examples of synthetic [Fe II] line emission images compared to the real image of NGC 1569, for a pre-shock density of $3\,\mathrm{cm}^{-3}$ and an emission lifetime of 10^5 yrs. The real image is shown in the upper left corner.

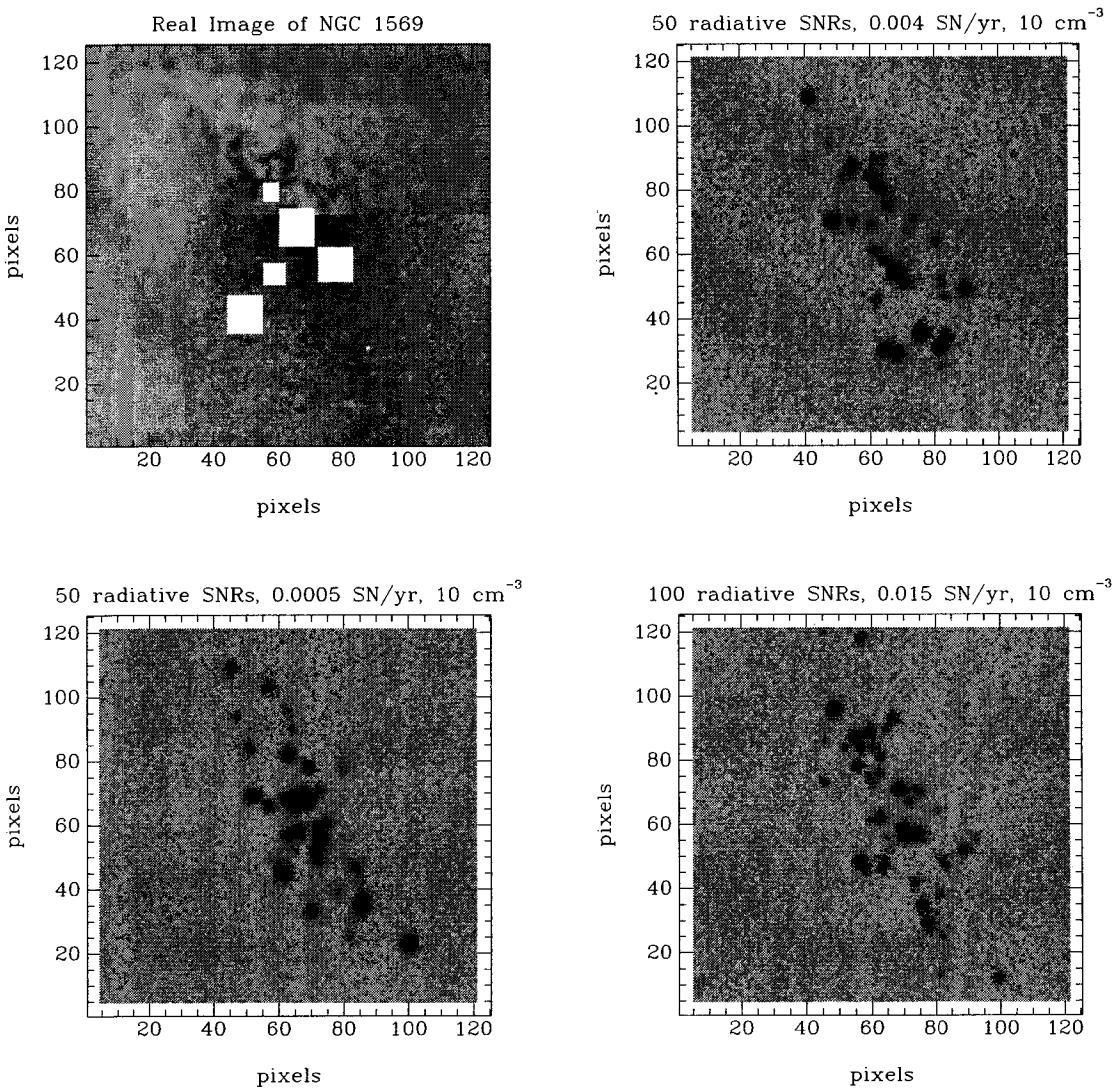

Figure 4.15: Examples of synthetic [Fe II] line emission images compared to the real image of NGC 1569, for a pre-shock density of $10\,\mathrm{cm}^{-3}$ and an emission lifetime of 10^5 yrs. The real image is shown in the upper left corner.

4.2.4 NGC 5253

The line images of NGC 5253 display an unusual feature in the SSC-5 area, characterized by very strong near-infrared [Fe II] line emission and a low [Fe II]/Paβ line ratio. The [Fe II]/Paβ ratio of that area suggests that the [Fe II] line emission does not originate from supernova remnant activity, but rather from photoionization caused by the very young and unusual star cluster nested in this large H II region. To avoid contamination from sources other than SNRs, the area around SSC-5 has been masked out and ignored in the goodness-of-fit tests.

Also, in contrast with NGC 1569, the SSCs in NGC 5253 were not overexposed. To allow the study of the extended [Fe II] line emission we judged that the flux emitted by the SSCs, possibly not caused by SNRs, had to be ignored. The clusters were masked out and were also ignored in the goodness-of-fit tests. It should be noted that the clusters, SSC-5 included, account for less than 5% of the total [Fe II] luminosity in NGC 5253.

As we did for NGC 1569, the compact [Fe II] sources detected in NGC 5253 (all seven of them) were reproduced from their observed properties and added to the artificial SNR populations to help in the accuracy of the fit, and increase the sensitivity of the fit to the unresolved emission.

The results from the goodness-of-fit tests are illustrated in Figure 4.16 for each of the 5 ambient densities considered. These are goodness-of-fit maps of the ν_{SN}–N_{SNR} parameter space. As before, the dashed lines indicate the age of the SNR populations. The older a SNR population model is, the more unrealistic it becomes due to the limitations of the model regarding the late-time evolution of the SNRs, especially beyond 10^5 yrs (see Section 4.2.1).

The examination of the goodness-of-fit maps reveals quite clearly that the lowest density models are strongly rejected ($0.5\,cm^{-3}$, Figures 4.16 (a) and 4.22 (a)). In the unlimited lifetime scenario, too many unrealistically old and large SNRs would

be required to add up to the total [Fe II] luminosity observed. When the emitting lifetime is restricted to 10^5 yrs, an extremely large number of emitting SNRs, and a very high supernova rate, are required, in contradiction with other observations (e.g. Beck et al., 1996; Martin and Kennicutt, 1995).

At the other end of the spectrum, the goodness-of-fit map of the highest density models ($10\,cm^{-3}$, Figures 4.16 (e) and) 4.22 (e) suggests reasonable agreement at some specific point in parameter space. However, a quick look at the corresponding synthetic images (Figures 4.21 and 4.27) suffices to reject the $10\,cm^{-3}$ scenario: the average luminosity and the number of resolved sources are much higher than what is observed.

As mentioned above, one particular feature of NGC 5253 is a dominant [Fe II] source that is in the area around SSC-5. Although we tried to minimize its effect by masking most of it out, we can still detect its influence on the goodness-of-fit tests: the large [Fe II] luminosity models are favoured. In other words, the goodness-of-fit minima will tend to occur at larger N_{SNR} than what should be the case if the emission associated to SSC-5 had been completely eliminated.

This effect really complicates the analysis. Indeed, the goodness-of-fit test results do not seem to agree well with what the synthetic images show us, and when they do, they do so for very old SNR populations that our model does not treat rigorously.

The goodness-of-fit tests for a pre-shock density of $3\,cm^{-3}$ identify a strong, well defined minimum at N_{SNR}=400 and ν_{SN}=0.008 SN/yr (Figures 4.16 (d) and 4.22 (d)). The agreement between the synthetic and the real images, however, is not very convincing (Figures 4.20 and 4.26). Already at a modest density of $3\,cm^{-3}$ the SNRs are, on average, too luminous and too small. We conclude that the extended [Fe II] emission cannot be reproduced with such an average density.

Lowering the ambient density does help in the creation of an extended component as the SNRs can grow larger; but then a large increase in the number of [Fe II]-emitting SNRs, and in the age of the SNR population, is required to account for the

total [Fe II] flux and the number of resolved sources. The synthetic images in the unlimited lifetime scenario appear to be in better agreement with the observations. This may be an indication that the diffuse [Fe II] emission originates in supernova-driven galactic winds rather than in large individual SNRs.

Despite the various contradictions, all evidence seems to argue against a high supernova rate. Supernova rates between 0.003 and 0.008 SN/yr are favoured on the grounds of both the goodness-of-fit tests and synthetic images. Indeed, large supernova rates imply the presence of a larger number of bright compact SNRs than what is allowed by the observations.

Scrutinizing the parameter space at n_0 of $1\,\mathrm{cm}^{-3}$ and $2\,\mathrm{cm}^{-3}$, it is found that a reasonable agreement between the real image and the synthetic one is achieved for $n_0 = 1.5\,\mathrm{cm}^{-3}$, $\nu_{\mathrm{SN}} = 0.005\,\mathrm{SN/yr}$ and the combined flux of ~ 750 [Fe II]-emitting SNRs. The supernova rate we find for NGC 5253 is almost equal to the rate found for NGC 1569; similar supernova rates are expected since the star formation rates in both galaxies are very similar (Martin, 1997). The range of acceptable values for the parameters is summarized in Table 4.2.

4.2.5 Discussion

The pre-shock densities

The average pre-shock densities required to reproduce the morphology of the [Fe II] line emission in both galaxies are much lower than what is observed in the large starburst galaxies like M82 and NGC 253 ($\sim 100\,\mathrm{cm}^{-3}$). In both NGC 1569 and NGC 5253, we find pre-shock densities of $\sim 1\,\mathrm{cm}^{-3}$. Since the ISM electron density observed in both galaxies is $\sim 100\,\mathrm{cm}^{-3}$, similar to the electron density required to explain the [Fe II] line emission as SNR induced, it appears likely that a significant fraction of the ISM is under the influence of SNRs, or in other words, in a post-shock state rather than a pre-shock state. Already for a $10\,\mathrm{cm}^{-3}$ pre-shock density scenario,

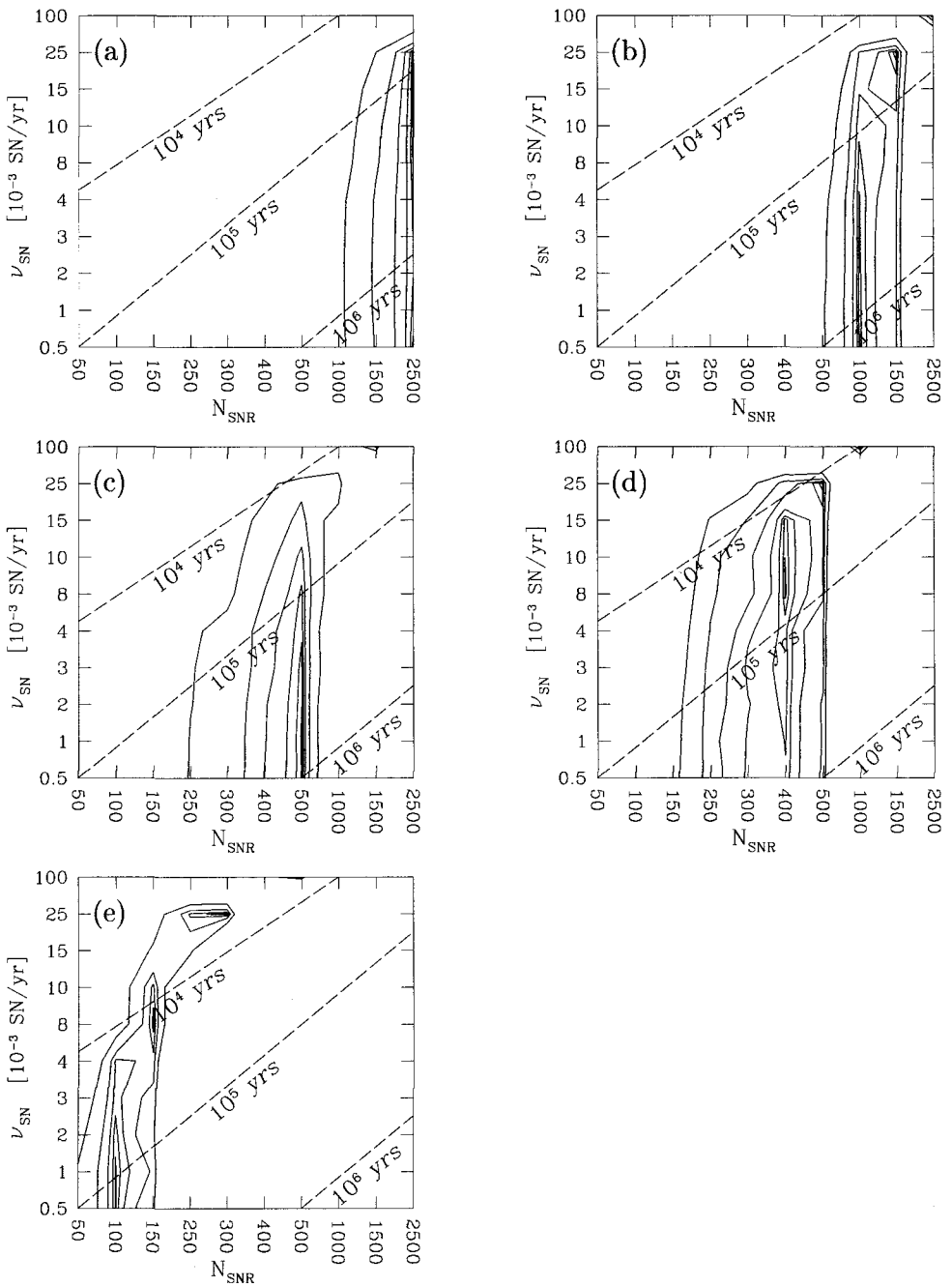

Figure 4.16: Results from the goodness-of-fit tests on the images of the simulated SNR populations of NGC 5253. No limits on the [Fe II]-emitting lifetime of the remnants were applied on these models. Shown are five ν_{SN}–N_{SNR} slices of the parameter space: **(a)** $n_0 = 0.5\,\mathrm{cm}^{-3}$, **(b)** $n_0 = 1\,\mathrm{cm}^{-3}$, **(c)** $n_0 = 2\,\mathrm{cm}^{-3}$, **(d)** $n_0 = 3\,\mathrm{cm}^{-3}$, **(e)** $n_0 = 10\,\mathrm{cm}^{-3}$. The dashed lines indicate the age of the SNR populations; populations older than 10^5 yrs are more affected by the limitations of the model (see Section 4.2.1).

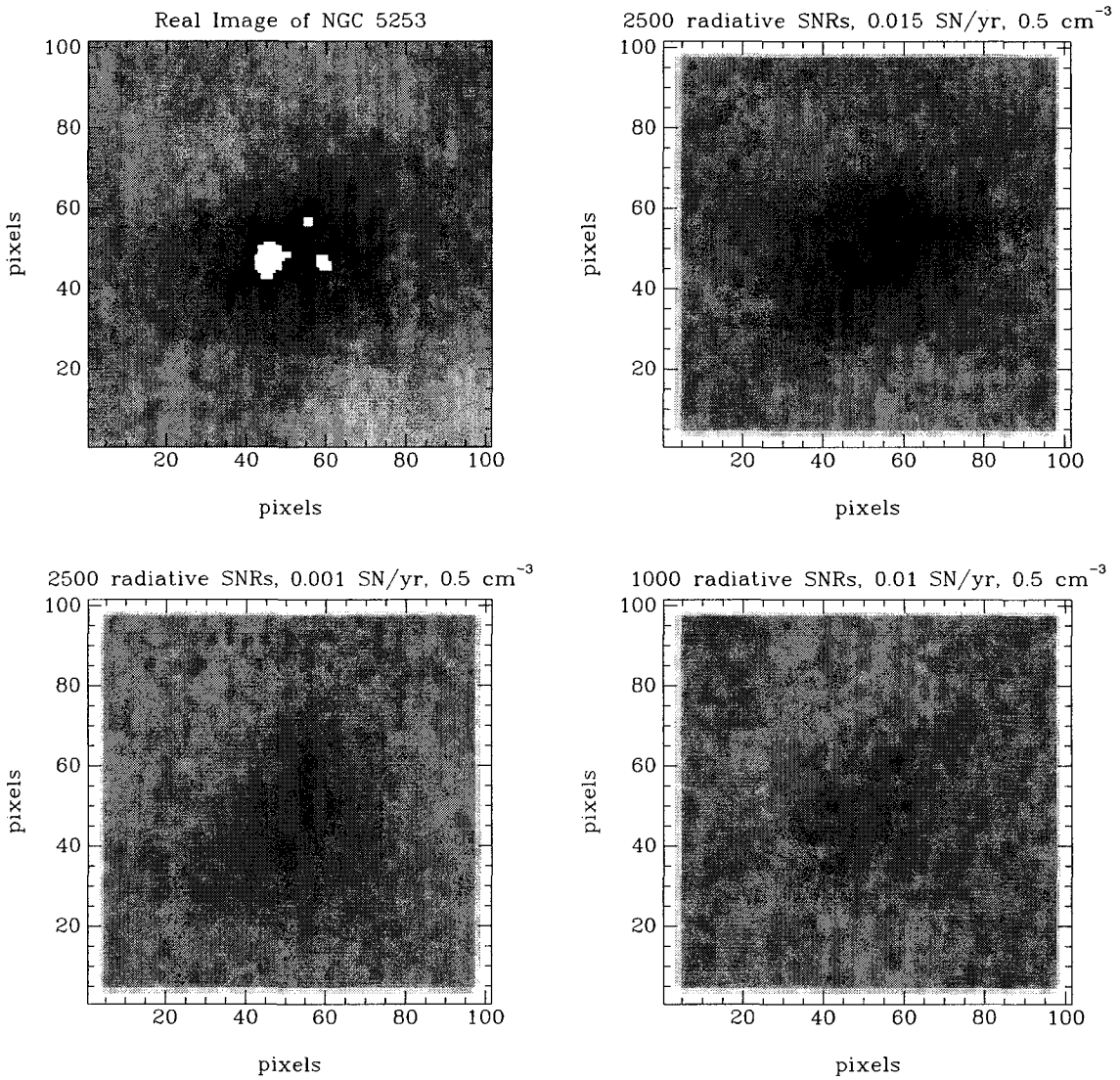

Figure 4.17: Examples of synthetic [Fe II] line emission images compared to the real image of NGC 5253, for a pre-shock density of 0.5 cm $^{-3}$ and no limits on the emission lifetime of the remnants. The real image is shown in the upper left corner.

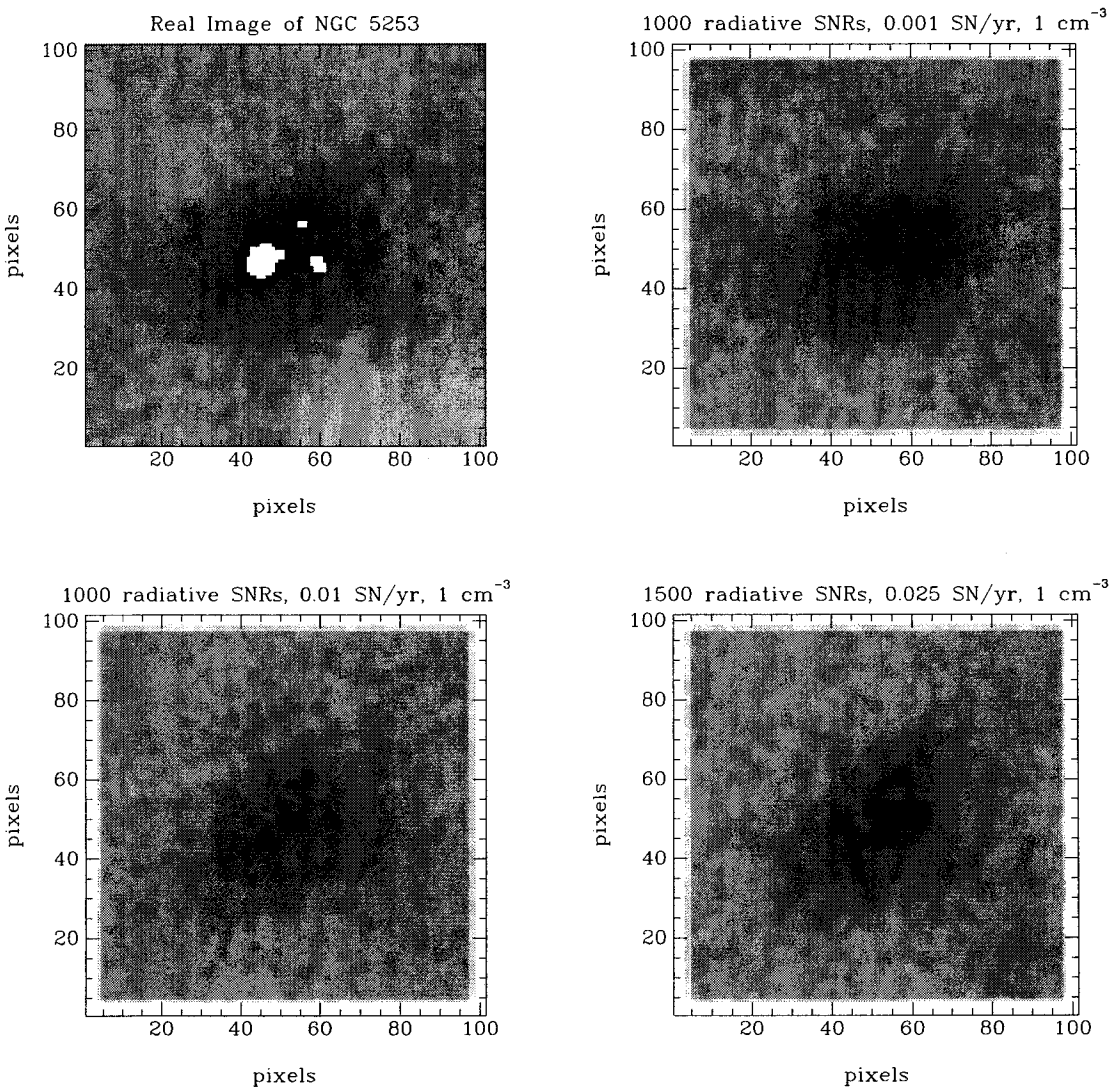

Figure 4.18: Examples of synthetic [Fe II] line emission images compared to the real image of NGC 5253, for a pre-shock density of 1 cm $^{-3}$ and no limits on the emission lifetime of the remnants. The real image is shown in the upper left corner.

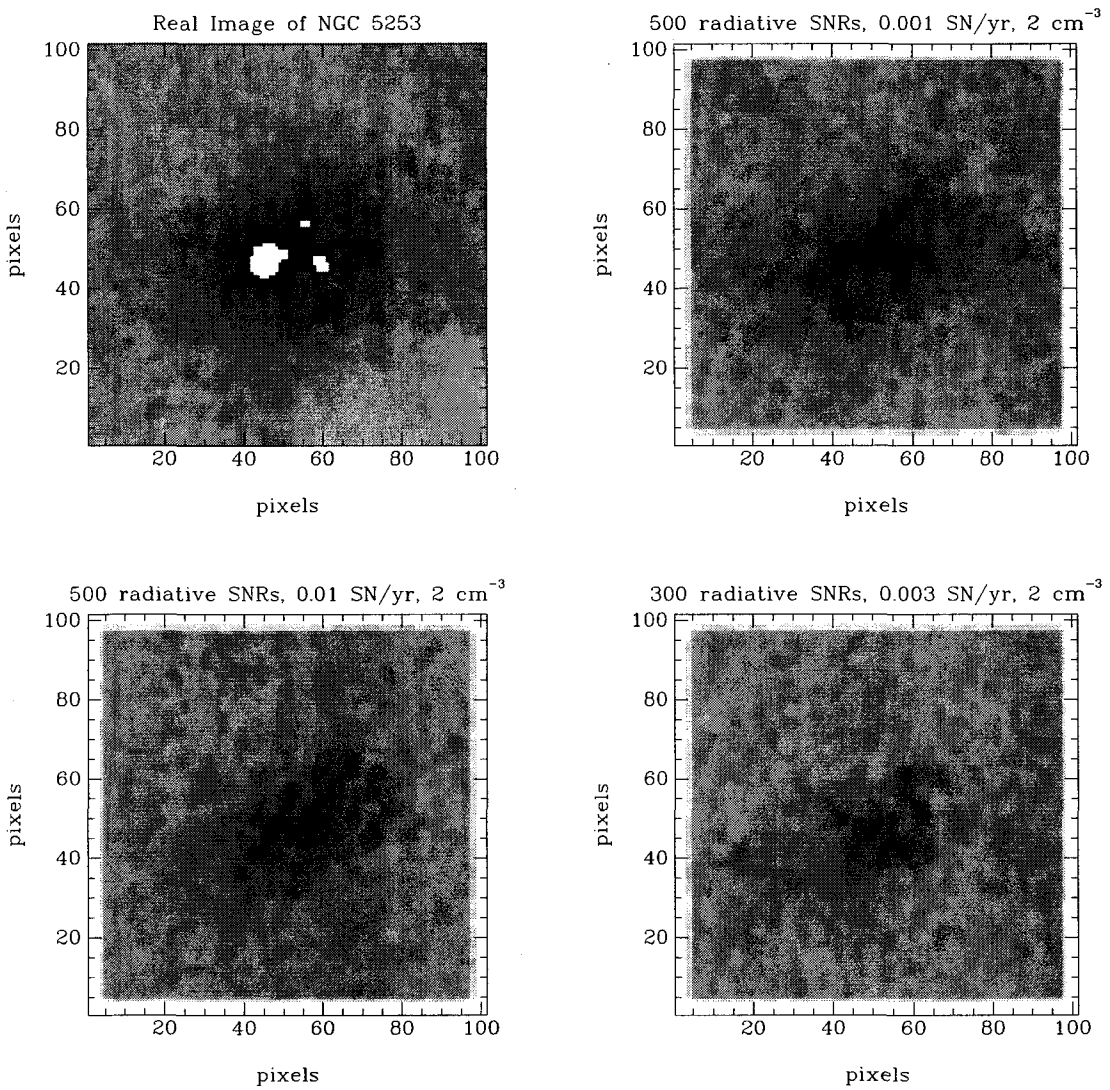

Figure 4.19: Examples of synthetic [Fe II] line emission images compared to the real image of NGC 5253, for a pre-shock density of $2\,\mathrm{cm}^{-3}$ and no limits on the emission lifetime of the remnants. The real image is shown in the upper left corner.

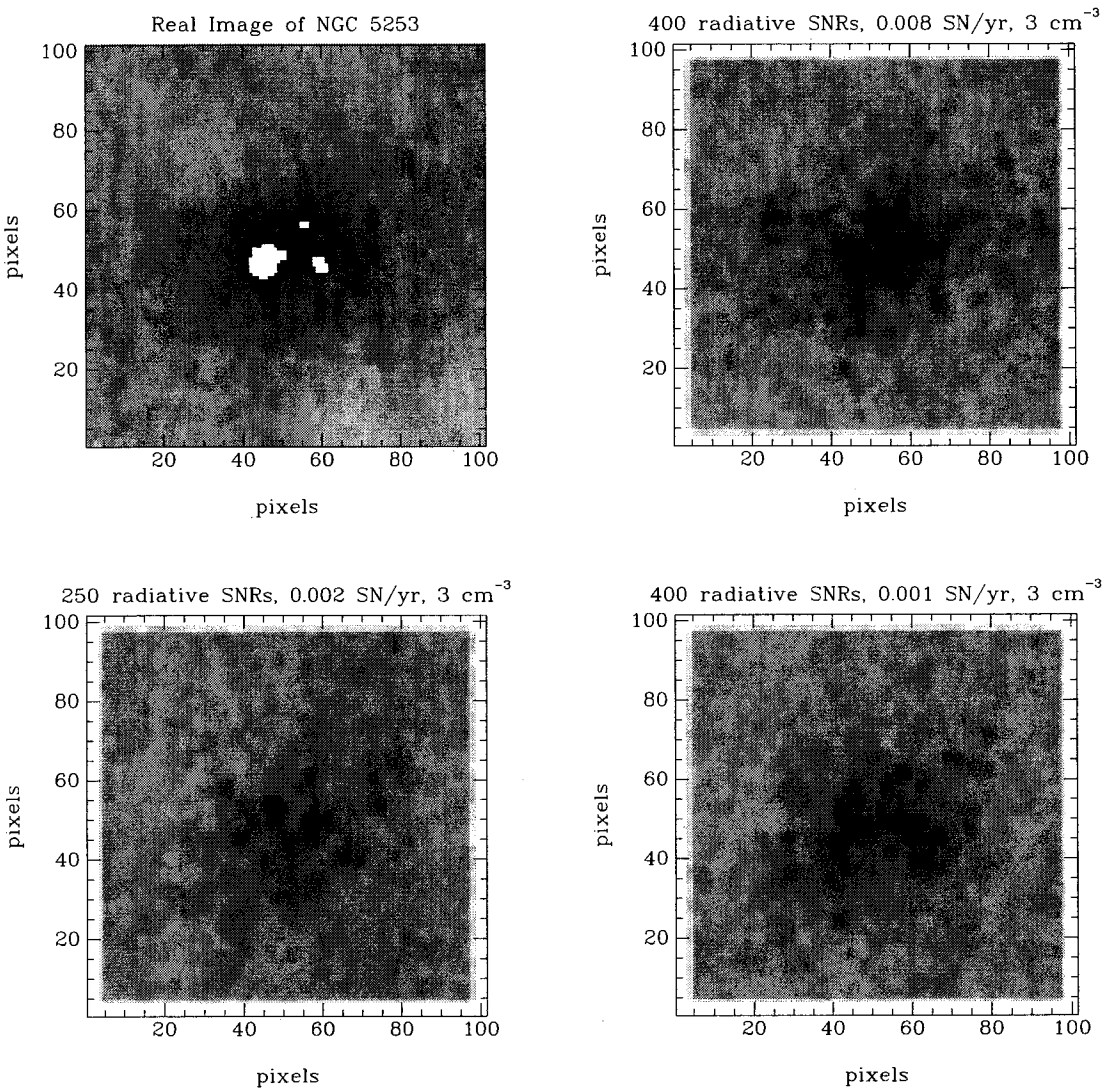

Figure 4.20: Examples of synthetic [Fe II] line emission images compared to the real image of NGC 5253, for a pre-shock density of $3\,\mathrm{cm}^{-3}$ and no limits on the emission lifetime of the remnants. The real image is shown in the upper left corner.

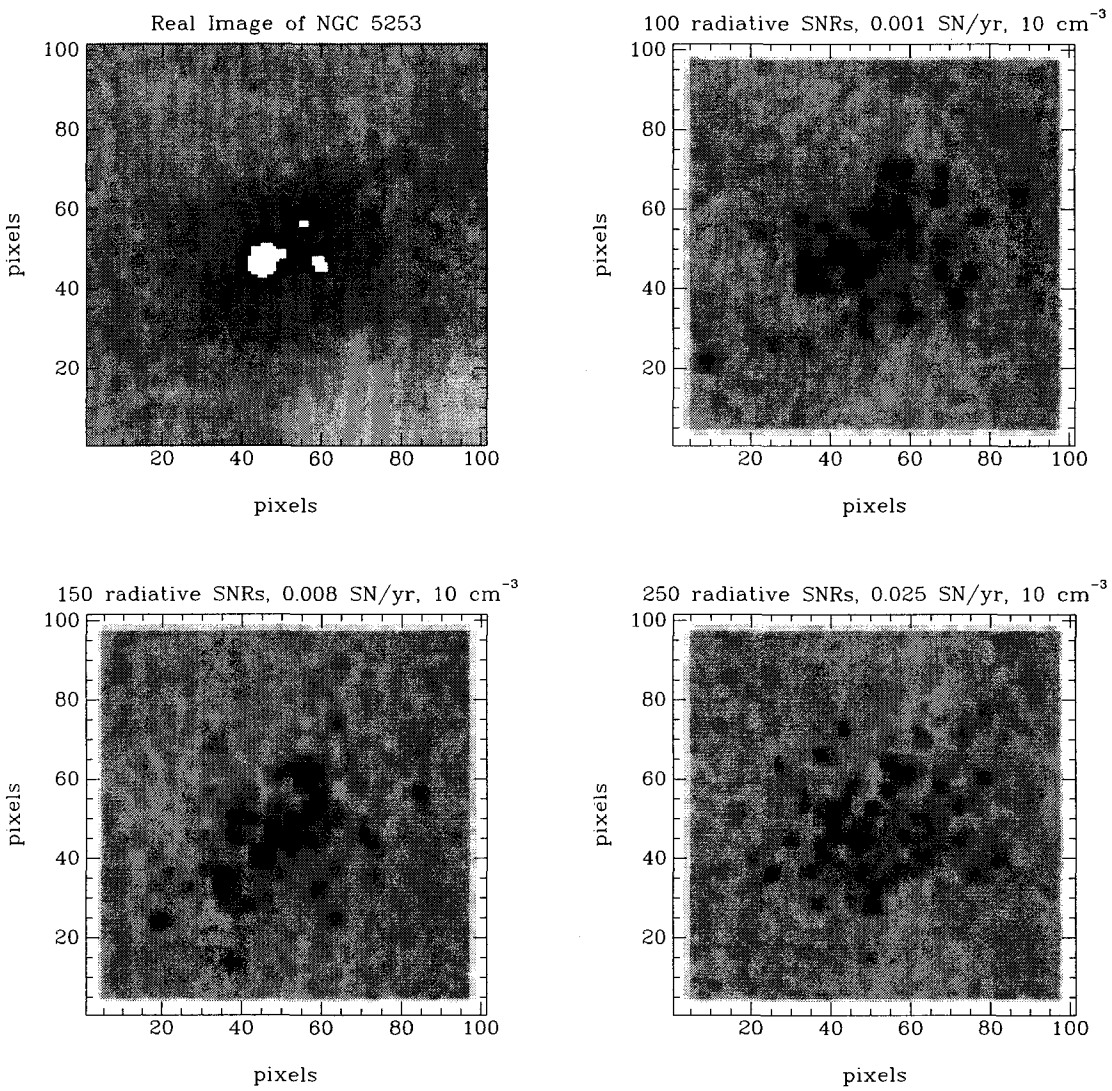

Figure 4.21: Examples of synthetic [Fe II] line emission images compared to the real image of NGC 5253, for a pre-shock density of $10\,\mathrm{cm}^{-3}$ and no limits on the emission lifetime of the remnants. The real image is shown in the upper left corner.

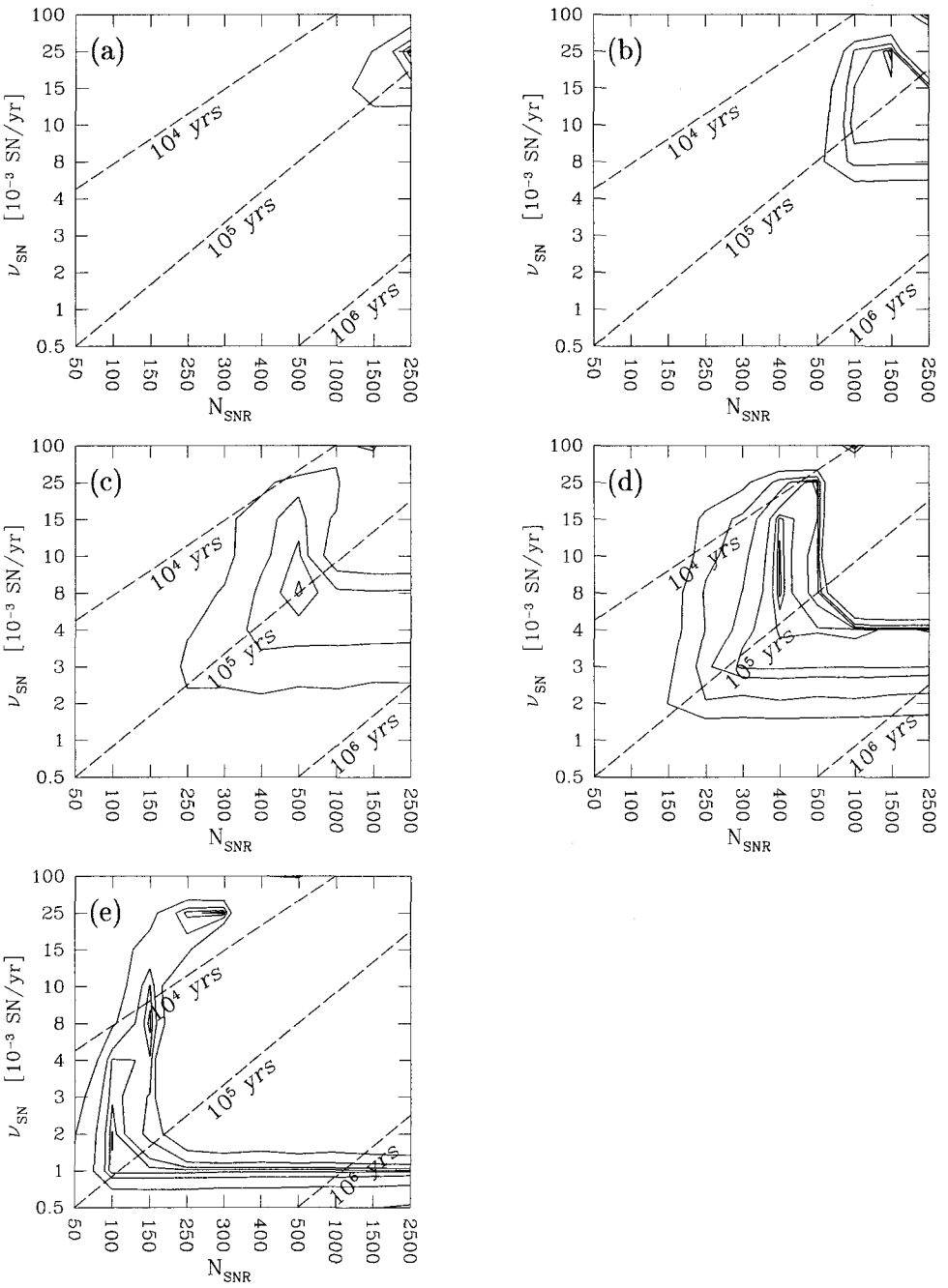

Figure 4.22: Results from the goodness-of-fit tests on the images of the simulated SNR populations of NGC 5253. Shown are five ν_{SN}–N_{SNR} slices of the parameter space: **(a)** $n_0 = 0.5\,\mathrm{cm}^{-3}$, **(b)** $n_0 = 1\,\mathrm{cm}^{-3}$, **(c)** $n_0 = 2\,\mathrm{cm}^{-3}$, **(d)** $n_0 = 3\,\mathrm{cm}^{-3}$, **(e)** $n_0 = 10\,\mathrm{cm}^{-3}$. The dashed lines indicate the age of the SNR populations. For models with a SNR population older than 10^5 yrs, the goodness-of-fit statistic is no longer sensitive to the total number of SNRs (see Section 4.2.2).

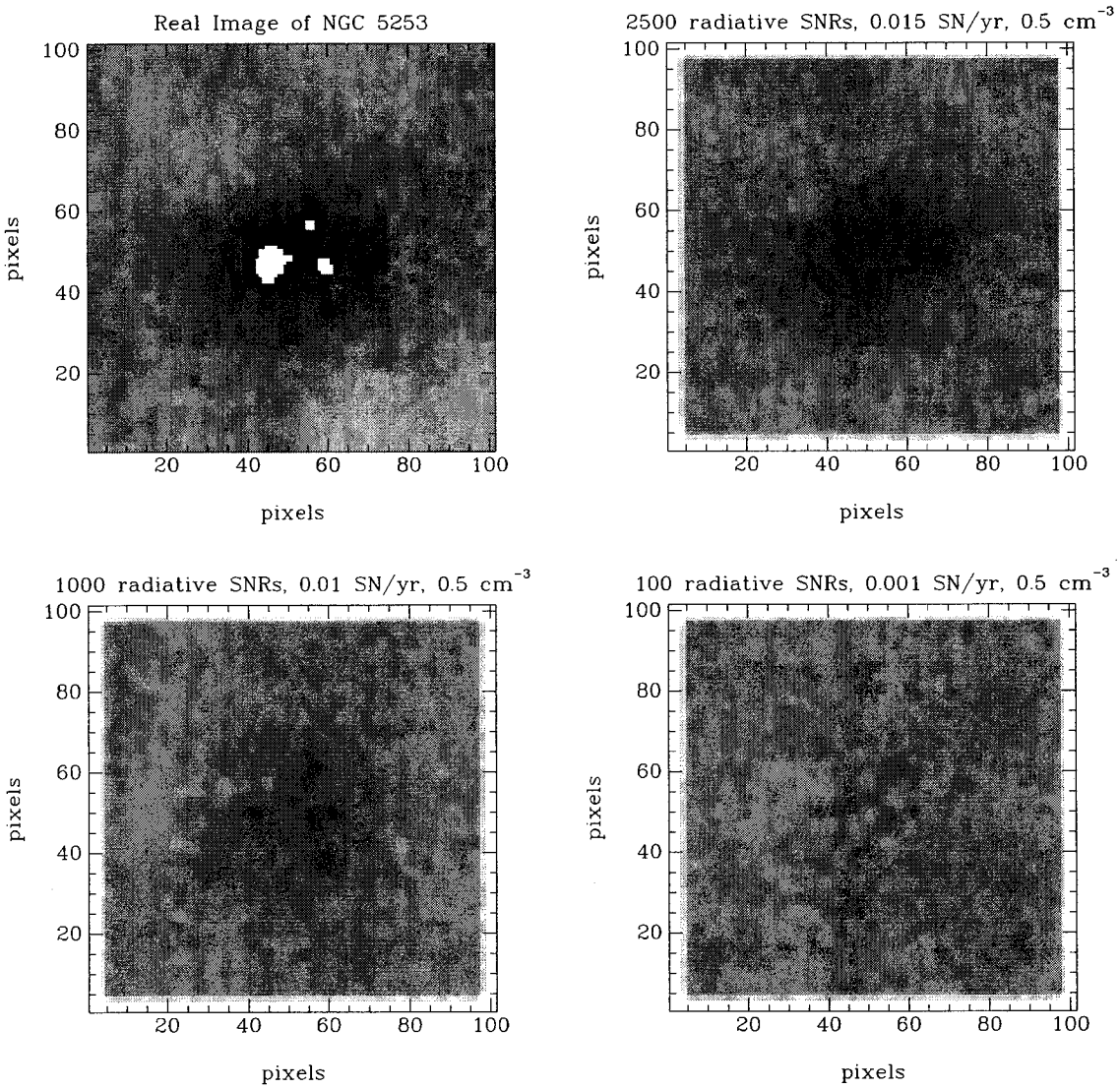

Figure 4.23: Examples of synthetic [Fe II] line emission images compared to the real image of NGC 5253, for a pre-shock density of $0.5\,\mathrm{cm}^{-3}$ and an emission lifetime of 10^5 yrs. The real image is shown in the upper left corner.

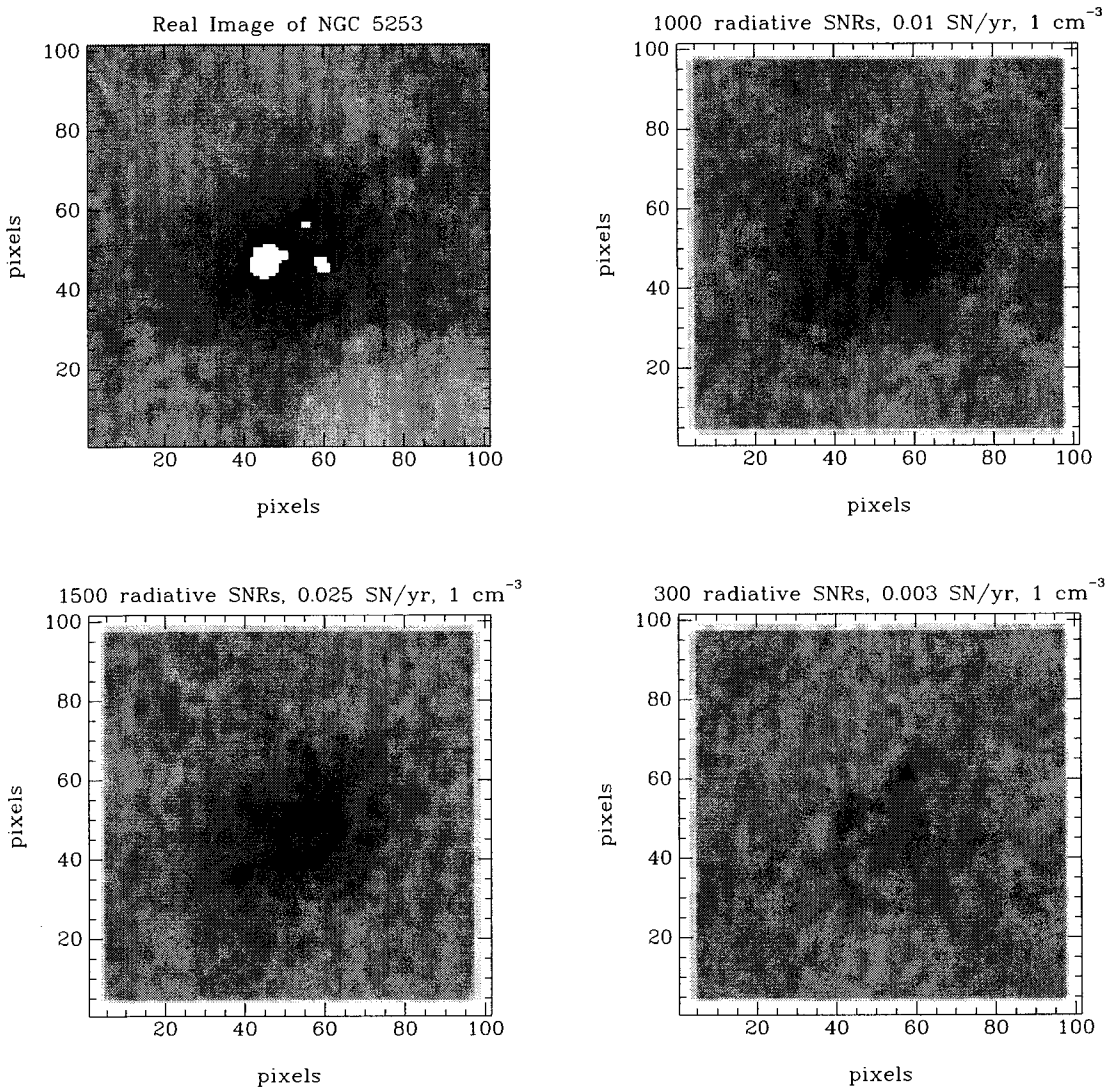

Figure 4.24: Examples of synthetic [Fe II] line emission images compared to the real image of NGC 5253, for a pre-shock density of $1\,\mathrm{cm}^{-3}$ and an emission lifetime of 10^5 yrs. The real image is shown in the upper left corner.

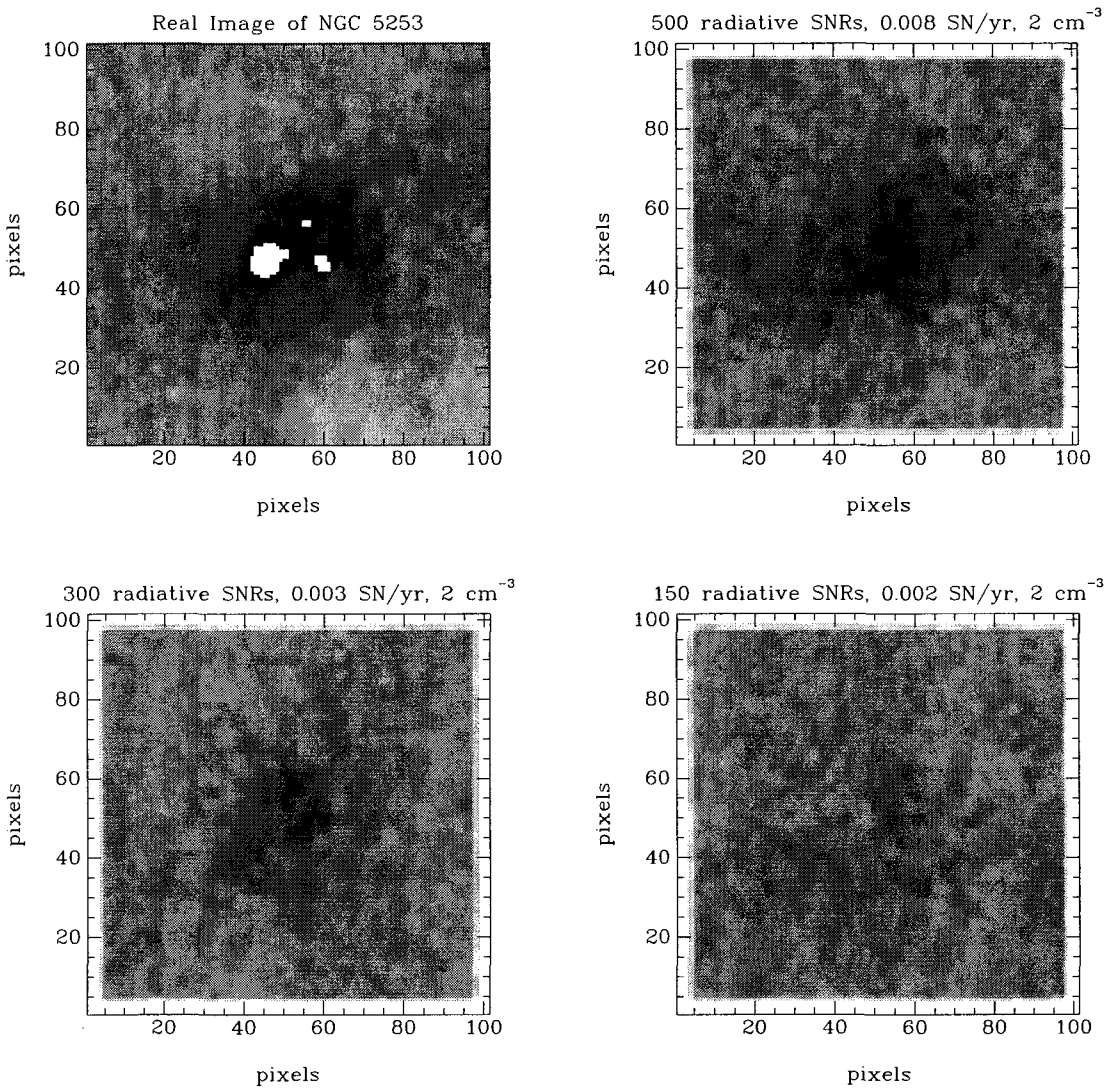

Figure 4.25: Examples of synthetic [Fe II] line emission images compared to the real image of NGC 5253, for a pre-shock density of $2\,\mathrm{cm}^{-3}$ and an emission lifetime of 10^5 yrs. The real image is shown in the upper left corner.

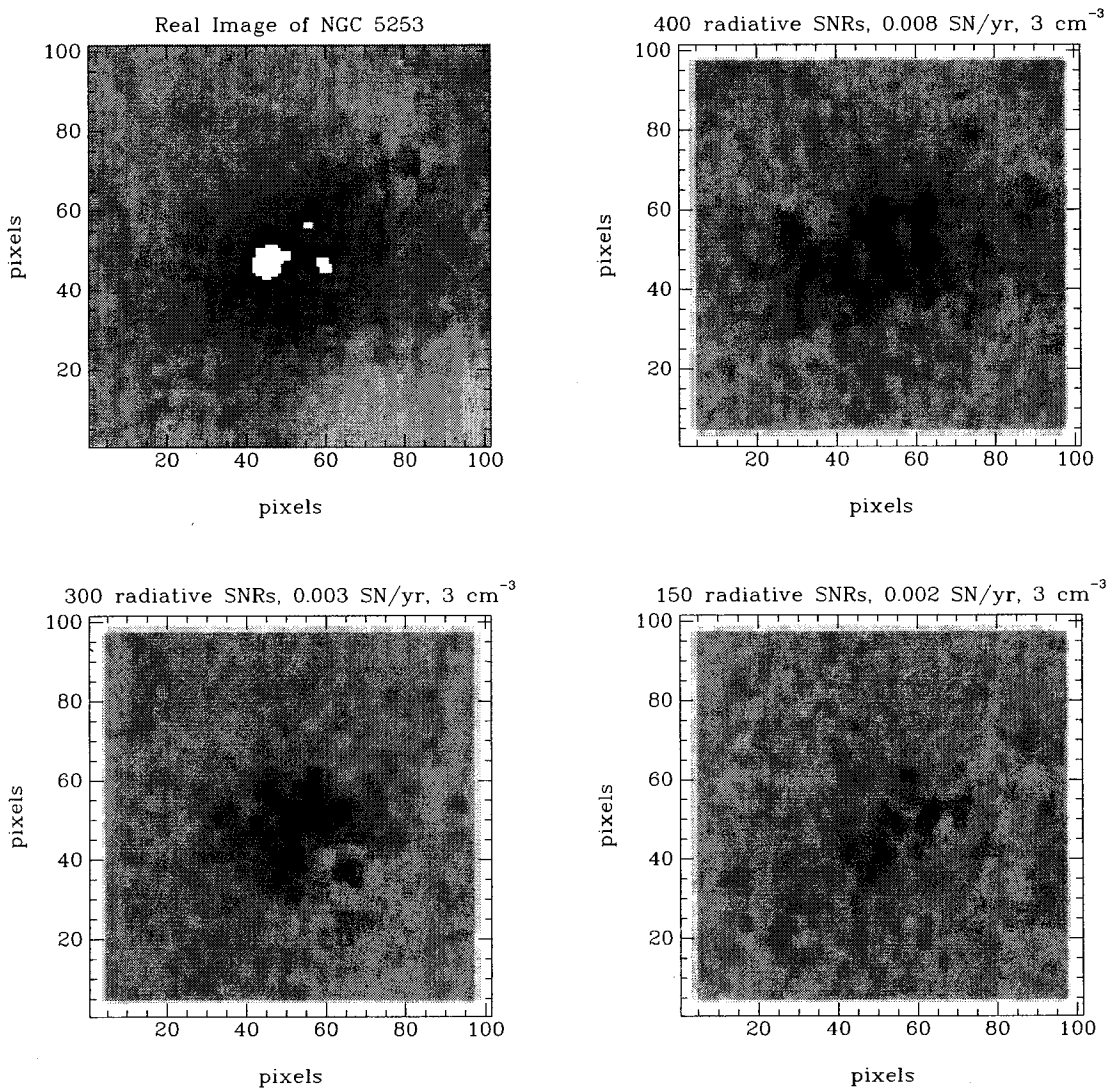

Figure 4.26: Examples of synthetic [Fe II] line emission images compared to the real image of NGC 5253, for a pre-shock density of $3\,\mathrm{cm}^{-3}$ and an emission lifetime of 10^5 yrs. The real image is shown in the upper left corner.

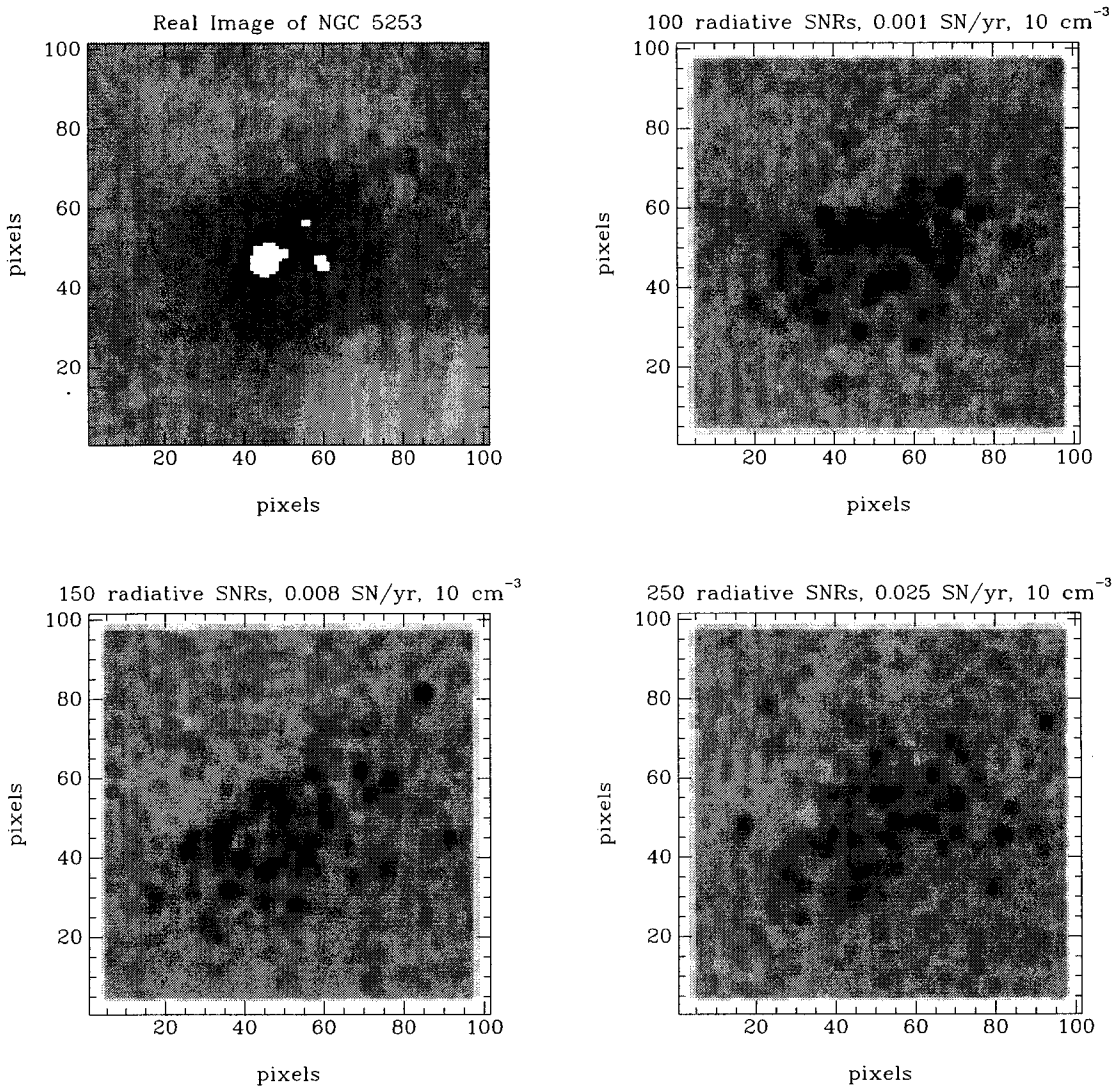

Figure 4.27: Examples of synthetic [Fe II] line emission images compared to the real image of NGC 5253, for a pre-shock density of $10\,\mathrm{cm}^{-3}$ and an emission lifetime of 10^5 yrs. The real image is shown in the upper left corner.

it is impossible to reproduce the morphology of the [Fe II] emission: the disagreement would simply become worse if we tried a pre-shock density of $100\,\mathrm{cm}^{-3}$.

Additional evidence for an ISM under the influence of supernova remnant shock fronts is provided by ROSAT X-ray images of NGC 1569. These images show that the hot gas in this galaxy is circumscribed by the system of expanding Hα filaments surrounding the starburst core (Heckman et al., 1995).

The supernova rate in NGC 1569

The supernova rate found for NGC 1569 falls within the range of previous estimates. Waller (1991) scaled current ionizing star formation rate in NGC 1569 to the rate observed in the Milky Way, and derived a supernova rate of about $0.004\,\mathrm{SN\,yr}^{-1}$. More recently, optical HST images allowed photometry of the stellar population in the centre of NGC 1569. From the star formation rate derived from a comparison with evolutionary population synthesis models, Greggio et al. (1998) estimate that $2\text{-}3\times10^5$ type II supernovae would have occurred over the last 0.1 Gyr. This leads to a mean supernova rate of $0.0025\,\mathrm{SN\,yr}^{-1}$. It should be noted that this last estimate is an average over 0.1 Gyr, which is a relatively long time span in the history of a starburst galaxy. While Greggio et al. conclude that the star formation rate has been mostly constant during that period, they cannot exclude short variations in the star formation rate. A short burst in the recent history of the galaxy can explain a slightly higher *current* supernova rate; it is this latter quantity that the [Fe II] line emission is sensitive to.

Non-thermal synchrotron radio emission is directly associated with SNRs and can be used to estimate the supernova rate. Based on the average energy of a SNR (Woltjer, 1972), the total non-thermal energy content of NGC 1569 (Israel and de Bruyn, 1988) implies the occurrence of 5×10^5 supernova explosions during the last starburst episode. If the starburst episode lasted 100 Myr, as suggested by Greggio

et al., we obtain a supernova rate of 0.005 SN/yr.

Other supernova rate estimates for NGC 1569 can be derived from ν_{SN}–$L_{[Fe\ II]}$ relations but, as discussed before (Section 4.1.2), we question the blind use of these relations. For example, using the ν_{SN}–$L_{[Fe\ II]}$ relation derived by Calzetti (1997), and our estimate of the [Fe II] luminosity[4] for NGC 1569, we find a supernova rate of $0.0004\,yr^{-1}$, an order of magnitude lower than the other estimates, including ours. In this case, the problem originates in the average luminosity used to derive the relation ($\langle L \rangle = 10^3\,L_\odot$).

The supernova rate in NGC 5253

The case of NGC 5253 is more complex. The difficulties encountered trying to reproduce the [Fe II] line emission in NGC 5253 hints at the possibility that a significant portion of the extended [Fe II] line emission in NGC 5253 originates from sources other than shock fronts from individual SNRs.

The very young super-star cluster (and its immediate surroundings) radiates strongly across the electromagnetic spectrum. This area of the galaxy has attracted most of the attention of other researchers studying NGC 5253, for good reason. This star cluster is now believed to be the youngest SSC known (Gorjian et al., 2001; Calzetti et al., 1997; Turner et al., 1998). Unfortunately for us, this means that most of what is currently known regarding NGC 5253 concerns that specific region of the galaxy, rather than the whole starburst core.

From stellar population synthesis of ionizing star clusters, Esteban & Peimbert (1995) attempted to estimate the number of type II SNe that would have exploded in the young super-star cluster at the centre of NGC 5253. They found a very low supernova rate of $(0\text{–}2)\times10^{-5}$ yrs which corresponds to 0–7 type II SNe. However, it is important to understand that this rate applies only to the star cluster. The cluster

[4]Converted to $L_{[Fe\ II]\lambda1.257\,\mu m}$ to conform to the ν_{SN}—$L_{[Fe\ II]}$ relation in Calzetti (1997)

is believed to be about 3 Myr old, which means that only the most massive stars ($\sim 120\,M_{\odot}$) have now reached the end of their life. The supernova rate is therefore expected to be very low in that cluster. This picture also agrees with the weakness of non-thermal synchrotron emission, which also suggests a very low number of SNRs in that area (Beck et al., 1996; Turner et al., 1998).

An estimate of the global number of SNRs in NGC 5253 has been derived from soft X-ray emission. A SNR colliding with a superbubble wall would generate 8×10^{35} ergs/s (Chu and Mac Low, 1990). From their soft X-ray measurements, Martin and Kennicutt (1995) estimate the number of SNRs to be around 800. This agrees well with our own estimate and suggest a much larger supernova rate than the one observed by Esteban and Peimbert in the young SSC.

From the photometric properties of the star clusters in NGC 5253, Caldwell and Phillips (1989) concluded that the central star-forming complex (the whole nuclear region, not just the young SSC region) is a recent event that started $\sim 10^7$ yrs ago. This leaves enough time for the most massive stars to reach the supernova stage of their evolution.

Another piece of evidence suggesting the presence of a significant number of SN events in NGC 5253 comes from the detection of a complex system of SNRs and stellar wind-blown Hα loops and filaments surrounding the nuclear region (Marlowe et al., 1995). These observations support our conclusions regarding the number of [Fe II]-emitting supernova remnants in NGC 5253 ($\sim$750 SNRs), and the current supernova rate ($\sim$0.005 SN/yr) derived from the [Fe II] line emission.

[Fe II] emission from the N5253-C005 super-star cluster area

It seems clear now that the bulk of the SN activity in NGC 5253 has so far occurred away from the young SSC area. Yet, the peak of the [Fe II] line emission coincides with the super-star cluster. The [Fe II]/Paβ ratio measured and the youth

of the SSC suggest a large amount of ionizing radiation. [Fe II] line emission can, under specific conditions, be produced through blackbody photoionization (Mouri et al., 2000), and such an origin cannot be ruled out. But let us first consider the possibility of a supernova remnant origin.

The [Fe II] line emission, in the shock-heated ionization scenario, has been shown to depend strongly on the post-shock electron density (Morel et al., 2002). There are a number of measurements of the electron density within a $\sim$10 pc radius about the young SSC. Compared to the observed H92α radio recombination line, models indicate an electron density of $\sim 10^4\,\mathrm{cm}^{-3}$ (Mohan et al., 2001). Also, the radio continuum emission peaks around the SSC, and suggests an optically thick nebula with $\langle {n_e}^2 \rangle^{1/2} \sim 5000\,\mathrm{cm}^{-3}$ (Turner et al., 1998). Finally, the modeling of the soft X-ray emission has led to an estimated ambient density of $n_0 = 100\,\mathrm{cm}^{-3}$ in the immediate vicinity of the cluster (Strickland and Stevens, 1999). Clearly, there is a significant density difference between the SSC area and the rest of the starburst core. Under such high densities it becomes possible to generate very [Fe II] luminous supernova remnants, like the ones observed in M82.

The [Fe II] flux associated with the source we identify as N5253-C005 is observed to be 640 $L_\odot$. With the high densities observed at the cluster's position, a single SNR could easily account for such a luminosity. If we consider the whole area surrounding the cluster — the region we designate N5253-O001 — the luminosity measured rises to 1740 $L_\odot$. Again, one or two SNRs would be sufficient to explain the [Fe II] luminosity. *However, in this scenario, the morphology of the emission does not agree with a supernova remnant origin*: bright and compact SNRs would have been detected in our images as such. Instead we see a very smooth and bright [Fe II] region.

All evidence argues in favour of a blackbody photoionization origin for the [Fe II] emission in the vicinity of the young starburst cluster. Although this observation should raise a certain level of concern regarding the use of the integrated [Fe II] line emission of a galaxy to measure the supernova rate, it should be pointed out that the

[Fe II] region N5253-O001 accounts for less than 5% of the total [Fe II] luminosity observed in NGC 5253.

The [Fe II]/Paβ line ratio in starburst galaxies

Imagine a scenario in which a galaxy experiences a starburst with *global* characteristics similar to the ones observed in N5253-O001 — i.e. very young, with the predominant [Fe II] emission mechanism being blackbody photoionization rather than supernova remnants. In this case the [Fe II]/Paβ ratio would become a valuable diagnostic tool. The [Fe II]/Paβ ratio is a measure of the importance of shock excitation relative to photoionization. Indeed, the [Fe II]/Paβ ratio measured for the [Fe II] region in NGC 5253 is much lower than what is considered typical for a supernova remnant (e.g. Table 1.1).

In Figure 4.28, we compare the [Fe II] λ1.644 μm /Paβ line ratio observed in different types of sources. The [Fe II]/Paβ line ratio in SNRs is on average two orders of magnitude larger than in the Orion nebula. The global [Fe II]/Paβ line ratio for the starburst galaxies falls in the intermediate range, as is expected since they harbour both supernova remnants and H II regions. The data on the NGC 5253 star clusters is particularly interesting as it shows a large variation in the [Fe II]/Paβ ratio. The youngest star cluster, N5253-C005, displays the lowest [Fe II]/Paβ ratio, an indication that the photoionization processes dominate over shock excitation. Larger line ratios are observed for the older clusters. As a stellar population evolves the number of hot, photoionizing stars decreases while the number of SNRs from type II supernova explosions increases.

The [Fe II]/Paβ line ratio for the whole nuclear area of NGC 5253 agrees well with the ratios observed in NGC 1569 and M82. This indicates that, despite the presence of a strong source in which photoionization processes appear to dominate, the [Fe II] line emission from the starburst core of NGC 5253, as a whole, most likely originates

from shock-heated regions associated with supernova remnants. As explained before, this is also what our models suggest.

4.2.6 Summary

The results obtained from the analysis of the extended [Fe II] line emission in NGC 1569 and NGC 5253 support our earlier conclusion regarding the ambient density in these two galaxies. Unlike what is observed in other starburst galaxies, the ambient, or pre-shock density in NGC 1569 and NGC 5253 must be of the order of $1\,\mathrm{cm}^{-3}$. Ambient densities of $100\,\mathrm{cm}^{-3}$ or larger have been observed in other starburst galaxies, as in M82 and in NGC 253, but such densities in NGC 1569 and NGC 5253 are strongly rejected by our analysis.

This large difference in pre-shock densities has a profound impact on the average [Fe II] luminosity of the supernova remnants, which in turn will affect the total [Fe II] luminosity of the galaxies. This means that the naive ν_{SN}–$L_{[\mathrm{Fe\ II}]}$ relations currently used to estimate the supernova rate do not apply to all galaxies, but only to M82-like galaxies.

We have shown that a reliable supernova rate *can* be measured from the [Fe II] luminosity of a galaxy, but the knowledge of the average pre-shock density of the ISM, and the extent to which the ISM is affected by the SNRs, is essential. For example, in NGC 1569 and NGC 5253, the ISM appears to be mostly in a post-shock state, while in M82, the impact of the SNRs is limited to small density enhancements in the ISM.

The bright [Fe II] region in the vicinity of the young super-star cluster N5253-C005 does not have a supernova remnant origin. Rather, a blackbody photoionization origin is a more plausible explanation. As explained in Mouri et al. (2000), [Fe II] line emission can arise from exceptional H II regions; N5253-C005 surely qualifies as being exceptional. The observed [Fe II]/Paβ line ratio does favour a blackbody

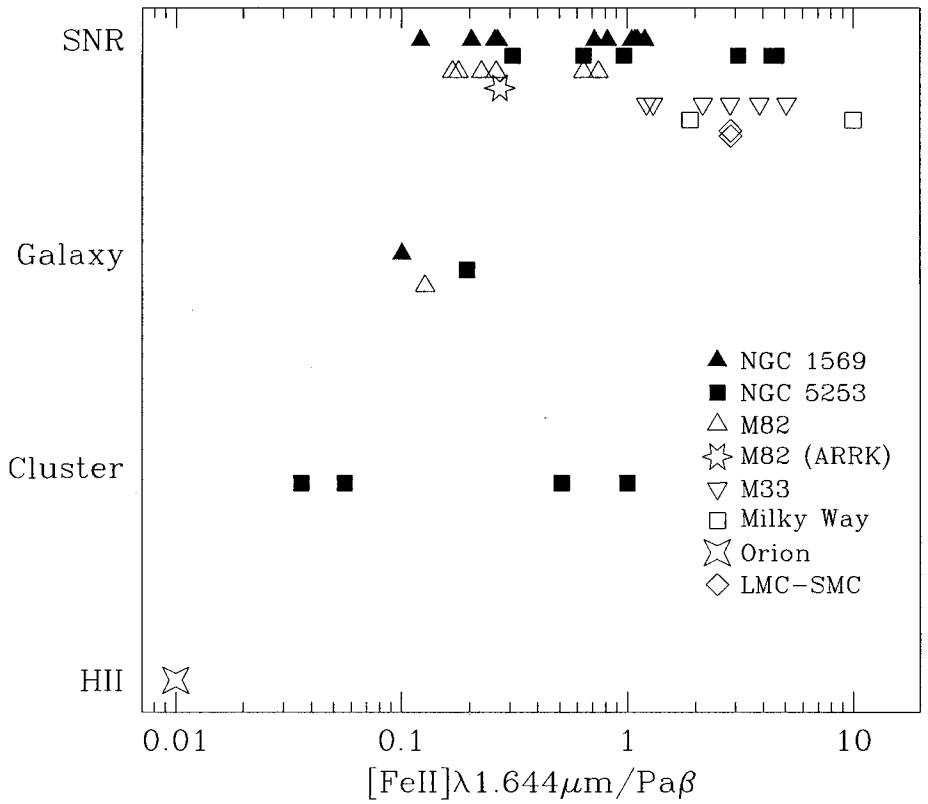

Figure 4.28: The [Fe II] λ1.644 μm /Paβ line ratio for different types of sources — H II regions, star clusters, starburst galaxies, and supernova remnants. The [Fe II]/Paβ line ratio in SNRs is on average two orders of magnitude larger than in the Orion nebula. The global line ratio for starburst galaxies is intermediate between the pure SNR ratio and pure H II region ratio. The younger star clusters in NGC 5253 show a lower [Fe II]/Paβ ratio than the other clusters. The data points for the various data sets have been vertically offset for clarity. The M82 (ARRK) point corresponds to the average ratio measured in the M82 SNR sample studied by Alonso-Herrero et al. (2001). (*SNRs*: Tables 3.4, 3.10 and 4.1; *Galaxies*: Tables 3.4, 3.10 and Mouri et al. (2000); *Clusters*: Table 3.10; *H*II *Region*: Lowe et al. (1979).)

photoionization emission mechanism over shock-heating.

The [Fe II]/Paβ line ratios observed for the galaxies NGC 1569 and NGC 5253 is found to be larger than previous estimates; the latter were based on spectroscopic observations centred on the large super-star clusters in each galaxies. These SSCs are biased toward low [Fe II]/Paβ ratios. The ratios we measured for the starburst galaxies are intermediate between the ratios characteristic of SNRs, and those of H II regions. In starburst galaxies, the [Fe II]/Paβ ratio for the whole galaxy represents the relative importance of shock-heating from SNRs versus photoionization from H II regions. This ratio is therefore a useful diagnostic tool to assess the origin of the bulk of the [Fe II] line emission in distant galaxies for which it is not possible to resolve the [Fe II] features.

Chapter 5

Conclusions

Because of its link to supernova remnants, the near-infrared [Fe II] line emission is becoming a valuable tool for the study of the global impact of supernova explosions on actively star-forming galaxies. In the previous chapter, we have made use of this probe to examine several properties of nearby starburst galaxies, and of their SNR population. The purpose of the project was to further explore the potential of the [Fe II] line emission as a supernova rate indicator.

Narrow-band imaging of three starburst galaxies has led to the detection of 10 supernova remnant candidates in NGC 1569, and 7 candidates in NGC 5253. It was found that the compact sources account for about $\sim 10\%$ of the total [Fe II] line emission, the bulk of the emission coming from an extended component. No significant [Fe II] emission was detected in NGC 3738.

The comparative study of the properties of the new SNR candidates, and our analysis of the extended component of the [Fe II] emission, have led us to the following conclusions:

- The [Fe II] luminosities of the SNRs we detected in NGC 1569 and NGC 5253 are similar to the luminosities observed for remnants in quiescent galaxies (e.g. Milky Way, LMC, M33). The average luminosity is two orders of magnitude

fainter than the typical luminosity of the M82 supernova remnants. Contrary to what was previously believed, we conclude that SNRs in starburst galaxies are not necessarily brighter than their counterparts in quiescent galaxies. Our observations do not support a quiescent–starburst dichotomy in the SNR [Fe II] luminosity distribution.

- Considering the electron densities measured in NGC 1569 and NGC 5253, and the dependence of the [Fe II] luminosity on this quantity, we conclude that a significant fraction of the ISM, in both galaxies, must be under the influence of SNR shock fronts in order to explain the [Fe II] luminosity of the remnants we detected.

- This work has shown that the extended component of the [Fe II] emission in NGC 1569 and NGC 5253 can be explained as originating from a large population of unresolved radiative SNRs in a moderately low ambient density ($n_0 \sim 1\,\mathrm{cm}^{-3}$) environment.

- In starburst galaxies, the integrated [Fe II]/Paβ line ratio represents the relative importance of shock-heating from SNRs versus photoionization from H II regions. Since the extended [Fe II] emission dominates over the compact sources, the [Fe II]/Paβ line ratio is robust to the presence of a few very young super-star clusters, as we have shown for NGC 5253. This ratio is therefore a useful diagnostic tool to assess the origin of the bulk of the [Fe II] line emission in distant galaxies for which it would not be possible to resolve the individual [Fe II] features.

- The [Fe II]-emitting lifetime of a SNR is limited only by the duration of the radiative phase. It is dependent on the ambient density at the supernova remnant's position. Previous estimates of the [Fe II]-emitting lifetime of SNRs in M82 (10^4 yrs) are not representative of SNRs in all starburst galaxies. Indeed,

we have detected in NGC 1569 and NGC 5253 [Fe II]-emitting supernova remnants as old as 10^5 yrs. The short lifetime observed in M82 is likely due to the higher density environment, which accelerates the evolution of the supernova remnants.

- We find no evidence to support grain destruction as the cause of the increased [Fe II] emission at the position of the supernova remnants. Rather, our observations and results can be explained by radiative processes in the shock-heated gas of supernova remnants.

- We caution against the blind usage of Supernova rate – [Fe II] luminosity relations derived from average properties of SNRs in extreme starburst galaxies like M82. The large difference in pre-shock densities has a profound impact on the average [Fe II] luminosity of the supernova remnants, which in turn will affect the total [Fe II] luminosity of the galaxies. We argue that the use of M82 to scale the Supernova rate – [Fe II] luminosity relation is ill-advised as the average luminosity of the SNRs in M82 is high not because the supernova rate is high but because the pre-shock density is large.

The important differences between the properties of the supernova remnants in our sample starburst galaxies and the larger starbursts, like M82, underline the need for a systematic survey of nearby star-forming, and quiescent, galaxies. Not only would such a survey help in the calibration of [Fe II] line emission from supernova remnants, but, in the process, it would lead to a better understanding of the impact of the starburst phenomenon on the host galaxy.

Such survey is just now becoming possible; near-infrared detectors have recently grown larger (wider field of view), and are now of a much better quality than five years ago. Additionally, the introduction of near-infrared adaptive optics systems on large telescopes increases the distance at which a galaxy can be observed with sufficient spatial resolution to detect individual supernova remnants.

The number of supernova remnants that have been searched for [Fe II] emission is quite small; the number of remnants from which [Fe II] emission has been detected is even smaller. If we are to pursue the use of the [Fe II] line emission as a tracer of the supernova activity, a survey of known supernova remnants is essential. Although difficult to obtain, n_e measurements are probably the key to a better understanding of the [Fe II] emission in SNRs. Also, the [Fe II]-emitting lifetime of a SNR is poorly constrained, and the time evolution of the [Fe II] luminosity should be examined.

Bibliography

2MASS: 2000, *2MASS Extended Objects - Release 2*, Two Micron All Sky Survey Team

Alonso-Herrero, A., Rieke, M. J., Rieke, G. H., and Kelly, D. M.: 2001, *Astrophys. & Space Science,* **276**, 1109

Arp, H. C. and Sandage, A.: 1985, *Astron. J.* **90**, 1163

Beck, S. C., Turner, J. L., Ho, P. T. P., Lacy, J. H., and Kelly, D. M.: 1996, *Astrophys. J.* **457**, 610

Benedict, G. F., McArthur, B. E., Fredrick, L. W., Harrison, T. E., Slesnick, C. L., Rhee, J., Patterson, R. J., Skrutskie, M. F., Franz, O. G., Wasserman, L. H., Jefferys, W. H., Nelan, E., van Altena, W., Shelus, P. J., Hemenway, P. D., Duncombe, R. L., Story, D., Whipple, A. L., and Bradley, A. J.: 2002, *Astron. J.* **124**, 1695

Berkhuijen, E. M.: 1986, *Astron. & Astrophys.* **166**, 257

Bersanelli, M., Bouchet, P., and Falomo, R.: 1991, *Astron. & Astrophys.* **252**, 854

Blondin, J. M., Wright, E. B., Borkowski, K. J., and Reynolds, S. P.: 1998, *Astrophys. J.* **500**, 342

Böker, T., Calzetti, D., Sparks, W., Axon, D., Bergeron, L. E., Bushouse, H., Colina, L., Daou, D., Gilmore, D., Holfeltz, S., MacKenty, J., Mazzuca, L., Monroe, B., Najita, J., Noll, K., Nota, A., Ritchie, C., Schultz, A., Sosey, M., Storrs, A., and Suchkov, A. T. S. N. G.: 1999, *Astrophys. J. Supp.* **124**, 95

Bremnes, T., Binggeli, B., and Prugniel, P.: 2000, *Astron.& Astrophys. Supp.* **141**, 211

Burstein, D. and Heiles, C.: 1984, *Astrophys. J. Supp.* **54**, 33

Caldwell, N. and Phillips, M. M.: 1989, *Astrophys. J.* **338**, 789

Calzetti, D.: 1997, *Astron. J.* **113**, 162

Calzetti, D., Armus, L., Bohlin, R. C., Kinney, A. L., Koornneef, J., and Storchi-Bergmann, T.: 2000, *Astrophys. J.* **533**, 682

Calzetti, D., Kinney, A., and Storchi-Bergmann, T.: 1994, *Astrophys. J.* **429**, 582

Calzetti, D., Meurer, G. R., Bohlin, R. C., Garnett, D. R., Kinney, A. L., Leitherer, C., and Storchi-Bergmann, T.: 1997, *Astron. J.* **114**, 1834

Cardelli, J. A., Clayton, G. C., and Mathis, J. S.: 1989, *Astrophys. J.* **345**, 245

Chu, Y.-H. and Mac Low, M.-M.: 1990, *Astrophys. J.* **365**, 510

Cioffi, D. F., McKee, C. F., and Bertschinger, E.: 1988, *Astrophys. J.* **334**, 252

Clements, E. D.: 1983, *M.N.R.A.S.* **204**, 811

Condon, J. J. and Yin, Q. F.: 1990, *Astrophys. J.* **357**, 97

Corliss, C. and Sugar, J.: 1982, *J. Phys. Chem. Ref. Data* **11**, 135

Crowther, P. A., Beck, S. C., Willis, A. J., Conti, P. S., Morris, P. W., and Sutherland, R. S.: 1999, *M.N.R.A.S.* **304**, 654

Davidge, T. J., Le Fevre, O., and Clark, C. C.: 1991, *Astrophys. J.* **370**, 559

de Vaucouleurs, G., de Vaucouleurs, A., Corwin, H. G., J., Buta, R. J., Paturel, G., and Fouqué, P.: 1991, *Third Reference Catalogue of Bright Galaxies*, New York:Springer

Devost, D., Roy, J., and Drissen, L.: 1997, *Astrophys. J.* **482**, 765

Dopita, M. A., Dodorico, S., and Benvenuti, P.: 1980, *Astrophys. J.* **236**, 628

Esteban, C. and Peimbert, M.: 1995, *Astron. & Astrophys.* **300**, 78

Forbes, D. A., Ward, M. J., and Depoy, D. L.: 1991, *Astrophys. J. Letters,* **380**, L63

Forbes, D. A., Ward, M. J., Rotaciuc, V., Blietz, M., Genzel, R., Drapatz, S., van der Werf, P. P., and Krabbee, A.: 1993, *Astrophys. J. Letters,* **406**, L11

Förster Schreiber, N. M., Genzel, R., Lutz, D., Kunze, D., and Sternberg, A.: 2001, *Astrophys. J.* **552**, 544

Freedman, W. L., Wilson, C. D., and Madore, B. F.: 1991, *Astrophys. J.* **372**, 455

Georgiev, T. B., Karachentsev, I. D., and Tikhonov, N. A.: 1997, *Astron. Letters* **23**, 514

Gibson, B. K., Stetson, P. B., Freedman, W. L., Mould, J. R., Kennicutt, R. C., Huchra, J. P., Sakai, S., Graham, J. A., Fassett, C. I., Kelson, D. D., Ferrarese, L., Hughes, S. M. G., Illingworth, G. D., Macri, L. M., Madore, B. F., Sebo, K. M., and Silbermann, N. A.: 2000, *Astrophys. J.* **529**, 723

González-Delgado, R. M., Leitherer, C., Heckman, T. M., and Cerviño, M.: 1997, *Astrophys. J.* **483**, 705

Gordon, S. M., Kirshner, R. P., Long, K. S., Blair, W. P., Duric, N., and Smith, R. C.: 1998, *Astrophys. J. Supp.* **117**, 89

Gorjian, V., Turner, J. L., and Beck, S. C.: 2001, *Astrophys. J. Letters,* **554**, L29

Graham, J. R., Wright, G. S., and Longmore, A. J.: 1987, *Astrophys. J.* **313**, 847

Greenhouse, M. A., S., S., Woodward, C. E., Fischer, J., Thompson, K. L., Forrest, W. J., Pipher, J. L., Raines, N., Smith, H. A., Watson, D. M., and Rudy, R. J.: 1997, *Astrophys. J.* **476**, 105

Greenhouse, M. A., Woodward, C. E., Thronson, H. A., Rudy, R. J., Rossano, G. S., Erwin, P., and Puetter, R. C.: 1991, *Astrophys. J.* **383**, 164

Greggio, L., Tosi, M., Clampin, M., de Marchi, G., Leitherer, C., Nota, A., and Sirianni, M.: 1998, *Astrophys. J.* **504**, 725

Greve, A., Tarchi, A., Hüttemeister, S., de Grijs, R., van der Hulst, J. M., Garrington, S. T., and Neininger, N.: 2002, *Astron. & Astrophys.* **381**, 825

Hawarden, T. G., Leggett, S. K., Letawsky, M. B., Ballantyne, D. R., and Casali, M. M.: 2001, *M.N.R.A.S.* **325**, 563

Hayes, D. S. and Latham, D. W.: 1975, *Astron. J.* **197**, 587

Heckman, T. M., Armus, L., and Miley, G. K.: 1990, *Astrophys. J. Supp.* **74**, 833

Heckman, T. M., Dahlem, M., Lehnert, M. D., Fabbiano, G., Gilmore, D., and Waller, W. H.: 1995, *Astrophys. J.* **448**, 98

Ho, L. C. and Filippenko, A. V.: 1996, *Astrophys. J. Letters,* **466**, L83

Hunter, D. A.: 1982, *Astrophys. J.* **260**, 81

Hunter, D. A.: 1984, *Astrophys. J. Letters,* **276**, L35

Hunter, D. A., Gallagher, J. S., and Rautenkranz, D.: 1982, *Astrophys. J. Supp.* **49**, 53

Hunter, D. A. and Hoffman, L.: 1999, *Astron. J.* **117**, 2789

Hunter, D. A., O'Connell, R. W., Gallagher, J. S., and Smecker-Hane, T. A.: 2000, *Astron. J.* **120**, 2383

Israel, F. P.: 1988, *Astron. & Astrophys.* **194**, 24

Israel, F. P. and de Bruyn, A. G.: 1988, *Astron. & Astrophys.* **198**, 109

Israel, F. P. and van Driel, W.: 1990, *Astron. & Astrophys.* **236**, 323

Jones, A. P., Tielens, A. G. G. M., and Hollenbach, D. J.: 1996, *Astrophys. J.* **469**, 740

Jones, A. P., Tielens, A. G. G. M., Hollenbach, D. J., and McKee, C. F.: 1994, *Astrophys. J.* **433**, 797

Kawara, K., Taniguchi, Y., and Nishida, M.: 1988, *Astrophys. J. Letters,* **328**, L41

Knop, R. A., Armus, L., Larkin, J. E., Matthews, K., Shupe, D. L., and Soifer, B. T.: 1996, *Astron. J.* **112**, 81

Kobulnicky, H. A., Kennicutt, R. C., and Pizagno, J. L.: 1999, *Astrophys. J.* **514**, 544

Kobulnicky, H. A. and Skillman, E. D.: 1997, *Astrophys. J.* **489**, 636

Kobulnicky, H. A., Skillman, E. D., Roy, J., Walsh, J. R., and Rosa, M. R.: 1997, *Astrophys. J.* **477**, 679

Kotilainen, J. K., Forbes, D. A., Moorwood, A. F. M., van der Werf, P. P., and Ward, M. J.: 1996, *Astron. & Astrophys.* **313**, 771

Landolt, A. U.: 1990, *Pub. Astron. Soc. Pacific,* **102**, 1382

Lowe, R. P., Moorhead, J. M., and Wehlau, W. H.: 1979, *Astrophys. J.* **228**, 191

Lumsden, S. L. and Puxley, P. J.: 1995, *M.N.R.A.S.* **276**, 723

Lumsden, S. L., Puxley, P. J., and Doherty, R. M.: 1994, *M.N.R.A.S.* **268**, 821

Marlowe, A. T., Heckman, T. M., Wyse, R. F. G., and Schommer, R.: 1995, *Astrophys. J.* **438**, 563

Martin, C. L.: 1997, *Astrophys. J.* **1997**, 561

Martin, C. L.: 1998, *Astrophys. J.* **506**, 222

Martin, C. L. and Kennicutt, R. C.: 1995, *Astrophys. J.* **447**, 171

Mathewson, D. S., Ford, V. L., Dopita, M. A., Tuohy, I. R., Long, K. S., and Helfand, D. J.: 1983, *Astrophys. J. Supp.* 51

McKee, C. F. and Hollenbach, D. J.: 1980, *Ann. Rev. Astron. & Astrophys.* **18**, 219

McKee, C. F. and Truelove, J. K.: 1995, *Physics Report,* **256**, 157

Meurer, G. R., Heckman, T. M., Leitherer, C., Kinney, A., Robert, C., and Garnett, D. R.: 1995, *Astron. J.* **110**, 2665

Mohan, N. R., Anantharamaiah, K. R., and Goss, W. M.: 2001, *Astrophys. J.* **557**, 659

Morel, T., Doyon, R., and St-Louis, N.: 2002, *M.N.R.A.S.* **329**, 398

Mouri, H., Kawara, K., and Taniguchi, Y.: 2000, *Astrophys. J.* **528**, 186

Mouschovias, T.: 1976, *Astrophys. J.* **207**, 141

Nussbaumer, H. and Storey, P. J.: 1988, *Astron. & Astrophys.* **193**, 327

O'Connell, R. W., Gallagher, J. S., and Hunter, D. A.: 1994, *Astrophys. J.* **433**, 65

Oliva, E., Moorwood, A. F. M., and Danziger, I. J.: 1989, *Astron. & Astrophys.* **214**, 307

Osterbrock, D. E.: 1989, *Astrophysics of Gaseous Nebulae and Active Galactic Nuclei,* University Science Books, Mill Valley, California

Ostriker, J. P. and McKee, C. F.: 1988, *Rev. Mod. Phys.* **60**, 1

Prahdan, A. K. and Zhang, H. L.: 1993, *Astrophys. J. Letters,* **409**, L77

Press, W. H., Teukolsky, S. A., Vetterling, W. T., and Flannery, B. P.: 1992, *Numer-*

ical Recipes in C – The Art of Scientific Computing, Cambridge University Press, second edition

Reach, W. T., Rho, J., Jarrett, T. H., and Lagage, P.-O.: 2002, *Astrophys. J.* **564**, 302

Reynolds, S. P. and Moffett, D. A.: 1993, *Astron. J.* **105**, 2226

Rogstad, D. H., Lockhard, I. A., and Wright, M. C. H.: 1974, *Astrophys. J.* **193**, 309

Roye, E. W. and Hunter, D. A.: 2000, *Astron. J.* **119**, 1145

Saha, A., Sandage, A., Labhardt, L., Schwengeler, H., Tammann, G. A., Panagia, N., and Macchetto, F. D.: 1995, *Astrophys. J.* **438**, 8

Sakai, S. and Madore, B. F.: 1999, *Astrophys. J.* **526**, 599

Sandage, A., Saha, A., Tammann, G. A., Labhardt, L., Schwengeler, H., Panagia, N., and Macchetto, F. D.: 1994, *Astrophys. J. Letters,* **423**, L13

Sandage, A. and Tammann, G. A.: 1987, *A Revised Shapley-Ames Catalog of Bright Galaxies*, Carnegie Institution of Washington Publication, Washington: Carnegie Institution, 1987, 2nd ed.

Schneider, S. E., Thuan, T. X., Mangum, J. G., and Miller, J.: 1992, *Astrophys. J. Supp.* **81**, 5

Seaquist, E. R. and Bignell, R. C.: 1976, *Astron. & Astrophys.* **48**, 421

Sedov, L. I.: 1959, *Similarity and Dimensional Methods in Mechanics*, Academic Press, New York

Seward, F. D., Harnden, F. R. J., Murdin, P., and Clark, D. H.: 1983, *Astrophys. J.* **267**, 698

Smith, N.: 2002a, *M.N.R.A.S.* **337**, 1252

Smith, N.: 2002b, *M.N.R.A.S.* **336**, L22

Strickland, D. K. and Stevens, I. R.: 1999, *M.N.R.A.S.* **306**, 43

Tacconi, L. J. and Young, J. S.: 1985, *Astrophys. J.* **290**, 602

Taniguchi, Y., Kawara, K., Nishida, M., Tamura, S., and Nishida, M. T.: 1988, *Astron. J.* **95**, 1378

Taylor, C. L., Hüttemeister, S., Klein, U., and Greve, A.: 1999, *Astron. & Astrophys.* **349**, 424

Taylor, G. I.: 1950, *Proc. R. Soc. London A* **201**, 159

Thornton, K., Gaudlitz, M., Janka, H.-T., and Steinmetz, M.: 1998, *Astrophys. J.* **500**, 95

Tremonti, C. A., Calzetti, D., Leitherer, C., and Heckman, T. M.: 2001, *Astrophys. J.* **555**, 322

Turner, J. L., Ho, P. T. P., and Beck, S. C.: 1998, *Astrophys. J.* **116**, 1212

van den Bergh, S.: 1980, *Pub. Astron. Soc. Pacific,* **92**, 122

Vanzi, L. and Rieke, G. H.: 1997, *Astrophys. J.* **479**, 694

Waller, W. H.: 1991, *Astrophys. J.* **370**, 144

Walsh, J. R. and Roy, J.: 1989, *M.N.R.A.S.* **239**, 297

Wilner, D. J., Reynolds, S. P., and Moffett, D. A.: 1998, *Astron. J.* **115**, 247

Woltjer, L.: 1972, *Ann. Rev. Astron. & Astrophys.* **10**, 129

Woosley, S. E. and Weaver, T. A.: 1986, *Ann. Rev. Astron. & Astrophys.* **24**, 205

Appendix A

Data Reduction — Selection of Images

In this appendix, we present a selection of images illustrating the various steps of the data reduction. This will help the reader visualize the effect and the importance of the data preprocessing. These images complement the chapter on data reduction (Chapter 2) in which each step is discussed in details.

First, a sequence of science images is illustrating the effect of the preprocessing is presented (Figure A.1). Then, examples of the calibration images used in the preprocessing are shown (Figures A.2: Bad pixel mask, A.3: Dome flat, A.4: Blank sky field, and A.5: Illumination and fringe patterns).

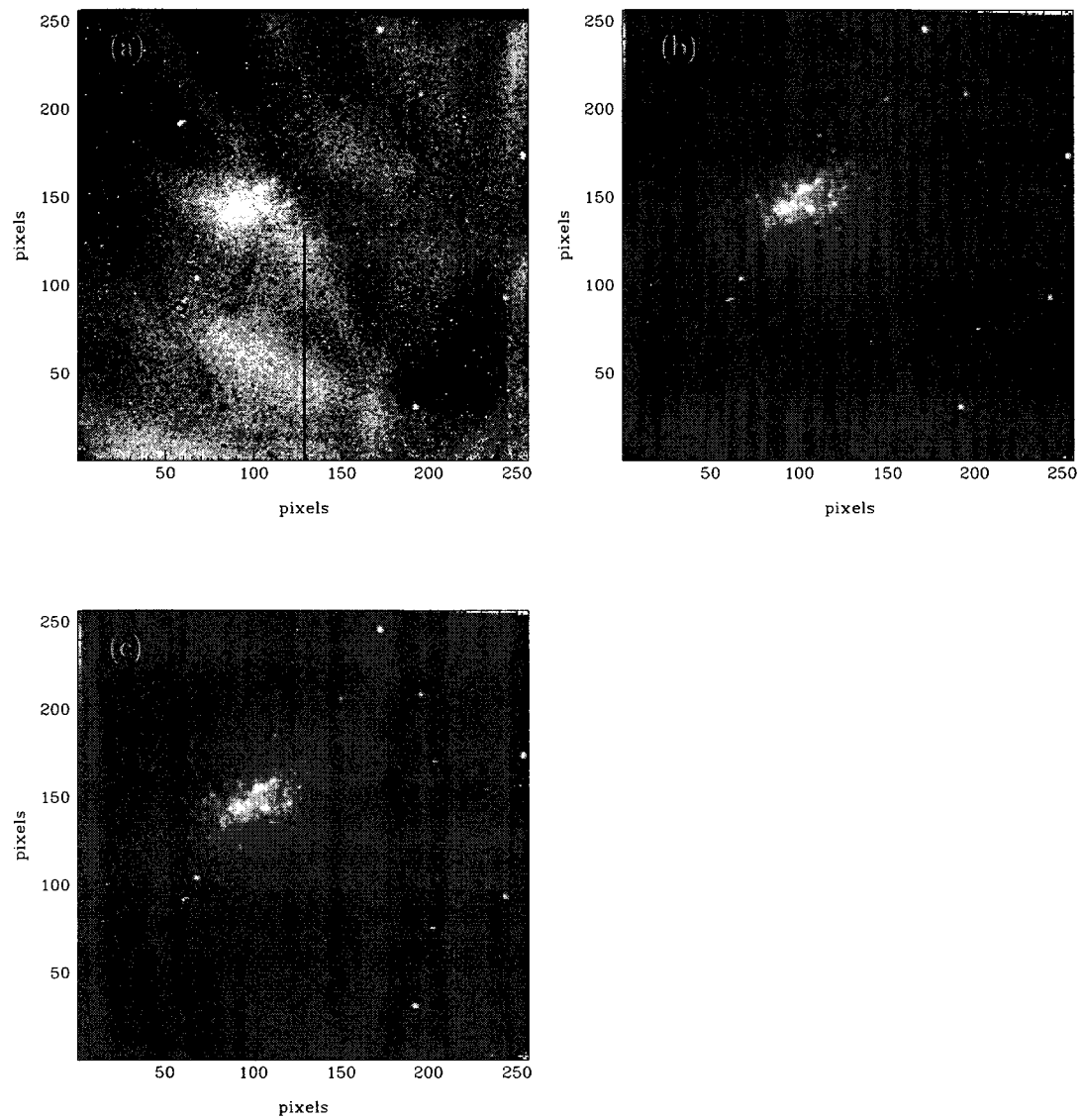

Figure A.1: Single narrow-band [Fe II] exposure of NGC 5253. This sequence shows the effect of the preprocessing of the raw images as described in Section 2.2.1. **(a)** No correction has been applied to this image. The pixel-to-pixel variation (flat-field) effect dominates the image: the galaxy is barely visible. **(b)** Corrected for dark current, bad pixels and flat-field. **(c)** Further corrected for illumination and fringing patterns.

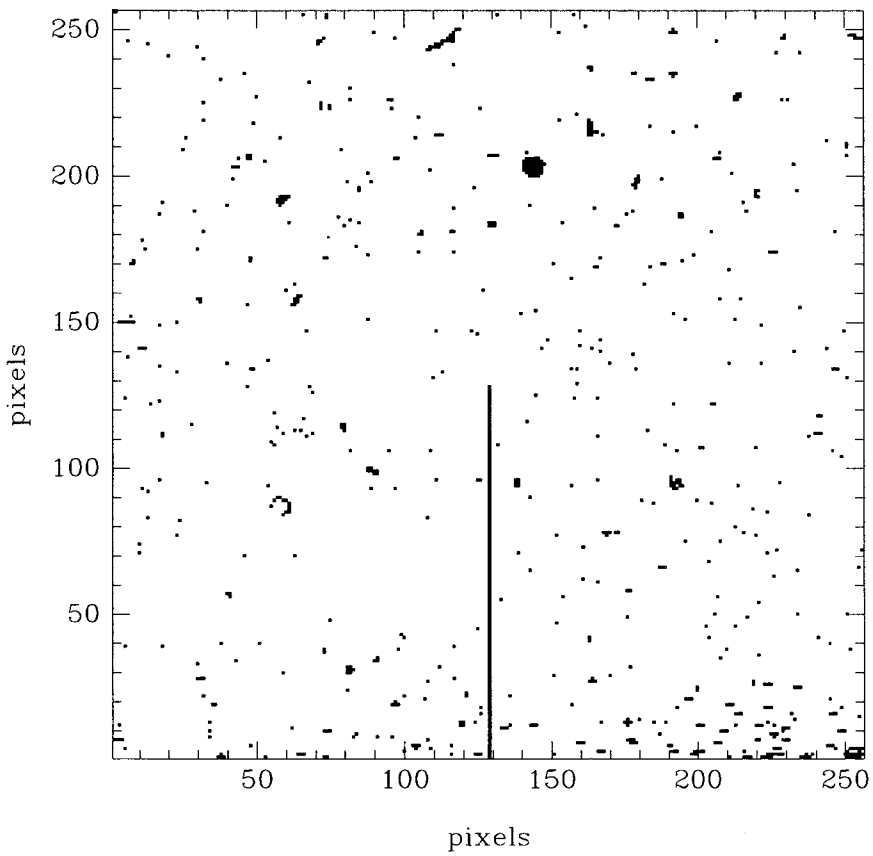

Figure A.2: Mask of the bad pixels found on the REDEYE camera.

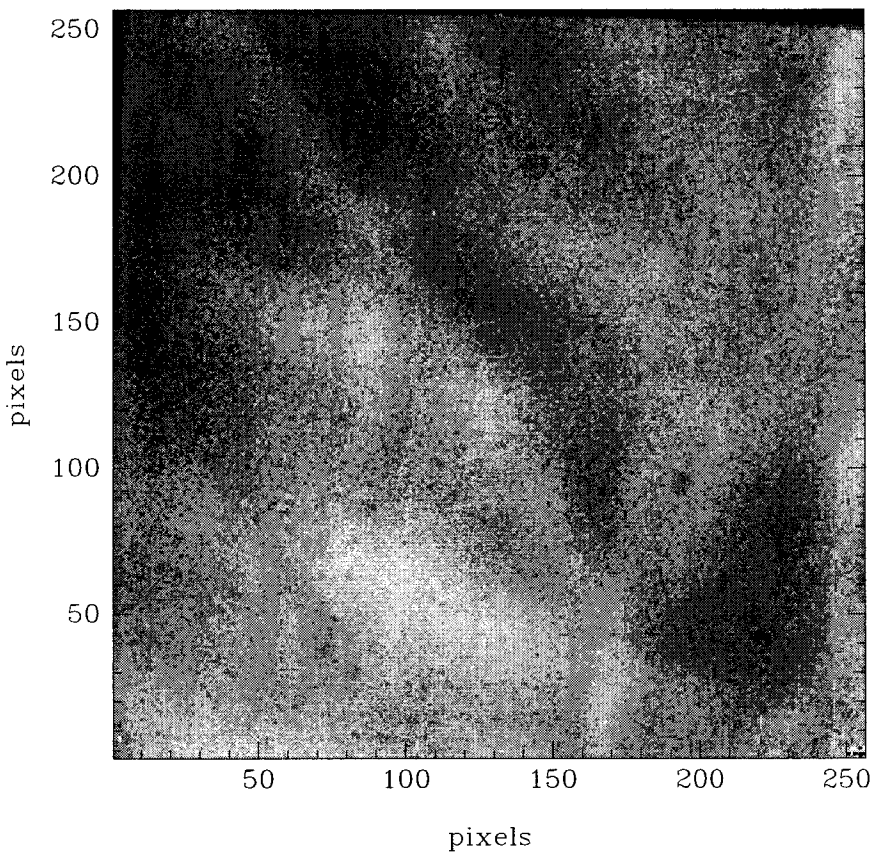

Figure A.3: Final dome flat field for the [Fe II] narrow-band filter. This image is used to correct the [Fe II] science images for the camera's pixel-to-pixel variation.

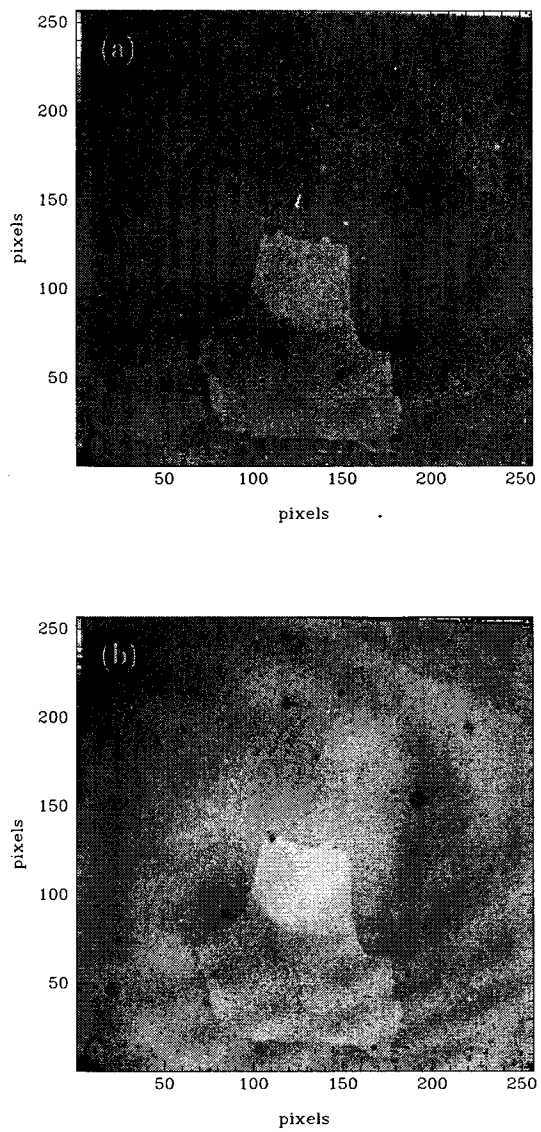

Figure A.4: Images of a blank sky field. **(a)** Single [Fe II] exposure of a blank sky field. This image has been corrected for dark current, bad pixels and pixel-to-pixel variation (flat-field). Only a handful of faint stars can be (barely) seen (e.g. at (140,170) and (235,180)). **(b)** [Fe II] blank sky flat field. This image is made of a series of dithered images of a field devoid of bright stars like the one shown in (a). This image was used to obtain the illumination and fringe pattern for the [Fe II] filter (Figure A.5).

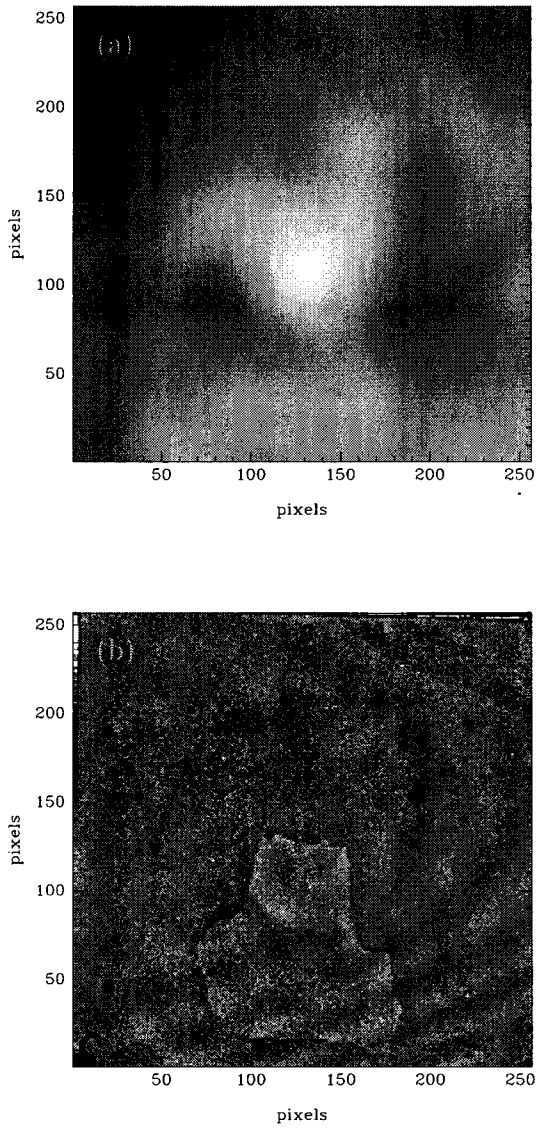

Figure A.5: Illumination and fringe patterns for the [Fe II] filter. These calibration images were obtained from the blank sky image shown in Figure A.4b. **(a)** Illumination pattern. **(b)** Fringe pattern. Along with the fringe pattern, a few remaining camera defects (e.g. dirt) show up. As it is shown in Figure A.1, the fringe image shown here is successful in correcting the fringe pattern as well as the defects (compare A.1b to A.1c).

Appendix B

Filters

Presented below are the warm and cool transmission curves for the RedeyeW filters that were used in this work. The warm transmission curves are actual scans made at 293 K. The cool transmission curves were calculated from the warm curves assuming a blueward shift of 0.004%/°C (Canada-France-Hawaii Telescope website, maintained by Todd Szarlan). The cool transmission curves are calculated for 77 K, the operating temperature of the Redeye camera.

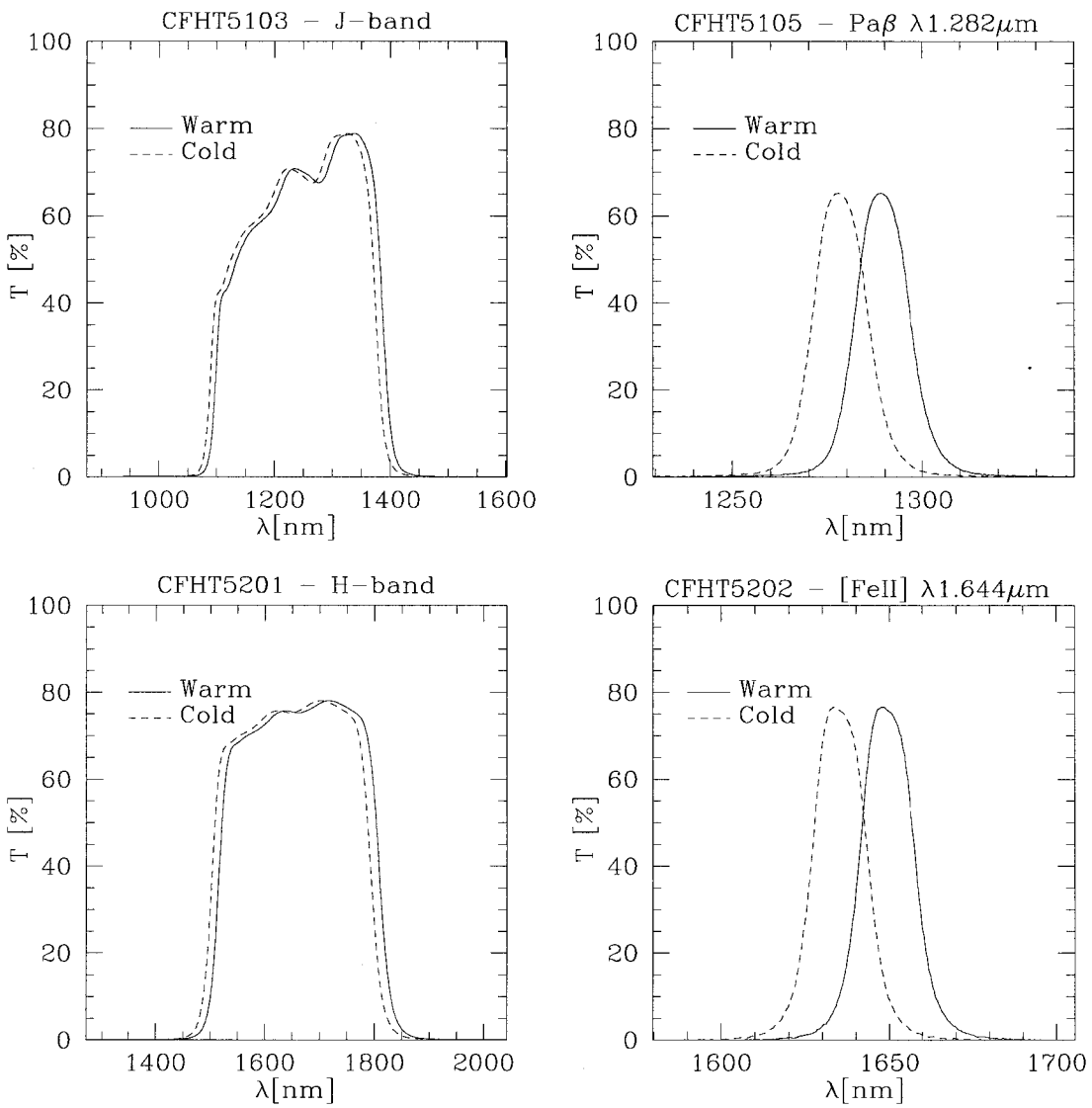

Figure B.1: Transmission curves of the RedeyeW filters.

Appendix C

Plates — [Fe II] Sources

In this appendix are presented the images of the compact [Fe II] sources detected in NGC 1569 and NGC 5253. Each source is described and discussed in Chapter 3, specifically Sections 3.2.2 for NGC 1569, and 3.4.2 for NGC 5253.

C.1 Details Regarding the Figures

Common characteristics

For each thumbnail image, the contrast has been adjusted to show as much flux and morphological information as possible. Care was taken to emphasize the presence, or the absence, of a continuum or Paβ source coincident with the [Fe II] source.

For reference, the upper left panel offers a wider field of view, in the light of the [Fe II] emission line, overlaid with a scaled box centred on the source.

All images have the orientation given by the compass in the upper right panel. The celestial coordinates are the coordinates of the [Fe II] source. The lower four panels are centred on these coordinates within half a pixel.

The plate scale of the RedeyeW camera is 0.5″/pixel.

NGC 1569

The field of view of the [Fe II] wide field image is 70″×70″. The section was taken out of a mosaic of three images: Fields 1 and 2, and the deep central field (see Table 2.4). The blank areas in the centre of the galaxy are regions saturated by the light of bright star clusters. The white rectangle in the North-West corner corresponds to an area that has not been observed. The epoch of the coordinates is *J2000.*

The field of view of each of the lower four panels is 12.5″×12.5″, centred on the [Fe II] source's position. At the adopted distance to NGC 1569 (2.5 Mpc, see Section 3.2.1), 1 arc second corresponds to 12.1 pc.

The contours are expressed in multiples of the standard deviation of the sky background, σ, and represent the flux above the sky background. For the continuum subtracted [Fe II] images, $\sigma = (10, 3, 5.5)$ ADU for Fields 1, 2, and Central, respectively, or, in physical units, $\sigma = 19. \times 10^{-21}\,\mathrm{Wm}^{-2}$, $\sigma = 5.8 \times 10^{-21}\,\mathrm{Wm}^{-2}$, and $\sigma = 11. \times 10^{-21}\,\mathrm{Wm}^{-2}$.

NGC 5253

The field of view of the [Fe II] wide field image, a section of the NGC 5253 Field 1, is 60″×60″. The epoch of the coordinates is *J2000.* The field of view of each of the lower four panels is 12.5″×12.5″, centred on the [Fe II] source's position. At the adopted distance to NGC 5253 (3.33 Mpc, see Section 3.4.1), 1 arc second corresponds to 16.1 pc.

The contours are expressed in multiples of the standard deviation of the sky background, σ, and represent the flux above the sky background. For the continuum subtracted [Fe II] image of NGC 5253, $\sigma = 4$ ADU, or $\sigma = 7.7 \times 10^{-21}\,\mathrm{Wm}^{-2}$. Note that for some sources, the contours are not evenly spaced. In those cases, tighter contours seemed necessary to better illustrate the morphology of the [Fe II] line emission.

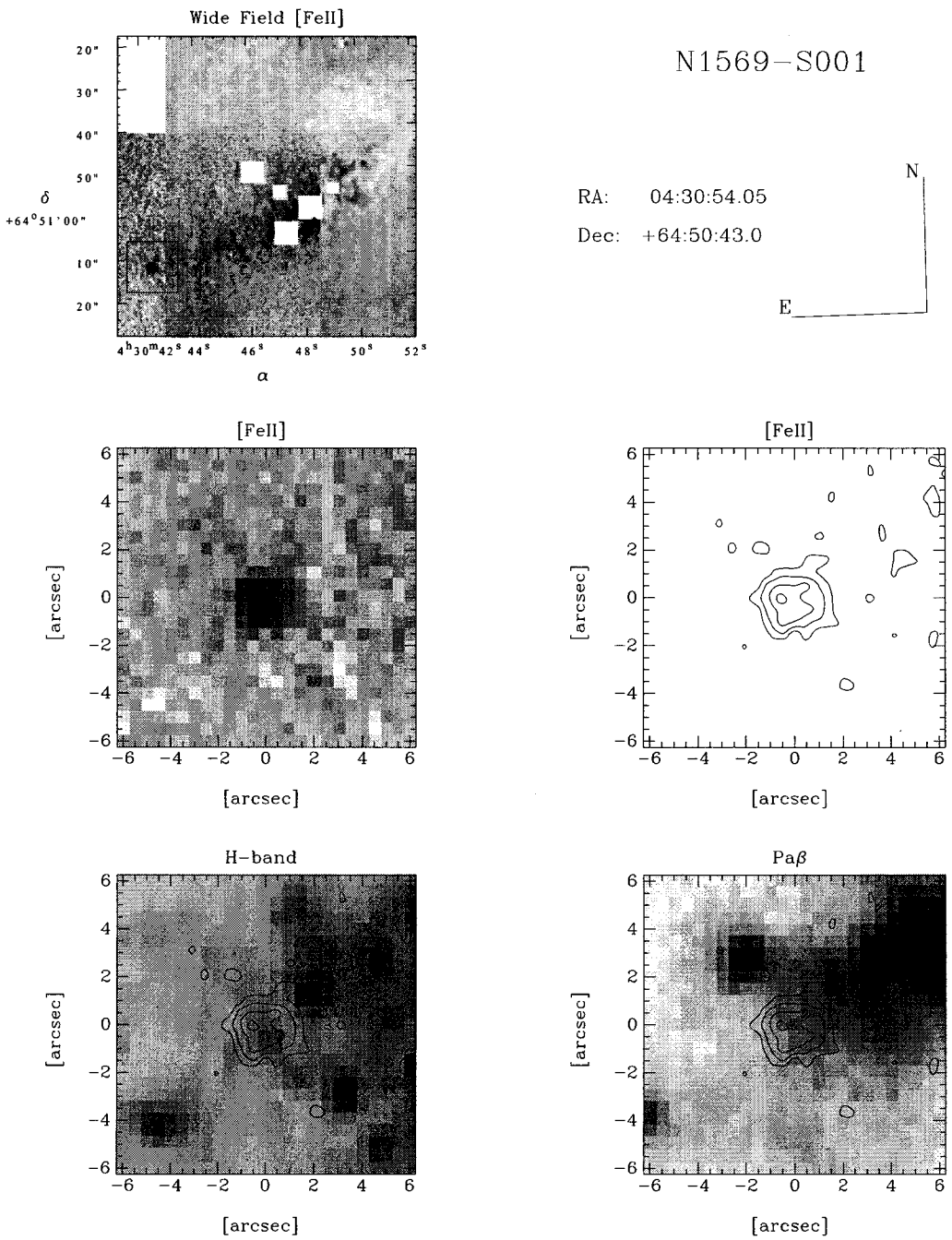

Figure C.1: Comparison of the [Fe II] λ1.644 μm image and contour map of N1569-S001 with the H-band and Paβ λ1.282 μm images. The contours are drawn from 3σ to 9σ, with steps of 2σ. Refer to Section C.1 for more details.

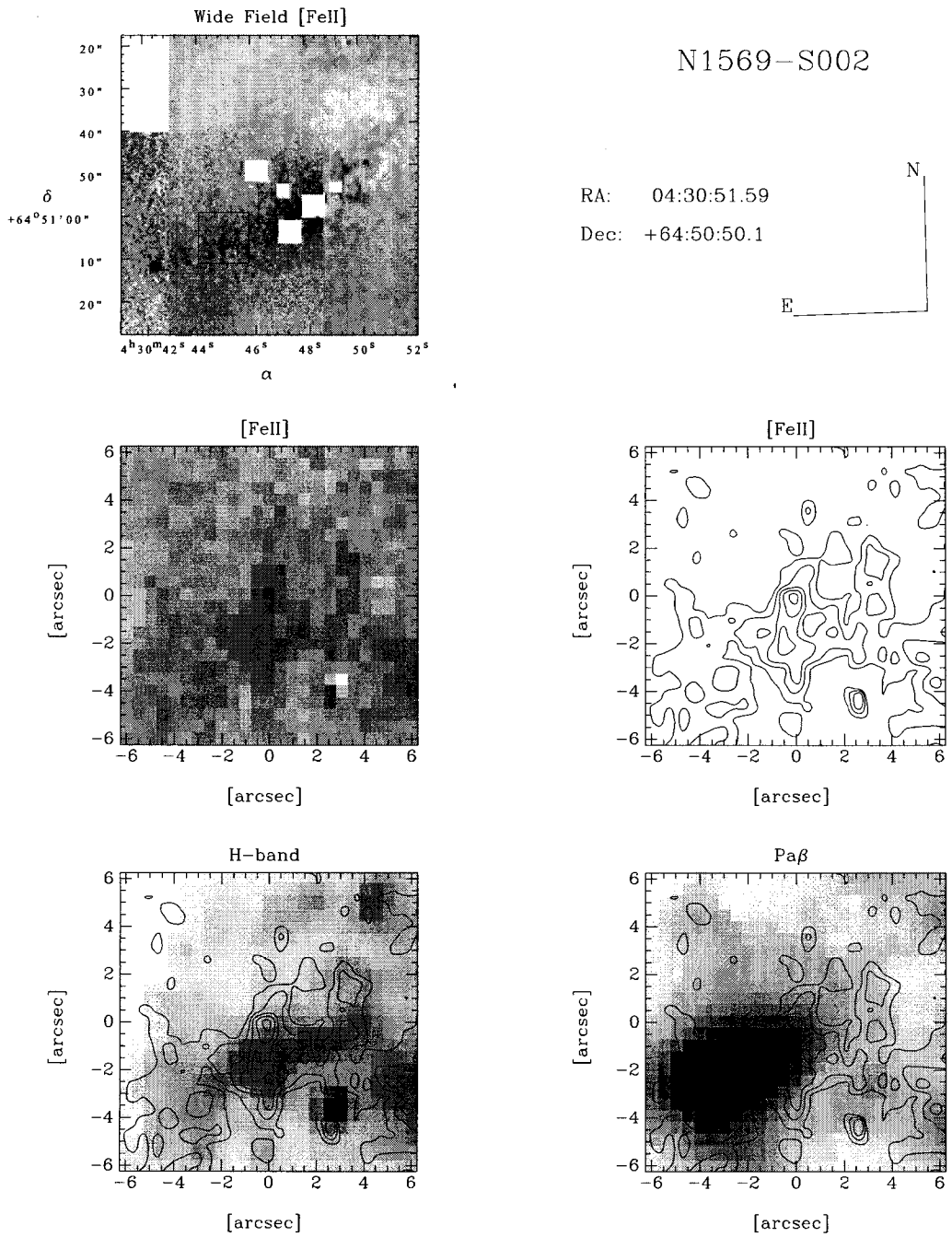

Figure C.2: Comparison of the [Fe II] λ1.644 μm image and contour map of N1569-S002 with the H-band and Paβ λ1.282 μm images. The contours are drawn from 4σ to 12σ, with steps of 2σ. Refer to Section C.1 for more details.

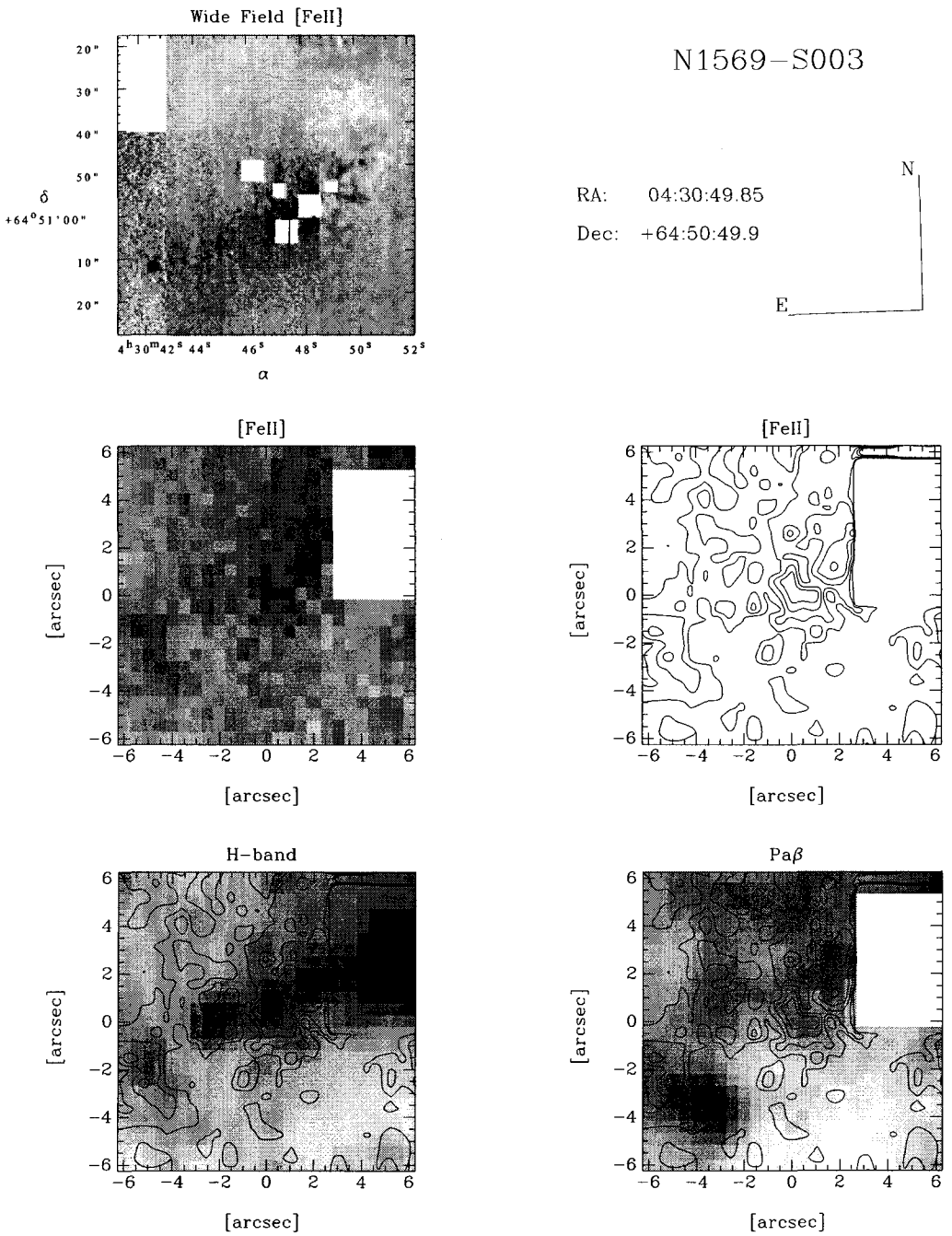

Figure C.3: Comparison of the [Fe II] $\lambda 1.644\ \mu$m image and contour map of N1569-S003 with the H-band and Paβ $\lambda 1.282\ \mu$m images. The contours are drawn from 4σ to 12σ, with steps of 2σ. Refer to Section C.1 for more details.

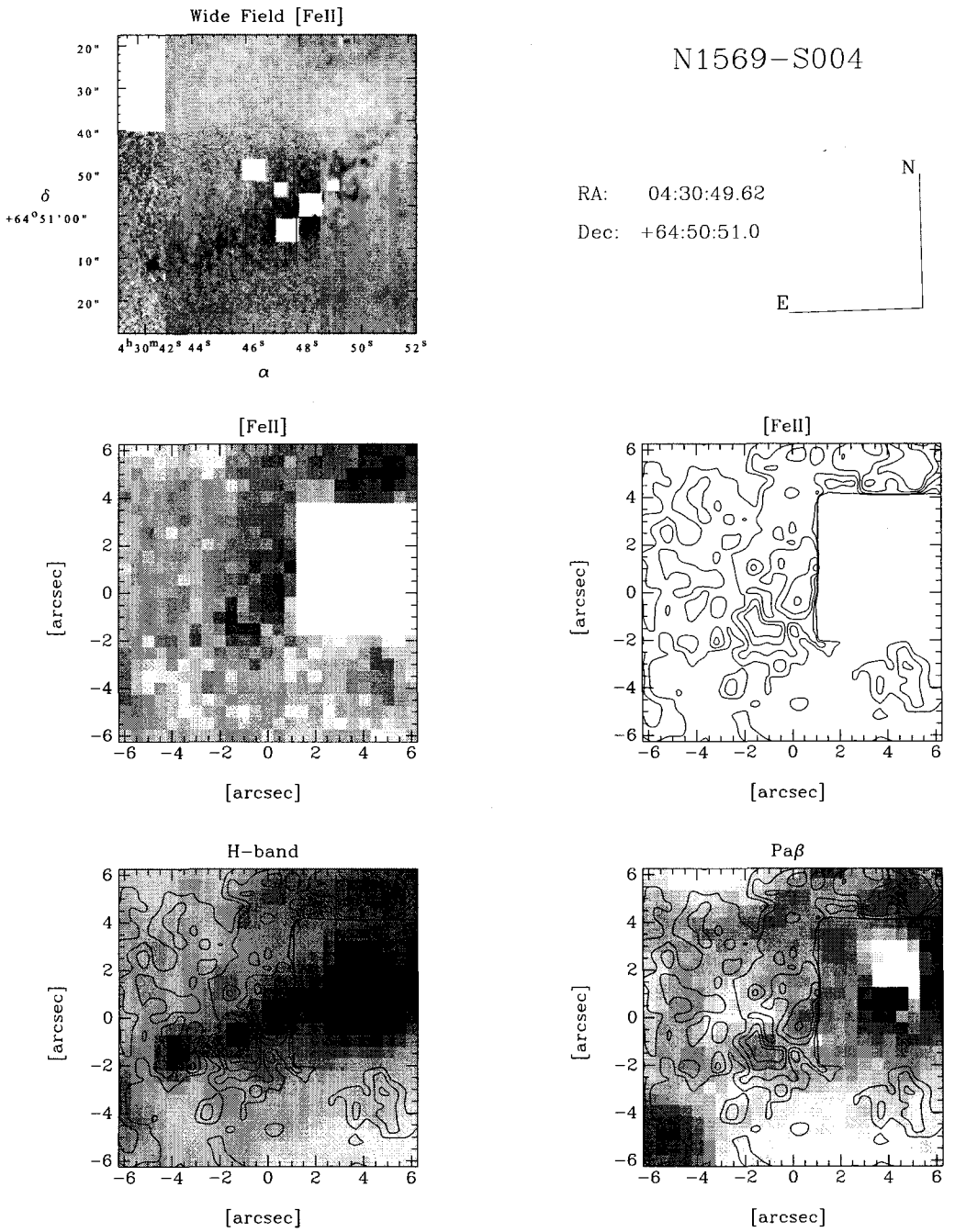

Figure C.4: Comparison of the [Fe II] λ1.644 μm image and contour map of N1569-S004 with the H-band and Paβ λ1.282 μm images. The contours are drawn from 4σ to 12σ, with steps of 2σ. Refer to Section C.1 for more details.

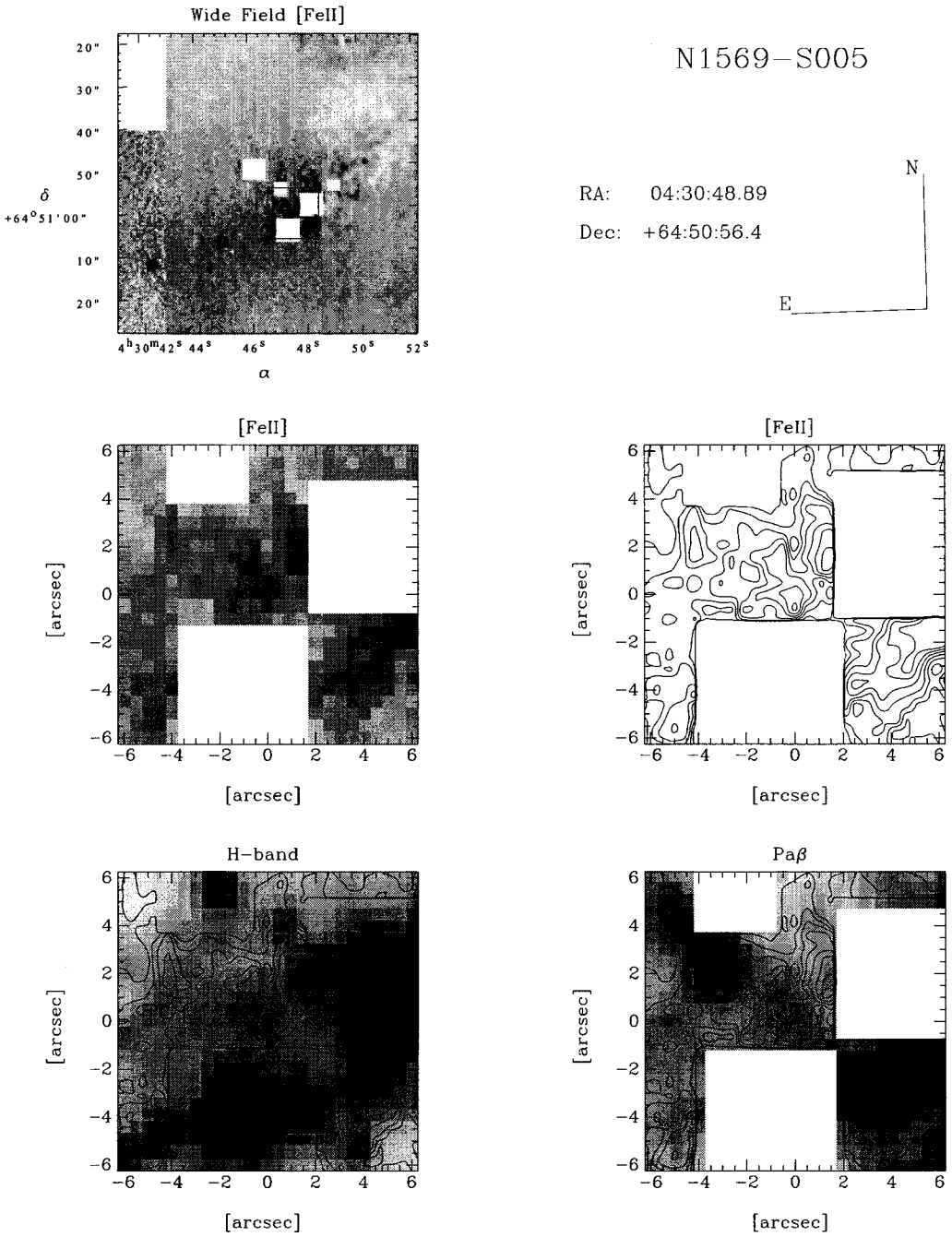

Figure C.5: Comparison of the [Fe II] λ1.644 μm image and contour map of N1569-S005 with the H-band and Paβ λ1.282 μm images. The contours are drawn from 4σ to 16σ, with steps of 2σ. Refer to Section C.1 for more details.

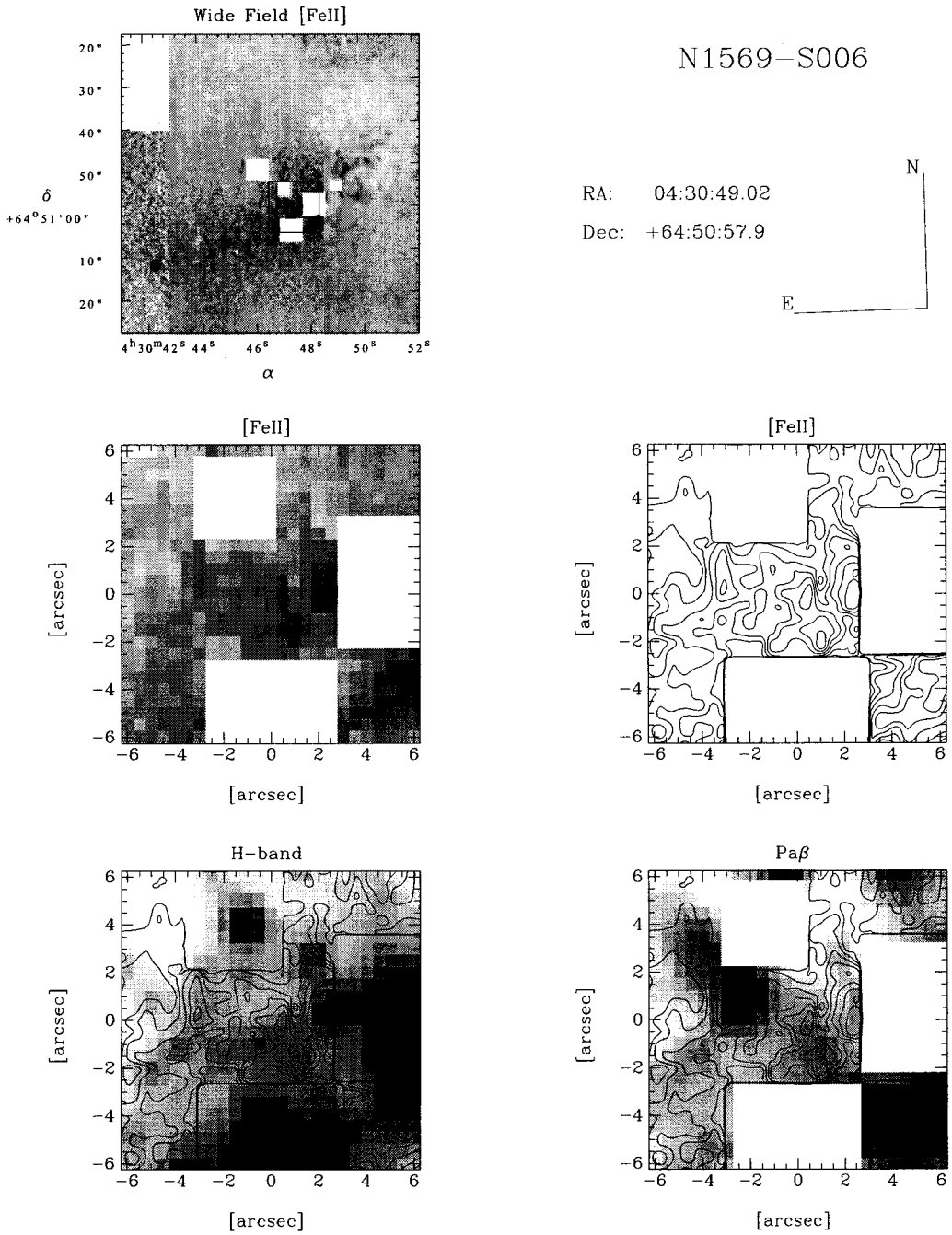

Figure C.6: Comparison of the [Fe II] $\lambda 1.644\ \mu$m image and contour map of N1569-S006 with the H-band and Paβ $\lambda 1.282\ \mu$m images. The contours are drawn from 3σ to 15σ, with steps of 2σ. Refer to Section C.1 for more details.

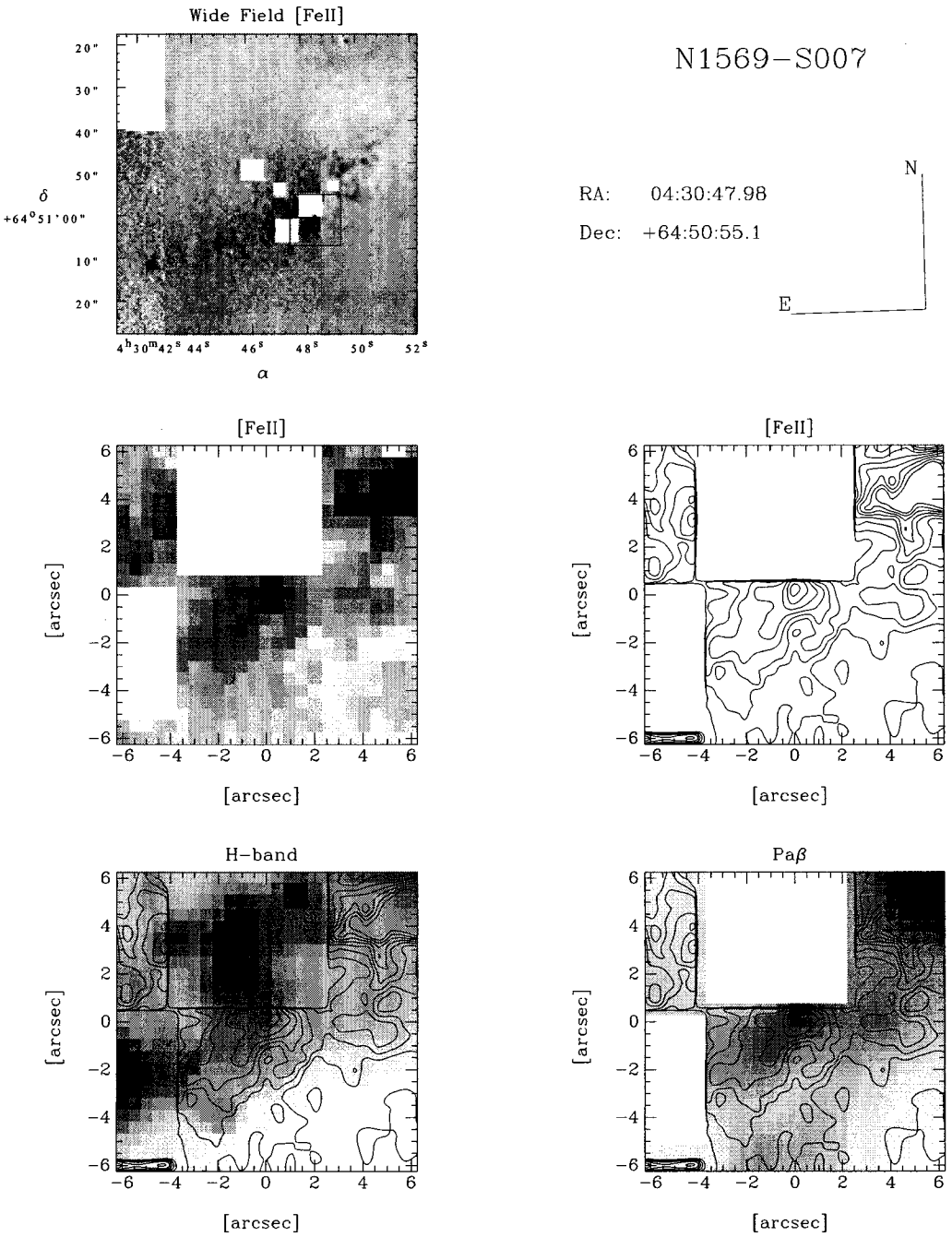

Figure C.7: Comparison of the [Fe II] λ1.644 μm image and contour map of N1569-S007 with the H-band and Paβ λ1.282 μm images. The contours are drawn from 3σ to 24σ, with steps of 3σ. Refer to Section C.1 for more details.

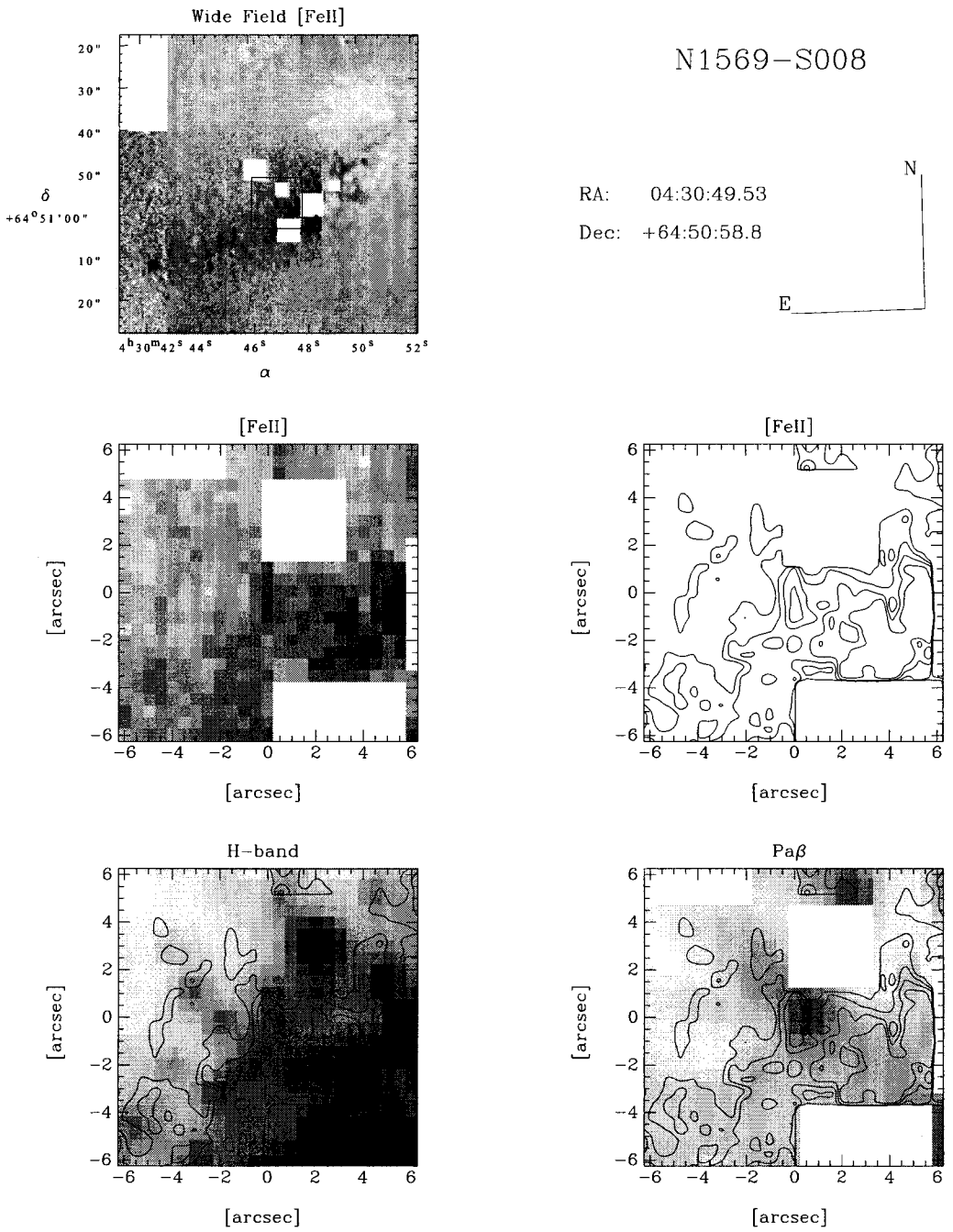

Figure C.8: Comparison of the [Fe II] λ1.644 μm image and contour map of N1569-S008 with the H-band and Paβ λ1.282 μm images. The contours are drawn from 4σ to 10σ, with steps of 2σ. Refer to Section C.1 for more details.

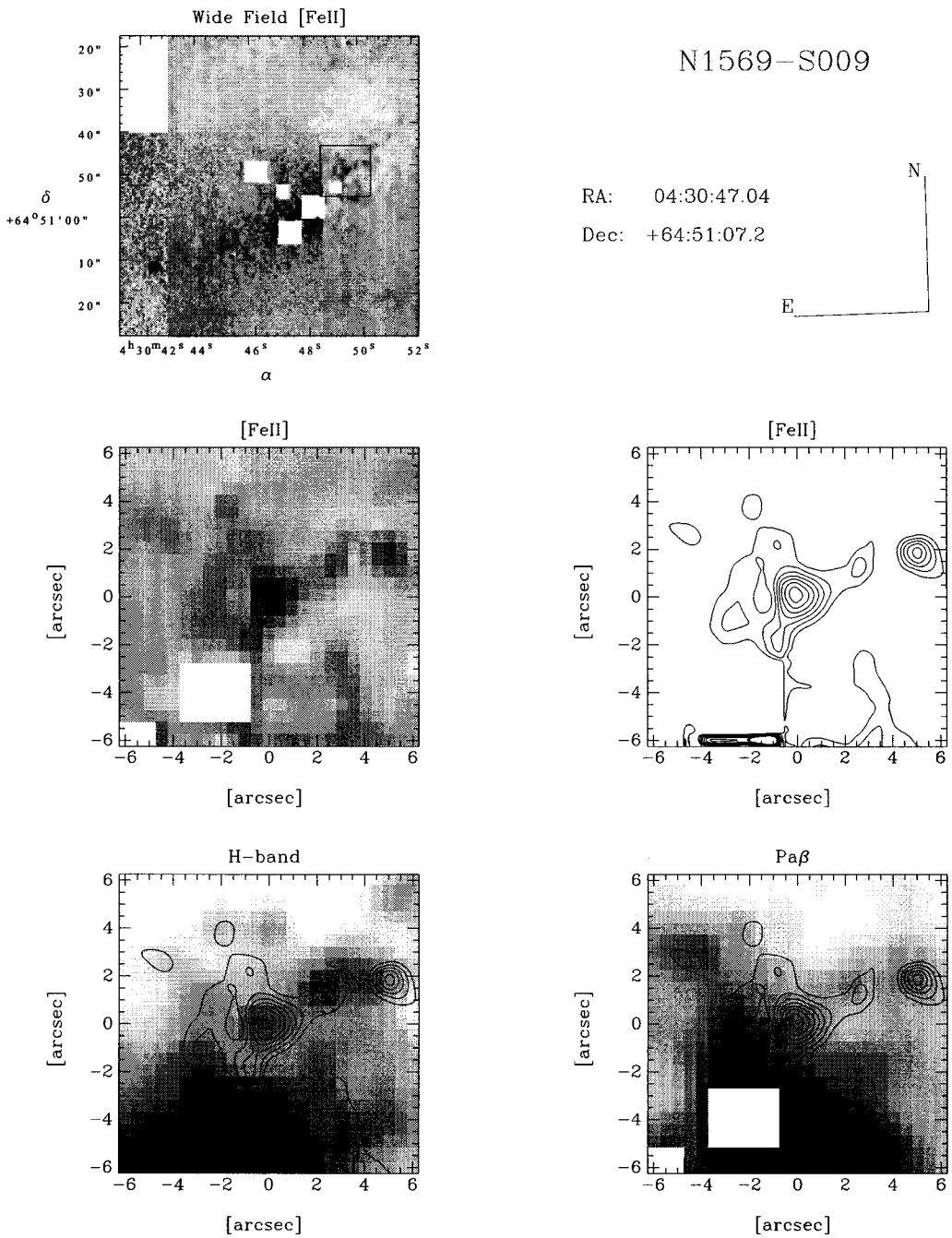

Figure C.9: Comparison of the [Fe II] λ1.644 μm image and contour map of N1569-S009 with the H-band and Paβ λ1.282 μm images. The contours are drawn from 3σ to 21σ, with steps of 3σ. Refer to Section C.1 for more details.

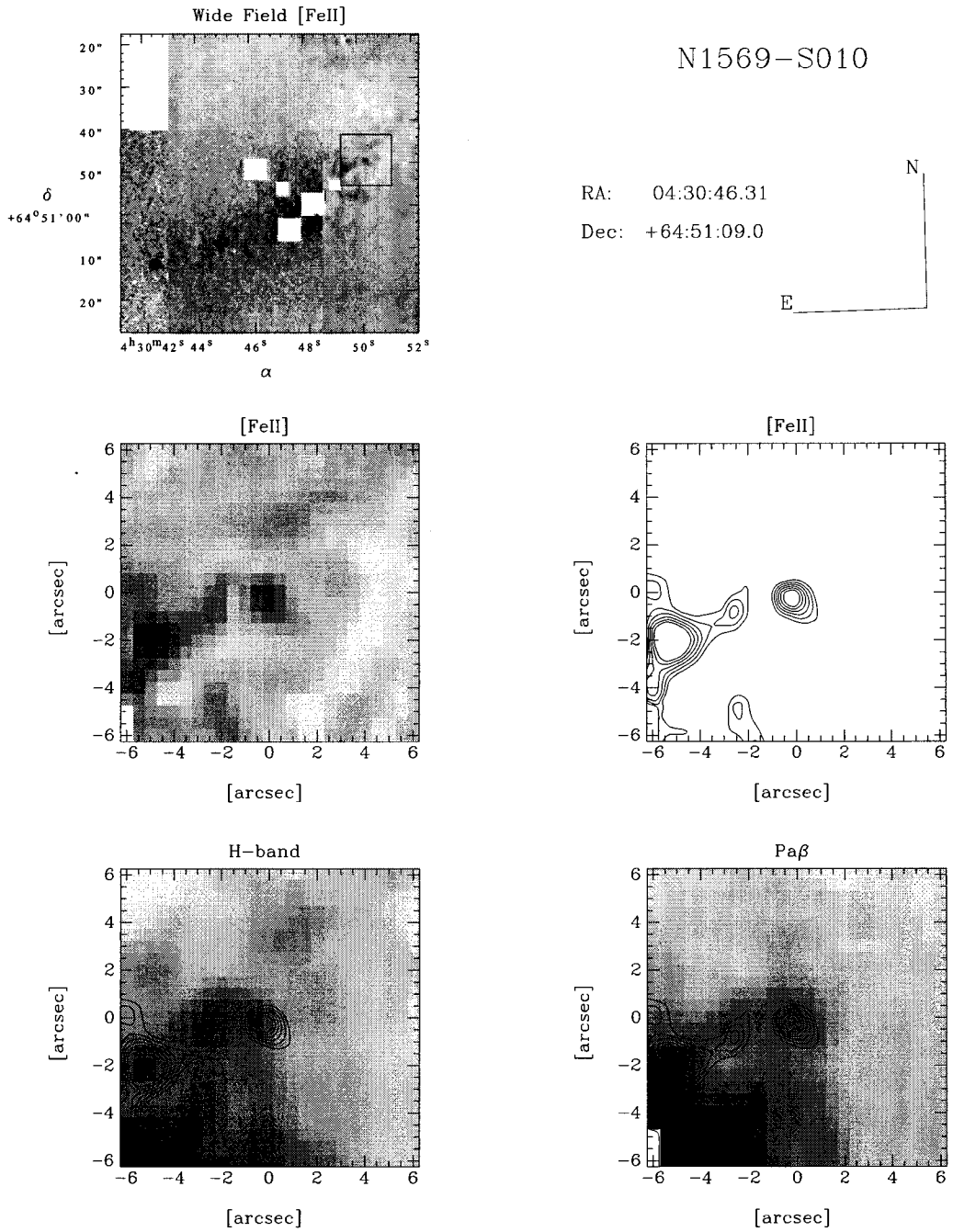

Figure C.10: Comparison of the [Fe II] λ1.644 μm image and contour map of N1569-S010 with the H-band and Paβ λ1.282 μm images. The contours are drawn from 3σ to 13σ, with steps of 2σ. Refer to Section C.1 for more details.

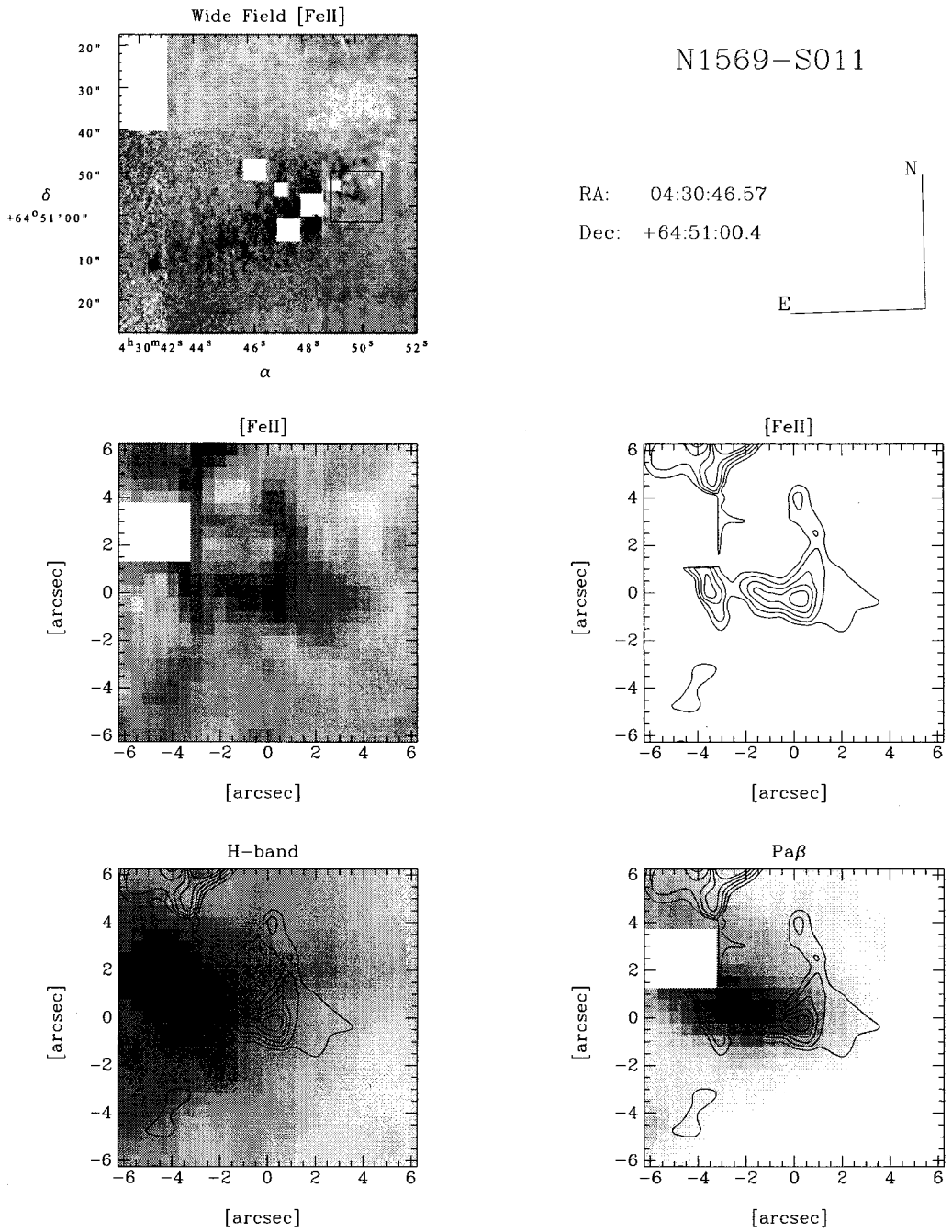

Figure C.11: Comparison of the [Fe II] $\lambda 1.644\ \mu$m image and contour map of N1569-S011 with the H-band and Paβ $\lambda 1.282\ \mu$m images. The contours are drawn from 3σ to 11σ, with steps of 2σ. Refer to Section C.1 for more details.

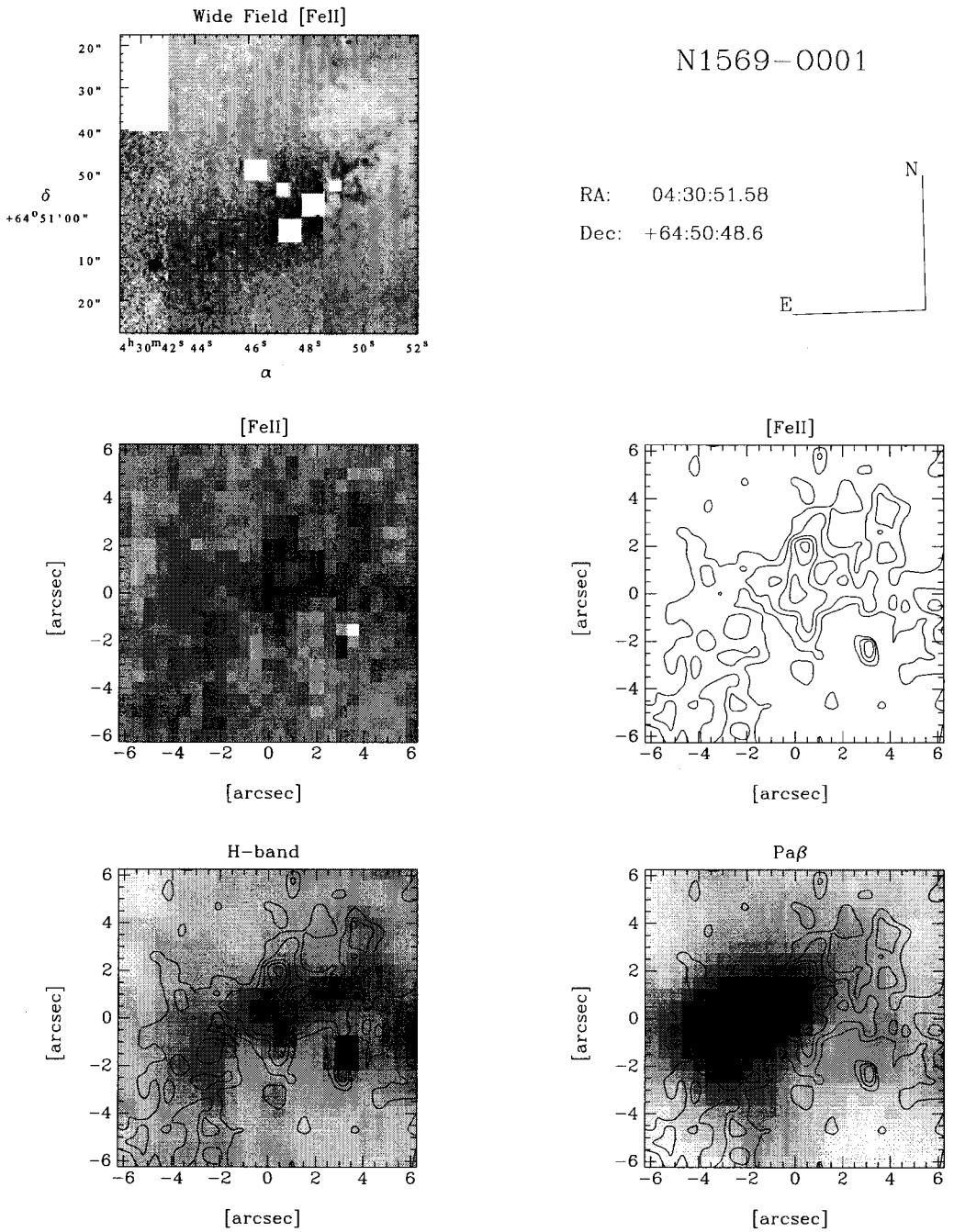

Figure C.12: Comparison of the [Fe II] λ1.644 μm image and contour map of N1569-O001 with the H-band and Paβ λ1.282 μm images. The contours are drawn from 4σ to 12σ, with steps of 2σ. Refer to Section C.1 for more details.

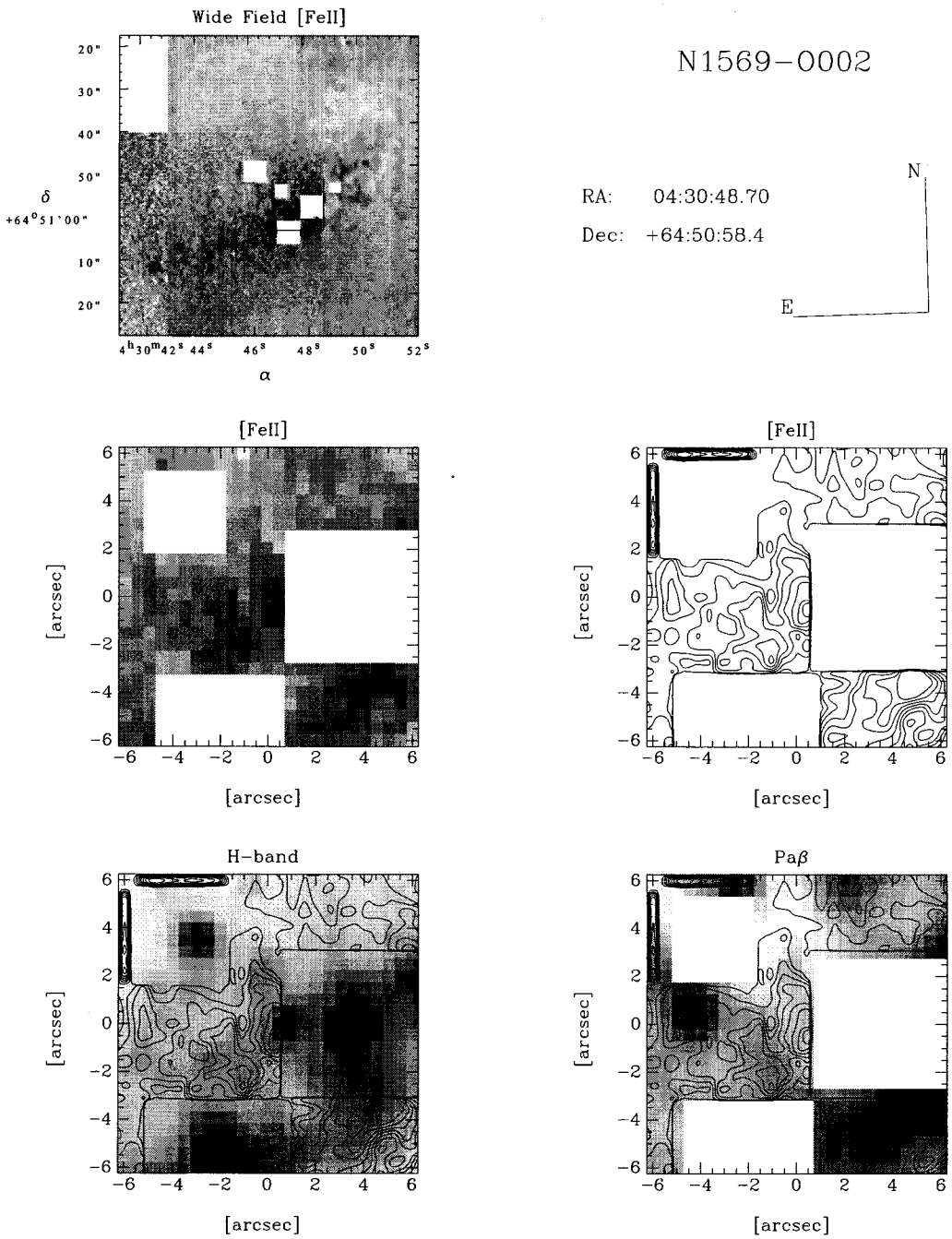

Figure C.13: Comparison of the [Fe II] λ1.644 μm image and contour map of N1569-O002 with the H-band and Paβ λ1.282 μm images. The contours are drawn from 4σ to 18σ, with steps of 2σ. Refer to Section C.1 for more details.

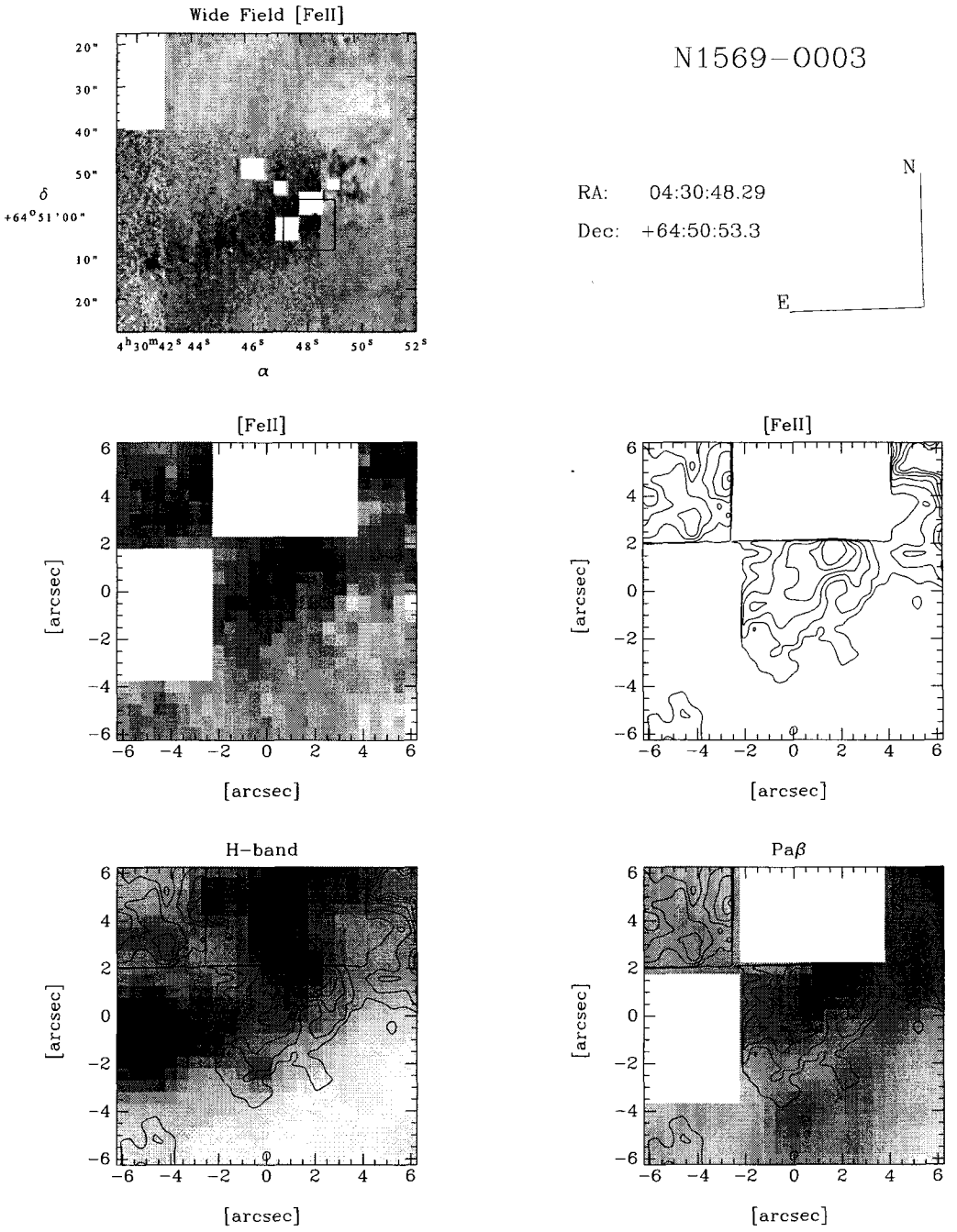

Figure C.14: Comparison of the [Fe II] λ1.644 μm image and contour map of N1569-O003 with the H-band and Paβ λ1.282 μm images. The contours are drawn from 4σ to 19σ, with steps of 3σ. Refer to Section C.1 for more details.

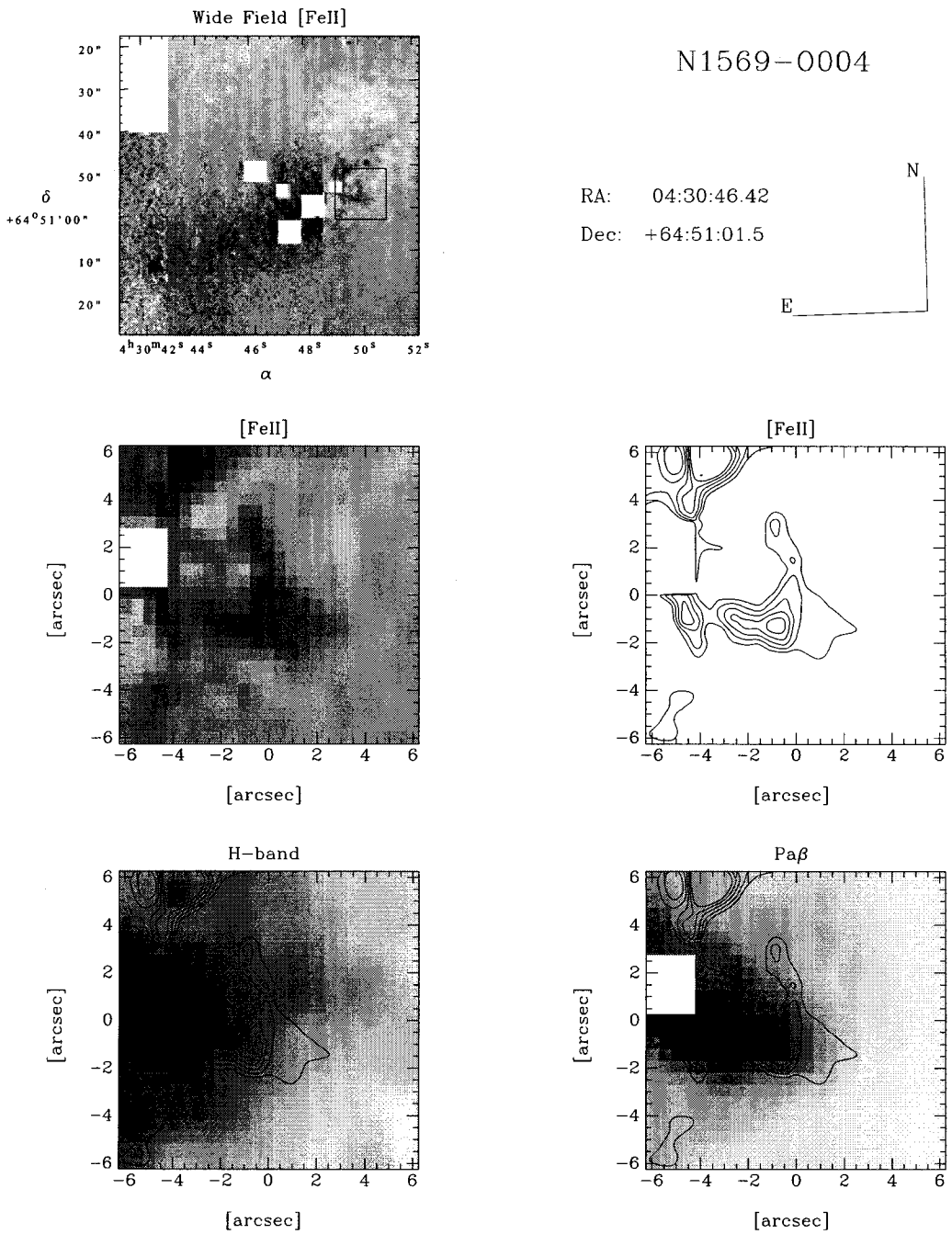

Figure C.15: Comparison of the [Fe II] $\lambda 1.644\ \mu$m image and contour map of N1569-O004 with the H-band and Paβ $\lambda 1.282\ \mu$m images. The contours are drawn from 3σ to 11σ, with steps of 2σ. Refer to Section C.1 for more details.

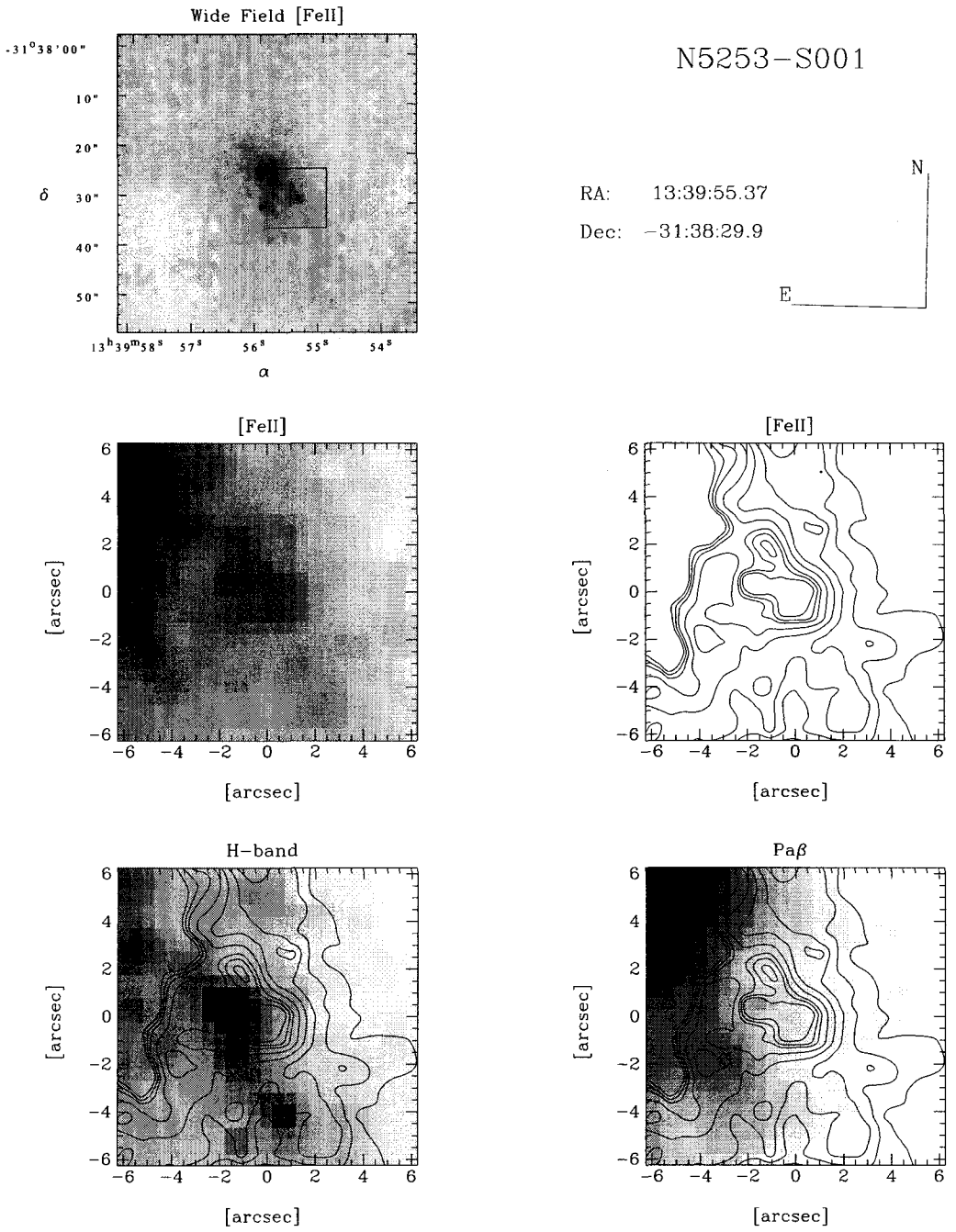

Figure C.16: Comparison of the [Fe II] λ1.644 μm image and contour map of N5253-S001 with the H-band and Paβ λ1.282 μm images. The contours are drawn for 3, 5, 7, 9, 11, 13, 14, 15 σ. Refer to Section C.1 for more details.

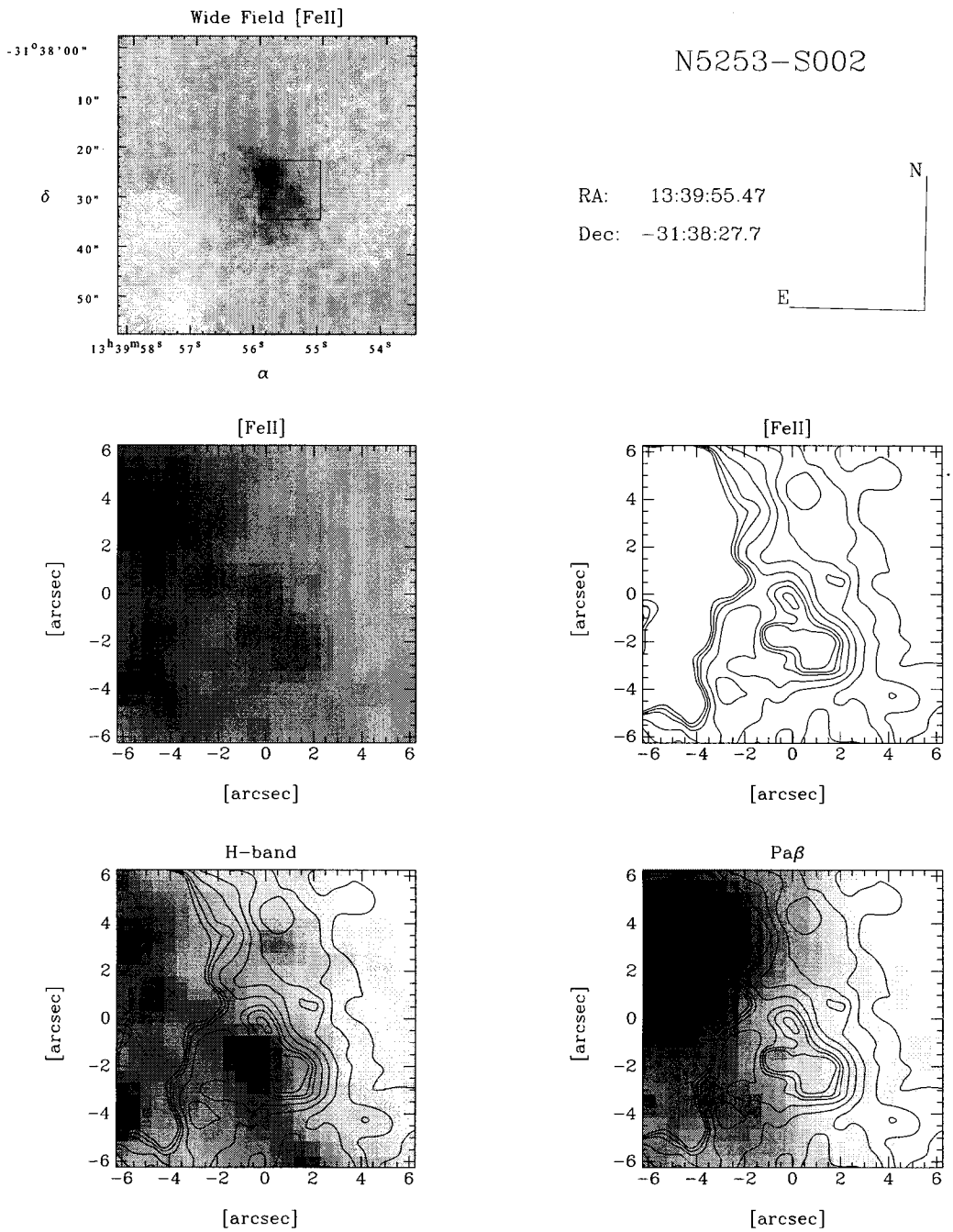

Figure C.17: Comparison of the [Fe II] λ1.644 μm image and contour map of N5253-S002 with the H-band and Paβ λ1.282 μm images. The contours are drawn for 3, 5, 7, 9, 11, 13, 14, 15σ. Refer to Section C.1 for more details.

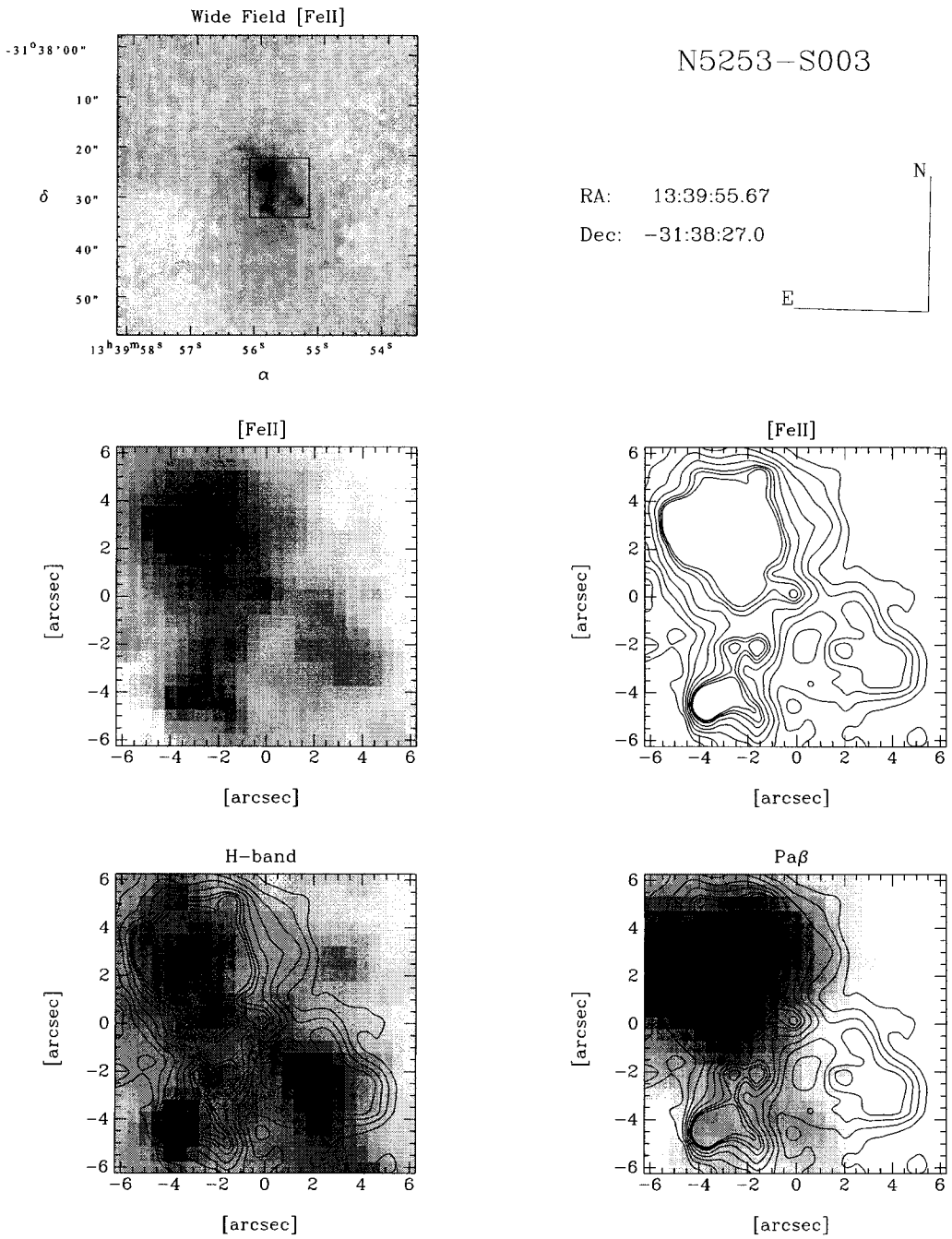

Figure C.18: Comparison of the [Fe II] λ1.644 μm image and contour map of N5253-S003 with the H-band and Paβ λ1.282 μm images. The contours are drawn for 8, 10, 12, 14, 16, 18, 19, 20 σ. Refer to Section C.1 for more details.

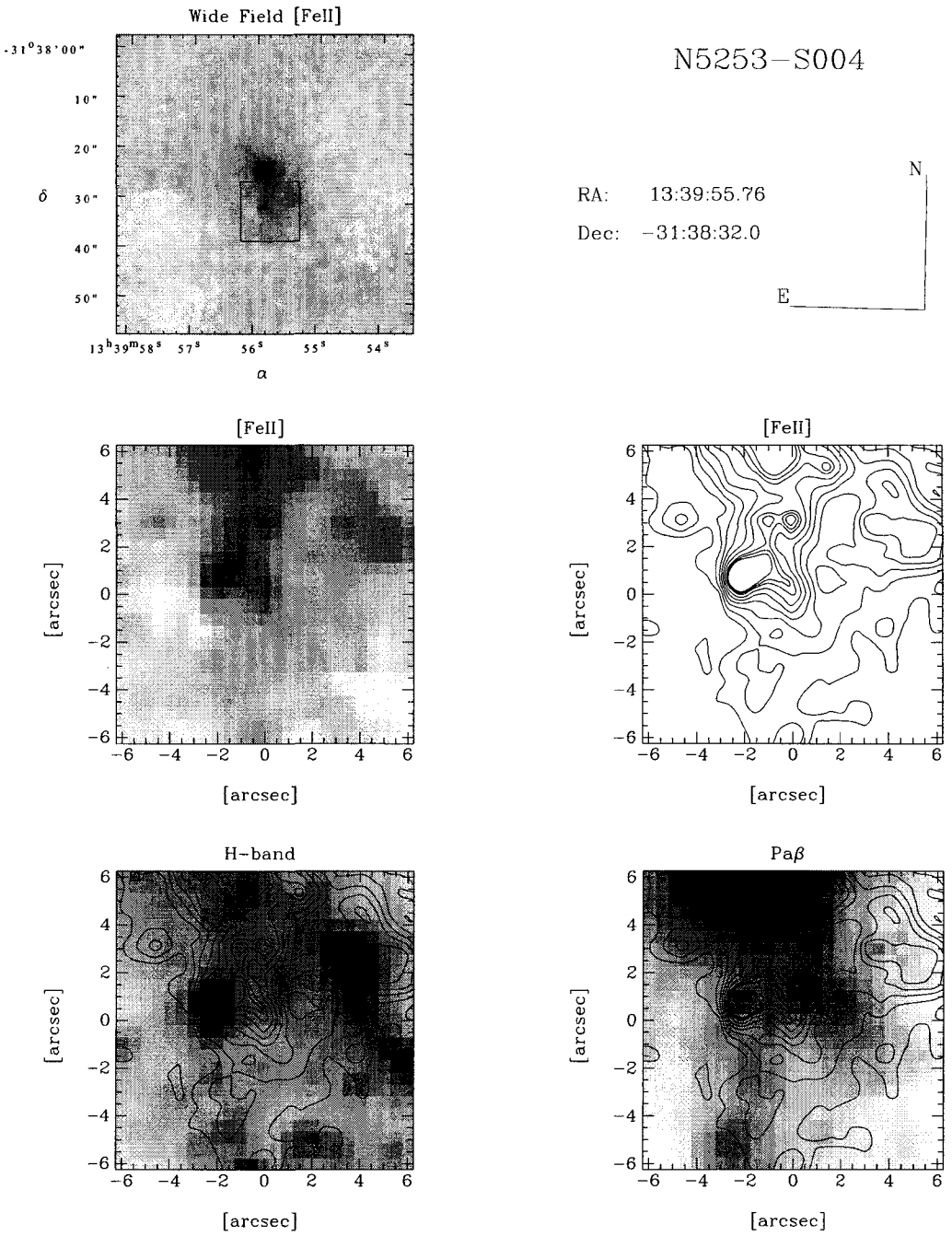

Figure C.19: Comparison of the [Fe II] λ1.644 μm image and contour map of N5253-S004 with the H-band and Paβ λ1.282 μm images. The contours are drawn for 7, 9, 11, 13, 15, 17, 19, 20, 21 σ. Refer to Section C.1 for more details.

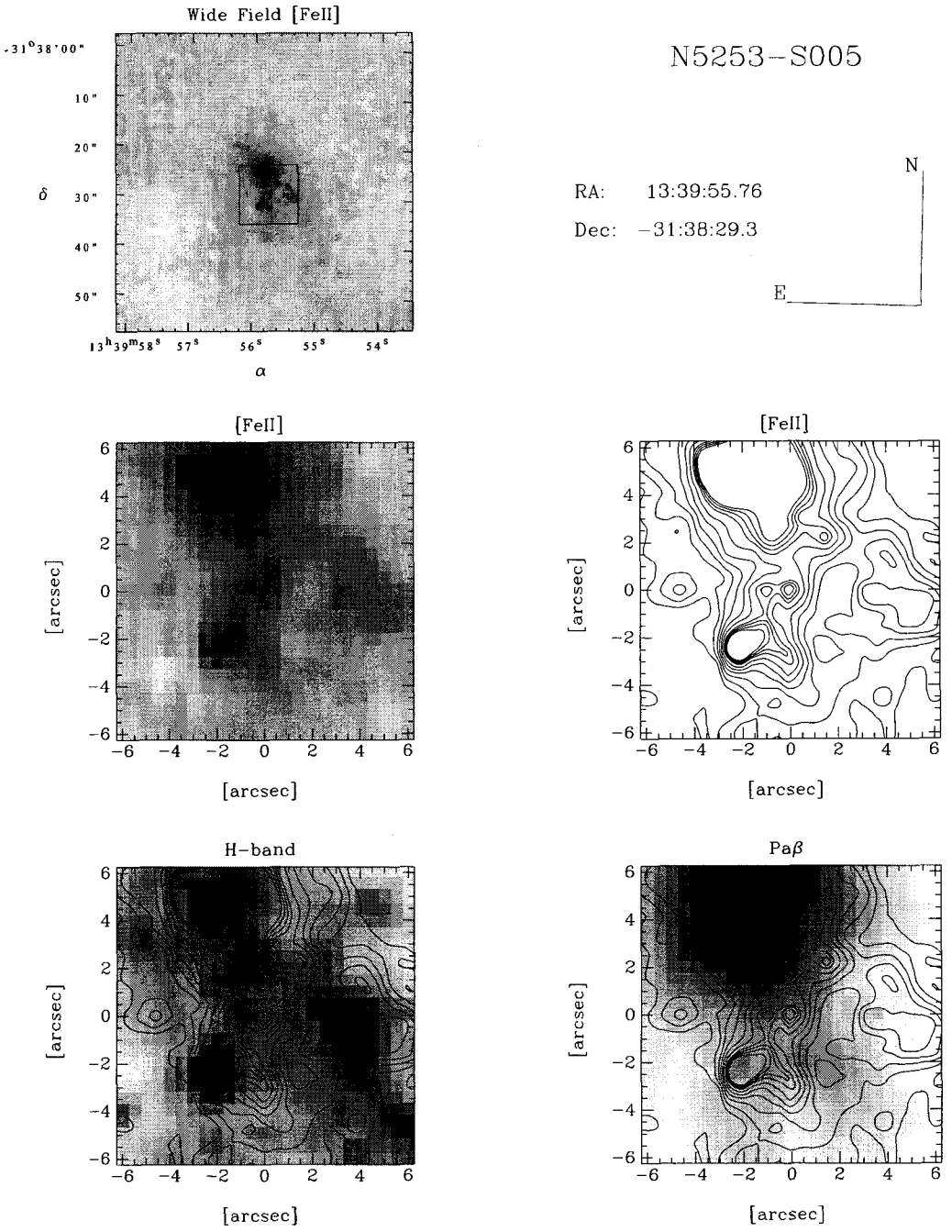

Figure C.20: Comparison of the [Fe II] $\lambda 1.644\ \mu$m image and contour map of N5253-S005 with the H-band and Paβ $\lambda 1.282\ \mu$m images. The contours are drawn for 7, 9, 11, 13, 15, 17, 19, 20, 21, 22 σ. Refer to Section C.1 for more details.

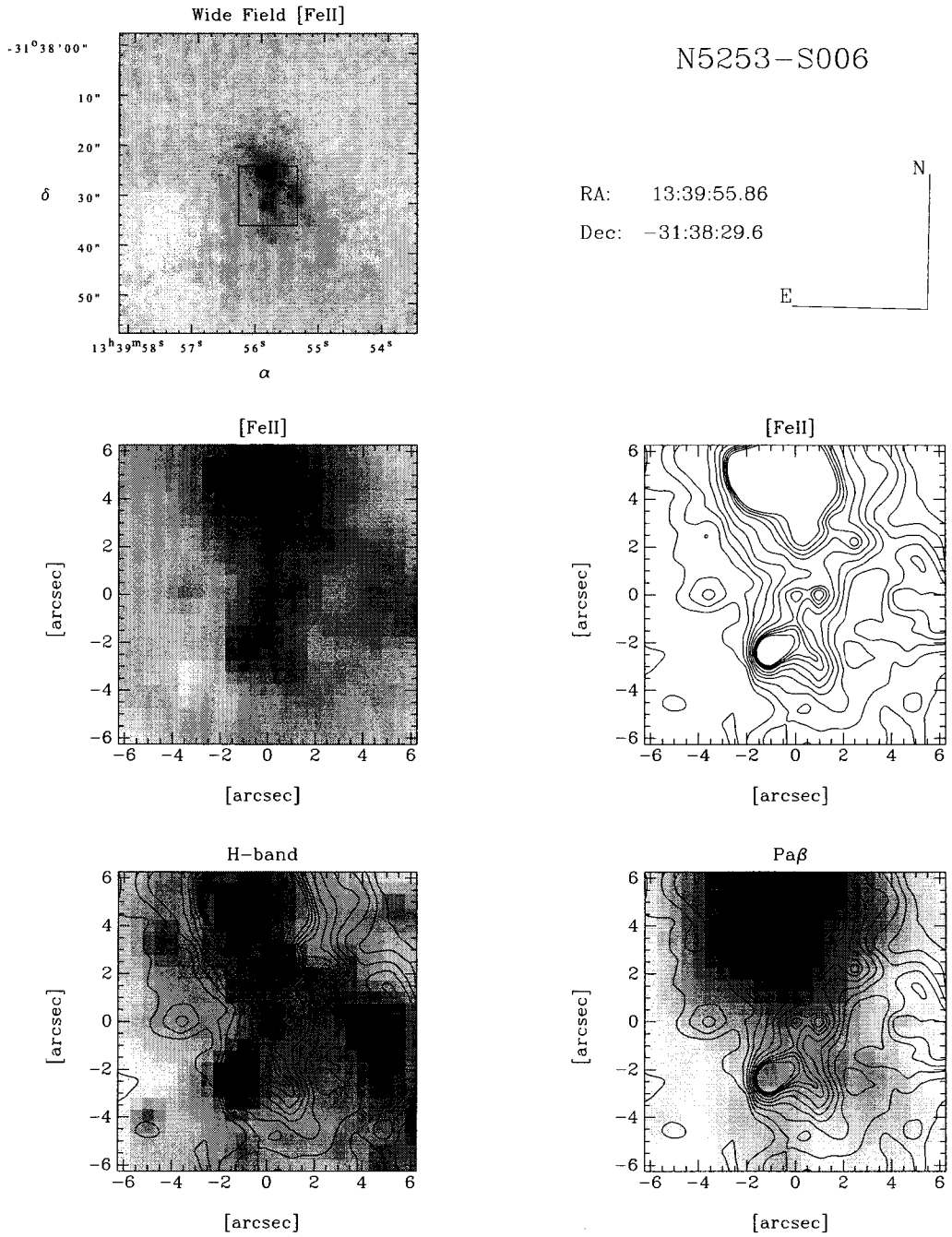

Figure C.21: Comparison of the [Fe II] λ1.644 μm image and contour map of N5253-S006 with the H-band and Paβ λ1.282 μm images. The contours are drawn for 7, 9, 11, 13, 15, 17, 19, 20, 21, 22 σ. Refer to Section C.1 for more details.

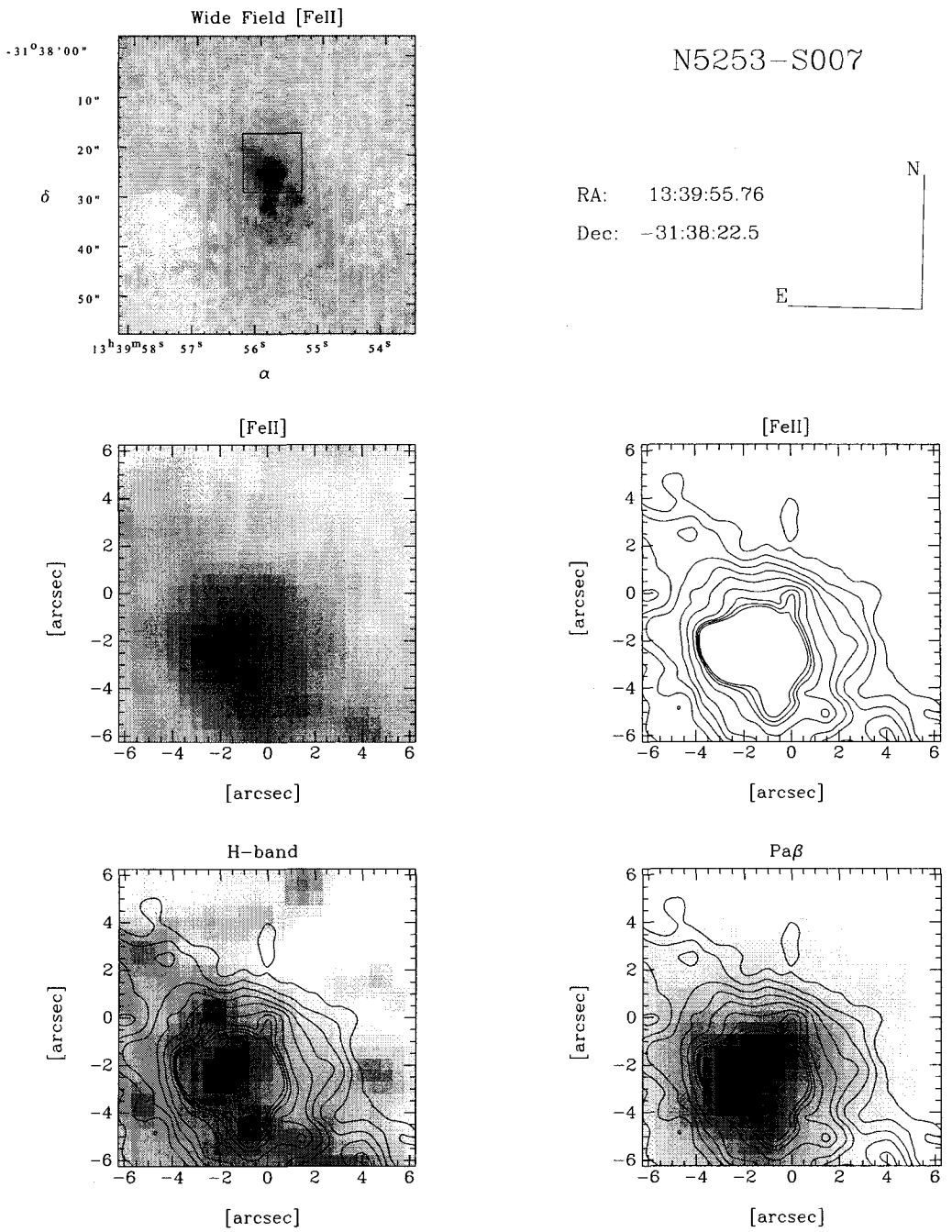

Figure C.22: Comparison of the [Fe II] $\lambda 1.644\ \mu$m image and contour map of N5253-S007 with the H-band and Paβ $\lambda 1.282\ \mu$m images. The contours are drawn for 7, 9, 11, 13, 15, 17, 19, 20, 21 σ. Refer to Section C.1 for more details.

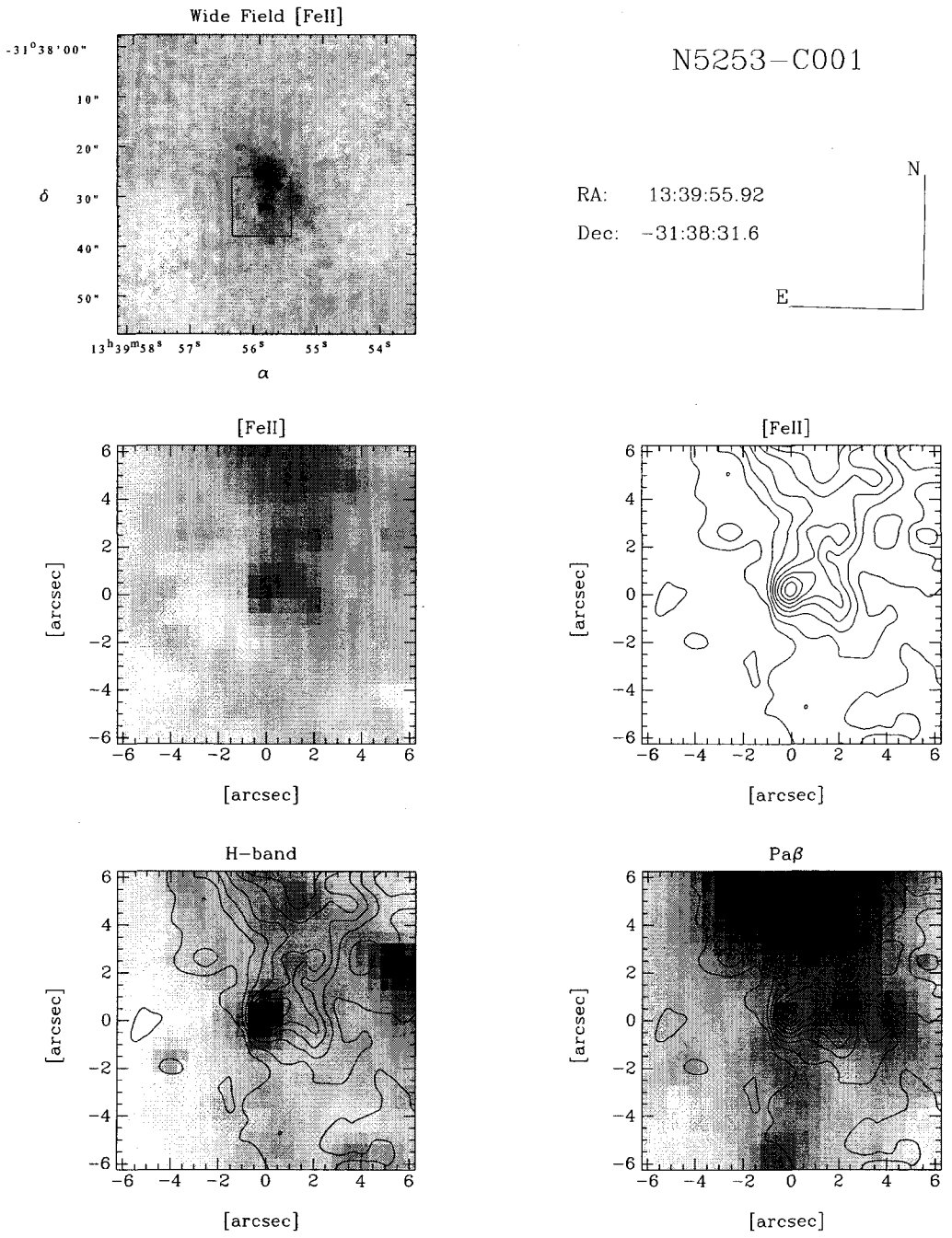

Figure C.23: Comparison of the [Fe II] λ1.644 μm image and contour map of N5253-C001 with the H-band and Paβ λ1.282 μm images. The contours are drawn for 7, 10, 13, 16, 19, 22, 25, 28 σ. Refer to Section C.1 for more details.

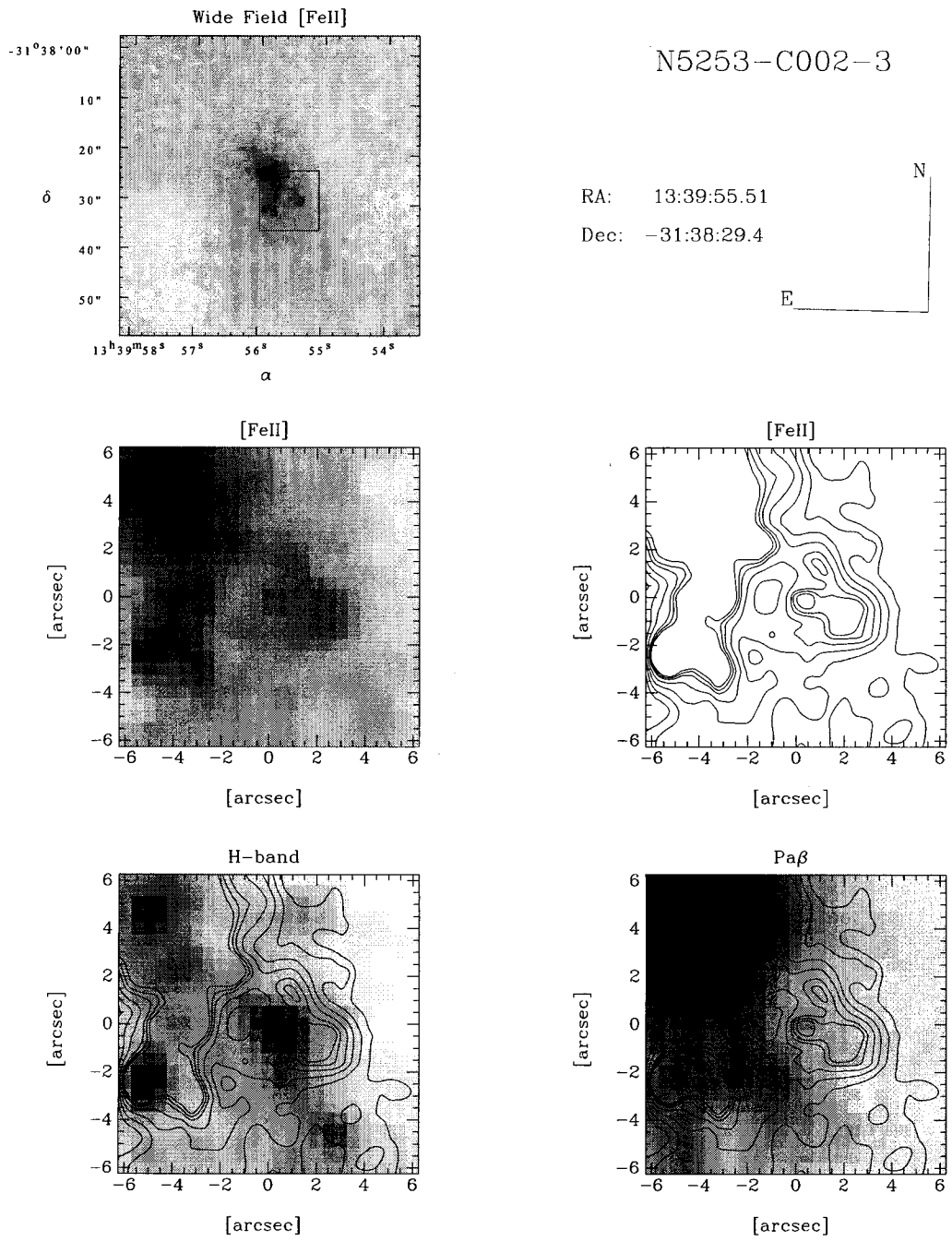

Figure C.24: Comparison of the [Fe II] λ1.644 μm image and contour map of N5253-C002-3 with the H-band and Paβ λ1.282 μm images. The contours are drawn for 6, 8, 10, 12, 14, 15, 16 σ. Refer to Section C.1 for more details.

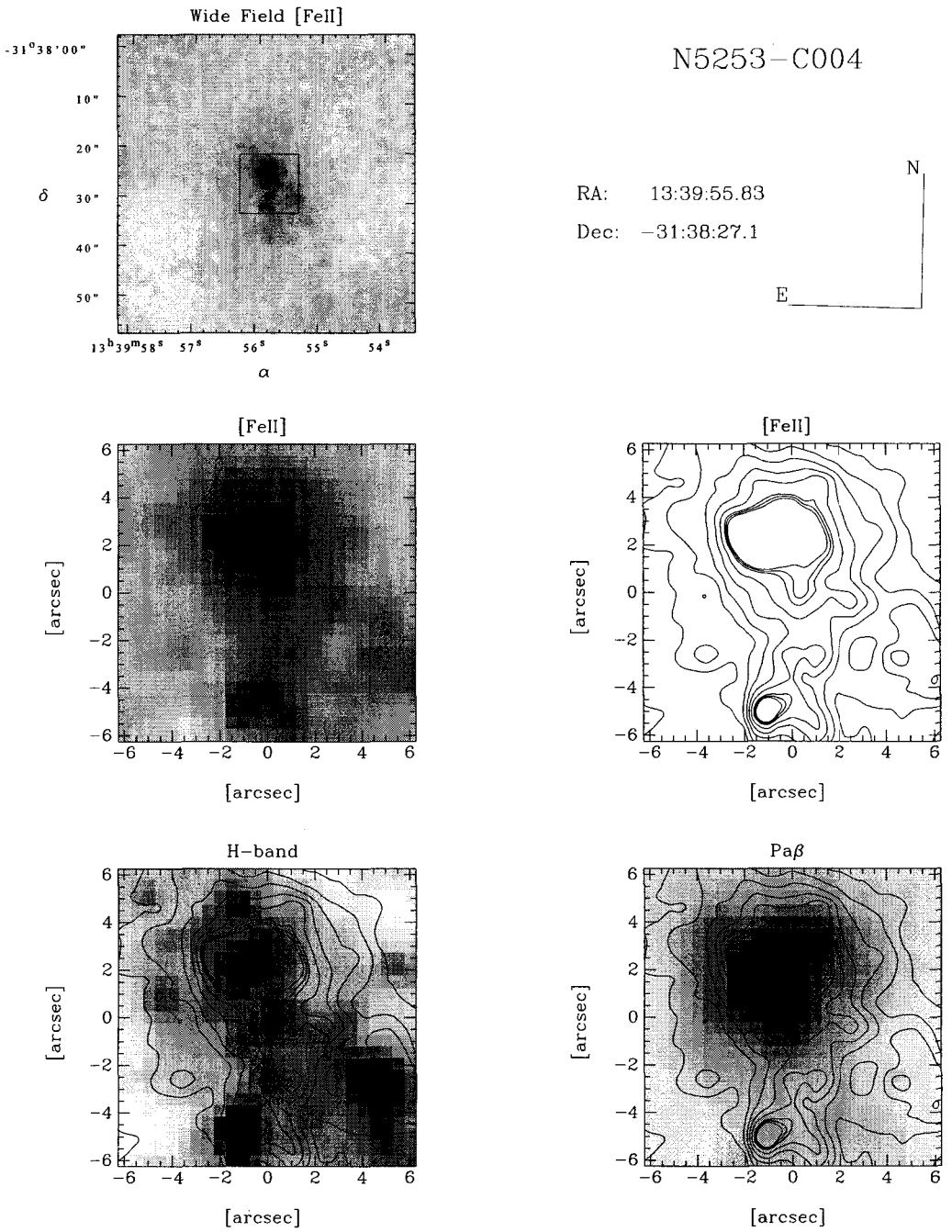

Figure C.25: Comparison of the [Fe II] λ1.644 μm image and contour map of N5253-C004 with the H-band and Paβ λ1.282 μm images. The contours are drawn for 7, 10, 13, 16, 19, 22, 23, 24 σ. Refer to Section C.1 for more details.

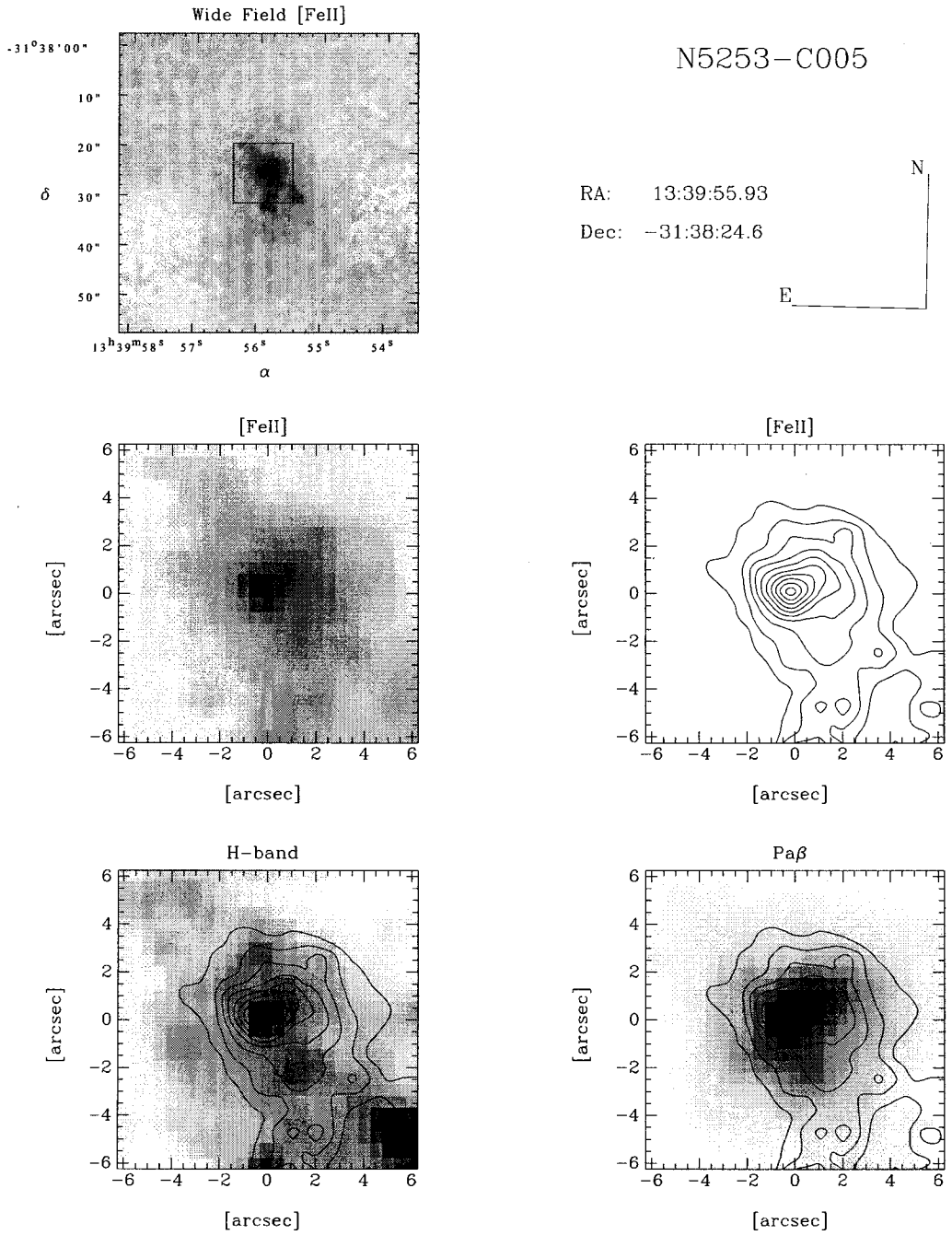

Figure C.26: Comparison of the [Fe II] λ1.644 μm image and contour map of N5253-C005 with the H-band and Paβ λ1.282 μm images. The contours are drawn from 12σ to 48σ, with steps of 4σ. Refer to Section C.1 for more details.

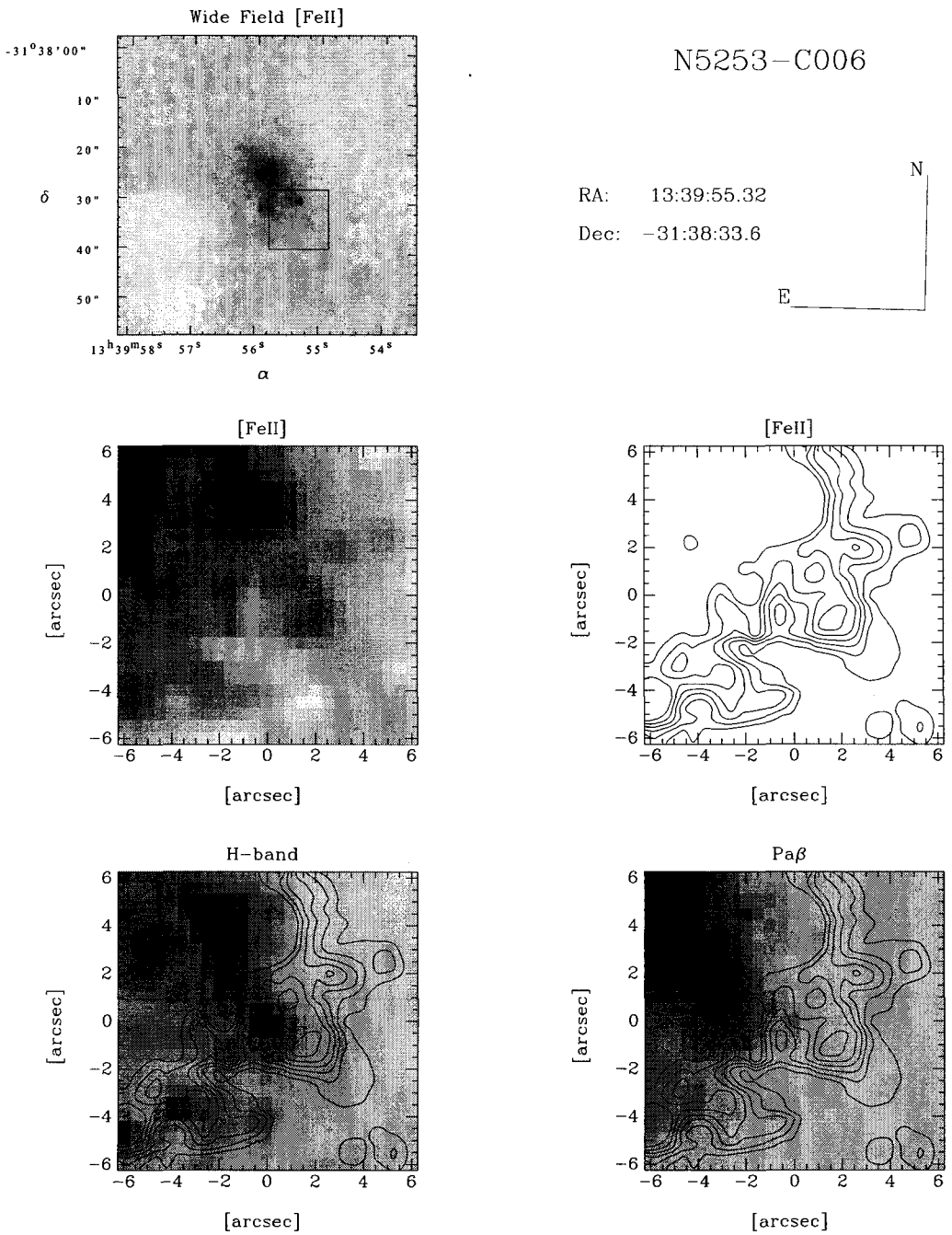

Figure C.27: Comparison of the [Fe II] λ1.644 μm image and contour map of N5253-C006 with the H-band and Paβ λ1.282 μm images. The contours are drawn from 3σ to 8σ, with steps of 1σ. Refer to Section C.1 for more details.

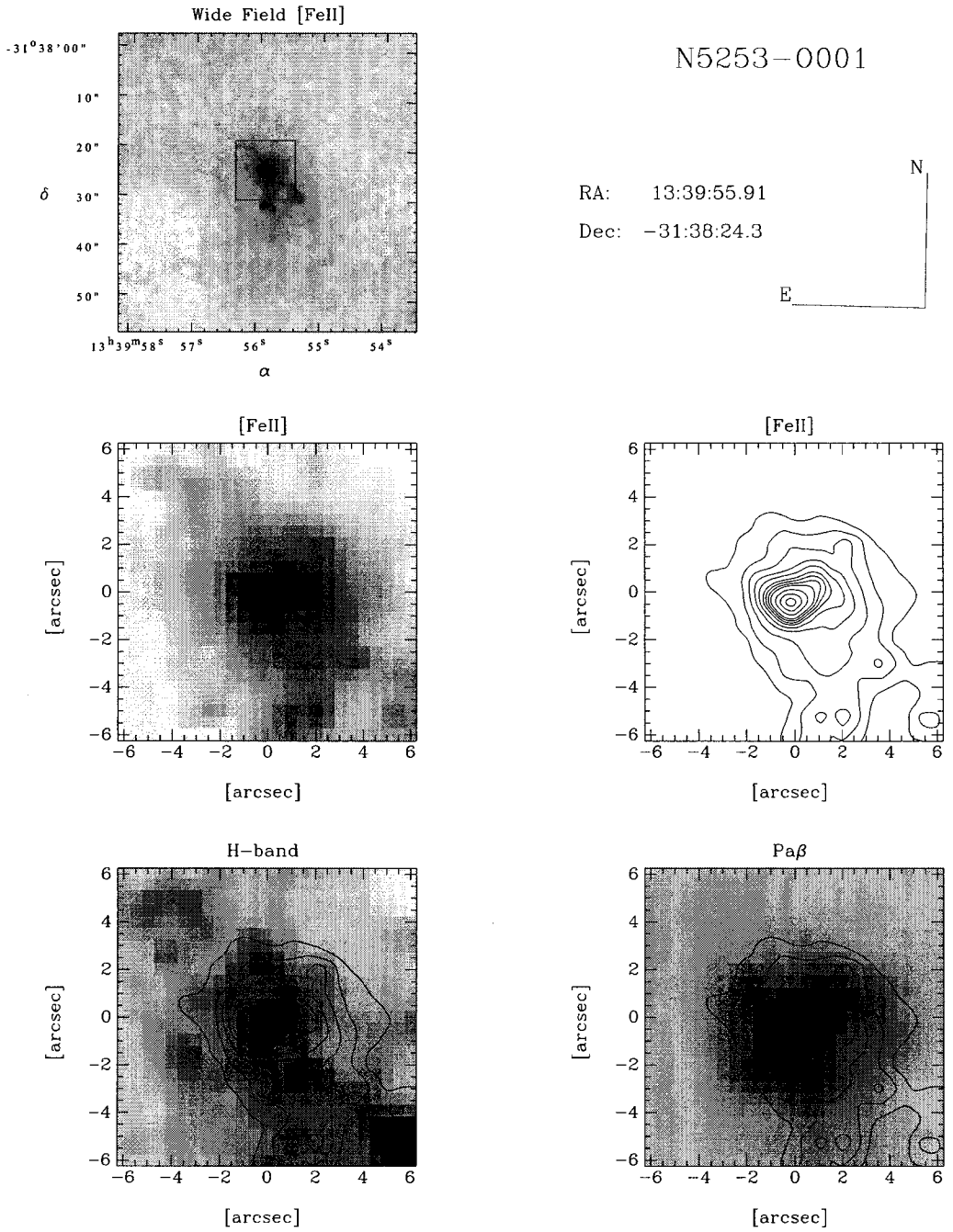

Figure C.28: Comparison of the [Fe II] λ1.644 μm image and contour map of N5253-O001 with the H-band and Paβ λ1.282 μm images. The contours are drawn from 12σ to 48σ, with steps of 4σ. Refer to Section C.1 for more details.

Appendix D

Guide to the Extended Emission Model

Here is the outline of the algorithms used in Chapter 4 to model the extended [Fe II] emission from populations of radiative supernova remnants. The details regarding each step are discussed in Section 4.2.1.

D.1 Outline of the Algorithms

D.1.1 Goodness-of-fit Test [*snrpopfit*]

The user defines a parameter grid to explore. The axes of this grid are the number of SNRs to generate (N_{SNR}), the supernova rate (ν_{SN}), and the pre-shock density (n_0). An aperture, centred on the region of interest, must also be specified by the user.

Other parameters specific to the creation of an artificial SNR population and an artificial image should be set. See *Artificial SNR Population [mksnrpop]* and *Artificial Image [artimg]* later in this appendix (Sections D.1.2 and D.1.3).

snrpopfit

- *Real Image*: Measure total flux and standard deviation within aperture

Loop over the grid parameters (N_{SNR}, ν_{SN}, n_0)
- Create SNR population [*mksnrpop*]
- Create artificial image [*artimg*]
- Mask out undesired pixels
- *Artificial Image*: Measure total flux and standard deviation within aperture
- Calculate goodness-of-fit
- Write to file

End Loop

D.1.2 Artificial SNR Population [*mksnrpop*]

This routine generates an artificial population of supernova remnants. Each remnant is defined by a galactocentric position, a diameter, and a [Fe II] surface brightness. All these values are in physical units.

Input Parameters

- N_{SNR}, ν_{SN}, n_0, [Fe II]-emitting lifetime
- *Spatial Distribution*:
  - scale radius [pc]
  - ellipticity
  - position angle
- *SNR diameters*:
  - Cumulative number–diameter relation for radiative SNRs
- *Luminosities*:
  - Morel et al. (2002) luminosity–n_e relation
  - Shock compression ratio. Gaussian distribution with an average of 30 and σ from Morel et al.

mksnrpop

Loop N_{SNR} times
- Assign galactocentric position
- Assign diameter
- Assign surface brightness if in [Fe II]-emitting regime.

End Loop
- Write population to file

D.1.3 Artificial Image [*artimg*]

This routine creates an image of the SNR population. The image will have the instrumental and noise characteristics specified by the user.

Input Parameters

- Artificial SNR population
- Distance to the SNR population [Mpc]
- X, Y position of the centre of the population
- *Sky*:
  - Seeing ["]
  - Sky background [ADU/pixel/second]
- *Instrument*:
  - Pixel scale ["/pixel]
  - Gain [e^-/ADU]
  - Read noise [ADU]
  - Flux calibration [Wm^{-2}/ADU]
- *Noise*:
  - Poisson noise from real image narrow-band image
  - Additional noise representing effect of data preprocessing
- *Exposure*:
  - Exposure time [s]
  - Number of exposures

artimg

- *Real Image*: Measure Poisson noise

Loop over N exposures

- Add SNR population to image (position, diameter and flux scaling)
- Add sky background
- Multiply by exposure time
- Convolve with seeing
- Add Poisson noise
- Add Read-out noise

End Loop

- Average N exposures
- Remove background
- Add pre-processing noise
- Write image